SPIN PARITY MEASUREMENT OF CENTRALLY PRODUCED $(\pi^+\pi^-)$ IN PROTON-PROTON COLLISIONS AT 800 GeV/c

A Dissertation Presented

by

KYRIACOS MARKIANOS

Submitted to the Graduate School of the
University of Massachusetts Amherst in partial fulfillment
of the requirements for the degree of

DOCTOR OF PHILOSOPHY

February 1998

Department of Physics and Astronomy

SPIN PARITY MEASUREMENT OF CENTRALLY PRODUCED $(\pi^+\pi^-)$ IN PROTON-PROTON COLLISIONS AT 800 GeV/c

A Dissertation Presented

by

KYRIACOS MARKIANOS

Approved as to style and content by:

[redacted]
Edward P. Hartouni, Chairperson

[redacted]
John Donoghue, Member

[redacted]
Michael N. Kreisler, Member

[redacted]
Murugappan Muthukumar, Member

[redacted]
John Donoghue, Department Head
Physics and Astronomy

ACKNOWLEDGMENTS

This lengthy project has taught me above all to depend on others to help me bring my work to fruition. The E690 collaboration has been a small and stimulating group, and I would like to thank all of its members. Ed Hartouni has been my mentor from the start of this effort and has offered his guidance in Massachusetts, Chicago and California. He supported me in pursuing a topic, meson spectroscopy, that our group was not familiar with. His experience with experimental hardware and the nuances of data analysis has been crucial to my education as a physicist and the completion of this dissertation.

Mike Kreisler's leadership and management skills, along with his ability to quickly see through the confusing details of data analysis, were central to the success of this experiment and to my thesis. This project would not have been possible without the pioneering work of the spokesperson for the experiment, Bruce Knapp. His creativity and meticulous attention to detail resulted in an experimental apparatus that in many respects outperformed the original design goals. Gaston Gutierrez was the first to recognize how well suited our apparatus and data sample are for meson spectroscopy. He introduced me to the subject and our work together on problems of partial wave analysis moved this thesis forward. David Christian's advice went beyond the narrow focus of a single experiment and helped me understand physics and physicists. Through the years Alan Wehmann has been a very effective, supportive and unusually calm member of the E690 collaboration. I would also like to acknowledge the help of Christina Berisso, Gerrardo Moreno and Dennis Wesson.

With Al Gara I shared more than the experimental effort. He has been a true inspiration in pursuing unorthodox methods for solving practical and theoretical problems. Along with Ed Hartouni he helped me overcome "hardware fears" and get used to calmly working on experimental problems without the expectation that everything

should work at first try. This happened both while laboring on the data acquisition system of the experiment at Fermilab or while replacing the head gasket of my car's engine at his parents' house in Chicago. With Bill Sippach I had minimal interaction but I came to admire him through the results of his design work for the hardware processor and acquisition system of this experiment.

My fellow graduate students, Brian Derro, Julian Felix, Eric Gottschalk, Shuyu Lee, Marco Reyes, Modesto Sosa, Jorge Uribe, Mike Wang, and Lawrence Wiencke have been companions with whom I shared ideas and frustrations through many years. In particular I thank Mike Wang for the conversations we shared on Interstate 80 from Chicago to California and during two years at Livermore.

I would like to thank the staff at the University of Massachusetts, at FNAL and at LLNL: Judy Ksieniewicz, Ann Cairl, Al McConkey, Dianne Quilty, Bruce Worden, Frank Juravic and Pat Smith helped me greatly with their technical and administrative support. James Walker has been most helpful over the years smoothing communication with the Graduate School administration.

John Donoghue taught me high energy physics from the perspective of a theorist. He and Murugappan Muthukumar were supportive members of my dissertation committee at the University of Massachusetts. S. U. Chung generously shared his preprints on meson spectroscopy that proved crucial to my analysis.

My parents Eleni and Georgos Markianos along with my brother Grigoris have been consistently supportive from afar. Brigitte and Werner Poiger have been tolerant and amused with my inquiry into "exotic states" that have not moved past the candidate stage after all these years. Finally I would like to thank my companion and spouse Uta Poiger who shared the ups and downs of the whole process. Frankly, without her presence and support this work would have never been completed.

ABSTRACT

SPIN PARITY MEASUREMENT OF CENTRALLY PRODUCED $(\pi^+\pi^-)$
IN PROTON-PROTON COLLISIONS AT 800 GEV/C

FEBRUARY 1998

KYRIACOS MARKIANOS, B.A., ARISTOTELIAN UNIVERSITY OF THESSALONIKI

M.A., UNIVERSITY OF MASSACHUSETTS AMHERST

Ph.D., UNIVERSITY OF MASSACHUSETTS AMHERST

Directed by: Professor Edward P. Hartouni

Experiment E690 at Fermilab recorded 5.5 billion $p + p \rightarrow p + X$ events using an 800 GeV/c proton beam and a liquid hydrogen target, during the 1991 fixed target run. We use a 0.5 billion subset of this sample, to study the reaction $p + p \rightarrow p_s(\pi^+\pi^-)p_f$ for dipion invariant mass between threshold and 2.3 GeV/c^2. We perform a partial wave analysis for dipion invariant mass between threshold and 1.5 GeV/c^2. The assumption of S-wave dominance near threshold is sufficient to determine a single, continuous solution throughout the considered mass spectrum. Precision measurement of the production amplitude aids the mapping the low lying meson spectrum. Other possible studies using this data sample and analysis technique are: (1) the extension of the amplitude analysis above the 1.5 GeV/c^2 mass region using a the full event sample, and (2) the study of the produced amplitudes as a function of the relative angle between the two proton planes.

TABLE OF CONTENTS

LIST OF TABLES

LIST OF FIGURES

CHAPTER 1

INTRODUCTION

Experiment E690 at Fermilab recorded 5.5 billion $p + p \rightarrow p + X$ events using an 800 GeV/c proton beam and a liquid hydrogen target during the 1991 fixed target run. A subset of 0.5 billion events from this sample is used to perform amplitude analysis for the reaction $p + p \rightarrow p_s(\pi^+\pi^-)p_f$ for dipion invariant masses between threshold and 2.3 GeV/c^2. Here p_s stands for slow or target proton, and p_f for fast or beam proton. We treat the reaction as a two-step process in which the interaction of the two protons produces a meson which subsequently decays into two pions, independent of the final state protons (see Figure 1.1).

The reaction is characterized by the distribution of the final state particles in terms of their longitudinal momenta. For the great majority of events the two final state protons and the dipion system are kinematically well separated (Figure 1.2). In the overall center of mass system, the two final state protons have longitudinal momentum close to the maximum allowed ($x_F \pm 1$), where x_F (Feynman x) is defined as the longitudinal momentum of the particle divided by the maximum momentum the particle can have in this reaction, while the dipion system distribution is confined in the central region (x_F close to 0). The longitudinal momentum distribution of the dipion (meson) state is the reason that such a reaction is referred to as "central production".

The kinematics of central production suggest that the central meson is produced through a double exchange process (Figure 1.1). This is the justification for analyzing the interaction as a two-step process. The goal of this thesis is twofold: to measure the quantum numbers of centrally produced mesons and to measure how the relative intensity of the produced states changes as a function of the parameters describing the final state

protons (for example four-momentum transfer (t), or relative angle of proton planes). We use the two pion momentum vectors to determine the mass and width of the produced states. In addition, we use the angular distribution of the two final state pions to perform a partial wave analysis and determine the spin and parity of the states produced.

One of the reasons for interest in central production is that this kind of interaction is considered a rich production environment for exotic states [1]. When the dominant theory of strong interactions (QCD) was proposed more than twenty years ago, one of the novel and unexpected (from SU(3)) consequences of the theory was the prediction of states that are neither baryons (qqq) nor mesons ($q\bar{q}$). These "extraordinary" or exotic states are referred to as glueballs (gluon-only bound states, gg), multi-quark states (four or six quark states, $q\bar{q}q\bar{q}$, $qqqqqq$), or hybrids (quark gluon bound states, $gq\bar{q}$). After 20 years of searching in numerous experiments, no conclusive evidence exists for an exotic state. [2]

Experimental searches for exotic states have concentrated mostly on attempts to observe gluon-only states (gg). This is because of the expectation that such states will have distinct signatures. Exotic states which contain valence quark constituents are expected to be more difficult to distinguish from conventional states than glue only states. The searches can be classified by the production mechanisms they use to produce the exotic states. Experimenters have looked for reactions in which production of glue rich states might be favored over production of conventional states. A reaction is considered gluon rich if there is a restriction in the propagation of quarks from the initial state particles to the particles of interest in the final state. Historically, the reactions considered fertile ground for exotic states are [1]:

* J/Ψ radiative decay
* $p\bar{p}$ annihilation.
* Central production

I will restrict the discussion to mesons since they are the states observable in our apparatus, given the requirement that the two initial state protons survive the interaction. A main reason that it is difficult to demonstrate conclusively that a given state is a glueball is the absence of an undisputed criterion that distinguishes between conventional and exotic mesons. Unfortunately exotic states do not come with flags revealing their identity. Rather, the most reliable method to identify exotic states is by a process of elimination. If more than one state occupies a position in a given SU(3) or SU(6) spin parity multiplet, one of the extra states must be non-conventional. First, the spin parity multiplets of conventional states must be filled with observed states from experiment. Extra states observed experimentally to have the same assignments as states already in the spin parity multiplet do not fit the quark constituent model. This is feasible for the low lying meson multiplets, with members that have masses up to about 2 GeV/c^2. It is much more difficult for higher mass states because the states are much closer in terms of mass and much more difficult to distinguish from each other. An additional source of confusion is the possible existence of "molecular states". Here the term "molecular state" refers to a short lived bound state of two conventional mesons. In such a four valence quark configuration the resulting state would be best described as the bound state of two distinct meson wavefunctions. The grouping of the four quarks in two distinct pairs distinguishes such states from the $q\bar{q}q\bar{q}$ exotics mentioned above. For the $q\bar{q}q\bar{q}$ exotics we expect all four valence quarks to have a totally symmetric wave function with respect to the valence quark constituents.

A current list of light meson assignments from the Particle Data Group [3] (PDG) is shown in Table 1.1. We can see from the table that there are multiplet positions that are not assigned with experimentally observed states. There are also multiplet positions that are controversial and have more than one candidate assignment. In addition to the states mentioned in the table, there are states in the full listings of the PDG that have not been clearly observed or have been observed by only one experiment. Conversely, there are

additional states not mentioned in the table which have been observed by more than one experiment and their existence is not disputed. However, they are difficult to classify since their positions are occupied in the multiplet assignments and exhibit properties that make them likely but controversial glueball candidates. The states that belong to the last category have received the most attention in recent years. Of this group, those considered the most interesting are: $f_1(1420)$, $f_0(1500)$ and $f_J(1710)$. All three of the states are predominantly observed in the "glue rich" production mechanisms mentioned earlier.

The $f_1(1420)$ has a puzzling history due to different spin parity (J^{PC} where J is the spin, P is the parity and C is charge conjugation quantum number) assignments given to the state by experiments conducted in different production environments. It was observed [4] in $\pi^- p \to K_S^0 K^{\pm}\pi^{\mp} n$ with spin parity 1^{++} and mass 1426 MeV/c^2. Two years later a report from $J/\Psi \to K^+K^-\pi^0$ observed [5] a state with spin parity 0^{-+} and mass 1440 MeV. This led to the suggestion that two different states are produced, depending on the production mechanism: a conventional meson, named E(1420) with $J^{PC} = 1^{++}$, and a possible glueball the ι(1440) with $J^{PC} = 0^{-+}$. The so called E/ι puzzle became more complicated when neither of the states was observed in K^- induced reactions. The LASS collaboration observed [6], in $K^- p \to K_S^0 K^{\pm}\pi^{\mp}\Lambda$, a resonance at 1530 MeV with spin parity 1^{++}. Since conventional meson $s\bar{s}$ states are expected to be favored in K^- induced reactions, the non-observation of the E(1420) by LASS cast doubt on the $s\bar{s}$ content hypothesis of this state. In central production, experiments WA-76 [7] at CERN and FNAL E690 [8] both observed with high statistics a state at 1420 MeV with $J^{PC} = 1^{++}$ in the reaction $pp \to p_f K_S^0 K^{\pm}\pi^{\mp} p_s$. Since central production is not a reaction that favors $s\bar{s}$ production, these observations make it unlikely that $f_1(1420)$ is a conventional state. The most likely candidate for the isosinglet 1^{++} multiplet is the state observed by LASS, noted as $f_1(1510)$ in the PDG table. Therefore the $f_1(1420)$ has currently no place in the conventional $q\bar{q}$ spectrum, but its nature its still not resolved. The history of this state

underscores how important it is to observe a resonance in more than one production environment.

The $f_0(1500)$ and $f_J(1710)$ have been observed in more than one production environment. Although the spin of the $f_J(1710)$ is not resolved, its existence around 1710 MeV/c^2 is not disputed. Interest in both states is related to advances in the theoretical understanding of the meson spectrum. A recently published theorem [9] on the mass of the lowest lying glueball asserts that the lowest (in terms of mass) lying state should have $J^{PC} = 0^{++}$. This agrees with recent results from Lattice QCD calculations. There are two Lattice QCD results that attempt to calculate the properties of low lying glueballs and identify physical states that correspond to the calculation results. For the lowest lying state the UKQCD [10] collaboration predicts mass M=1550±50 MeV/c^2 and width Γ=245±50 MeV/c^2 respectively, while the prediction from the IBM group [11,20] is M=1740±70. The UKQCD collaboration identifies as the corresponding physical state the (currently noted) $f_0(1500)$. At the time the study was published, the state was observed by the GAMS collaboration [12] with mass 1590 MeV and with higher statistics by the Crystal Barrel collaboration [13] in the process $p\bar{p} \rightarrow \eta\eta\pi^0$ with mass 1560±25 MeV/c^2 and width 245±50 MeV/c^2. Later, the Crystal Barrel collaboration performed a simultaneous analysis of the final states $\pi^0\pi^0\pi^0$, $\pi^0\pi^0\eta$ and $\pi^0\eta\eta$. The new analysis [14] found the mass and width of the state to be 1500±10 MeV/c^2 and 154±30 MeV/c^2 respectively. Hence the current notation $f_0(1500)$.

Proximity to the mass and width of a Lattice QCD calculation is not the only argument that makes $f_0(1500)$ a good glueball candidate. The quantum numbers reported by Crystal Barrel ($J^{PC} = 0^{++}$), classify the state in a nonet with more observed physical states than the $q\bar{q}$ model can accommodate (see Table 1.1). Of course the same argument can be used for other states in the nonet. In order to distinguish which state does not fit, we need a classification scheme at least for the members of this nonet. I will return to this

issue after presenting the arguments advanced by the IBM Lattice group. This group favors the $f_J(1710)$ with spin assignment $J^{PC} = 0^{++}$ as the manifestation of the lowest lying glueball. Over the years the assignment for the state has changed between $J^{PC} = 0^{++}$ and $J^{PC} = 2^{++}$.

The state has been clearly observed only in "gluon rich" production environments. In J/Ψ decays the state was observed by the MARK III collaboration in the reaction $J/\Psi \to \gamma K^+K^-$ and $J/\Psi \to \gamma K_s^0 K_s^0$. The spin parity determination [15] for the state was 2^{++}. However, further analysis [16] revealed a significant spin 0 component for the state. The state was observed clearly in central production by the Omega spectrometer at CERN in the reactions $pp \to p_f K^+K^- p_s$ and $pp \to p_f K_S^0 K_S^0 p_s$. They used only the K^+K^- sample for spin parity analysis and found [17] $J^{PC} = 2^{++}$. FNAL E690 has observed [18] the same state in the reaction $pp \to p_f K_S^0 K_S^0 p_s$ and found that the state is compatible with both assignments but the most likely assignment is $J^{PC} = 0^{++}$. Although the state decays mostly to kaons, indicating a probable $s\bar{s}$ content, it is not observed in K^-p reactions. The LASS collaboration studied the reaction $K^-p \to K_s^0 K_s^0 \Lambda^0$. They report [19] no signal in the $f_J(1710)$ region, making unlikely the classification of the state as a predominantly $s\bar{s}$ meson. In addition to the observations about the $f_J(1710)$ the LASS collaboration finds in the 1500 MeV region the well established $f_2(1525)$ and very small S-wave contribution, therefore offering the same argument on $s\bar{s}$ content for both the $f_J(1710)$ and $f_0(1500)$. After their initial publication on the glueball spectrum, the IBM Lattice group published another study [21] where they examine the possibility that neither state is a pure quarkonium or a pure glueball. They find that $f_0(1500)$ is a mostly $s\bar{s}$ state while $f_J(1710)$ is mostly a glueball.

In the previous paragraph the statement that a meson can be mostly a glueball has to do with the fact that states can interfere through final state interactions. In the previous discussion we assumed the validity of the static quark model as a guide to meson

spectroscopy and a one to one correspondence between ideally mixed quark states and the physical states observed in the laboratory. Although this picture works well for pseudoscalar and vector mesons (where departure from the ideal SU(3) states is small), the classification is not as clear for the scalar mesons.

In fact the QCD properties that lead to the search for exotic states dictate that the meson picture should be much more complicated than the static quark model description. Instead of "bare" quarks we have to deal with quark currents surrounded by a cloud of gluons and a sea of $q\bar{q}$ pairs. The complexity introduced by the many body problem makes QCD not yet calculable from first principles in the low energy regime (also known as the confinement regime). This is a problem that afflicts also the Lattice QCD calculations mentioned above. The lattice QCD groups make the computation manageable through a technique known as "quenching". In essence the effect of $q\bar{q}$ pair production is not allowed to enter the calculation and is instead approximated with the use of observed properties of the well established vector and pseudoscalar mesons. Since at the present time there is no exact QCD solution to the low energy spectrum, we are forced to use either the predictions of Lattice QCD or phenomenological models that use model dependent assumptions to classify the spectrum.

Although these phenomenological models do not offer an exact solution they provide valuable insight into the properties of the meson spectrum. There is a variety of methods that have been used in the construction of phenomenological models. They range from models that use a simplified version of the QCD Langrangian and introduce the full Langrangian later as a symmetry breaking effect to models that use just quantum mechanics and conservation laws to relate the results of several experiments. The large number of models developed over the years presents too vast a topic to cover here. I will restrict the discussion to two recent computations that try to classify the 0^{++} nonet.

The first is a model developed by N. Tornqvist [22] and sheds light on the significance of interactions in the mass, width and shape of the mesons that compose the multiplet. The calculation starts with the "bare QCD" configuration which corresponds to the static quark model. Here the ad hoc assumption is that we know the mass and composition in terms of quark content of the states, assuming that no interactions are present and the states are stable. With the introduction of interactions each state can be written as an expansion of the "base state" plus the possible decay states given energy conservation and the conservation of quantum numbers in the decay process. The method is applied for both the well established 1^{--} multiplet and the 0^{++} multiplet whose states we want to identify. For the 1^{--} states the result is the physical states observed in the laboratory, not far from the initial assignments. The effect of interactions is much more significant for the 0^{++} mesons because unlike the 1^{--} (vector) mesons the decay channel to two S-wave pseudoscalars is available ($0^{++} \rightarrow 0^{-+}0^{-+}$). The differences are dramatic. The mass of the 0^{++} multiplet members shifts by more than 400 MeV/c^2, although the mass hierarchy implied by the mass of the strange quark is preserved. Although it is a model calculation, the model is valuable for the minimal set of assumptions it uses to demonstrate the possible differences between "pure states" and the states observed in the laboratory. A second model by Amsler and Close [23] attempts a similar calculation. The difference is that instead of the nine $q\bar{q}$ seeds used by Tornqvist they consider 10 seeds, nine $q\bar{q}$ seeds plus a glueball (gg) seed. Here the term seed implies the initial, unpertubed states used for the calculation. They use perturbation theory to derive the mass and width of the observed mesons. Among the final assignments they find, the $f_0(1500)$ is mostly a glueball while the $f_j(1710)$ is mostly an $s\bar{s}$ state.

A different attempt to extract information about the meson spectrum is the use of conservation laws, and in particular universality of amplitudes and conservation of probability (unitarity of S-matrix). This is a different approach because the starting point is not an assumption about the constituents and their interactions that leads to the calculation

of "stable" bound states. Here the attempt is to calculate and relate the production amplitudes in various reactions. The meson states and their mass and width are inferred from the poles of the scattering matrix. This method allows one to relate experimental measurements from a number of different production mechanisms such as central pp production and heavy flavor meson decays (e.g. $J/\Psi \rightarrow \phi\pi\pi$) using the universality of the $\pi\pi$ scattering amplitude.

A study using the S-matrix universality that is relevant to the measurement presented here was performed by Au, Morgan and Pennington [24] (AMP). At the time of publication the study relied mostly on data from the ISR Axial Field Spectrometer (AFS) measurements [25]. This is the first high statistics measurement for double Pomeron production of the $pp \rightarrow p\pi^+\pi^- p$ final state. The conditions for the application of the Au, Morgan and Pennington method are fairly severe. The only waves that are allowed to enter the picture are isospin 0 and S=0 waves. This reduces the dimensions of the S-matrix and makes use of the Unitarity constraint feasible. These conditions match the properties of double Pomeron exchange at small four momentum transfer (t). Furthermore, they restrict the final states that enter the analysis to $\pi\pi$ and $K\overline{K}$ by imposing an upper limit to the mass spectrum under consideration at 1 GeV. With this limit, the only channel that is not accounted for is the 4π final state. The cross section for this final state below 1 GeV is sufficiently small that it can be ignored.

Using these restrictions they proceed to calculate the poles of the scattering matrix and conclude that three 0^{++} states exist with mass below 1 GeV. They tentatively name them $f_0(991)$, $f_0'(988)$ and $f_0(900)$. Since this is again the 0^{++} multiplet with its oversubscribed spectrum, they conclude that only two of the states have a place in the multiplet classification of conventional mesons and one of them has to be an extra state. The model draws its parameters from the "classic" pion scattering data [26] in $\pi^- p \rightarrow \pi^+\pi^- n$, and the $pp \rightarrow p\pi^+\pi^- p$, $pK^+K^- p$ data from the AFS experiment mentioned

above. Application of the results to new data from Mark III and DM2 in charmed decays ($J/\Psi \rightarrow \phi\pi\pi, \phi K^+K^-$) revealed inconsistencies that forced the authors to reevaluate their claims [27,28]. They attribute the discrepancies to the sensitivity of the method to the relative cross section for $\pi\pi$, $K\overline{K}$ production near kaon threshold. The method is most sensitive to the measurement by the AFS collaboration. The AFS measurement is performed at the ISR, where the central meson is produced almost stationary in the laboratory. Therefore the decay products are not boosted in the laboratory and the resulting inefficiencies require significant acceptance corrections. We note that these concerns will not be a factor in the measurement reported in this thesis. Because the FNAL E690 measurement is performed in a fixed target environment the boost is significant ($\gamma \equiv 20$) and detector acceptance varies slowly as a function of the analysis variables, the only significant variation is the dependence of acceptance on the x_F distribution of the central meson. Although the subsequent publications reevaluate the accuracy of the initial claims, the authors insist that the method requires a narrow (50 MeV/c^2) state at 1 GeV which they note as $f_0(S^*)$ and is responsible for the phase shift observed in $\pi^- p \rightarrow \pi^+\pi^- n$ and the sharp drop at 1 GeV observed in the pion spectrum of central production. This is in disagreement with an alternative parametrization by Zou and Bugg that claims a wider state [29]. As proof for that claim, they offer a comparison of the predictions of the two models for the pion spectrum in the decays $J/\Psi \rightarrow \phi\pi\pi, \phi K^+K^-$. They state that in terms of input from the data the most important measurement remains a precise cross section ratio for $\pi^+\pi^-, K^+K^-$ final states close to 1 GeV in central pp reactions.

Other experiments that have measured the centrally produced $\pi^+\pi^-$ state are a series of fixed target experiments performed at CERN using the OMEGA spectrometer (WA76, WA91 and WA102) and another ISR experiment, the Split Field Magnet (SFM) collaboration. Although the series of fixed target experiments at CERN has good acceptance and adequate statistics, there are significant reservations about the use of this data set in the study mentioned above. One of the problems is the use of the final state

slow proton (target proton) as an on-line selection trigger. For double Pomeron (double diffractive) interactions the slow proton has very small longitudinal momentum in the laboratory and appears as a particle traveling perpendicular to the beam direction. In order for the slow proton to "survive" multiple scattering and emerge from the target, minimum p_t requirements must be satisfied. For the target used by the OMEGA spectrometer the minimum momentum is about 200 MeV/c. Since the four momentum transfer (t) in the kinematics region of the experiment is approximately equal to $-p_t^2$ the trigger requirement dramatically reduces the number of events with small four momentum transfer (t). The result is departure from the low t production regime where double Pomeron exchange is expected to dominate. This is evident in the K^+K^- spectrum [30] of the experiment where a prominent $\phi(1020)$ peak appears. Since $\phi(1020)$ has $J^{PC} = 1^{--}$ the state cannot be the product of the collision of two $J^{PC} = 0^{++}$ exchange particles (Pomerons).

The OMEGA spectrometer group performed a coupled channel analysis [30] on their $\pi^+\pi^-, K^+K^-$ data, using a scheme quite different from the AMP method. Instead of using a unitarity constraint they require that resonances have the same mass and width in the two channels but allow for independent, interfering "background" production in the two final states. An interesting result from this analysis is that it attributes the sharp drop in the $\pi^+\pi^-$ mass spectrum at 1500 MeV to a resonance present in both $\pi^+\pi^-, K^+K^-$ channels with mass 1472 MeV and width 195 MeV, remarkably close to the $f_0(1500)$ reported by the Crystal Barrel collaboration. In a later study [31] they compare the $\pi^+\pi^-$, $\pi^+\pi^-\pi^+\pi^-$ spectra and confirm the 1500 MeV state in the $\pi^+\pi^-$ spectrum. They do not observe the same state in the 4π final state. The two studies do not analyze the angular distribution of the $\pi^+\pi^-$ final state and are based exclusively on fits of the mass spectra observed. Compared to the OMEGA spectrometer measurements the data sample to be presented in this thesis has better statistics, higher center of mass energy and no restrictions for low t

scattering but lacks a sensitive recoil detector in the vicinity of the hydrogen target for background suppression.

In a different effort to identify exotic states, the Split Field Magnet collaboration (SFM) at the ISR studies the dependence of the $\pi^+\pi^-$ spectrum in low t, $pp \rightarrow p\pi^+\pi^- p$ reactions to correlations in the final state protons [32]. In particular they study the correlation of the $\pi^+\pi^-$ mass spectrum to the angle between the $\vec{p}_t$ vectors of the two diffractive protons. They find that there is a correlation, most prominent in the mass region of $f_2(1270)$, a well established $q\bar{q}$ meson. Another search for correlations in the final state protons was reported later by the OMEGA spectrometer [33]. The investigation was prompted by a puzzling change in the mass spectra observed by the experiment after an upgrade to their detector. The addition of a second recoil detector for trigger on the slow diffractive proton changed the ratio of events with protons scattering to the same side of the detector over the number of events scattering in opposite directions. This led to a classification of the sample in same side/opposite side triggers. The difference in the two samples is a remarkable suppression of well established conventional mesons when the two protons scatter in the same direction. In a follow up publication [34], they choose to classify the sample as a function of a variable called difference in transverse momentum $dp_t = \sqrt{\vec{p}_{t(f)} - \vec{p}_{t(s)}}$,where $\vec{p}_{t(f)}$, $\vec{p}_{t(s)}$ are the fast and slow final state proton transverse momenta respectively. Although the variable lumps together events that have small four momentum transfers (t) with events that have significant momentum transfers but similar transverse momentum for the final state protons, it offers a remarkable filter for the suppression of conventional mesons and enhancement of glueball candidate states. In particular, for low values of dp_t in the $\pi^+\pi^-$ sample, the $\rho(770)$ and $f_2(1270)$ disappear although they are quite prominent for data with high dp_t. In a similar fashion in the K^+K^- sample, the $f_J(1710)$ signal is enhanced for low dp_t. Similar examples are offered for other final states. In a publication titled "A Glueball-$q\bar{q}$ filter in Central Hadron Production", F. E. Close and A. Kirk attempt to provide an explanation for the correlations

observed by the OMEGA collaboration [35]. They cover plausible theoretical arguments for the origin of the mass spectrum dependence on dp_t but they admit no obvious or rigorous theoretical explanation. Nevertheless they argue that the empirical observations are so dramatic that they warrant further investigation and point to the possibility of using the proton correlations as a filter for distinguishing between conventional and exotic mesons. Here it is worth noting that the assumption that Pomeron-Pomeron production dominates central pp reactions, important in the Au, Morgan and Pennington parametrization of pion scattering, does not allow for the final state proton correlations mentioned above. If the correlations are confirmed, one either has to allow for additional physics, or has to limit observations to a kinematic regime in which these correlations vanish. Again the data sample in this thesis offers the opportunity for such an investigation.

In conclusion the work presented here is going to contribute in both the measurement of relative cross sections of $\pi^+\pi^-, K^+K^-$ near the K^+K^- threshold and in the study of correlations between final state protons and their impact on the observed $\pi^+\pi^-$ spectrum. Because the statistics are much higher than any other experiment in this regime and the acceptance varies very slowly as a function of the analysis variables, this experiment has the opportunity to provide valuable and reliable information about the centrally produced meson spectrum.

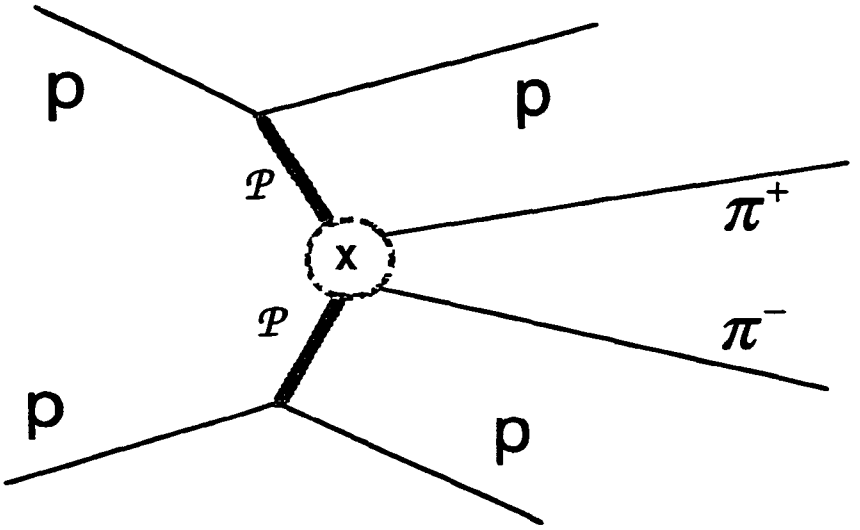

Figure 1.1 Central production as a two-step process. Here the exchange particles are noted as pomerons. In general any Reggion can be exchanged.

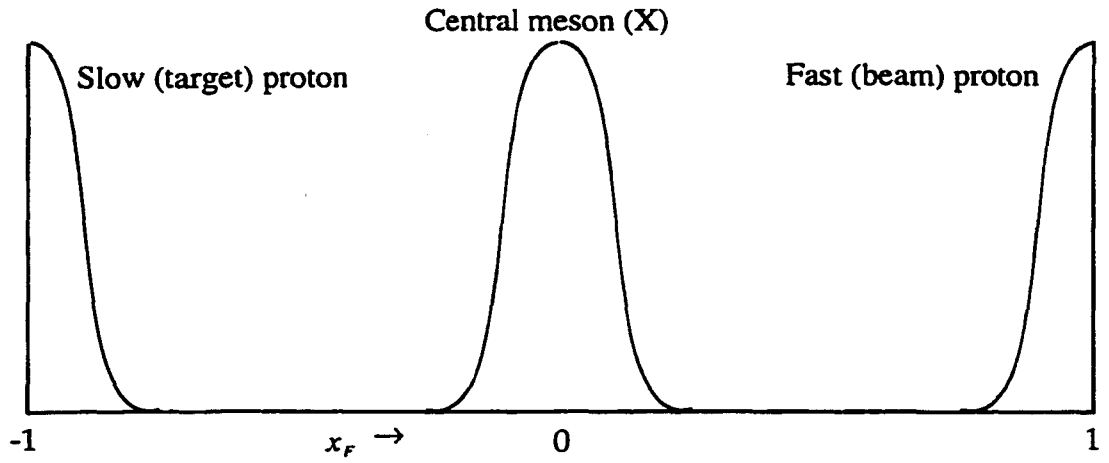

Figure 1.2 Central production, expected x_F distribution.

Table 1.1 Meson assignments from Particle Data Group.

$N\ ^{2S+1}L_J$	J^{PC}	$u\bar{d}, u\bar{u}, d\bar{d}$ $I=1$	$u\bar{d}, u\bar{u}, d\bar{d}$ $I=0$	$\bar{s}u, \bar{s}d$ $I=1/2$
$1\ ^1S_0$	0^{-+}	π	η, η'	K
$1\ ^3S_1$	1^{--}	ρ	ω, ϕ	$K^*(892)$
$1\ ^1P_1$	1^{+-}	$b_1(1395)$	$h_1(1170), h_1(1380)$	K_{1B}
$1\ ^3P_0$	0^{++}	$a_0(980) / a_0(1450)$	$f_0(400-1200) / f_0(980) / f_0(1370)$	$K_0^*(1430)$
$1\ ^3P_1$	1^{++}	$a_1(1260)$	$f_1(1285), f_1(1510)$	K_{1A}
$1\ ^3P_2$	2^{++}	$a_2(1320)$	$f_2(1270), f_2'(1525)$	$K_2^*(1430)$
$1\ ^1D_2$	2^{-+}	$\pi_2(1670)$		$K_2(1770)$
$1\ ^3D_1$	1^{--}	$\rho(1770)$	$\omega(1600)$	$K^*(1680)$
$1\ ^3D_2$	2^{--}			$K_2(1820)$
$1\ ^3D_3$	3^{--}	$\rho_3(1690)$	$\omega_3(1670), \phi_3(1850)$	$K_3^*(1780)$
$1\ ^3F_4$	4^{++}	$a_4(2040)$	$f_4(2050), f_4(2220)$	$K_4^*(2045)$
$2\ ^1S_0$	0^{-+}	$\pi(1300)$	$\eta(1295)$	$K(1460)$
$2\ ^3S_1$	1^{--}	$\rho(1450)$	$\omega(1420), \phi(1680)$	$K^*(1410)$
$2\ ^3P_2$	2^{++}		$f_2(1810), f_2(2010)$	$K_2^*(1980)$
$3\ ^1S_0$	0^{-+}	$\pi(1770)$	$\eta(1760)$	$K(1830)$

CHAPTER 2

APPARATUS

2.1 Overview

The experiment was designed to study a subset of proton-proton interactions where at least one of the interacting protons survives the reaction. For this experiment, 800 GeV/c protons interact with a 14.3 cm, 2% interaction length liquid hydrogen target. For all events recorded we require that the beam proton survives the reaction and that it is reconstructable.

The design of the experiment concentrated on the capability to fully reconstruct charged final states at very high interaction rates. Except for the veto counters, which provide very crude momentum and position measurements, there are no detector elements capable of measuring neutral particles. Reconstruction of neutral particles is restricted to decays of neutrals to charged final states (e.g., neutral kaons to two charged pions) and conversion of gamma rays in the target assembly.

During the design stage great care was taken to facilitate high rate operation of the spectrometer. The rate of operation is set by the recovery time of the detector elements after an interaction, and the readout time, the time it takes to digitize and readout an event. We employ only two basic types of detectors: drift chambers, and phototubes for scintillation or Cherenkov light collection. The phototubes have inherently fast recovery times, mached by the scintillator decay times. The drift chambers used are of the "mini drift" type with typical drift times of 35 ns and recovery times around 70 ns. To keep the readout time short, the spectrometer is highly segmented and reads data out in parallel communication streams. Also, the event triggers are arranged in a pipeline sequence, so that when an event

fails a trigger test in the sequence, testing is interrupted and the detector becomes available for another interaction.

Most of the detector elements and readout electronics for this experiment come from experiment BNL766. Both BNL766 and FNAL690 study proton-proton interactions, but the kinematic regions are very different. BNL766 uses a 28 GeV/c proton beam and studies both diffractive and central production. For FNAL690 the beam energy is 800 GeV/c and due to kinematics and detector size, we study only diffractive production. We require that the beam proton survives the interaction. Therefore the momentum scale of the beam proton and the new particles produced are very different. This necessitates two very different scales for the detector elements that measure the incoming/outgoing proton and the products of the reaction (see Figure 2.1).

A) For the beam proton an unusually long ***beam spectrometer*** is used. The total length of the spectrometer is 1/6 of a mile. It uses eight mini-drift chambers to reconstruct the beam particle trajectory before and after interaction in the hydrogen target. The outgoing beam proton travels through a string of magnets with a total field integral of 40 Tm (nominal momentum "kick" 12 GeV/c). This allows measurement of the outgoing beam momentum with a resolution of $\sigma \leq 500$ MeV/c. The beam spectrometer accepts tracks with momentum from 600 to 800 GeV/c and transverse momentum acceptance is independent of longitudinal momentum for transverse momentum less than 1 GeV/c. For most recorded events the outgoing proton has momentum lower than 750 GeV/c. Because the cross section decreases exponentially as a function of transverse momentum squared, the vast majority of events have a beam proton with transverse momentum well below 1 GeV/c. Therefore beam proton acceptance is very good for all events produced.

B) The products of the reactions are measured by a six chamber ***multiparticle spectrometer***. Five of the six chambers reside within a large aperture dipole magnet with a nominal momentum "kick" of 0.35 GeV/c. The sixth chamber is mounted on the

downstream end of the magnet. The multiparticle spectrometer is just 8 feet long and capable of resolving high multiplicity events with track momenta between 0.15 and 30 GeV/c. Exclusive (fully reconstructed) events with more than fifteen tracks have been reconstructed successfully. For tracks measured in all six chambers with momenta below 20 GeV/c the momentum resolution is $\Delta p / p = \pm 0.002 p$.

In addition to the two drift chamber systems, a highly segmented **Cherenkov counter** and a system of scintillation counters are employed for particle identification and triggering. A picture of the magnet with the drift chamber system along with the target and the direct particle identification detectors is shown in Figure 2.2.

The Cherenkov counter is positioned just after the multiparticle spectrometer. It has 96 toroidal mirrors pointing to an equal number of phototubes that provide pulse height and timing information. The radiator is Freon 114 at atmospheric pressure and the threshold momenta for pion/kaon/proton are 2.55/9/17 GeV/c.

The **time-of-flight system** (TOF) consists of 102 scintillation counters. The majority of the counters are arranged in two clusters in the middle (Middle Hodoscope) and the rear end of the detector (Rear Hodoscope). The system can distinguish protons from pions for momenta up to 1.5 GeV/c and pions from kaons for momenta up to 1 GeV/c.

In addition to the hodoscopes, there are scintillators employed to trigger event acquisition, and veto unwanted events. Most of these counters are deployed in the target region. A small counter just upstream of the hydrogen target, called the target counter (TC), is used to initiate the trigger sequence and serves as the time reference for all timing measurements in an event. Four counters perpendicular to the beam line, just upstream of the hydrogen target, cover the aperture of the spectrometer and are used to veto beam halo ("the veto thing" or TVT). The hydrogen target is surrounded by 12 scintillation counters (sandwiched with lead for neutral detection) used to veto events with particles that do not

enter the spectrometer (veto box). A similar system of four counters covers the frame of the first drift chamber (veto collar). We want to enhance the number of events with an interacted beam proton that survives the interaction. To this end there is a system of counters after the last beam chamber (forward hodoscope, FH) which is used as a trigger on events with a proton that scattered out of the beam envelope.

Electronic signals from the detector elements are amplified, digitized, read out, and written to tape by a set of electronics called the Transport System. Signals from the drift chambers are amplified by electronics residing on the chamber frames and discriminated (for noise rejection) by electronics next to the detector. From there the signals travel over 200' long cables and the time of arrival is measured, digitized and stored by 400 cards called TDC's. The TDC's read out only the channels that produce a signal during an event gate, a method called "zero suppression". Of the 15000 instrumented wires, typically less than 300 are read out per event. The TOF and Cherenkov signals follow a similar path but for these systems a pulse height measurement is also performed. Some of the TOF signals are routed to the electronics through a second shorter, faster path. The early arriving signals are used to make a decision whether an interaction of interest occurred and therefore if the detector should be read out.

Events that pass trigger requirements are digitized and read out to a set of 12 intermediate storage buffers. From there they are routed to a multiplicity counting hardware processor. If enough drift chamber hits are recorded, they are transferred to a VME computer system and written to VHS tape.

The accelerator would deliver beam, at a constant rate, for 20 seconds every 60 seconds (one "spill"). Typical operation conditions for the detector were 5×10^6 to 10×10^6 protons/sec beam rate and 10^4 events/sec surviving all trigger requirements. Given that the average event size is just under 1 Kbyte, this event rate translates to a data

rate of 10 MBytes/sec. The tape drive writing speed was smaller, 4 MBytes/sec, so we accumulated data to solid state memory and continued writing "off spill".

Track reconstruction was performed by a special purpose hardware processor, which consisted of 700 non-commercial electronic boards.

With the exception of the beam spectrometer and the VME computer system, all major detector elements come from the predecessor of this experiment, BNL E766. The detector hardware and the majority of the electronics mentioned above were designed and constructed by members of the collaboration specifically for the two experiments. Detailed descriptions of design, construction and performance can be found in various publications [36-41] and theses [42-46].

2.2 Multiparticle Spectrometer and Magnet

Charged tracks from interactions in the hydrogen target propagate through and are reconstructed in the multiparticle spectrometer. This spectrometer consists of six mini-drift chambers placed in a 240 ton, large aperture, dipole magnet. The size of the magnet is 2.5 x 1.2 x 2.2 meters in x,y,z where the z coordinate is along the direction of the beam and y is along the vertical.

Five of the six chambers lie within the magnet aperture. To reduce multiple scattering in the space between the drift chambers, there is a rigid picture frame box filled with helium preceding each chamber. The wire chambers and helium boxes are bolted on an aluminum cart. The whole cart assembly can be moved out of the magnet aperture for maintenance, on a set of rails fastened on the magnet. During data taking, the cart and chamber assembly form a rigid body, and the cart itself is bolted (spring loaded) to the magnet. Thus the geometry of the system is easily reproduced after a maintenance access.

The sixth and largest chamber is mounted on the Cherenkov counter frame and during data taking is positioned at the downstream end of the magnet. The chamber apertures vary between 0.76 x 0.46 and 1.8 x 1.2 meters (horizontal x vertical). Detailed size and operation parameters can be found in Table 2.1. Diagrams of the drift chamber system and the magnet are shown in Figures 2.2 and 2.3.

Positioning the drift chambers inside the magnet aperture makes track reconstruction more difficult, since curved tracks must be reconstructed. On the other hand, measurements near the target system help resolve the pattern recognition problem. Also proximity to the target provides large geometric acceptance, important for the complete reconstruction of charged final states. The horizontal and vertical geometric angular acceptance were ± 580 and ± 410 mrad respectively. An advantage of positioning the drift chamber system very near the target is that the overall size, and therefore the cost, of the detector was kept small despite the very large acceptance of the system. The disadvantage of the limited length of the spectrometer is an inability to measure high momentum tracks accurately. We accept and accurately measure particles with momenta between 0.15 GeV/c and 20 GeV/c. Although we can resolve the trajectory of much higher momentum tracks the momentum measurement resolution deteriorates rapidly for momenta above 20 GeV/c.

All six drift chambers have a similar construction. There are 11 wire planes per chamber. Four anode planes of instrumented, sense wires alternate with five cathode planes. There are two ground planes at the ends of the chamber. The ground planes provide a clearing field and electrostatic stability. The wire orientations for the anode (instrumented) planes are -21.6^{0},-7.63^{0},7.63^{0}, and 21.6^{0} with respect to the vertically oriented magnetic field. The wires in the cathode and ground planes are vertical. Wires for each plane are glued on a fiberglass (G-10) frame, which in turn is supported by the aluminum frame of the chamber. The thickness of the G-10 frame controls the anode to cathode distance, which is only 3.25 mm. The small spacing reduces the typical drift time

to about 35 ns and the chamber memory time to around 70 ns, therefore allowing for operation of the chambers at megacycle rates. However, small spacing does not allow large multiplication of the ion trail. To compensate, we use very small diameter anode wires and a gas that yields a large number of ion pairs per unit length of ionization. The gas mixture is 71% argon, 25% isobutane, 4% methylal. The anode wires are gold plated tungsten with a diameter of 20 or 25 μ m, depending on the chamber. With this configuration and 2 kV voltage we achieved gains of 10^6.

High chamber efficiency is very important for the reconstruction of complex final states and our chamber efficiency is well above 99% for every plane. The maximum number of hits for a track that intersects all six chambers is (4 planes per chamber)x(6 chambers)=24. Therefore we define efficiency for a chamber plane as:

$$\frac{\text{\# of tracks with 24 chamber hits}}{\text{Sum of tracks with 24 hits, plus tracks with 23 hits}}$$

where the hit is missing from the chamber plane for which we estimate efficiency.

We use the measured wire-hits to reconstruct particle trajectories. It is very difficult to do so when there are a large number of tracks, since as the number of tracks increases the number of the wire hits combinations that can produce a track grows very fast. The reason is that wire hits do not provide a fixed space point where the track intersects the chamber. Given a wire-hit, the track can lie anywhere along the wire. In addition, the drift time measurement conveys information about the distance of the track trajectory from the wire, but no information whether it passed to the left or right of the wire. For example consider that we use only two anode planes (views) and we want to resolve space points on an anode plane for the trajectory of two tracks. In this case there are four candidate space points. If we allow for left-right assignment of drift times the number of candidate space points is 16. To solve the problem we use a two step approach. First we solve the pattern

recognition problem. We find the track trajectory using only the wire hit information. After tracks are found, we assign the drift time so that the χ^2 of the track is improved.

To resolve the pattern recognition problem, we employ multiple, redundant anode planes (views). The orientation and number of anode planes (views) is unusual for a fixed target experiment. Traditionally, one of the anode planes is oriented perpendicular to the main component of the magnetic field. Since tracks bend perpendicular to the magnetic field, wire hits from all chambers in this view lie (to a good approximation) on a straight line. This simplifies the pattern recognition problem at least when only a few tracks are measured (You need only two points to determine a straight line. For a curve you need at least three). The measurement is augmented by one or two anode planes at small angles with respect to the magnetic field. The approach in this experiment is different. Instead of relying on a "no-bend" anode plane, we use 2 pairs of planes and take advantage of the redundant measurements. The measurement precision is the same for both pairs. Trajectories that form a track only in one of the two pairs are rejected. The small anode to anode spacing (between 2 and 3.5 mm) allows us to solve the pattern recognition problem without using the drift time. In addition, small wire spacing reduces the sharing of wire hits among tracks. The six chambers employ a total of 11,264 instrumented (anode) wires. Drift times are assigned after hit assignment to tracks to increase the precision of the measurement.

A significant factor in the precision of momentum measurements is the effect of multiple scattering on the track trajectory. The amount of material in the spectrometer was kept low with the use of helium volumes between the chambers and careful selection of materials for chamber construction. Each chamber, (including wires, windows and ionization gas) contributed only 0.15% of a radiation length of material.

Precise position measurement, coupled with the very small amount of material in the system and detailed knowledge of the magnetic field, provide excellent momentum

measurements. For tracks measured in all six chambers the momentum resolution is $\Delta p / p = \pm 0.002 p$. The mass resolutions for Λ^0 and K_s are 1.75 and 4.5 MeV/c^2 (FWHM) respectively.

More details about the construction and operation of the drift chamber system can be found in reference [42].

2.3 Beam Spectrometer

We reconstruct the beam particle trajectory using eight small aperture mini drift chambers (see Figure 2.1). The first three are placed before the multiparticle spectrometer. They measure the slope of the incoming beam particle and are used to extrapolate its trajectory through the hydrogen target. The remaining five chambers measure the trajectory of the outgoing beam proton, and in conjunction with a string of small aperture magnets, determine its momentum. Because the incoming beam is monochromatic, measurement of the outgoing proton momentum yields the momentum transferred to the target system. To achieve a high precision measurement, we place the chambers far away from the interaction point and use a string of magnets with a high field integral: the distance between the first and last chamber is 870 ft; the field integral is 12 GeV/c.

In addition to the momentum transfer measurement, we use the beam track trajectory to constrain the position of the primary interaction vertex. The large distance between beam chambers allows the determination of the primary vertex coordinates perpendicular to the axis of the beam with a precision that is much higher than the one achieved using tracks reconstructed in the multiparticle spectrometer.

The beam spectrometer was designed to operate efficiently with high beam rates. The accelerator delivers beam with nearly uniform intensity, for 20 seconds out of every

minute of operation (one beam spill). The beam intensity is controlled by a pinhole and a typical intensity during the beam spill 5 MHz (10^8 protons per spill). The beam proton momentum is 800 GeV/c with dispersion $\Delta p / p < 1.5 \times 10^{-4}$. The beam line was configured to deliver a 2 by 20 mm horizontal ribbon beam profile at the target. The elements of the beam line are shown in Figure 2.4.

The size of the beam suggests the use of small aperture chambers. We use two types of chambers. For the three incoming and first three outgoing chambers the aperture is 4x6 inches. For the last two chambers the aperture is larger, due to scattering in the hydrogen target and because the magnet string spreads the beam as a function of the momentum transferred. The aperture for the last two chambers is 8x15 inches and the anode to anode spacing is increased from .040 to .060 inches. Detailed size and operation parameters can be found in Table 2.2.

The construction of the beam chambers is very similar to the construction of the large aperture chambers used in the multiparticle spectrometer. As is the case for the multiparticle spectrometer chambers, there are four anode planes at -21.6^0,-7.63^0,7.63^0, and 21.6^0 with respect to the vertical. To form the five cathode and two ground planes, hard temper aluminum foil is used, instead of wire planes. The anode to cathode distance (.055 inches) is even smaller than in the multiparticle spectrometer, because the operation rate is much higher. The incoming chambers are able to reset and produce a signal at a rate equal to the beam rate, not just the interaction rate.

Signals from the anode wires are amplified by electronics mounted on the chamber frames. The differential output is driven to leading edge discriminators. The time of arrival of the discriminator output is digitized by TDC cards identical to the ones used for the multiparticle spectrometer chambers. The long distance of several chambers from the electronics room causes distortion and attenuation of the electronic pulses. Therefore "repeater" electronics cards are used to regenerate the signal. The TDC's encode the time

of arrival in 2.5 ns bins. For the average drift velocity of 40 μm/ns in the chamber one TDC bin corresponds to a distance of 100 μm in the chamber.

We operate the small chambers under high pressure (30 psig) to improve efficiency and space resolution. The large beam chambers were not designed to go much above ambient pressure and were never operated above 7 psig. For the small chamber windows, a 2 mil Kapton sheet is used as a gas seal. The pressure is contained by Kevlar cloth clamped on the Kapton window. The cloth represents 1.35×10^{-4} radiation lengths of material, which is less than the radiation length of the 2 mil Kapton window used as a gas seal. For the two larger chamber windows, only a 10 mil Mylar sheet is used. For both types of chambers we use a gas mixture consisting of 82% argon, 15% isobutane, 3% methylal. With this gas mixture, and high voltages of 2.1 kV and 1.4 kV for the small and large chambers respectively, the efficiency is well above 99%.

Since the target is only 2% of an interaction length, the majority of the beam particles do not scatter in the hydrogen target. Therefore the majority of ionization from the beam particle is concentrated in a small area, about 0.5 cm^2 for all chambers. The small beam spot implies that the majority of high voltage current is drawn by few wires in each chamber. To minimize efficiency loss due to radiation damage effects, the incoming beam chambers were moved twice during the run, so that no beam spot accumulated more than an average charge of 0.36 C/cm. A small drop in efficiency for one of the outgoing small chambers was corrected by increasing the high voltage from 2.0 to 2.1 kV. With the measures mentioned above, the chambers were fully efficient for the duration of the run.

The r.m.s. error for position measurement is 90 μm for the small chambers and 125 μm for the large chambers. The momentum resolution for the overall system is $\sigma \leq$ 500 MeV/c. This is the resolution achieved without corrections for small changes to the geometry during the run. For example the vertical position of the chambers would change

as a function of day and night changes in temperature. A more detailed description of the beam spectrometer operation and performance can be found elswhere [47].

It is worth mentioning that momentum is measured with respect to the uninteracted beam tracks. A sample of uninteracted beam tracks, recorded with the hydrogen target empty, defines the trajectory of the 800 GeV/c beam particle. For each event we use the known geometry of the spectrometer, and the position and field strength of the magnets, to assign the difference between the 800 GeV/c particle reference trajectory and the measured trajectory to a momentum difference. In other words if the accelerator was delivering protons with momentum of 799 GeV/c instead of 800 GeV/c, we would not be able to tell the difference. The absolute calibration of the beam energy is known to less than 1%.

2.4 Scintillation Counters and Time of Flight System

A large number of scintillation counters are used for particle identification and triggering. Although the counters come in a variety of shapes and serve different purposes, they share a common construction and readout design. For all counters, the scintillator is Pilot-U and scintillation light is transported through a short Lucite light guide to an EMI 9954B photomultiplier. To insure stable output gain and minimize electron transit times, only six stages of the 12-stage photomultipliers are used. A preamplifier at the base of each photomultiplier produces three output signals, one analog and two digital. The analog signal is used to measure the pulse area, which is proportional to the ionization deposited by a particle. Of the two digital signals, one is used to measure the time of flight for the ionizing particle, and the second is routed through a faster, shorter cable to the electronics that form the trigger decision. The counters are clustered in three regions of the spectrometer: the target, the multiparticle spectrometer and at the end of the beam spectrometer. All counters participate in the formation of the trigger decision. Precise time

of flight measurement is crucial only for the two hodoscope arrays in the multiparticle spectrometer. The rest of the counters are used primarily for triggering, with the exception of the veto counters that surround the hydrogen target which are also used as a crude recoil detector.

2.4.1 Target Region

A small counter (51 mm x 51 mm x 2 mm) just upstream of the hydrogen target signals the arrival of a beam proton (target counter or TC). The signal from this counter is used as the reference time with respect to which all other time measurements are made. Between the target counter and the hydrogen target there is a system of four counters used to veto beam halo (The Veto Thing or TVT). The four counters are arranged so that they form a 3.2 cm by 1.3 cm square opening to allow passage of the proton beam. The hydrogen target is surrounded by 12 scintillation counters to flag events with particles that do not enter the spectrometer (veto counters). The counters form a truncated, four sided pyramid around the hydrogen target. Every veto counter consists of five pieces of 3 mm thick Scintillator, interleaved with four pieces of 3 mm thick lead for neutral detection. The veto counter coverage is augmented by four similarly constructed counters that cover the frame of the first chamber in the multiparticle spectrometer (Veto collar). We used the veto counter signals for topology selection during data analysis, but we did not use them for on line triggering with the exception of a small subset of the data set. In particular, we used the veto counter system as a crude recoil detector in the analysis of centrally produced final states.

2.4.2 Multiparticle Spectrometer

Most of the scintillation counters in the detector are located in the multiparticle spectrometer region and are clustered in the middle (Middle Hodoscope) and the rear end of the spectrometer (Rear Hodoscope). The 102 counter configuration forms the Time Of

Flight (TOF) system for identification of non-relativistic particles. The time of flight system uses time of arrival measured by a counter, in conjunction with the momentum measurement from the drift chamber system, to determine the mass and therefore the identity of a particle. For particles reaching the Rear Hodoscope, the system can distinguish protons from pions for momenta up to 1.5 GeV/c and pions from kaons up to 1 GeV/c. For particles that reach only the Middle Hodoscope, the shorter flight path results in proton-pion separation for momenta up to 0.9 GeV/c.

The Middle Hodoscope is located between chambers 4 and 5. The counters form a picture frame (see Figure 2.5) that detects particles which intersect the first four chambers but are unlikely to reach the Rear Hodoscope. The counters do not interfere with the trajectory of particles that propagate through all six spectrometer chambers and therefore do not introduce material in the path of these particles. Of the 30 scintillators used to form the Middle Hodoscope, 12 are 762 mm x 51 mm x 13 mm and form the top and bottom of the picture frame, while the remaining 18 are 298 mm x 79 mm x 13 mm and form the frame sides. The side counters are positioned at a 45° angle in the X-Z plane around the vertical. Although the Middle Hodoscope counters are positioned within the magnetic field, the photomultipliers must be in a relatively field free region, since the magnetic field interferes with electron transport in a photomultiplier. Hence, an opening was provided on each side of the magnet to position the photomultipliers outside the magnetic field.

The rear hodoscope is mounted at the end of the spectrometer magnet, just upstream of the last drift chamber (chamber 6). A total of 72 counters, arranged in two rows cover completely the downstream aperture of the spectrometer. The large number of counters reduces the probability that two or more particles share the same counter and therefore reduces the probability for confusion in the time of flight assignment. All scintillators are 610 mm x 51 mm x 3 mm except for four counters in the middle of the array, which are 5

cm shorter. The short counters create a 10 cm x 10 cm rectangular opening for the proton beam.

Overall, the Time Of Flight system achieved a detection efficiency of more than 95%. The signals from the photomultiplier bases were digitized by custom-made electronic cards with a time of flight bin size of 127 psec. The whole system, including scintillator and readout electronics, achieved a σ=600 psec arrival time measurement, which translates to proton-pion separation for momenta up to 1.5 GeV/c in the Rear Hodoscope and 0.9 GeV/c in the Middle hodoscope. The custom-made electronics for the photomultiplier base amplifier-discriminator, along with the digitizing cards, are shared by all counters in the system. They are described in detail elsewhere [38,43].

2.4.3 Beam Spectrometer

The last system of scintillators in the beam path is the Forward Hodoscope (FH). It is located at the end of the beam line, after the last beam spectrometer drift chamber. A total of eight 12.5 x 10 cm scintillators cover the entire aperture of the last beam chamber. Two of the scintillators deviate from a rectangular shape so that they leave a 32 mm by 13 mm rectangular opening for protons that do not scatter outside the beam envelope (see Figure 2.6). To reduce accidental triggers, the scintillators overlap and we require that at least two counters are on for a scattered proton trigger. This information is used to form the third level trigger in the data acquisition system. The inclusion of this third trigger level significantly improves the number of interactions which can be recorded, because it introduces a minimum momentum loss requirement for the beam particle. The use of the forward hodoscope as part of the detector trigger was complicated by the long distance between the location of the counters and the electronics room. The method we employed to accommodate the late arrival of the signal is described in the trigger section.

2.5 Cherenkov Counter

For the study described in this paper, we are interested in the central production of mesons near the x_F=0 region. Since the center of mass system after a proton-proton collision in this experiment is moving rapidly in the laboratory ($\gamma \approx 20$), the momenta of the meson decay products are usually too high for time of flight identification. For direct particle identification in this study, an extremely important detector element is the Cherenkov counter. It takes advantage of the Cherenkov radiation emitted by a charged particle propagating in a medium where the speed of light is lower than the speed of the particle. For this detector, filled with atmospheric pressure Freon 114, Cherenkov radiation threshold momenta for π/K/p are 2.54/9/17 GeV/c.

The detector is positioned just downstream of the multiparticle spectrometer magnet (Figures 2.2, 2.3) and covers the entire spectrometer aperture. Every particle propagating through all six of the spectrometer chambers enters the active volume of the counter. In fact, the last drift chamber is mounted on the aluminum box that houses the Cherenkov counter, and has an aperture equal to the counter window. Cherenkov light is focused by 96 toroidal mirrors, each one pointing to a single photomultiplier. The mirrors are glued on two support planes. The support planes have a 120° angle between them and a 30° angle with respect to the vertical. A side view of the counter is shown in Figure 2.7. The support structure is a lightweight honeycomb material (Dupont trademark "NOMEX") with a density of 0.31 lbs/ft^2. The mirror positions and shapes are optimized to focus light from relativistic particles originating at the hydrogen target and traveling in straight lines through the spectrometer. This is a realistic approximation for a relativistic particle produced by an interaction in the hydrogen target, but focusing is not as good for particles with significant curvature, or for particles originating from secondary vertices downstream of the hydrogen target. To collect more light from such particles, a reflective cone surrounds each photomultiplier. Photomultipliers and their bases along with the associated readout cables

are positioned on the top and bottom of the Cherenkov housing, and therefore away from the path of any particle.

The radiator is Freon 114 ($C_2Cl_2F_4$) at atmospheric pressure, with an index of refraction n=1.0015. This results in a threshold speed $\beta_{th} = 1/n$ =0.9985c. As can be seen from Figure 2.7, the particle path length in the radiator varies between 50 cm and 100 cm. Therefore a fully relativistic particle has a light cone projection at the mirror position with a diameter that varies between 5.5 cm and 11 cm [45]. Since the smallest mirrors we use are 15.3 cm x 17.6 cm, a maximum of four mirrors can be illuminated by a single particle. There are six mirror types, distinguished by size and curvature, but only three mirror sizes [42]. The small mirrors (15.3 cm x 17.6 cm) are positioned close to the beam particle trajectory, at the center of the detector. This is the area where the highest track density is expected and where the light cone diameter at the mirror is smaller, due to the shorter path in the radiator. The large mirrors occupy the edges of the detector (see Figures 2.3, 2.7). Overall the high segmentation of the Cherenkov counter readout (96 channels) reduces confusion caused by sharing of the same readout channel by more than one radiating particle. All events selected for this study required a beam proton in the beam spectrometer. Thus there is always a fully relativistic beam particle traveling through the central region of the Cherenkov counter. The four central mirrors are always illuminated by the Cherenkov light cone of that particle. The beam path in the radiator is short, and produces a light cone with a diameter that is only 5.5 cm, much smaller than the dimensions of the central mirrors (15.3 cm x 17.6 cm). Since every beam particle radiates, other particles radiating in the four central cells cannot be properly identified. We attempted to minimize this effect by masking the beam particle light cone with a 5.5 cm diameter circular piece of black paper positioned at the center of the counter. The goal was to collect only light radiated into the unmasked region of the central mirrors by particles other than the beam proton. Unfortunately, masking was not complete and for every event there is a photomultiplier signal above threshold for all four central cells. At this point of the analysis

process we are not able to interpret information from the four central cells and therefore they are not used for direct particle identification in this study.

Cherenkov light in Freon 114 has a spectrum which extends into the ultraviolet region (Freon has a transmission cutoff is at 2200 $\mathring{A}$). Since the photomultipliers have maximum quantum efficiency at an optical wavelength of 4200 $\mathring{A}$, we coat the photomultiplier windows with p-terphenyl which converts ultra-violet light to 4600 $\mathring{A}$ and increases the amount of light available for detection. However, the light signal reaching the Cherenkov photomultipliers is weaker than the signal in the scintillator counter system. Hence we use one more photomultiplier amplification stage, for a total of seven out of twelve possible dynode stages. This provides sufficient sensitivity to separate photomultiplier noise from the signal from a single photoelectron. A preamplifier at the base of each photomultiplier produces two output signals, one analog and one digital. The digital signal is used to measure time of arrival and helps us reduce out of time background measurements. The analog signal is proportional to the amount of light collected by a mirror and is the measurement used for particle identification.

The number of photons emitted by a relativistic particle can be expressed as

$$\frac{N}{N_{max}} = 1 - \frac{p_{th}^2}{p^2} \qquad (1)$$

where the threshold momenta, p_{th}, for π/K/p are 2.54/9/17 GeV/c [48]. For electrons the threshold is much lower, (0.0094 GeV/c) but electrons originating at the hydrogen target must have momenta much higher than the threshold momentum in order to reach the counter mirrors. Most particles with momenta lower than 0.5 GeV/c are swept out of the spectrometer aperture by the magnetic field before they reach the Cherenkov counter. Therefore all electrons transversing the counter are fully relativistic and radiate the maximum number of photons. For a fully relativistic particle we observe on average, depending on the mirror/photomultiplier pair, between 10 and 15 photoelectrons. The

maximum number of photoelectrons depends on the average radiator path length for a given mirror, the efficiency of the optics, and variations in the performance of photomultipliers and associated electronics. The number of photoelectrons detected (#P.E.) from a particle is calculated by summing over all photomultipliers with signals above noise:

$$\#\text{P.E.} = \sum_{\text{mirrors}} \frac{\text{ADC} - \text{pedastal}}{\text{Gain}} (\#\text{P.E. for } \beta = 1 \text{ particle}) \qquad (2)$$

where the calibration is performed for each mirror independently. A "relevant" photomultiplier is one of the four possible photomultipliers in which Cherenkov light could be collected, based on the trajectory measured in the spectrometer.

Given the momentum measurement for a particle and its projection in the Cherenkov counter we can use (1) to predict the number of photoelectrons we expect to measure for a particular identity hypothesis (p_{th} depends on the particle mass, and therefore on the particle identity). We compare the number of photoelectrons predicted for this hypothesis with the analog output of the Cherenkov counter, normalized to number of photoelectrons by formula (2). There are two methods to do the comparison. The first method treats the device as a threshold counter. An hypothesis is called inconsistent if the number of photoelectrons predicted exceeds a limit and no signal is observed, or if we observe some number of photoelectrons while none is predicted.

The second method uses a more sophisticated analysis and allows differentiation between two particle types in a momentum region where both particle types are above the Cherenkov radiation threshold. The difference in Cherenkov light intensity between two particle types is greatest when the particle momentum is just higher than the threshold momentum of the particle with the larger mass [46]. Since measurement of the number of photoelectrons is a low statistics sampling (expected number of photoelectrons for a $\beta=1$ particle is between 10 and 15, and for a particle that is not fully relativistic even less) we employ Poisson statistics. We compare the number of photoelectrons expected to the

number of photoelectrons observed and derive a confidence level for a particular hypothesis. If the confidence level is below 0.001 the hypothesis is labeled inconsistent. If the confidence level is above 0.1 the hypothesis is labeled as a good identification. For this analysis a particle is labeled as compatible with any identification hypothesis with confidence level above 0.001. If a particle misses the Cherenkov counter aperture it is labeled compatible with any identity hypothesis.

2.6 Data Acquisition and Trigger

We want to use the available beam time efficiently to record as many events as possible relevant to the physics topics we want to study. The event recording rate is determined by three factors; (1) the recovery time for the detector elements; (2) the time to decide if an interaction relevant to our physics goals occurred (trigger system); and (3) the time for the electronics to digitize the measurements and transport them to the output tape drive (Transport System). Beyond the need for efficient triggers and readout speed, the system should be cost effective and reliable. The E690 trigger and data acquisition system was designed to handle interaction rates greater than 10 MHz and event recording rates greater than 12 KHz (about 12 MBytes/sec) from a detector with more than 15,000 channels. Most of the electronics used are custom made boards designed and constructed by members of this collaboration with emphasis on easy implementation, calibration and maintenance. A diagram of the trigger and Transport System is shown in Figure 2.8.

2.6.1 Readout System Principles

For this experiment it is not easy to draw the boundary between the trigger and Transport System, since we accomplish trigger efficiency by incrementally reading out the detector. We arrange the trigger requirements in a pipeline. For three out of the four pipeline stages, we interrupt the detector readout as soon as an interaction fails a trigger

requirement. For the fourth trigger stage (processor multiplicity logic), the event is completely digitized and the detector is available for the next event while the fourth trigger requirement is examined. Therefore, I will describe the trigger and readout systems in parallel. As will be made clear in the detailed description of the trigger stages, the tests to determine if a trigger requirement has been satisfied become increasingly more complex (and time consuming) as we progress down the pipeline. The additional complexity can be afforded because as we progress down the pipeline, the number of events which require testing is reduced. The readout system employs the highly parallel, pipelined, data-driven architecture of the Nevis Transport System (NTS). The high parallelism of the architecture manifests itself in the concurrent digitization of all detector channels and the readout of the digitized information through several parallel data streams. An example of a pipelined operation is the decoupling of the fourth trigger stage (multiplicity logic) from the detector front end by data buffers. In addition to decoupling the fourth trigger stage, a number of events can be stored in the pipeline that extends from the detector digitization electronics to the tape drive . Extensive buffering allows us to smooth event readout and minimizes delays due to event pile up. Finally, efficient operation of the trigger and Transport System is accomplished with the use of a data driven architecture. Once the system is initialized by a host computer, trigger, readout, and merging of the parallel data streams into a contiguous event proceeds without the use of external commands. No external intervention is required to route the data or reset electronic components between events or between beam spills. The behavior of the electronic boards is determined by the data itself. This control scheme allows concurrent operation of electronic boards under local control and the elimination of delays associated with computer interrupts. The system provides, also under local control and without a host computer intervention, "zero suppression", readout limits per drift chamber plane and high level digital signal processing for rejection of adjacent or out of time drift chamber wire hits.

2.6.2 Trigger Pipeline

We take advantage of the detector ability to readout tens of thousands of events per second and avoid restrictive triggers that isolate particular final states. The only firm requirements are that a proton-proton interaction occurred, that the beam proton survived the reaction, and that the beam proton is reconstructable in the beam spectrometer. We accomplish this by arranging in a pipeline the following four triggers:

1) Trigger Gate Initial (TGI) requires the presence of a beam proton and the production of at least one charged particle: a signal from the target counter in coincidence with a signal from the Rear or Middle Hodoscope.
2) Trigger Gate 2 (TG2) requires the absence of beam halo (no signal from the TVT) and a signal from at least one hodoscope counter.
3) Trigger Gate 3 (TG3) uses the Forward Hodoscope array to require that the beam proton scattered outside the envelope of the unscattered beam.
4) After detector digitization and readout are completed, the hardware processor multiplicity logic is used to count the number of wire chamber hits in the multiparticle spectrometer and beam spectrometer. We require enough wire hits to reconstruct at least one track in the beam spectrometer and require at least one hit in the multiparticle spectrometer.

2.6.3 Signals Before Digitization

Before a detailed discussion on the trigger requirements, I will give a brief description of the electronic signals we need to digitize and read out to tape. We employ only two basic types of detectors: drift chambers, and photomultipliers for scintillation or Cherenkov light detection.

For drift chambers, the anode wire signal is first amplified and shaped by preamplifiers mounted on the chamber frames. The signal is further amplified and

compared against a threshold level by discriminators residing close to the chambers. The discriminator output is a standardized differential pulse at ECL levels that travels in 200 foot long cables to the Time to Digital Converters (TDC). The cable introduces a 300 ns delay and serves as analog storage for the drift chamber signal until a trigger decision is made. Each channel has its own preamplifier, discriminator and time to digital converter. Therefore we process all channels in parallel and minimize the detector readout time.

For photomultiplier signals the readout path is more complicated. In addition to time, we measure pulse height and some of the signals are used to form the trigger decision. Every photomultiplier is attached to a base containing a voltage divider for the photomultiplier, an amplifier and a discriminator. There are three output pulses available from each base: an analog output from the amplifier and two "digital" outputs with standard height and opposite polarity from the discriminator. The analog output is used for the pulse height measurement. The two digital signals are used for: a) time of flight measurement and b) trigger decisions in the Fast Trigger Logic system (FTL). We measure time of flight for all photomultipliers (Cherenkov and scintillator counters) but only scintillator signals are used for the trigger.

From the base, the analog signal goes directly through coaxial cable to the digitization cards. One of the two digital signals (Digital plus) is used for the definition of the Trigger Gate Initial (TGI). For the TGI we use only signals from the target counter and the two Hodoscopes. The digital signal from each hodoscope counter is immediately processed through logical OR gates with the output of other counters within a group (one-half of the Middle Hodoscope counters or one-quarter of the Rear Hodoscope counters) and the resulting signal (Fast OR or FOR) is transferred through relatively short foam core cable to the TGI electronics. The second digital signal (Digital minus) is routed to eight channel cards in the electronics room (Photomultiplier Discriminator Latch or PDL) that standardize the signal. On the condition that a TGI gate is present, the PDL produces

output pulses with a leading edge fixed with respect to the TGI gate and width proportional to the arrival time of the digital signal, plus a minimum width of 12 ns. The fixed minimum width facilitates logical operations. Each PDL card produces three outputs, used for the second level trigger and the time of flight measurement:

1) All channels in a particular card that are active within the TGI gate are processed through an OR gate and made available to the second level trigger module (TG2).
2) The number of active channels within the TGI gate is summed and the result is transferred to a module called the Majority Logic. The Majority Logic sums all PDL inputs from the Middle and Rear Hodoscope and makes the result available to the second level trigger module (TG2).
3) The standardized digital signal is routed though flat ribbon cable to the Time to Digital Converters (TDC).

Because the second level trigger decision initiates the digitization of pulse height and time of flight signals, we delay the arrival of the output used for time of flight with respect to the other two outputs using cable delay. The PDL modules along with the associated cable delays control the relative timing of signals used for the second level trigger (TG2) and the time of flight measurement. Notice that the trigger sequence is initiated by the TGI output (gate) and all timing is relative to this gate.

2.6.4 TGI

Now I can proceed to describe the trigger requirements in detail. A typical TGI trigger required the following:

1) the presence of a signal from the target counter (TC).
2) the presence of a signal from at least one counter from either the middle or the rear hodoscopes (Fast OR).

3) the absence of a TGI signal in the previous 30 ns.

4) the absence of the Master Gate signal.

The target counter, positioned just in front of the hydrogen target, signals the presence of a beam proton. Coincidence with the Fast OR from the Hodoscope counters, signals the production of at least one secondary charged particle. Requirements (3) and (4) effectively turn off the detector readout in cases that the interaction is not recordable. A 30 ns minimum between TGI signals is required to minimize the residue from previous beam protons. The Master Gate signal prevents detector readout if the detector is not ready for data recording. The Master Gate signal is true if:

a) There is a beam gate. (i.e. the beam is present).

b) The drift chamber system high voltage is on.

c) The beam line magnets are on.

d) The manual gate switch is on.

The TGI requirements mentioned above were used throughout the data run except for a small subset of the data where requirement (2) (Fast OR) is relaxed. We use this sample for calibration purposes.

2.6.5 TG2

A successful TGI activates the PDL and TG2 electronic modules. For a typical TG2 trigger, the requirements were:

1) A TGI strobe.

2) Absence of a Halo Counter signal ($\overline{TVT}$).

3) A Majority Logic signal that at least one counter from the middle or Rear Hodoscope was on (GT0).

4) Absence of a self imposed hold signal due to an event that did not satisfy the TG2 trigger but left a lot of tracks in the drift chamber system.

5) Absence of a hold signal, due to the readout of a previous event.

The Halo Counter rejects TGI triggers due to beam halo. For a small subset of the data sample, in addition to the Halo Counter ($\overline{TVT}$), the absence of a signal from the Veto Counters ($\overline{VETO}$) was required. The Veto Counters flag particles escaping the detector aperture. For flexibility in the definition of the trigger requirements, conditions (2), (3) and (4) are processed by a lookup memory table accessible through the host computer. For condition (2) the input to the lookup table is the OR signal from the PDL module that handles the veto counters. For condition (3) the input comes from the Majority Logic counter sum (GT0). Finally, for condition (4) we use the Majority Logic output that asserts that more than four counters were on (GT3). In this case the TG2 remains inactive for a minimum of 140 ns independent of the TG2 trigger decision. The final TG2 condition (5) is generated downstream of the TG2 module, by the electronic cards responsible for event digitization and readout. A successful TG2 initiates digitization and readout of the event. While the sequence is in progress, the readout control cards send a hold signal that prevents further TG2 gate generation.

2.6.6 Prescales

Since a hold signal prevents second level trigger generation, not all TGI gates are processed by the TG2 electronics. In such a case the TGI strobe is simply ignored. The TG2 electronics record the number of TGI triggers the TG2 was able to process, and these triggers are referred to as live TGI triggers. After a predetermined number of live TGI triggers (typically 256 or 4096), an event is accepted without further requirements. Such events are called prescale events and are tagged so that they can be identified and used for calibration during the analysis. Further down the trigger pipeline prescale events can be rejected by subsequent trigger requirements, but there is always a fraction of prescale

events designated to survive all triggers independent of trigger conditions. We distinguish between prescale events subject to trigger selection and prescale events that survive independent of trigger requirements, using the event number assigned to each event by the TG2 electronics. A prescale event with event number which is a multiple of 2^{15} survives independent of trigger requirements.

2.6.7 TG3

A successful TG2 gates the third level trigger (TG3). The only additional requirement for a successful TG3 is a coincidence between Forward Hodoscope counters. The inclusion of this third trigger level significantly improves the number of interactions which can be recorded, because it introduces a minimum momentum transfer requirement for the beam particle. It rejects events for which the beam particle breaks up and is not measured in the Beam Spectrometer.

The Forward Hodoscope coincidence is a requirement that would be easily handled by the second level trigger electronics, if the signal could arrive in time to be considered with the rest of the TG2 requirements. The distance between the FH and the electronics room is too long for such an arrangement. The TG3 is a very simple module designed to take advantage of the readout controller capability to reset the digitization electronics while digitization is in progress. A successful TG2 output is used to gate the TG3 and to initiate event digitization. The Forward Hodoscope signal, and therefore the TG3 trigger decision, arrives after the start of digitization but before the readout sequence is in progress. If the TG3 requirement is satisfied, digitization and readout proceed uninterrupted. Otherwise, a reset signal is generated and the partially digitized event is eliminated before the start of the readout sequence. The implementation of the TG3 depends on the fact that the digitization time is constant, independent of event size, since digitization of the more than 15,000 drift chamber and more than 200 scintillator channels is performed in parallel.

2.6.8 Digitization Cards and Segmenters

Drift chambers TDC's measure the drift time in 2.5 ns bins. For photomultiplier signals, the Pulse Height and Time system (PHT) digitizes the pulse area and time of arrival in nominal bins of 0.31 pC and 0.125 ns respectively. The drift chamber, counter, and fast trigger electronic cards reside in three different crate types with distinct physical and electrical layouts. For all three systems there are dedicated readout cards called Segmenters (one per physical crate). The Segmenters are responsible for the readout sequence through the back-plane and the transfer of data to a single crate of intermediate buffers. The intermediate buffers (Block Buffers) decouple the front end of the readout system from the processor and tape drive systems.

The Segmenters for the scintillator and drift chamber systems invoke a priority encoding scheme that allows readout only from channels that recorded information during the TG2 gate (zero suppression). The drift time measurement is combined with the drift chamber wire number, and the ADC/TDC measurement pair from the PHT system is combined with the photomultiplier number. The Segmenters add to each word their own identity since multiple crates are necessary to accommodate the large number of channels. For the multiparticle spectrometer drift chambers, each drift chamber view is digitized in a separate crate. Four Segmenters output the information recorded in the four chamber views to a single data stream (cable) that transfers the data to the Block Buffers. Because the Beam Chambers have comparatively few instrumented wires, multiple Beam Chamber views are processed per crate. A total of 10 data streams (cables) transfer the drift chamber data to an equal number of Block Buffers, while a single cable is used for the scintillator data. One more data stream (for a total of 12) with information from the Fast Trigger Logic system completes the event readout.

Drift chamber TDC Segmenters are fairly complex boards and allow processing at the readout level. They perform drift time to drift distance mapping and a readout sequence

check. Because a drift chamber might have a cluster of wires turned on by a single track, the Segmenters are capable of picking wires with short drift times and dropping wires with larger drift times, based on a comparison of drift times from three adjacent wires. Wire planes where wires were dropped or a readout sequence error was found were tagged for later study. The Segmenters limit the number of hits that can be read to 31 wires per drift chamber plane. Reconstruction of events with more wires per plane is very unlikely due to the complexity of such an event, therefore reading out more measurements does not significantly increase the number of reconstructable events. The wire hit limit increases readout speed and reduces the buffer memory size required for storage of at least one complete event in each stage of the read-out pipeline.

The entire process of triggering, digitizing and reading out an event to Block Buffers depends strongly on track multiplicity and takes from a few hundred nanoseconds to a few microseconds. The average readout time was 4 μs.

From the Block Buffers, the event is transferred to the Hardware processor. The Hardware processor outputs the original data streams, along with the result of its own calculation, to a second set of Block Buffers. At this point the parallel data streams are merged to a single contiguous event. The Block Buffers sequentially read-out the information through the crate back-plane to a single electronic board which transfers the merged data stream to the host computer for recording on magnetic tape. The data driven architecture allows us to zero suppress, tag measurements with detector element identification information, and assemble the readout streams into a contiguous event, without the use of external commands. The process is sometimes referred to as *event building*. Concurrent, independent readout of the 12 parallel data streams provides fast and efficient operation of the front end electronics. The pipeline created by the Segmenters, Block Buffers, Processor and second set of Block Buffers can hold at least one event per

stage. Therefore we can concurrently operate on a separate event in each stage of the pipeline without loss of read-out speed.

2.6.9 Multiplicity Logic

The fourth, and last, test in the trigger pipeline is the Multiplicity Logic algorithm (MLOG). The calculation and event selection was performed by the hardware processor, and it was used for the entire data run. Operation principles and technical details regarding the Hardware processor can be found in Chapter 2.7 of this manuscript. The hardware processor selects events based on the number of wire "clusters" in the drift chamber system. A cluster is defined as a series of contiguous drift chamber wire numbers. The number of clusters in one of the four chamber views is approximately equal to the number of charged tracks intercepting a chamber. There are cases where the number of charged tracks can be larger than the number of clusters, e.g., if more than one track shares the same wire. Also, although more rare, the opposite can be true. If a wire hit is due to noise, the number of tracks can be smaller than the number of clusters. Although cluster counting is not as accurate as actually doing the reconstruction and counting the number of reconstructed tracks, the algorithm offers a good approximation and is much faster than track reconstruction.

In the hardware processor, cluster counting is performed by a single electronic board type (multiplicity logic) designed for, and used only in this algorithm. For the multiparticle spectrometer drift chambers, one multiplicity logic board is used per chamber. It counts and orders the number of clusters in each of the four chamber views into four 5-bit fields (counting range is 0 to 15 plus an overflow bit). Only three of the four cluster counts are transferred to the output cable and used for triggering. The three 5-bit data fields are organized into a single data word, with the cluster count from the least populated view occupying the least significant bits. The next to least count follows in the next 5-bit data

field and the next to highest count occupies the most significant bits. The count from the view with the highest number of clusters is ignored.

For the beam spectrometer chambers, there are far fewer wires per view. In order to reduce the amount of readout hardware, more than one view per chamber is combined into a single data block and more than one drift chamber is transferred per data stream. We use a multiplicity logic board per data stream. Since the multiplicity logic boards treat a data block as a chamber view and a data stream as an individual drift chamber, merging complicates the interpretation of the result. The multiplicity logic 15-bit output word may contain 5-bit cluster counts from more than one drift chamber. Because more than one view is combined to a single data block, the 5-bit count is the sum of clusters from two or four views, depending on the chamber. The four data streams used for beam chamber readout are:

1) Incoming chambers 1,2 & 3: four views per data block for a total of three blocks.
2) Outgoing chambers 1 & 2: two views per block for a total of four blocks.
3) Outgoing chamber 3: two views per block for a total of two blocks.
4) Outgoing chambers 4 & 5: same as the organization of 1 & 2.

We can see immediately how the interpretation of the result differs from the multiparticle spectrometer case. In the 15-bit output word, we designate numbers 1, 2, and 3 for the three output 5-bit fields. Number 1 refers to the field with the smallest count. For the three incoming beam chambers only fields 2 and 3 are non zero since the cluster count from the chamber with the maximum number of clusters is the ignored data field. Field 2 contains the sum of clusters in all four views from the chamber with the least number of wire clusters. Field 3 contains the sum of clusters from the chamber with the next-to-least cluster count.

The ten multiplicity logic boards output the calculation result (one word per board) to a single cable that transfers the result to an electronic board (Trigger Table) where the

results are checked and a trigger decision is made. The Trigger Table compares a predetermined subset of the 5-bit data fields to values stored in an internal memory table. If any one of the 5-bit fields is outside the limits stored in the memory table, a "failed trigger" bit is set and persists until the end of the test. Up to four such bits can be used for four independent trigger requirements. After all multiplicity words are examined, the four "failed trigger" bits are used to address another memory table. The output of this table is the trigger decision.

Only one set of MLOG trigger requirements was used for the entire run. The limits on the number of wire clusters per data block (5-bit field) are presented in Table 2.3. The four columns represent the four independent triggers used. If the series of requirements in any one of the four columns is satisfied, the event is transferred to the output Control Buffer crate. Events that fail all four requirements are eliminated in the processor. As can be seen in Table 2.3, very strict requirements were imposed on the beam spectrometer chambers. For the study of proton-proton diffraction dissociation, a reconstructed beam track is crucial. Events passing the MLOG requirements have at least one beam track with an excellent chance to be reconstructed off-line. Columns 1 and 2 in the table require a number of clusters consistent with the reconstruction of a single beam track. The requirements in columns 3 and 4 allow for a second (uninteracted) beam track. In this case for all but the last three chambers, the number of clusters required is consistent with one or two beam tracks. The last three chambers reside after the string of analyzing magnets, where an interacted beam track scatters outside the beam envelope and can be distinguished from an uninteracted track. Therefore the number of clusters is required to be consistent with exactly two tracks, distinguishable in all three chambers. The MLOG requirements for the multiparticle spectrometer chambers are minimal. Only the number of clusters in the next to least populated view is examined. For a successful trigger at least one hit is required for chamber 2 or chamber 3.

The MLOG algorithm provides a fast and efficient selection of events, mainly emphasizing the presence of a reconstructable beam track. Because the trigger is based on local counting of wire clusters and avoids the generation of cluster pairs necessary for track reconstruction, it can be accomplished at data transport speed. The only delay introduced with respect to data transport is the readout of the ten multiplicity logic words through a single cable to the Trigger Table module. This involves only 10 clock cycles, a small fraction of the 100 clock cycles necessary to transfer an average event from one buffer tier to the next. In addition to event selection, the MLOG processor performs a data integrity test. It checks that for every one of the 12 data streams, the correct number of blocks are present in every stream and that the words used to mark the end of a data block (completes) have the expected Segmenter identification data field (name). Another data integrity test is to verify that the data blocks transferred in parallel and used for multiplicity counting belong to the same event. When several data streams are read in parallel, there is a possibility that in one of the streams the event information is lost either due to a bad cable connection or because of a board failure. In such a case the assembled event directed for tape storage contains information from two events. Eleven of the twelve data streams contain information from one event, while the information from the next event is stored in the stream that failed. To check for such errors the processor uses information embedded in the event by the front end electronics. The Segmenters embed to each word marking the end of a data block (complete) a four bit number which is equal to the number of events read out since initialization, modulo 16 (block count). The processor checks that all blocks in an event have the same block count. If the processor detects an error in the sequence of names or the block count, it enters an error state and event readout is interrupted.

2.6.10 Host Computer

Events that satisfy the MLOG requirements are transferred to the second set of Block Buffers, where the parallel data streams are merged to a single contiguous event and

transferred through a single cable to the memory of a VME-bus computer (FORCE CPU-29). The computer controls a Honeywell VLDS tape drive that stores the data in standard VHS video tape. The accelerator would deliver beam for 20 seconds every 60 seconds (one "spill"). Because the speed at which the detector supplies data exceeded the speed of the tape drive, data would be accumulated in a memory and writing would continue "off spill". A few "typical" detector readout values follow: The beam intensity was 5×10^6 to 10×10^6 protons/sec. The detector was read out 50×10^3 times per second and 1 in 5 events would satisfy the multiplicity requirements. This would result in 10^4 events/sec directed for tape writing. The average event size was a little less than 1 KByte, so 10 MBytes/sec would be available for writing. The tape drive writing speed was 4 MBytes/sec. Thus we had to store the data in memory and continue writing "off spill". It took about $6x10^6$ events and 40 minutes to fill a VLDS tape. Approximately 5.5×10^9 events were recorded on 10^3 VLDS tapes during a 100-day period. We divided the data sample in groups with the same trigger requirements and reconstruction constants. Table 2.4 lists the trigger requirements used for the data acquisition. Only 4.6×10^9 events are listed. Events in groups earlier than group 4 were taken with a variety of different requirements. During that period we experimented with very different trigger conditions in order to determine an optimal set of trigger requirements.

2.7 Hardware Processor

The hardware processor functions as the last of the pipelined triggers in the data acquisition system and is designed to apply complex requirements at very high event rates. Event selection by the processor is performed in two stages. At the first stage, events are selected using wire hit multiplicity in the drift chambers. It is required that there are enough hits to reconstruct at least one beam track, and a non zero number of hits in the multiparticle spectrometer. This stage is called the multiplicity logic. Events that survive the multiplicity

cut enter the second stage of the processor, which performs track reconstruction. The events of interest at this stage of the analysis are the all charged, completely reconstructed final states. To enrich this sample we compare the longitudinal momentum lost by the beam particle, to the sum of longitudinal momentum for tracks reconstructed in the multiparticle spectrometer. Only the first stage of the processor was operational during data taking. We performed the track reconstruction and the event selection based on momentum balance off-line, after the end of the 1991 fixed target run.

2.7.1 Architecture and Design Principles

To achieve a high operation rate, the processor follows an architecture very different from the architecture of conventional computers. Conventional (Von Neumann) computers store data and instructions in memory. A central processing unit reads data and instructions and performs one operation at a time. The result is returned to memory and the process repeats until the task is completed. However, for a high rate application we want to perform many operations per clock cycle. To this end we use a data driven architecture that optimizes the operation speed versus the amount of hardware. Data "flows" through a network of interconnected operation units along with information about the task to be performed. The hardware processor system which we constructed performs more than 300 operations per clock cycle. As described below, that system consisted of more than 600 custom made circuit boards. The data driven architecture does not require central control of the computation process. Most decisions and computing are "local", so that there is no need to have information about the whole event. Because control is provided by the flow of data, many simple operations can be performed at once, within the same event. This fine parallelism and pipelining of operations within an event is different from the commercial approach of using several processors working concurrently on separate events. Our approach provides much higher throughput and is better suited for triggering applications.

We achieve a large number of operations per clock cycle because we can efficiently distribute the data to a large number of operation units. The data driven architecture allows us to split, replicate and merge the data stream without the use of sophisticated handshake protocols that establish point to point communications. Instead, board to board communication is achieved using a simple protocol derived from the Nevis Transport System (NTS) architecture. Every data word is transmitted along with information about the identity of the word. In more detail, every word contains a data field, a name field that allows modification of the operation, a control bit that specifies if it is a valid word (valid), a control bit that signifies if it is the last word in a series of words (complete), a control bit used to hold the data source if a destination is busy (hold), and a control bit used to abort the calculation if necessary (block annihilate). This word structure is shown in Figure 2.9. The use of control fields embedded in each data word allows the use of simple state machines that control the input and output of electronic boards. There is no need to count if the appropriate number of words were transmitted or received. Rather, data validation is accomplished by a simple look-up of the control bits. The use of a valid bit is necessary because sources always produce an output level on the cable whether there is data or not. For example, when there is no beam and therefore no data, there are words flowing out of the processor, but they are ignored. Also, it is common that during processing there are clock cycles when a board cannot produce an output because it is busy completing a calculation. The board still outputs a random data field but because of the absence of a valid control bit the information is ignored by the boards that follow in the pipeline. Hold signals propagate in a direction opposite to the data flow. A busy destination can set a hold that stops the dataflow from the source. This communication scheme is very simple and very efficient. It eliminates the need for central control of the event flow and all transfers are controlled locally by simple state machines. As long as there is valid data in the input, a board accepts and processes it. If there is no valid data available, the board continues to function but it does not produce valid output. The fact that the arrival of valid data triggers

and modifies the operation of electronic boards defines the data driven nature of the architecture.

Connecting a large number of boards through local buses (cables) requires the use of a chip technology with good bus properties. Throughout the processor we use ECL chips. Advantages of the technology include: availability at the time of design, insensitivity to noise, high clock rate and the ability to "wire or" the output of several boards to the same bus (cable). Moreover the technology is inexpensive and no bus driver chips are necessary. We are able to drive unshielded, tens of feet long cables at a clock rate of 20 MHz. Disadvantages of the technology include high power consumption and low gate density. Higher gate density would be desirable because it allows the consolidation of operations to a smaller number of boards. Nevertheless, the simple protocol allows a board to read in a word, process another and output yet another one on the same clock cycle, despite the use of very low cost, low gate density, double sided electronic boards.

Every board in the processor is designed to perform a specific operation. For example, there is a board whose only function is to add two numbers from two input streams (Arithmetic Operator), and a second to look-up if a predicted wire hit from track reconstruction was actually recorded (Map). Overall, a simple algorithm like the multiplicity logic requires only five board types. Because track reconstruction is a more complicated algorithm, over forty different board types are used in the entire processor.

Since the number of different board types can become very large for complicated algorithms, the design allowed for switches and wire connections that modify the behavior of a board. An Arithmetic Operator can be configured to perform addition or subtraction, or use only part of the data field for summation. In addition to physical configuration, we can alter the behavior of boards loading control registers and memory look-up tables from a conventional host computer. The latter approach does not require physical access and configuration of hardware. Limited access to cable and hardware modules reduces the

probability of altering a working part of the algorithm and makes modifications fast and reliable. We download control and processing information from a host computer wherever it is practical. In particular, we can download new reconstruction constants every time the detector is accessed for maintenance, and we can change the trigger requirements without access to the hardware.

Although downloading registers and memory look-up tables provides flexibility, substantial modifications to the algorithm must be implemented in hardware. The speed advantage of a special purpose machine over a conventional computer stems from concurrent execution of operations distributed throughout the hardware. We achieve a large number of concurrent operations by physically routing the data stream to the appropriate operation modules. The network of electronic boards and interconnecting cables can be though of as a "software program" in a conventional computer. To be more specific, in a conventional computer, one can use an instruction that stores the result of an addition to memory, so that it is available for a subsequent operation. In this processor, the result of the addition is routed by a physical cable to the next electronic module.

From the example above it is clear that the computation and the resulting trigger depends on the interconnection of boards and the physical configuration of these boards. Every time the algorithm changes it is necessary physically to reconfigure and recable the components. On the other hand, the elementary components can be rearranged and used as building blocks for a variety of algorithms. For example, the RD21 project at CERN designed a silicon vertex detector trigger using only boards from this hardware processor [49]. Also, there are modifications to an existing algorithm that can be easily accomplished. The addition of new detector components and therefore new data streams can easily be incorporated by adding a new data path in parallel with the existing algorithm. This is the case for the transition from E766 to E690, when beam spectrometer drift chambers were added to the detector.

On a larger scale the processor is divided into sections (subprocessors or subroutines). For example, there are separate sections for line finding, matching, fitting, and duplicate track removal (Figure 2.10). They are arranged in a pipeline since they are algorithms that have to be performed in sequence. In order to take advantage of the available hardware, we arrange for one event to process in the fitting section while the next event is at the matching section, and so on. This way there is an event at some stage of processing at each processor section. We separate the various subprocessors with tiers of buffers (Control Buffers). With the help of one controller board per buffer tier, Control Buffers are intelligent enough to check that the parallel data streams belong to the same event and allow only one event to process per section. Separation of subprocessors by buffer tiers allows implementation and checking of the hardware in incremental steps. Also, buffer tiers isolate the sub processors from each other, eliminating complex error propagation from one subroutine to the next. The buffer tiers for the beam spectrometer and the multiparticle spectrometer algorithms are shown in Figures 2.11 and 2.12.

2.7.2 Debugging Features

The implementation of a special purpose hardware processor presents challenges that do not exist in off-line event selection by a conventional computer. On conventional computers algorithms are implemented by writing programs in a high level computer language. All computer languages come with debugging tools that allow following the program flow for identification of erroneous code. With such tools two things are taken for granted: no hardware problems exist, and the algorithm executes one step at a time. Obviously, a novel special purpose hardware system does not come with ready-made debugging tools. Therefore, parallel development of hardware boards and software tools is necessary. Troubleshooting is further complicated by the concurrent execution of several instructions per clock cycle throughout the hardware. Finally, we need to distinguish between hardware failures and algorithm errors. In other words, a wrong result at the

output of the processor does not allow us to point conclusively either to a specific board that had a hardware failure, or to an algorithm error such as an improperly configured board.

These potential problems led to two important design features. First, every electronic board is connected to an independent, serial, low bandwidth debugging bus (called control bus or *cbus*). The bus provides non-destructive readout of the processor state. Second, the machine is synchronous and static and machine state evolution is controlled by a single external clock. When the external clock stops, the machine preserves its state and can be read and modified using the serial debugging bus.

The synchronous design makes the state evolution of the processor deterministic, and eliminates complex timing behavior. In addition, synchronous operation allows us to implement the simple communication protocol described in the previous section. The debugging bus, along with the static design, allows monitoring the processor state on a clock-by-clock basis. Although these design features provide the means to observe the intermediate state of the processor, it is not easy to make sense out of the state evolution of 600 boards one clock cycle at a time. To automate the task, we control the processor clock and the debugging bus through a conventional host computer. This host enables us to develop high-level diagnostic and debugging tools.

Before describing the software tools developed for deployment and management of the processor, it is worth presenting in more detail the method used to monitor the processor state. All boards are made of simple building blocks: mainly parallel/shift registers, static memory, counters and logic gates. Knowledge of the state of the components determines the state of the machine completely. The debugging bus allows the selection of a specific element (e.g., a register) on a single board in the system. In debugging mode only the selected element, in this case a register, is clocked. The content of the register is shifted out through the debugging bus one bit at a time. Once the contents

are completely read, the register returns to its initial condition. Since everything else is isolated from the clock, the processor state remains unaltered. Obtaining the content of a counter is more involved because the counters do not allow shift operations. To achieve non-destructive counter readout, the counter is "rolled" for a number of clock cycles equal to the full range of the counter. As this is done, the number of clocks necessary to reach "terminal count" is measured. It is possible not only to read, but also to write specific values to registers and counters. Thus, it is possible to read and write static memory controlled by register and counter chips. Therefore all elements that possess memory are accessible through the debugging bus and the state of the processor is completely determined.

Unfortunately, due to design exigencies, the last statement was not absolute for the hardware processor used in this experiment. There are a couple of boards that use "invisible" flip-flops in their state machines. In addition, most of boards use latches in their output stage. The latches are not readable through the Cbus. Nevertheless, all boards comply with the Cbus specification, and all boards use a visible input stage. So, in a worst case scenario, an error cannot propagate without detection for more than one board. Finally, connecting a large number of boards requires the use of a lot of cable connections. Access to the hardware content allows us to test the cable connections and efficiently eliminate a significant source of errors .

2.7.3 Software Tools

Conventional computers were used to develop software tools for debugging and managing the processor. The programs were written in FORTRAN and run on the processor host computer and other, independent machines. The general idea behind the software effort is to describe the numerous processor details in a software model and to use comparisons between model results and the hardware for debugging and maintenance. In the processor modeling we use two distinct software packages with different levels of

detail: the *simulator* and the *emulator*. The *simulator* models the arithmetic performed by the processor and calculates the final result of subroutines in a format identical to the processor result. The *emulator* is a far more detailed description of the hardware and models all electronic boards at the register level. Whereas the simulator provides a fast calculation of expected processor results, emulating at the register level is a very slow process. We can use the *simulator* to process 10,000 events per hour on a VAX 3100 computer. In contrast, it takes two hours for the *emulator* to process a single event on a Motorola 68030 microprocessor. Although the *emulator* may seem hopelessly slow, we never use it to model the entire processor at once; rather we emulate just one subroutine at a time. In the following I describe the procedures we used to compare the hardware to the software models and give a more detailed description of their capabilities.

The *emulator* software was not available for the Brookhaven phase of the experiment (BNL766), and was completed only during the FNAL690 run. The software is structured so that subroutines represent electronic boards, while physical setup and cabling are described in a configuration file. The *emulator* is a very detailed description of the hardware and is capable of predicting the state of every hardware component (e.g. register) on a clock by clock basis. The software is structured so that its components can be used for any processor algorithm. Once the subroutines that represent electronic boards are written and verified, we can specify any algorithm by simply editing a configuration file that describes cable interconnections and the content of look-up tables. Therefore, there is no need for new code development when we modify an existing algorithm, or introduce a new one.

The model is run on the host computer with a software interface that accepts the same command sequences as the hardware. Both hardware and software are initialized, and we load a problem to the buffer tier immediately preceding the subroutine to be checked. The host computer proceeds to clock the hardware and software model for one

clock cycle. Then, the content of the hardware components is read out by the host through the serial debugging bus. The result is automatically compared with the software prediction. If there is no discrepancy, the procedure repeats until all data propagate through the subroutine. If a discrepancy occurs (e.g., in a register), execution is interrupted, and the register that shows a content different than expected in the software model is presented to the user. This allows identification not only of the hardware board that failed, but also of the position within the board where the failure occurred. Component failure is not the only possible reason for a discrepancy. For many boards, switches and wire "patches" are used to specify the particular behavior of the board. Although it might seem easy to take the time and ensure that an individual board is configured properly, mistakes are to be expected in a multi-board configuration. The comparison of software and hardware results is an extremely powerful tool because making exactly the same mistake in both the software and the hardware is very unlikely. I want to emphasize how difficult it is to follow the state evolution of an event as it propagates through an algorithm without the aid of a software model. For every register, and every clock cycle, one has to ask the question: is this what the register content should be? To answer the question, one has to be familiar with the hardware design and compute on the fly the hardware evolution. Repeating this comparison for 300 clock cycles (a typical time for executing a subroutine) is a daunting task, much better performed by a computer. Finally, if after the completion of a subroutine, there are no software-hardware discrepancies and the result is still not the one expected, it is safe to point to an algorithm error. It would be hard to have the same level of confidence in the hardware, if comparisons relied on a "manual" calculation of the processor operation.

The *emulator* software was used not only to aid the setup of algorithms, but also to test individual boards before installation in the hardware processor. The host computer runs a set of tests automatically, and in case of a discrepancy the software presents the content of the failed component and the value predicted by the software. This is of

significant convenience because it allows one to concentrate on a limited area of the electronic board. In addition, collaborators not intimately familiar with details of the full processor, were able to debug individual boards.

The use of the *emulator* is limited by the time it takes to emulate a large collection of boards. We have to emulate every board in the system whether there is valid data in it or not. So, when we emulate a single event propagating through the entire processor every subroutine must be emulated for every clock cycle, despite the fact that the event cannot process in more than one subroutine at a time. It is far more efficient to emulate individual subroutines. To this end, we use the *simulator* intermediate results. Code was developed that reads the *simulator* output and automatically loads an intermediate buffer tier (tiers are shown in Figures 2.11, and 2.12). The event can then be processed through the subroutine using the *emulator*. The time needed to emulate an event through a subroutine is on the order of fifteen minutes. This process decouples the development of subroutines, and in principal allows parallel development of processor sections. In addition, because reading and writing intermediate results to buffer tiers is an automated process, it is easy and time efficient to check a single subroutine with a large sample of events. We use the simulator precalculated results to load a subroutine input tier, then clock the processor hardware only, and compare the result at the output tier with the *simulator* expectation, within a fraction of a second. Typically, we would check with the *emulator* that three or four events process correctly through a subroutine, and then use the *simulator* intermediate results to check a few thousand events. If a particular event failed the test, we would run it through the *emulator* to identify the problem.

The two software packages were complementary and helped us not only to set up the processor but also to monitor and maintain it during operation. After the machine was operational, we would periodically run 100,000 events through the hardware and check the result against the *simulator* prediction. In the rare cases that a hardware failure occurred,

we used the *simulator* to identify the faulty subroutine and the *emulator* to diagnose and fix the problem within the faulty subroutine.

The *simulator* is used for reasons beyond the intermediate and final result computation it offers. It is also used to generate the memory look-up tables that perform most arithmetic operations in the hardware processor. A few details about the computation are necessary. Floating point arithmetic is never performed in the hardware processor. Only fixed precision integer arithmetic is used. Variables often have to be rescaled to avoid arithmetic overflows. For most arithmetic operations, such as sum multiply, look-up tables are used and are loaded to the hardware through the serial debugging bus. The standard procedure is to specify a few reconstruction constants and to use them as input to the *simulator* software. The software automatically generates all processor look-up tables and saves them in a file that is used to download the hardware. When events are processed through the *simulator*, the same look-up tables are used to perform the calculation. Using this procedure, it is easy to produce intermediate results in a format identical to the one used by the hardware.

In addition to the software described above, there are special routines that download look-up tables, check the integrity of the debugging bus, and test the static memory of the processor boards. After the completion of the last software components, we were able to deploy the whole processor in a period of a few months and maintain the hardware with a very small effort. Unfortunately, the whole process ended after the data taking period was over and we were never able to use the entire processor on line. The software components that took the longest time to complete were the *emulator* subroutines that represent the electronic boards in the *emulator*. There is one subroutine for each one of the 40 different board types, and the development of each subroutine along with the corresponding memory testing and loading routines took a significant amount of time. In order to write an *emulator* software component, the author has to be intimately familiar with processor

principles and have a detailed knowledge of the electronic board. *Emulator* software components could have been easily written by the designers of the electronic boards. Unfortunately, the *emulator* software was not part of the initial processor plan and the designers of many of the boards were not available. The need for detailed emulation of the hardware components became apparent only after the first attempt to put together a large-scale hardware processor. With a large number of boards and many board types, it is difficult to follow the complex propagation of events through the hardware modules. The software shields us from hardware details and allows us to distinguish between setup errors and algorithm errors. The most intriguing aspect of the emulation software is the opportunity it offers for the development of new algorithms without the use of hardware. With the *emulator* one can specify a new algorithm and test feasibility and performance on a conventional computer. Once potential problems are identified and resolved, it is easy to implement the algorithm in hardware. This is to be contrasted with the initial mode of operation, where problems were identified and solved with the use, and rearrangement, of hardware modules.

2.7.4 Performance

There are two algorithms used for event rejection: measurement multiplicity in the drift chamber system, and the comparison of the momentum lost by the beam particle to the momentum of particles measured in the multiparticle spectrometer. The multiplicity algorithm ran on-line throughout the 1991-92 fixed target run and provided a reduction of the data stream by a factor of 5-10, depending on the trigger conditions. The multiplicity algorithm requirement was designed to select events with a reconstructable beam track. In particular the requirement was:

> Enough hits in the beam spectrometer exist to reconstruct a beam track and there is at least one hit in the multiparticle spectrometer.

The multiplicity logic stage used only forty of the more that 600 boards of the entire processor.

We selected events based on momentum balance off-line, six months after the end of data taking. That algorithm is divided into two major parts: reconstruction of the beam particle and track reconstruction in the multiparticle spectrometer (see Figure 2.10). The first part was operational during data taking but was never implemented on-line because the benefit is limited without the use of the multiparticle spectrometer result. Since the multiplicity result was already recorded on tape, we removed the multiplicity processor and used a system of three VME bus computers to send the recorded data to the processor and to save the output. Of the three computer systems, one was used for sending data, and two others for simultaneously recording the result in two separate output streams (see Figure 2.13). To one of the output streams we wrote all 5.5×10^9 events plus the reconstruction result (1-1 sample). For the second stream the VME bus computer would look-up the processor trigger words and record only events that satisfied the selection requirements:

1) # of veto counters on ≤ 1
2) Minimum of 1 track found in the multiparticle spectrometer.
3) Minimum of 1 beam track found
4) | (Sum of Pl in multiparticle spectrometer) - (momentum lost by beam)| < 3 GeV/c + (momentum lost by beam)/8
5) the event goes to the selected sample independent of the cuts above if the number of trailing zeroes in the event counter exceeds twelve (prescale). This was done so that we have part of the unbiased sample available in the selected sample for comparison.

This second sample, which we refer to as "processor skim", is 270 million events or about 5% of the entire data sample. The goal of the selection is to produce a sample rich in completely reconstructed all charged final states. Because in central production the slow

proton carries a negligible amount of longitudinal momentum and there is no charge balance requirement, the selection favors centrally produced charged final states. This is the reason we allowed a maximum of one veto counter to be on. This veto counter can be turned on by the missing slow proton. When the system became operational we were able to process 2500-3000 events per second. We finished processing the entire sample in a period of six months. This is a period longer than the 100 days of data taking. It is due to problems with the high speed tape drives and the fact that, unlike during the data recording period, we did not operate on a 24-hour schedule. By the time reconstruction was finished we had all the output events on VLDS tapes and the selected sample in Exabyte format. Although we carefully monitored the processor for computational errors during off-line processing, we failed to realize an algorithm error in the trigger output. The error was discovered a few months after the end of off-line processing. It did not affect the reconstruction result. Rather, after reconstruction we mapped the parameters of negative tracks to an erroneous longitudinal momentum value. Specifically, the mapping made longitudinal momentum proportional to curvature, instead of the correct, inversely proportional relation. The *simulator* used exactly the same erroneous look-up table and produced exactly the same error. The mistake limited the use of the selected data sample, but we were still able to use the reconstruction results from the 1-1 sample for vertex reconstruction.

The computational capabilities of the processor are remarkable. We were able to perform track reconstruction at a speed ten times higher than an 8 CPU Silicon Graphics work station (or more than 2500 events per second versus 250 events per second). But computational ability is not the most important advantage of the architecture. The processor is first and foremost an on-line trigger device with the ability to transport and select vast amounts of data. The modular design allows for expansion of the data in parallel streams, as many as necessary to meet the read-out needs of the experiment. For example, we were able to sustain data transfers to the input of the multiplicity logic processor at rates of 200 Mbytes/sec. If it were necessary to have a faster readout, we could double the number of

readout streams from 12 to 24 and double the data throughput. Because the trigger did not require the generation of combinations of hits (as is the case of line finding algorithm) the algorithm executed at data transport speed. The architecture is most suitable for simple sequential triggers with an increasing level of complexity, while the amount of data is reduced from stage to stage. Although the electronics industry is pushing hard for ever more computationally powerful machines with multiple CPU configurations, there is no commercial need for the high bandwidth necessary in high energy experiments. For this kind of processing the data driven architecture employed in this experiment has no rivals.

Table 2.1 Multiparticle spectrometer (JGG) drift chamber parameters and operating characteristics.

Drift Chamber Number	1	2	3	4	5	6
Horizontal Aperture (m)	0.762	0.914	1.524	1.524	1.524	1.829
Vertical Aperture (m)	0.457	0.610	1.016	1.016	1.016	1.219
Average Z Coordinate (m)	-1.017	-0.839	-0.513	-0.138	0.456	1.229
Anode Wire Diameter (μ m)	20	20	25	25	25	25
Cathode Wire Diameter (μ m)	102	102	102	102	102	102
Ground Wire Diameter (μ m)	102	102	102	102	102	102
Anode to Anode Wire Spacing (mm)	2.0	2.0	3.2	3.2	3.2	3.5
Cathode to Cathode Wire Spacing (mm)	1.1	1.1	1.1	1.1	1.1	1.1
Ground to Ground Wire Spacing (mm)	2.0	2.0	3.2	3.2	3.2	3.5
Anode to Cathode Plane Spacing (mm)	3.2	3.2	3.2	3.2	3.2	3.2
Anode Wire Tension (gram)	65	65	90	90	90	90
Number of Instrumented Wires	1536	1920	1920	1920	1920	2048
Cathode Voltage (kV)	-2.60	-2.60	-2.15	-2.10	-2.10	-2.05
Average Efficiency (%)	>99	>99	>99	>99	>99	>99
Gas Mixture	Argon 71%, Isobutane 25%, Methylal 4%					

Table 2.2 Beam chamber parameters and operating characteristics.

Beam Chamber Number	1, 2, 3, 4, 5, 6	7, 8
Horizontal Aperture (m)	0.152	0.381
Vertical Aperture (m)	0.102	0.203
Average Z Coordinate (m)	-188, -62, -5, 21, 35, 56	71, 78
Anode Wire Diameter (μ m)	12	15
Cathode Plane	13 μ m hard temper aluminum foil	13 μ m hard temper aluminum foil
Ground Plane	13 μ m hard temper aluminum foil	25 μ m hard temper aluminum foil
Anode to Anode Wire Spacing (mm)	1.0	1.5
Plane-Plane Spacing (mm)	1.4	1.4
Anode Wire Tension (gram)	20	35
Anode Wires per Plane	160	256
Instrumented Wires per Plane	64, 64, 64, 160, 160, 160	192, 256
Cathode Voltage (kV)	-2.1, -1.8, -2.2, -2.1, -2.1, -2.1	-1.4, -1.4
Average Efficiency (%)	>99	>99
Material in Radiation Lengths	0.24%	0.39%
Material in Interaction Lengths	0.06%	0.12%
Gas Mixture	Argon 82%, Isobutane 15%, Methylal 3%	

Table 2.3 Processor multiplicity trigger (MLOG). The four columns to the right contain the number of clusters required (inclusive) for the four independent triggers. We accept an event if the requirements in any one of the four columns are satisfied. The first column specifies the data field examined. The notation is: drift *chamber system-chamber number-cluster count rank*. We assign to the three ranked 5-bit data fields the numbers 1-least, 2-next-to-least, 3-next-to-most

	TRG_12			
	1	2	3	4
JGG—2—2	[2, 31]	—	[3, 31]	—
JGG—3—2	—	[2, 31]	—	[3, 31]
IBC—123—2	[3, 4]	[3, 4]	[3, 8]	[3, 8]
IBC—123—3	[4, 5]	[4, 5]	[4, 9]	[4, 9]
OBC—12—1	[1, 31]	[1, 31]	[2, 31]	[2, 31]
OBC—12—3	[2, 31]	[2, 31]	[3, 31]	[3, 31]
OBC—3—3	[1, 8]	[1, 8]	[3, 10]	[3, 10]
OBC—45—1	[1, 8]	[1, 8]	[3, 10]	[3, 10]
OBC—45—3	[1, 8]	[1, 8]	[3, 10]	[3, 10]

Table 2.4 E690 run summary.

Group	TGI	TG2	TG3	MLOG	Events
4 — 5	TC	GT1•$\overline{TVT}$	—	TRG_12	0.72×10^9
6	TC	GT0•$\overline{TVT}$	FH1•FH2	TRG_12	0.06×10^9
7 —12	TC•FOR	GT0•$\overline{TVT}$	FH1•FH2	TRG_12	2.96×10^9
13	TC•FOR	GT0•$\overline{TVT}$	FH1•FH2	TRG_12	0.54×10^9
13	TC•FOR	GT0•$\overline{TVT}$•$\overline{VETO}$	FH1•FH2	TRG_12	0.36×10^9

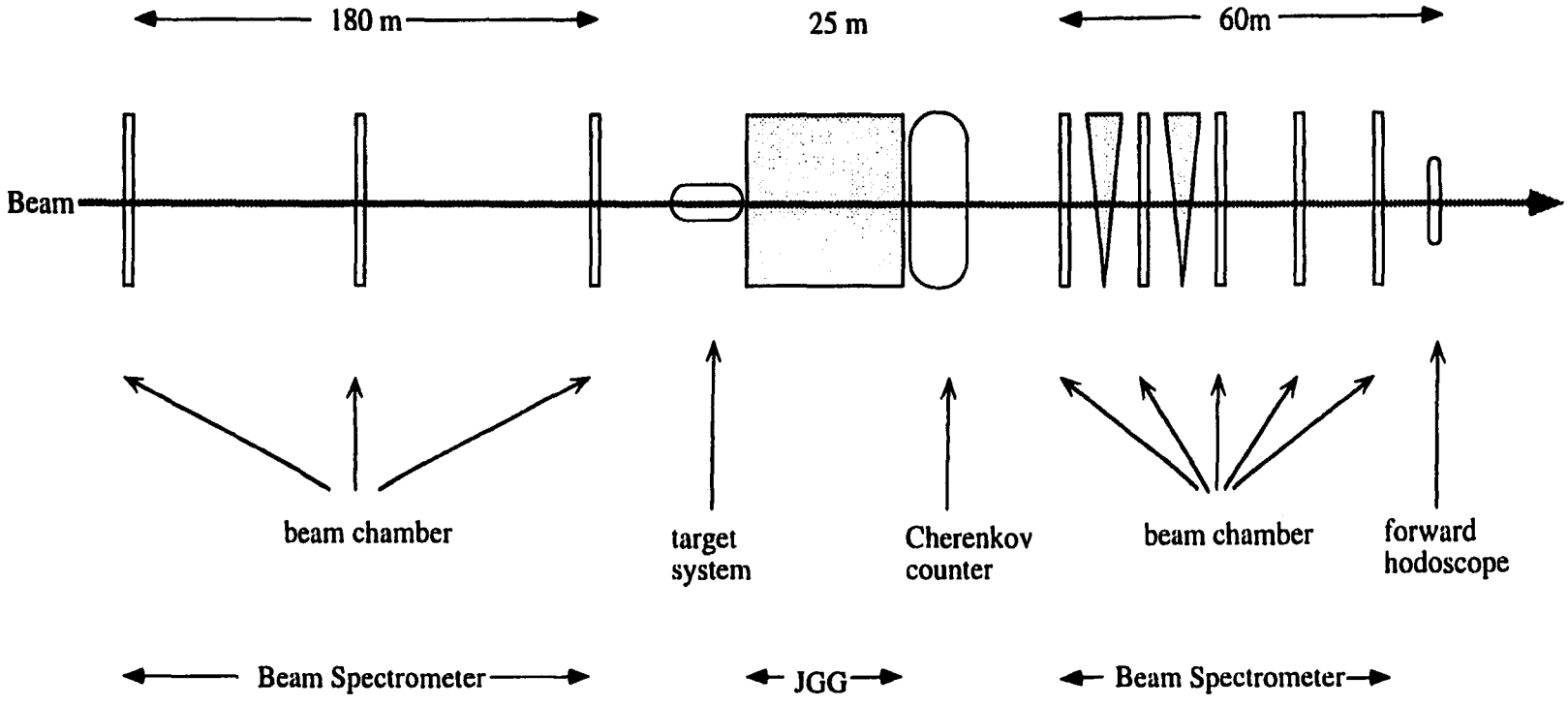

Figure 2.1 E690 spectrometer (not to scale).

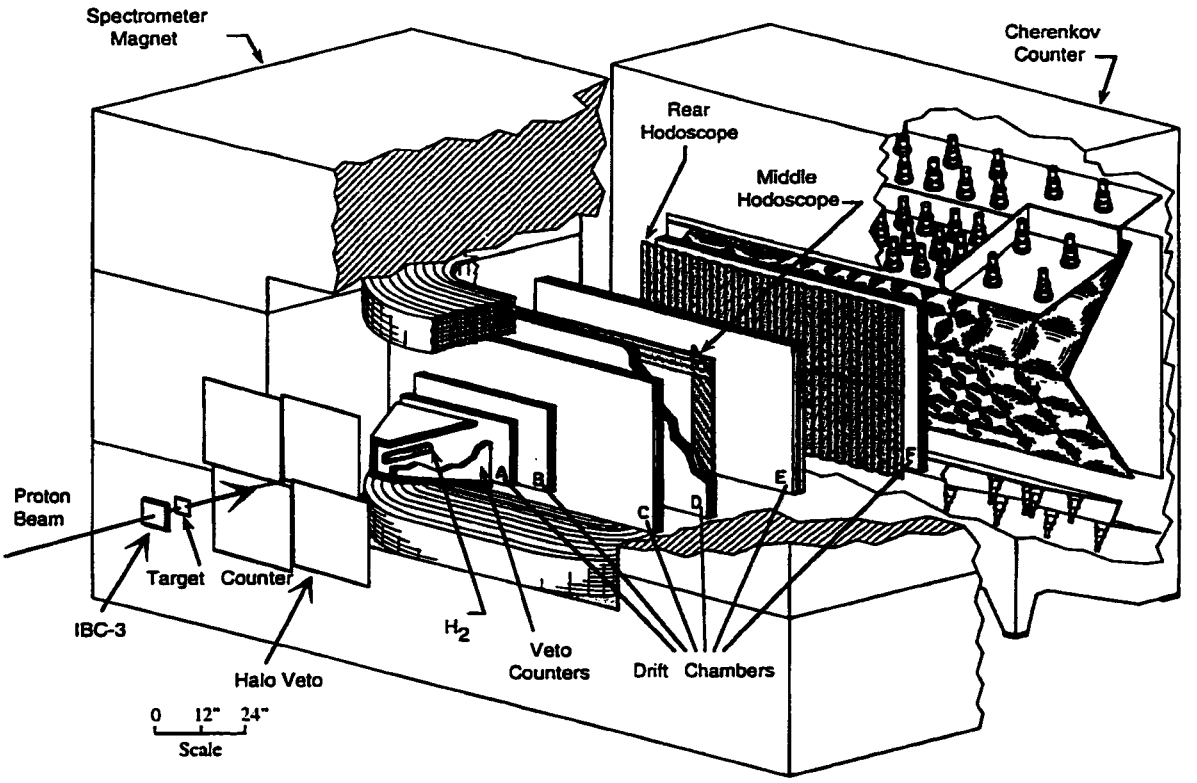

Figure 2.2 E690 multiparticle spectrometer. (JGG)

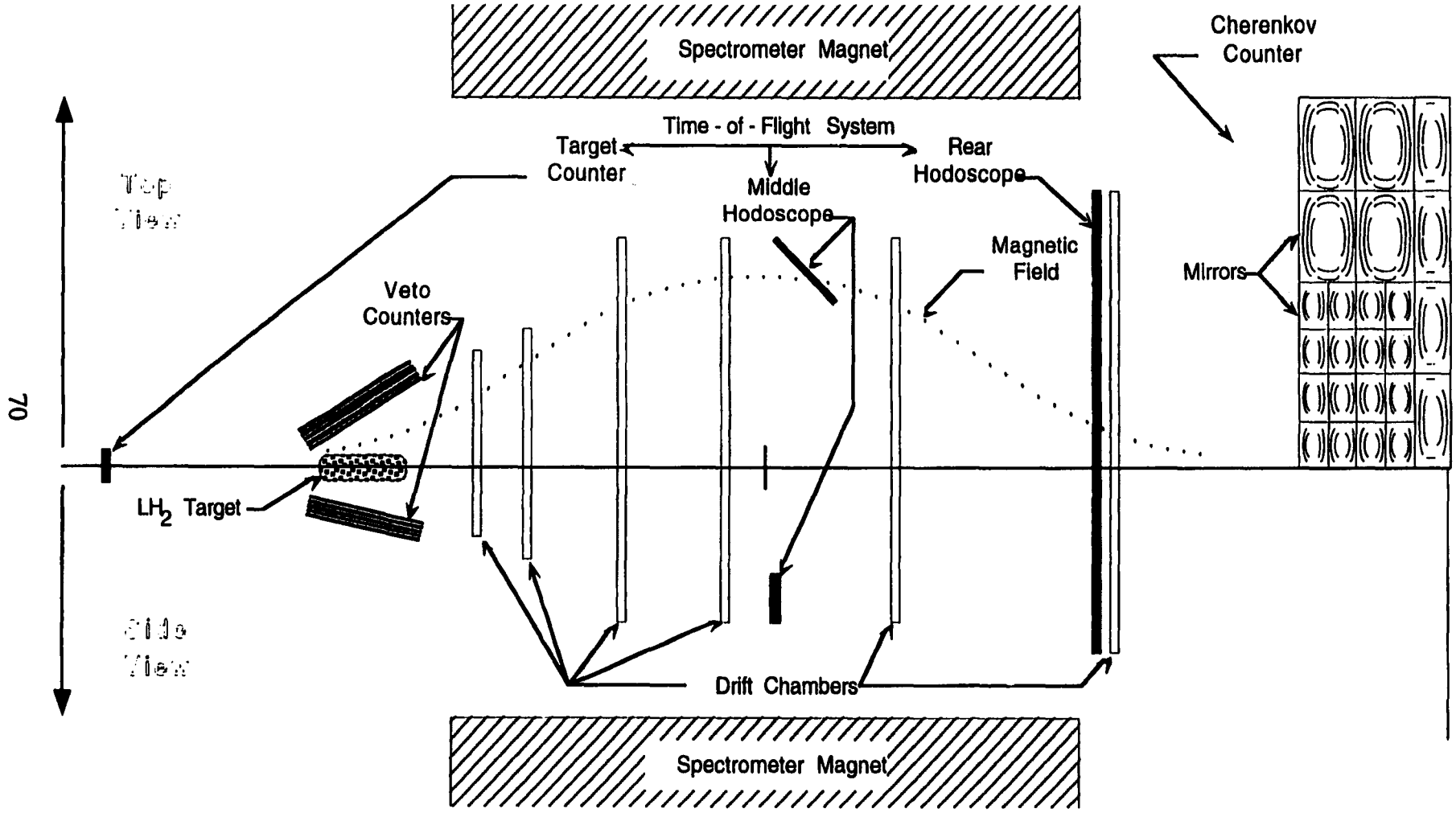

Fig. 2.3 Schematic view of the multiparticle spectrometer. The top view (xz plane) is represented above the center line; the side view (yz plane) is represented below the center line. The scale is approximately 1:22. The dotted line is a profile of the main (vertical) component of the magnetic field along the beam axis of the spectrometer.

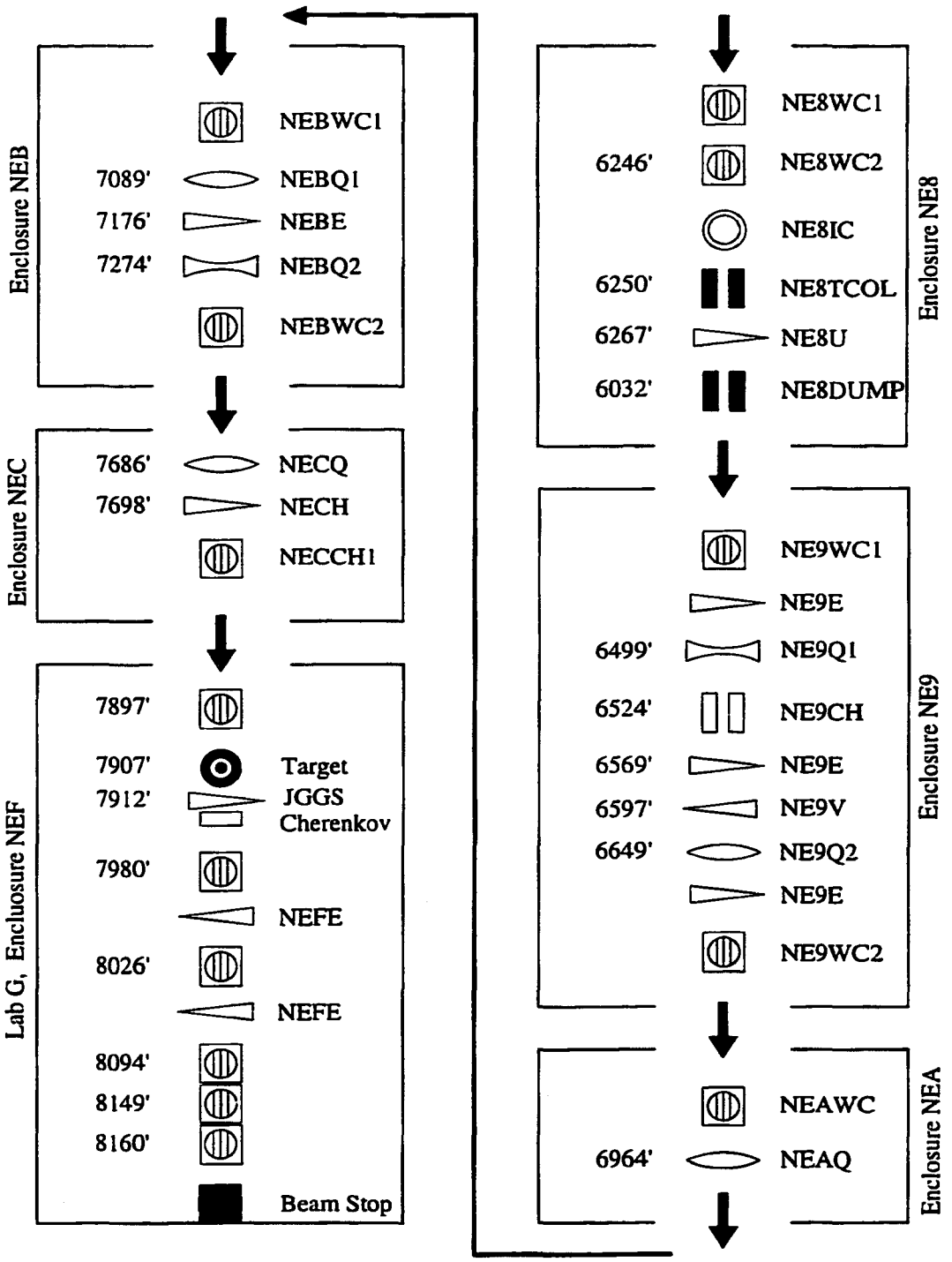

Figure 2.4 Neutrino east beam line. The numbers on the left are distances from Fermilab Tevatron. The arrows indicate the beam path.

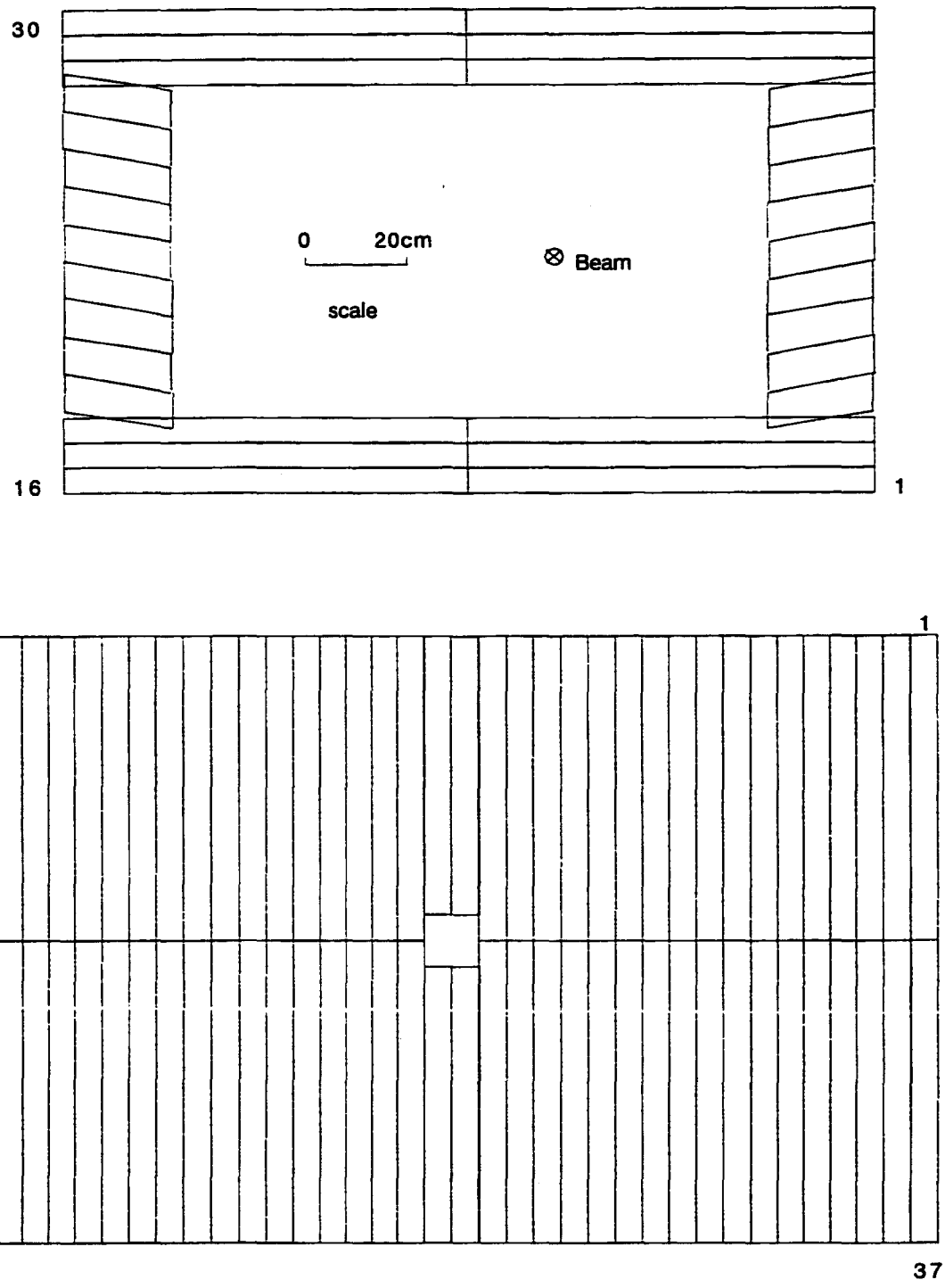

Figure 2.5 Scintillation counter positions for Middle (top) and Rear (bottom) Hododsopes.

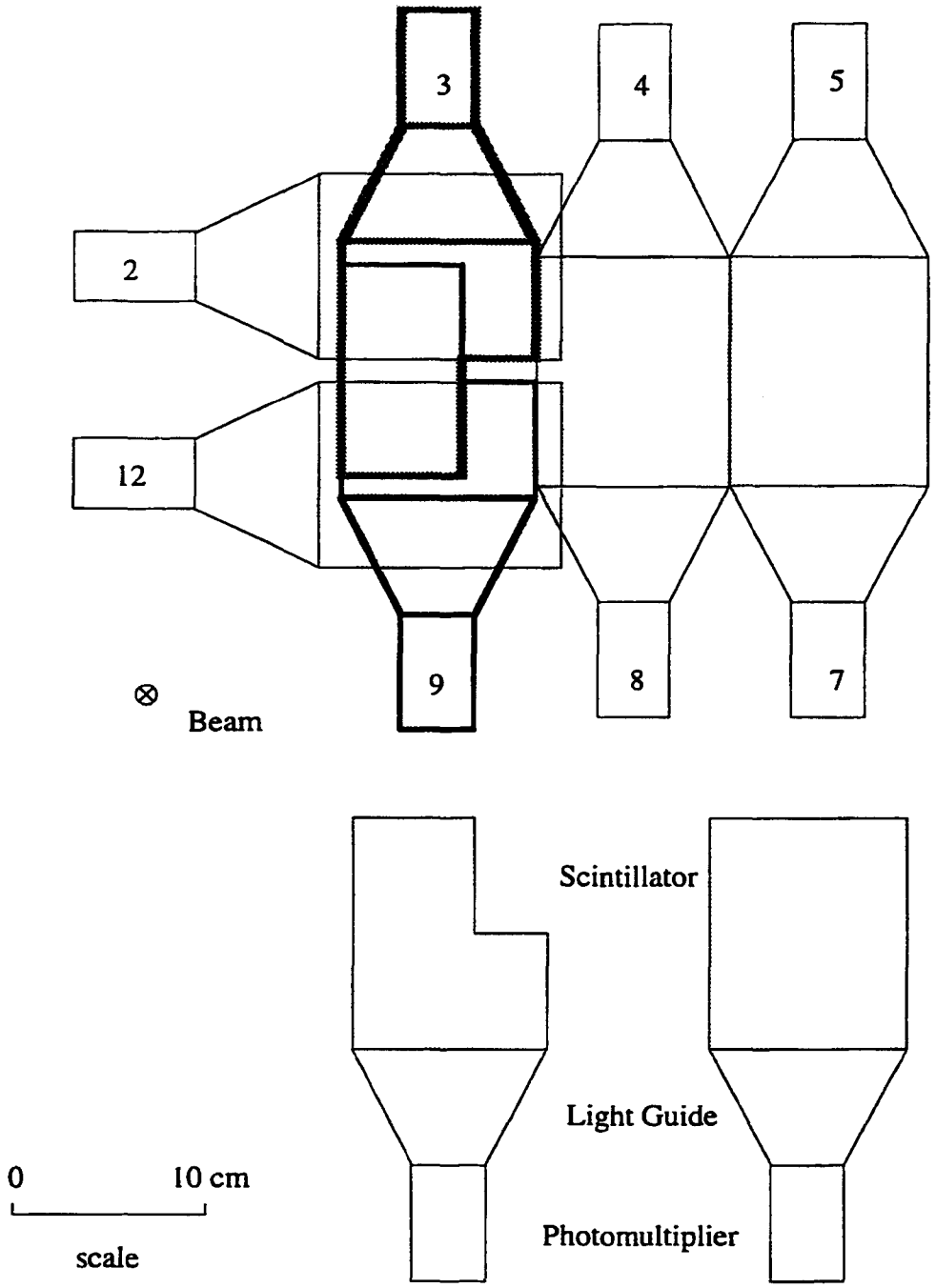

Figure 2.6 Positioning and coverage for Forward Hodoscope counters (top). The two scintillator shapes used to build the Hodoscope (bottom)

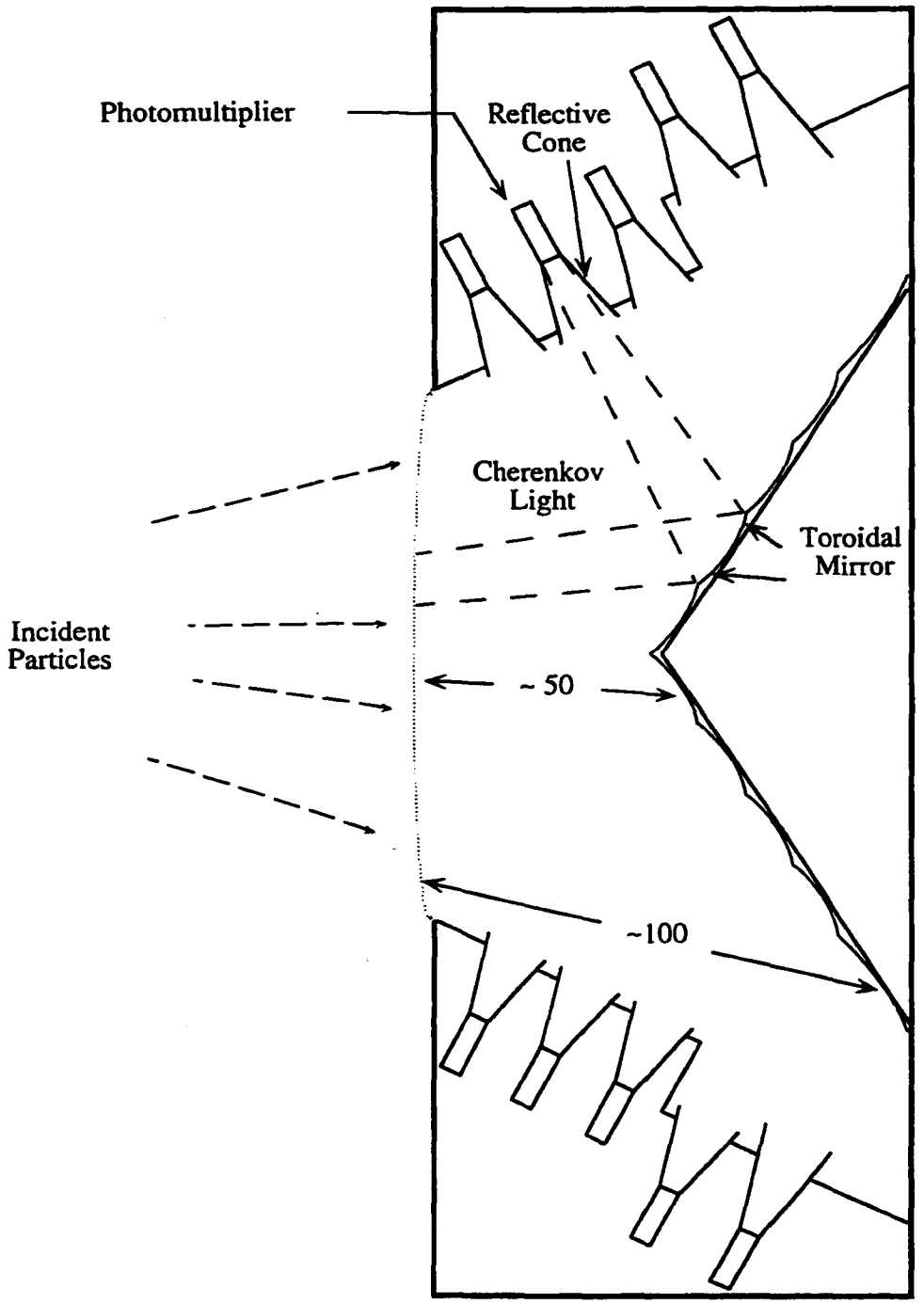

Figure 2.7 Side view of Cherenkev counter. The radiator is Freon 114.

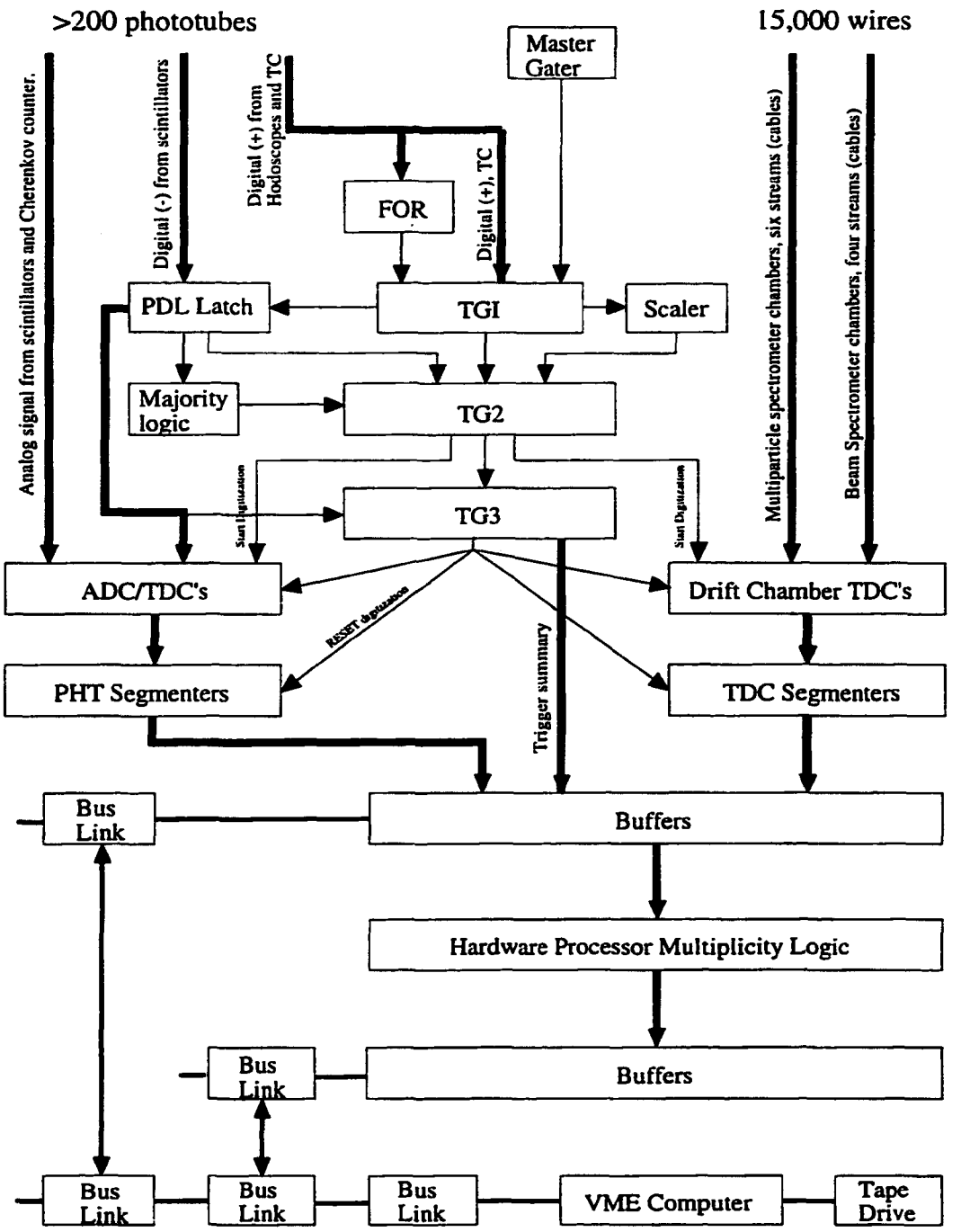

Figure 2.8 E690 data acquisition system.

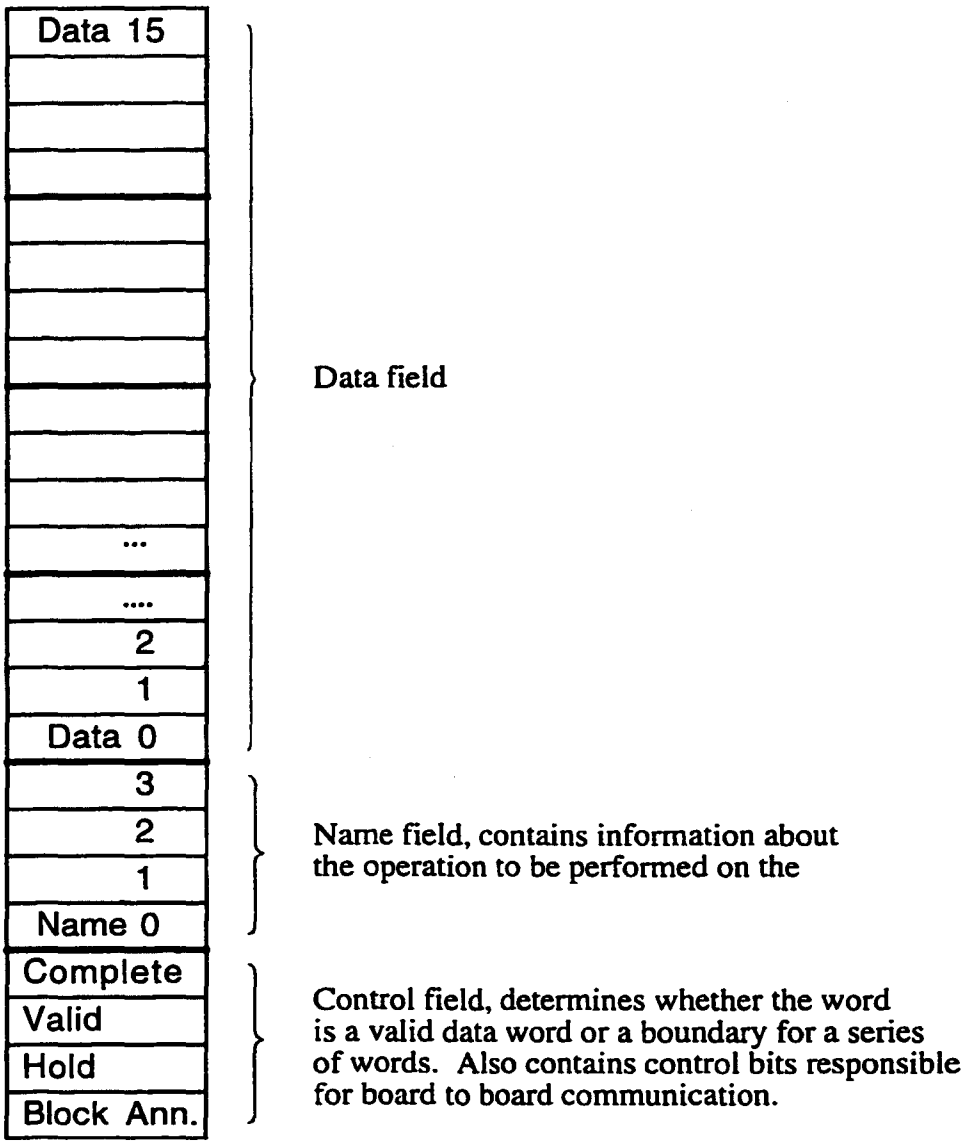

Figure 2.9 Processor word structure.

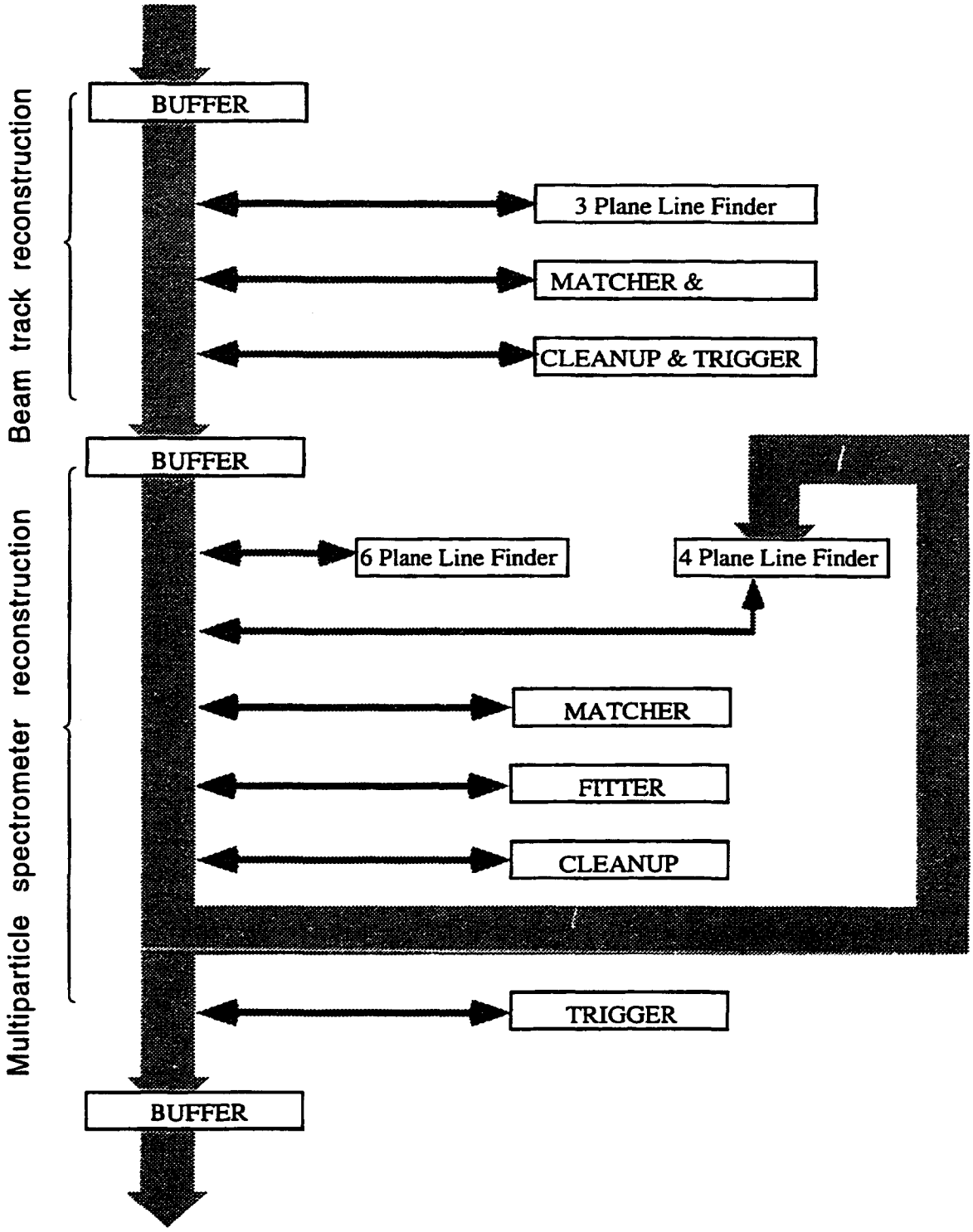

Figure 2.10 The block diagram of the E690 track reconstruction processor. The buffer tiers between reconstruction subroutines are omitted for simplicity.

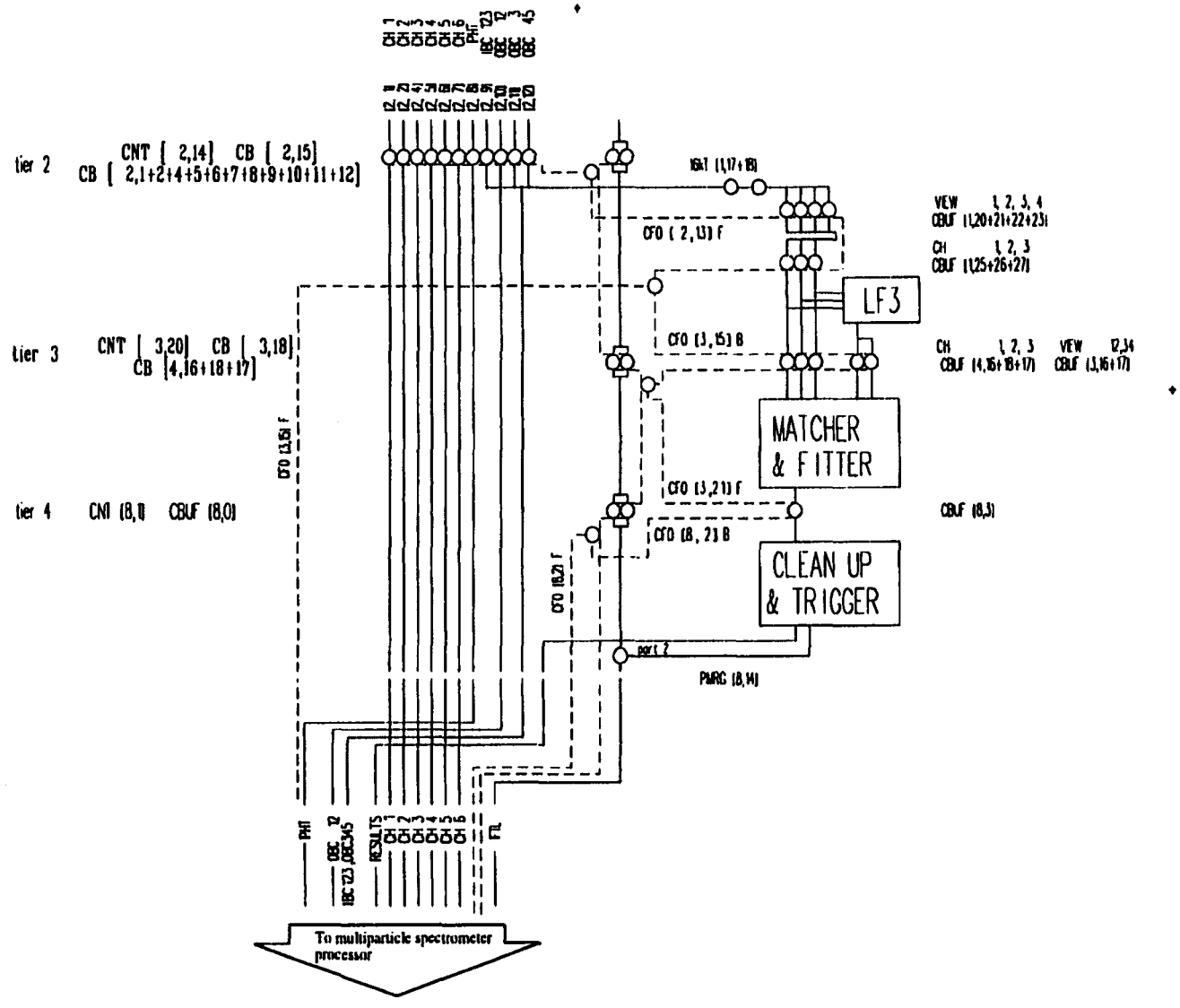

Figure 2.11 Beam spectrometer processor outline. Only the control boards are drawn. The computational subroutines are represented by boxes.

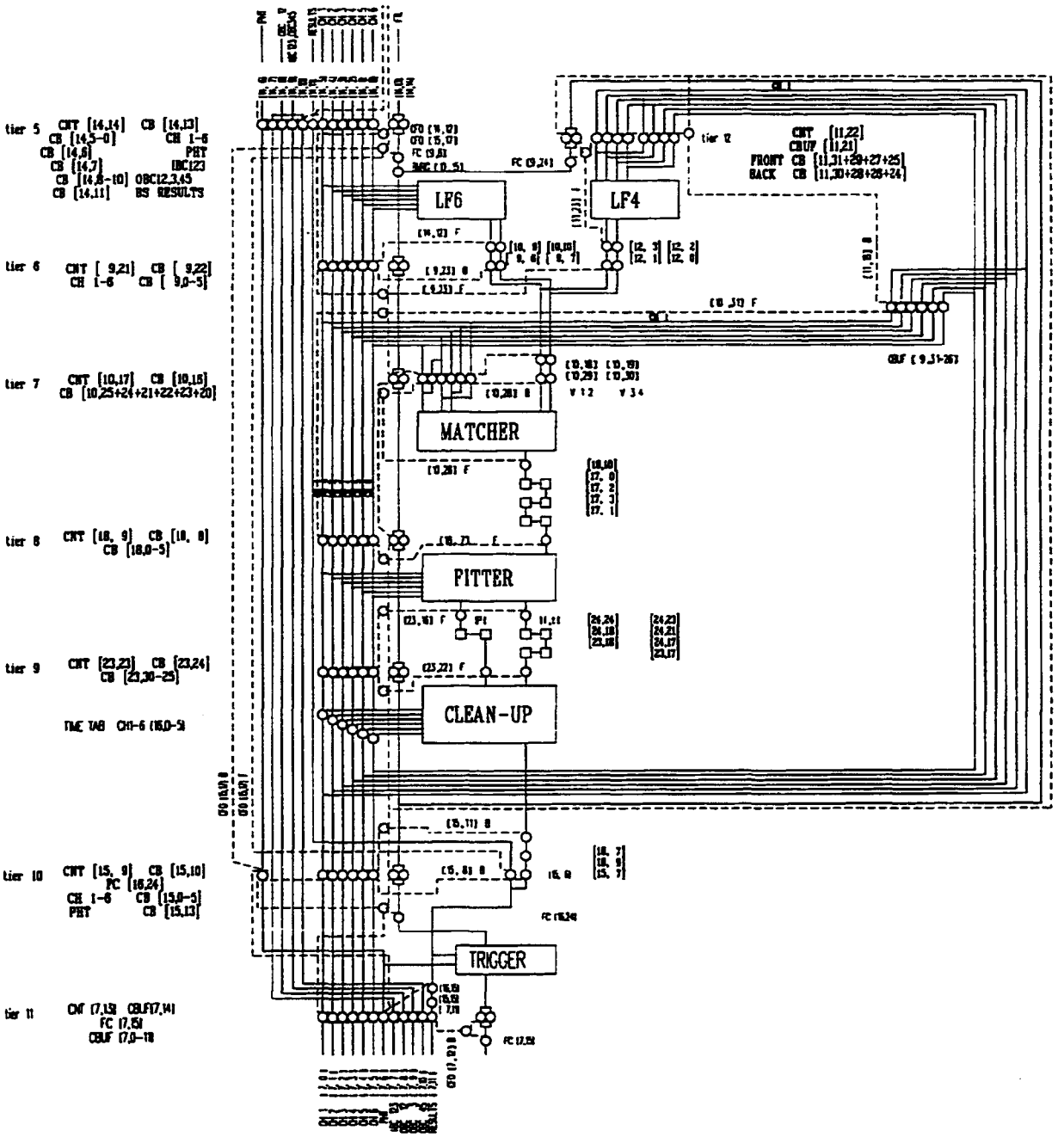

Figure 2.12 Multiparticle spectrometer control structure. Only control boards are drawn. The computational subroutines are represented by boxes. LF6 and LF4 stand for six plane and four plane line finder respectively.

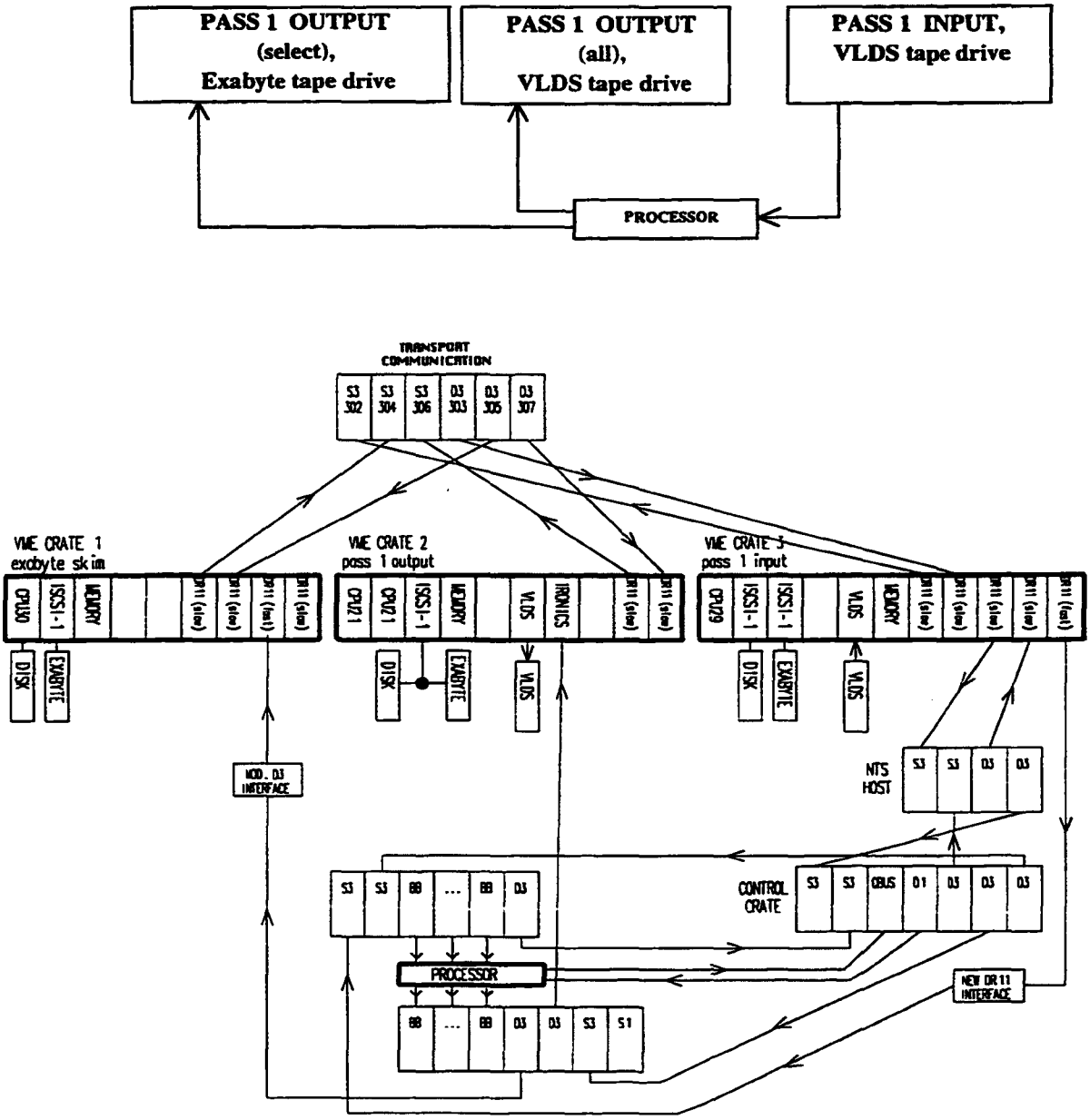

Figure 2.13 The Pass1 processing I/O control outline. The block diagram is shown at the top. The diagram used during the run to keep track of connection details is shown at the bottom of the figure.

CHAPTER 3

EVENT RECONSTRUCTION AND SELECTION

3.1 Definitions

After data collection, there is data processing necessary for, and common among all analysis efforts. It involves the reconstruction of charged tracks from drift chamber measurements and the identification of charged track intersection points (vertices). The processing is accomplished in two distinct steps we refer to as PASS1 and PASS2. The first processing step (PASS1) is performed by the hardware processor and involves reconstruction of beam and multiparticle spectrometer charged particle trajectories. The second step (PASS2) is performed by conventional computers and finds the primary collision vertex and secondary vertices from the decay of unstable particles into charged final states. At the end of PASS2, the event topology and the momentum vectors and origin of all charged tracks in the event is known and recorded. A more detailed account of the processing steps follows.

3.2 Track Reconstruction (PASS1)

The main reason for the separation of track reconstruction and vertex finding into two separate steps is the use of different hardware devices to accomplish the calculation. The first step is performed by the hardware processor which reconstructs beam and multiparticle spectrometer tracks much faster than any conventional computing device. Although the hardware processor solves the pattern recognition problem and reconstructs the majority of charged tracks, not all trajectories are resolved in the first step of processing. Rather, we find a subset of the tracks present in the multiparticle spectrometer,

tracks that span all six chambers of the Multiparticle Spectrometer, or the front four chambers or the back four chambers of the spectrometer. These three classes of trajectories represent the majority of reconstructed tracks. Wire chamber hits used for track reconstruction are tagged during processing. The remaining wire hits are used to find trajectories which are not members of one of these classes in a later reconstruction pass.

A block diagram of the algorithm used for track reconstruction is shown in Figure 2.10. There are separate hardware sections for the reconstruction of beam and multiparticle spectrometer tracks. The reason for the separation is both speed and different computation requirements. Since there are separate hardware sections we can increase the computation speed by processing concurrently more than one event in different hardware sections. The computation requirements are different because of the different parametrization used in the two spectrometer sections. Beam tracks can be reconstructed as two separate straight line segments, one line segment in the three incoming beam chambers and one line segment in the last three outgoing chambers. The multiparticle spectrometer lies within the magnetic field of the dipole magnet and therefore curved tracks must be reconstructed.

Nevertheless, except for the particular parametrization, the reconstruction algorithms are very similar. This is due to the identical configuration of anode planes in all drift chambers. All drift chambers have four anode planes (referred to as views) with wires oriented at -21.6^0,-7.63^0,7.63^0, and 21.6^0 with respect to the vertical. The four planes form two equivalent pairs (planes at -21.6^0 and 7.63^0 form one pair and the remaining two the second). The redundancy of view pairs allows us ideally to find each trajectory twice, independently, in each one of the two view pairs. This is useful in the case that one hit is missing in any one of the four planes, because the track trajectory can be determined by the pair with a complete set of hits. A more important benefit of the redundant measurements is the simplification of the algorithm that rejects hit combinations that do not form a three dimensional track.

Before a detailed presentation of the advantages of redundant measurements, an overview of the algorithm is presented. For both spectrometers (beam and multiparticle spectrometer) the calculation is divided in four stages: line finding, matching, fitting and duplicate rejection (see Figure 2.10). In the first stage (line finding) we combine hits from a single view and determine if they form a line within a view. Since the search is confined within a view, the number of combinations is limited. In other words we solve a two dimensional problem since the lines we find are not constrained *along* the direction of the wires that form the view. The lines found in each view are passed to the matcher stage where two dimensional lines from a view pair are combined to define a three dimensional trajectory. If we find n lines in one view and m lines in the second view the number of combinations that form candidate tracks is $n \times m$, while the number of real trajectories is somewhere between n and m. At this point we use the advantage of having redundant measurements to reduce the number of candidate trajectories with a very limited computational effort. For every candidate track defined by a pair of views, we compute the expected wire hits in the two remaining views. Then we compare the predicted wire hits with the measurement. If no more than one hit is missing, the candidate track parameters are passed to the fitter stage. This procedure eliminates most false candidates. Since the computation is performed independently for both view pairs, in an ideal case every track is parametrized and enters the fitter twice. In the fitter we use the wire numbers from all four views to reparametrize the track candidate. Since we have more measurements than the minimum necessary to define a trajectory, we use the initial parameters and the measurements to perform least squares fitting that improves the track parametrization. For both spectrometers (beam spectrometer and multiparticle spectrometer) we perform three iterations of least square fitting using just the measured wire numbers. Next, for the multiparticle spectrometer calculation only, the drift time measurements are used for a more accurate calculation, and another three iterations of least square fitting are performed. Finally the fitted parameters along with a ranking parameter representing the quality of the

fit are passed to the duplicate removal section. The ranking parameter is equal to the sum of the squares of the differences between predicted and measured wires plus a constant for every missing wire. If a track has poor ranking it is immediately dropped. The limit for track acceptance is set so that no more than one of all possible wire hits is missing for each trajectory. For example, six chamber multiparticle spectrometer tracks must have at least 23 of the maximum 24 wire hits assigned to the trajectory. For the remaining tracks we compare the fitted parameters to eliminate duplicates. If for two tracks the differences in all parameters are within preset limits, only the track with a better ranking parameter is kept. As stated before, in case of ideal chamber efficiency we expect each track to be fitted twice. Therefore we expect to reject about half of the fitted tracks.

The algorithm stages described above are common to all classes of tracks found during PASS1 processing. The algorithm takes advantage of the drift chamber design. In fact the drift chambers were designed with this algorithm in mind. The most notable characteristics of the chamber design are narrow wire spacing and redundant views per chamber. The narrow wire spacing allows us to solve the pattern recognition problem using just wire number information. Drift times are used only to improve the measurement precision. Redundant views allow us quickly to reject false track candidates without excessive computation.

Although we reconstruct all track trajectories using the four stages described above, there are significant differences within each stage, related to the different reconstruction requirements for different classes of tracks. A good example is the different line finding algorithms used in the multiparticle and beam spectrometers. For six chamber tracks we have to parametrize curved lines using six measurements per candidate line, while for beam spectrometer line segments we reconstruct straight line segments that span just three chambers. In the case of multiparticle spectrometer six chamber lines we reduce the number of combinations by solving the problem in two steps. First we find candidate lines

that span chambers one to four, and then we combine every one of the successful candidates with every hit in chamber six. In more detail, we first find all hit combinations between chambers one and four and for every pair we calculate the intercept of a straight line in chambers two and three. If there are hits in both chambers within a range of sixteen wires (road), centered at the predicted wire, we save the wire hit pair. Every pair of hits in chambers one and four that survives the test is combined with every hit in chamber six. The three hits are used to define a curved, second order line. We use this parametrization to predict and test for hits in a five wire road in chamber five. If hits are found, the same test is performed for chambers two and three. Finally three hit combinations that satisfy all tests are passed to the matcher stage. This line finding procedure is far more elaborate than the procedure used to define line segments in the beam spectrometer. For a straight line segment spanning only three chambers it is sufficient to perform only one test. We form all combinations in the two endmost chambers and check if a straight line calculation predicts hits in the middle chamber, within a five wire road. Algorithm differences, like the one illustrated for the four plane line finder, exist in all four stages of track reconstruction.

One of the prominent features of the algorithm outlined in Figure 2.10, is a loop in the multiparticle spectrometer data stream through the same hardware segments. This allows us to use the same hardware for matching, fitting and cleanup, for different classes of tracks. During the first pass, we find six chamber tracks and tag the hits that were used for reconstruction. Next, the data is routed to the four plane line finder, where we search for front four chamber (1,2,3, and 4) and back four chamber (3,4,5 and 6) lines. Both classes of four chamber lines are transferred and processed by the next three stages of the algorithm. In order to reduce the number of four chamber track candidates, wire numbers tagged during six chamber track finding are ignored. We make an exception and allow wire sharing only for the first of the four chambers used. This corresponds to Chamber 1 for front four and Chamber 3 for back four chamber tracks. We allow wire sharing because Chamber 1 is very close to the target, where we expect the highest track density.

The parameters used to define beam spectrometer three chamber line segments are simply the x and y coordinates of the track, at the two endmost chambers. For the curved tracks found in the multiparticle spectrometer we use four position and orientation parameters defined at chamber three ($x, y, {}^{dx}/_{dz}, {}^{dy}/_{dz}$), plus a parameter that defines the curvature of the track (sagitta). The four position and orientation parameters define a line connecting the two endmost space points of the track. The sagitta is the x coordinate of the distance between the track trajectory and the straight line defined by the other four parameters, at the track mid-plane. Note that the sagitta is approximately equal to ${}^{q}/_{P}$, where P represents the particle momentum and q the particle charge. In addition to the parameters mentioned above, for every track found we save a ranking parameter equal to the least square sum found by the fit plus a constant for every missing wire hit. More details about track reconstruction and parametrization can be found in [42]. Further details about the performance of PASS1 processing using the hardware processor can be found in Section 2.7 of this dissertation.

3.3 Vertex Reconstruction (PASS2)

The PASS1 output tapes contain all of the original detector information plus the parameters defining the track trajectories found during the first phase of processing. These tapes are used as input to the second analysis step (PASS2). The PASS2 phase of the analysis completes track finding for classes of tracks that are not searched for during PASS1 processing, and finds the primary collision vertex and secondary vertices from the decay of unstable particles into charged final states.

First, we use the two line segments found in the beam spectrometer to refit a single beam track through all eight of the beam chambers. Then we use the track trajectory to tag multiparticle spectrometer wire hits that lie on the beam track trajectory. The beam

spectrometer has long lever arms that allow precise measurement of the trajectory and therefore very good momentum resolution. In addition, we make a very precise measurement of the beam track path through the hydrogen target. We use this information to constraint the x and y coordinates of the primary collision vertex.

Next, we refit tracks already found in the multiparticle spectrometer. We use the track parameters found during PASS1 processing to propagate tracks through the drift chambers and tag the hits associated with each track. Then we attempt to associate front and back four chamber tracks that can form a single six chamber trajectory. Because low momentum six chamber tracks have large curvature, they fail the narrow "road" test used for six plane line finding. Such tracks are found during PASS1 processing as separate front and back four chamber tracks. After redefining such track pairs as a single six chamber track, we attempt to extend the remaining four chamber tracks beyond their defining chambers. For example we check if there are unused chamber five hits that allow a front four chamber track to span chambers one to five. Finally we use the remaining wire hits to search for a class of tracks we do not consider during PASS1 processing: tracks that span chambers two to five. For all the searches mentioned above, only unused wire hits are considered, significantly reducing the number of combinations available for track finding.

After we complete the search for track classes not addressed by the PASS1 reconstruction algorithm, we look for track intersections (vertices). The order of operations is very dependent on the final state (topology). For example, for the majority of events there is at least one reconstructed multiparticle spectrometer track originating at the primary collision vertex. Therefore it is reasonable to search first for the primary vertex and then to look for secondary vertices from the decay of unstable particles into charged final states. The problem with such an approach is that there are events for which such a choice is not practical. For such cases an iterative approach is required. Take as an

example the topology $pp \rightarrow p_{fast} K_S^0 K_S^0 p_{slow}$, with the target proton scattering outside the multiparticle spectrometer volume. Since the K_S^0 is neutral, we have to reconstruct its trajectory from the trajectory of its charged decay products ($K_S^0 \rightarrow \pi^+ \pi^-$). Only after determining at least one of the "composite" neutral tracks can we search for and find the primary vertex. This particular example illustrates the difficulty of constructing an algorithm that deals with every topology recorded by the multiparticle spectrometer.

Therefore we have to use an algorithm that proceeds on a case by case basis. We first check for intersection between the beam trajectory and any one of the multiparticle spectrometer tracks. If we find an intersection, defined when the distance of closest approach is smaller than a set limit, we save it as a vertex candidate. If more than one intersection is found we tag as primary vertex the vertex with the most tracks assigned to it. In the case that two vertices have the same number of tracks we tag the most upstream one as the primary vertex. Of course there are events where no intersections are found. Such is the case for the topology $pp \rightarrow p_{fast} K_S^0 K_S^0 p_{slow}$ mentioned above.

Whether a primary vertex is found or not, the next step is to search for secondary vertices from the decay of unstable particles into charged final states. We use the list of tracks that are not already assigned to a vertex (unassigned tracks) to form track pairs and check their distance of closest approach. Because we restrict the search to parent particles with charge -1,0, or +1, only tracks with opposite charge are considered. After the search is complete, we check if any one of the remaining unassigned tracks can be assigned to an existing vertex. We use the momentum vectors of particles assigned to a secondary vertex to reconstruct the trajectory of the "parent" particle. Then we check if we can assign the "composite" track to the primary vertex. If a primary does not already exist, we attempt to define one by checking the distance of closest approach between the new "composite " track and the beam track trajectory.

This is only the first iteration of vertex searching. In the first iteration, we use tight criteria of distance of closest approach to find only the best defined vertices. In subsequent iterations we relax the requirements in an attempt to find less well defined vertices, which occur because particles can suffer energy loss and multiple scattering in the detector material.

We use the vertex positions to define an additional space point constraint for the tracks assigned to a particular vertex. First we define the vertex position as the point in space that minimizes the sum of the distances of closest approach squared. Then we use the vertex position along with the drift chamber wire hits to refit the trajectories of each track assigned to a vertex. This significantly improves the reconstruction precision. In addition to improved resolution for track reconstruction, we use the primary vertex to search for tracks that span only the first three spectrometer chambers. Since we reconstruct curved tracks, a minimum of four space points is necessary for reconstruction.

The topology under consideration ($pp \rightarrow p_{fast}\pi^+\pi^- p_{slow}$) does not present many of the difficulties the vertex finding algorithm tries to tackle. It is a topology that its is fairly easy to identify because there are no secondary vertices and at least two of the multiparticle spectrometer tracks originate from the primary vertex in the hydrogen target. Nevertheless efficient vertex reconstruction of complicated final states is important for the identification and selection of the final state of interest. It also allows meaningful comparison of relative production rates between this and other final states (e.g. $pp \rightarrow p_{fast}K_S^0K_S^0p_{slow}$).

3.4 Selection of Final State $pp \rightarrow p_{fast}\pi^+\pi^- p_{slow}$

The next step of the analysis effort is the selection of a subset of the data sample containing only the reaction $pp \rightarrow p_{fast}\pi^+\pi^- p_{slow}$. Choosing the selection criteria we have to balance two conflicting requirements. While we want a pure sample (only $p_{fast}\pi^+\pi^- p_{slow}$ final

states), we want to avoid very aggressive selection criteria that can bias the distribution of the analysis variables. The choices made for the event selection are presented in this section. I present the number of events selected in each step and the effects of the selection on the distribution of the analysis variables. I also present the specific background interactions each step intends to eliminate.

The selection of the final sample is based on the results of the vertex reconstruction calculation. For this study we use only ~10% of the events recorded by the experiment (0.46×10^9 out of a total of 5.5×10^9 events). We use only a fraction of the total sample because, as will be demonstrated in the analysis section, the measurement is not limited by the statistical significance of the final sample. Rather, the most significant error source is the estimation of systematic effects.

Interest in central production is due to the kinematics of the interaction. As mentioned in the introduction, the final state protons are kinematically well separated from the new particles produced, which supports the hypothesis that the reaction proceeds through a double exchange mechanism. Therefore we treat the reaction as a two step process where the interaction produces an intermediate meson which subsequently decays via the strong interaction, for this study into two pions:

$$p + p \rightarrow p_s X p_f$$
$$X \rightarrow \pi^+\pi^-$$

The longitudinal momentum of the intermediate meson state (X) is restricted to within about 20% of the maximum longitudinal momentum. The detector acceptance is very sensitive to the longitudinal momentum distributions. To illustrate this point the table below presents the laboratory momenta in GeV/c for the two final state protons and the intermediate meson (X) as a function of the intermediate meson x_F. For this calculation the

mass for (X) is set at 1 GeV and the perpendicular momentum (p_t) for the three final state particles is set to zero.

x_F	p_s	X	p_f		p_{min} *for* π	p_{max} *for* π
-0.2	0.214	2.533	797.253		-0.041	2.574
-0.1	0.105	4.976	794.919		0.051	4.925
0.0	0.025	20.635	779.340		0.398	20.237
0.1	0.006	84.823	715.171		1.683	83.140

The assumption that $p_t = 0$ is a good approximation since in double diffraction perpendicular momentum for the final state protons is very limited. From the table we see immediately that the lab momentum of the slow (target) proton is very small in all cases and it is unlikely to observe it as a trajectory in the multiparticle spectrometer. For the vast majority of events the slow proton either stops in the target (the minimum momentum for a proton to exit the target is approximately 100 MeV/c) or escapes the multiparticle spectrometer volume as a wide angle track. Since we do not observe the slow proton we deduce its momentum vector from energy-momentum conservation. Another property that is evident from the table is the rapid increase of the lab momentum for the intermediate state as a function of x_F. Since the resolution of the multiparticle spectrometer deteriorates rapidly for particle momenta above 20 GeV/c, the probability for accurate reconstruction of events with $x_F > 0$ for the central meson (X) is very small. The conclusions above do not change significantly as a function of the invariant mass for the (X) system. The same table for mass of the X system equal to 1.7 GeV follows.

x_F	p_s	X	p_f		p_{min} *for* π	p_{max} *for* π
-0.2	0.221	7.295	792.484		-0.047	7.342
-0.1	0.116	13.209	786.675		0.036	13.173
0.0	0.042	35.080	764.878		0.218	34.862
0.1	0.016	92.884	707.100		0.623	92.262

This simple calculation justifies our choice to concentrate on events with only two tracks observable in the multiparticle spectrometer. Next I will give a brief list of the selection criteria used to define the final analysis sample. Not all of the selection criteria were used to reduce the sample size. We want to study the effect of selection criteria on the physics analysis, therefore only "soft" cuts were used to reduce the data sample to a manageable size. We use this reduced data sample to apply different sets of final selection criteria. Comparison of the results for different sets of final selection cuts allows us to distinguish between physics and artifacts produced by the selection criteria. I describe the sequence of steps used to isolate a reduced data sample and finally I give a detailed account of the selection cuts used in this manuscript.

First a brief description of the selection criteria:

1) Track reconstruction requirements are at least one reconstructed track in the beam spectrometer and exactly two reconstructed tracks with opposite charge in the multiparticle spectrometer. There should be exactly one primary vertex with all tracks assigned to it.

2) Particle identification in the Cherenkov counter requires that both particles are pion compatible. This is a "soft" requirement that does not restrict the momenta of the pion candidate tracks. Later we use alternative requirements for better particle identification.

3) Missing longitudinal momentum (MPl), presumably the longitudinal momentum of the missing particle in the [-1,1] GeV/c range.

4) The rapidity gap between the missing proton and any one of the multiparticle spectrometer particles must be greater than 1.8 rapidity units. The purpose of this cut is to remove events that proceed through single diffractive processes, and the production of resonances, e.g. Δ^{++}.

5) Restriction of the x_F distribution for the central intermediate meson (X) to $-0.1 < x_F < 0.0$, so that we can easily integrate over x_F when we apply Monte Carlo corrections.

6) Restriction of p_t^2 for final state protons. As will be demonstrated later, a very effective cut for the rejection of events that do not correspond to the final state $p_{fast}\pi^+\pi^- p_{slow}$ is the restriction $p_t^2 < 0.1$ (GeV/c)^2 for the slow proton. This selection takes advantage of the steep p_t^2 distribution of the final state protons in double diffractive events. When we restrict $p_t^2 < 0.1$ for both final state protons we have a sample where we expect double Pomeron exchange to dominate.

7) Missing mass cut (MM2). The value of the missing mass is calculated by assigning the missing energy and missing momentum to the missing particle. For correct topology identification we expect the resulting value to be equal to the mass of the proton. This is a cut based on energy-momentum conservation and is used both for background rejection for estimation of the number of background events remaining after the application of selection cuts. The presentation of the effects of this cut is complicated by the earlier application of the missing longitudinal momentum

cut (3). I will show that all events selected by this cut survive the missing longitudinal momentum cut. Therefore the cuts can be applied in sequence.

For the reduction of the data sample to a manageable size we use only the first three cuts. The remaining cuts are used only in the final analysis stage. We select from two "source" samples. One is a sample of 100 million unbiased detector events processed by PASS2 without the application of selection criteria. The other sample is a subset from 360 million unbiased detector events, selected during PASS2 processing. Selection during PASS2 processing is a standard procedure in this experiment, aimed at the reduction of the amount of tape handling necessary for our analysis. For each of the physics topics pursued by the collaboration, we define a set of selection criteria that isolate a subset of the data sample necessary for the particular analysis. During PASS2 processing we write two output samples. An unbiased output stream that contains all input events and a second stream that contains events that satisfy the aforementioned selection criteria. The size of the second stream contains about 20% of the initial events. The selection from the two "source" samples was performed so that I can compare the event yield in the two cases and guard against mistakes during PASS2 selection.

From the two samples I produce a series of tapes that contain events which pass the first two selection cuts and a generous missing longitudinal momentum cut [-3,3] GeV/c. This is one of the selection requirements used for the second PASS2 output stream mentioned earlier. Therefore from now on I do not need to make a distinction about the "source" samples the events come from. The next step is to produce a series of tapes that contain the same events with a more tighter longitudinal momentum cut [-1,1] GeV/c, since this is the final cut used for analysis. The last data handling step is the "compression" of the selected events into a single file for easy processing. The large number of events available for analysis makes difficult the repetition of the analysis steps with small variations in the selection criteria. This step reduces both the storage and processing

requirements. We save only event variables necessary for the analysis and reduce the necessity of reevaluating the analysis variables with each analysis step. Also, the storage size of the final sample is reduced by a factor of 10.

As mentioned above, we use the missing mass distribution to estimate the number of missidentified events in our data sample. Figure 3.1 shows how the missing mass squared distribution changes as a function of the selection criteria. For the plots presented here I do not use the entire data sample. For this study it is sufficient to use events from a single VHS primary tape (tape #2774). The tape contains 6.518×10^6 unbiased detector events. Application of the first two selection criteria (vertex and "soft" Cherenkov identification) reduces the sample to 389,652 events. For this sample the missing mass squared is shown in Figure 3.1.a. The next 5 figures in the same page show the effects of the rapidity, x_F and p_t^2 selection criteria. The rapidity and x_F cuts do not have a significant effect on the signal to background ratio (Figures 3.1.b and 3.1.c). For the p_t^2 cut there are three plots. Figure 3.1.d shows the effect of restricting p_t^2 only for the fast proton; Figure 3.1.e only for the slow (missing) proton and Figure 3.1.f for application of both p_t^2 cuts. Although restricting p_t^2 for the fast proton has a significant effect, we see dramatic background reduction only from application of the slow proton p_t^2 cut.

The same plots are presented for alternative Cherenkov cuts in Figures 3.2 and 3.3. For Figure 3.2 we require that at least one of the two particles in the multiparticle spectrometer is identified by the Cherenkov counter as "exactly pion". Since the counter thresholds for pion/kaon/proton are 2.55/9/17 GeV/c, the positively identified particle has to have momentum between 2.55 and 9 GeV/c and intersect the counter aperture. For Figure 3.3 we require both particles to satisfy the "exactly pion" condition. The alternative requirements reduce the background significantly, but they also introduce a longitudinal momentum bias, and reduce the number of events available after the first two cuts, to 119,980 and 15,401 respectively. Note that the initial "soft" Cherenkov cut does not

require that a particle produce light in the Cherenkov counter. A low momentum particle that does not enter the counter aperture is considered pion compatible.

We fit the missing mass squared distribution using a Gaussian that represents the signal expected for a missing proton, and a second order polynomial for the background. We do not expect high quality fits because there are multiple background sources that can result in a complex shape for the background distribution. In addition we expect the background shape to change as a function of selection criteria. For example, we can have cases where there is more than one missing particle. This background source is greatly reduced when we restrict the missing transverse momentum. A second possibility is that we observe the final state of interest (two protons and two charged pions) but the particle momenta are such that the proton is measured in the multiparticle spectrometer and is considered a pion, while the missing pion has low momentum and is considered a missing proton. Such events are rejected by the rapidity and x_F selection requirements. A third possibility (for "soft" Cherenkov cuts) is a missing proton and two particles in the multiparticle spectrometer that are K^+K^- or $p\bar{p}$. Therefore we select a simple polynomial for the background distribution and we do not consider it a detailed description of the background shape. For a missing proton we expect the Gaussian distribution to peak at the square of the proton mass, 0.8 $(GeV/c^2)^2$. Because the calculation is very sensitive to the calibration of the beam spectrometer we see a systematic shift of the peak to 0.3 $(GeV/c^2)^2$. This shift does not affect our ability to select events using the missing mass distribution.

From Figures 3.1-3.3 we can see that the center and width of the Gaussian describing the missing proton changes slightly as a function of the selection criteria used to define the sample. As will be shown later, it also changes as a function of the invariant mass for the intermediate meson (X). Since I use tight missing mass selection criteria and the signal to background ratio does not change rapidly, I avoid using a different definition for the Gaussian every time I use the missing mass cut, and use a standard center and width

throughout this document. For the definition I use the fit in Figure 3.1f which has mean=0.3 $(GeV/c^2)^2$ and σ=0.84 GeV/c^2. Table 3.1 presents the ratio of integrals: Signal/Background, estimated from the fits in Figures 3.1 to 3.3. The integration range is $[-\sigma,\sigma]$, centered at the peak of the Gaussian.

Absent from the selection criteria used for the missing mass plots, is the missing longitudinal momentum cut (number (3) in the selection criteria outline). The reason is the correlation between the two selection criteria. I will show that the MPl cut is "generous" enough that it allows us to apply the MM2 cut as if the MPl cut never happened. To illustrate this, Figure 3.4.a shows the MM2 distribution before and after the application of the MPl cut. The vertical lines mark a $\pm\sigma$ distance from the peak of the Gaussian distribution. We can immediately see that the MPl cut is roughly equivalent to 1.5 σ cut on the MM2 distribution. In subsequent Figures (3.4.b-3.4.f) we apply the rest of the selection criteria outlined above. We see that by the time we apply the $p_t^2(slow)$ cut there are practically no events left within $\pm\sigma$. This is better seen if we use the number of events left after application of the MPl cut to scale the plot (Figure 3.5). In this plot, it is easier to see the number of events remaining after the application of the MPl selection. For Figures 3.4 and 3.5 we use "soft" Cherenkov identification selection. Figures 3.6 and 3.7 are the same as Figure 3.5, except for the use of more restrictive Cherenkov identification selection.

From the argument outlined above, it is clear that the MPl selection is redundant, since the same events can be selected using just the MM2 cut. The only reason we use this selection criterion is historical. Selection during PASS2 processing uses the MPl cut, so the cut is kept for continuity. The MM2 selection is used later, usually as a $[-\sigma,\sigma/2]$ cut. The selection using either one of the cuts is rather aggressive, eliminating a significant part of the signal. This is not a problem for this study, since the precision of the measurement

is dominated more by the estimation of systematic effects than by the statistical significance of the sample.

The x_F distributions for the final state protons and the central meson (X) are shown in Figures 3.8-3.10. As expected for central production the x_F distributions are clearly separated. Here it is important to note that the separations in x_F distributions are also forced by the acceptance of the spectrometer and the choice of the data sample. We select events with a missing slow proton. Therefore we restrict the slow proton x_F range. We require two particles in the multiparticle spectrometer and since the spectrometer acceptance is limited to particles with momentum between 0.1 and 25 GeV/c, the spectrometer shapes the x_F distribution of the central meson. For the vast majority of events the central meson has negative x_F. Although the apparatus allows for events with a central meson that has a large negative x_F value, the majority of events are produced near the x_F=0 region. The beam spectrometer accepts outgoing beam particles with momentum above 650 GeV/c, which imposes one more restriction to the x_F distribution. The effect of selection cuts on x_F distributions can be seen in Figure 3.8. For this Figure we use "soft" Cherenkov identification. The MPI requirement restricts the fast proton x_F because events with large momentum transfers to the target system have high momentum, poorly reconstructed tracks in the multiparticle spectrometer. The rapidity cut, as expected, further separates the slow proton and central meson x_F distributions. The restriction of the central meson to $-0.1<x_F<0.0$ changes the slow proton x_F distribution. It removes events close to x_F=-1. This is simply due to momentum conservation. The final two cuts, p_t^2 and missing mass, do not have any significant effect on the x_F distributions. The same observations apply to Figures 3.9 and 3.10, where we use more restrictive Cherenkov identification requirements. The only significant difference is the much more limited x_F distribution for the central meson. Since the counter thresholds for pion/Kaon/proton are 2.55/9/17 GeV/c, the positively identified particle has a limited momentum range which restricts the momentum distribution of the central meson.

Figure 3.11.a shows the missing longitudinal momentum (MPl) distribution after application of the first two selection cuts (vertex requirements and "soft" Cherenkov identification). The vertical lines mark the third cut ([-1,1] GeV/c MPl limit), used to define the data sample for this study. Figure 3.11.b (solid line) shows the MPl distribution after application of rapidity, x_F and p_t^2 cuts. Also shown is the MPl distribution after application of the missing mass squared cut (dash). We can see that there is a small calibration problem, since the MPl distribution is centered at about 200 MeV/c below zero. The application of selection cuts makes the MPl distribution more narrow. This is partly due to the reduction of background, but also due to the elimination of events that contain poorly measured, high momentum particles, through the application of cuts that restrict the central meson (X) lab momentum (e.g. x_F). Figures 3.11.c-3.11.f present the same plots for alternative Cherenkov identification selection criteria.

As mentioned earlier, the amount of background changes as a function of the invariant mass. In Figures 3.12 to 3.17, the missing mass squared distribution for 0.25 GeV/c^2 regions of the central meson (X) invariant mass is shown. In Figure 3.12 the simplest of selection criteria are used, namely vertex requirements (1) and pion compatibility in the Cherenkov counter (2). In Figure 3.13 we require in addition that rapidity (4), x_F (5) and p_t^2 (6) selection criteria are satisfied. This is the sample on which we base most of our analysis. We see from this figure that the background is more pronounced below 0.75 GeV/c. It is also a bit larger in the region of 1.0 to 1.25 GeV/c^2. As stated earlier, the fit of the signal with a Gaussian plus a second order polynomial background shows a small dependency of the Gaussian peak on the mass region fitted. We do not fit the last mass region (1.5 to 2.5 GeV/c^2) because there are not enough events for a reasonable fit. Figures 3.14 to 3.17 contain the same plots for more restrictive Cherenkov identification requirements.

So far we have judged the effects of the selection criteria by looking at the missing mass squared distribution. An alternative is to look at the effects of the selection criteria on the invariant mass distribution of the central meson (X). As can be seen in Figure 3.18, the invariant mass distribution falls rapidly after 1 GeV/c^2. Therefore, observation of the selection effects in the mass region above 1 GeV/c^2 requires better statistics than the single VHS tape we used so far. For the invariant mass distributions I use the whole sample used for this analysis (about 10% of all events recorded by the experiment). Figure 3.18 shows how the mass distribution is shaped by the selection criteria outlined earlier (see legend for cuts applied to each plot). In Figure 3.18.b we see the invariant mass after application of selection criteria (1) to (4) (vertex, Cherenkov, missing p_L and rapidity restrictions). In the same plot we see that successive application of the x_F selection cut does not alter (except for a change in scale) the invariant mass distribution. Small peaks in the mass distribution due to $\rho(770)$ and $f_2(1270)$ are clearly seen. As expected, application of p_t^2 cuts increases the probability that the final state observed is S-wave. This suppresses the higher spin resonances just mentioned. Further reducing the sample with the application of the missing mass cut does not change the distribution significantly. For a more detailed look at the high mass region, Figure 3.19 presents the effect of the same selection criteria in the mass interval 1 to 2.6 GeV/c^2. Here there are two prominent features: A drop of the invariant mass distribution at 1.5 GeV/c^2 almost as dramatic as the drop at 1 GeV/c^2, and the reduction of the signal presumably due to $f_2(1270)$ with the application of the p_t^2 selection criteria. Note that the dramatic drop at 1500 MeV/c^2 is exactly where the Crystal Barrel collaboration reports the glueball candidate $f_0(1500)$. Figures 3.20 to 3.23 contain the same plots for more restrictive Cherenkov identification cuts. The main difference here is the shape of the distribution near threshold. With application of "exactly pion" requirements, events near threshold are dramatically suppressed. The main reason for this suppression is not excessive background in the threshold region. Near threshold there is a very small amount of kinetic energy for the final state pions. Therefore there is a small

probability for any one of the pions to travel away from the beam proton trajectory. As mentioned in the Cherenkov counter section, the four central cells of the Cherenkov counter are not being used because the Cherenkov light from the beam proton keeps the mirrors always on. Therefore the application of Cherenkov cuts that require positive particle identification depletes the sample mostly near threshold. For the same reason "soft" Cherenkov identification is least effective in the threshold region.

The last two families of plots in the data selection concern the transverse momentum distribution of the final state protons. The distribution of the four momentum transfer (t) is very similar to the transverse momentum distribution because of the kinematics of the interaction (small difference in initial and final state longitudinal momentum)*. The four momentum transfer is a Lorentz invariant and is often used to characterize diffractive reactions. For completeness both variables are plotted for various cases.

Although the two final state protons are identical, we see that there are differences in the observed p_t^2 distributions due to detector acceptance. Figures 3.24 to 3.26 show the transverse momentum distribution for the slow (target) proton as a function of selection criteria, and Figures 3.27 to 3.29 show the same plots for the fast (beam) proton. Keep in mind that the slow proton is not observed, therefore we assign to the missing particle the

---

* For both initial state protons initial transverse momentum is equal to zero. For any one of the final state protons the four momentum transfer is:

$$t^2 = \left(E_i - E_i,\ \overline{P}_i - \overline{P}_f\right)^2$$

For relativistic final state protons, we can use the approximation:

$$E_i = \sqrt{\overline{P}_{L,i}^2 + m_p^2} \cong P_{L,i} + \frac{1}{2}\frac{m_p^2}{P_{L,i}}$$

$$E_f = \sqrt{\overline{P}_{L,f}^2 + \overline{P}_T^2 + m_p^2} \cong P_{L,f} + \frac{1}{2}\frac{m_p^2 + P_T^2}{P_{L,f}}$$

Then we can rewrite the four momentum transfer as:

$$t^2 = -P_T^2 - \frac{\Delta P_L}{P_{L,f}}P_T^2 + \frac{1}{4}\frac{P_T^2}{P_{L,f}^2} - \frac{\Delta P_L^2}{P_{L,f}P_{L,i}}m_p^2 + \frac{\Delta P_L}{P_{L,f}^2 P_{L,i}}P_T^2 m_p^2 + \left(\frac{\Delta P_L}{P_{L,f}P_{L,i}}m_p^2\right)^2$$

Given the x_F distributions we observe, the most significant term in the sum is P_T^2.

transverse momentum necessary to balance the event. As shown in the x_F distribution plots, there are differences in the longitudinal momentum distributions of the two protons. The main reason for the differences between the p_t^2 distributions is the acceptance of the beam spectrometer and the fact that the target proton is not observed by the apparatus. Before commenting on the slopes of the distributions, it is worth mentioning some striking differences between the slow and fast proton, visible in all selection stages. In the high p_t^2 region there are many more events for the slow (target) proton than for the fast (beam) proton. For all comments made here, keep in mind the logarithmic scale of the plots. The number of events near 1 $(GeV/c)^2$ is very small compared to the whole sample. One reason for the discrepancy is the acceptance of the beam spectrometer as a function of p_t^2. There is a cutoff limit for transverse momentum a little above 1 $(GeV/c)^2$. The limit of transverse momentum is correlated to the longitudinal momentum loss of the beam proton and is not a simple number. Nevertheless because the longitudinal momentum transfer of the beam proton for the sample we study is very limited, there is effectively no acceptance correction below 1 $(GeV/c)^2$. The main reason for the different number of events is the fact that we do not observe the slow (target) proton. In Figure 3.24 we can immediately see that if we do not apply strict selection criteria, it is impossible to fit a single exponential for the whole range between 0 and 1 $(GeV/c)^2$. This is due to missidentified events with more than one particle missing, or one missing particle that is not a proton. We expect such events to have higher p_t^2 since the particles can be decay products of intermediate states and have significant recoil momentum. This expectation is consistent with the effects of the p_t^2 cut on the missing mass squared distribution. We see a dramatic drop in the number of events with poor longitudinal momentum balance after application of the p_t^2 selection cut. This can be easily attributed to an increase of the ratio of correctly identified events to events with more than one missing particle.

Although the differences near p_t^2=1 $(GeV/c)^2$ are clearly visible in the logarithmic plots, they involve a small number of events, at least after the application of strict selection

cuts. A significant difference that involves a much larger number of events is a "dip" in the fast proton p_t^2 distribution at p_t^2=0. As can be seen from the plots, we lose events in the first two bins of the beam proton distribution (0.01 $(GeV/c)^2$ per bin). There are two reasons for the observed inefficiency: the forward hodoscope trigger requirement and the loss of efficiency the beam chambers suffer along the uninteracted beam trajectory.

The forward hodoscope trigger depends only on the position of the beam track at the end of the beam line. Event digitization and readout is aborted in the absence of a double coincidence for the forward hodoscope counters. As can be seen in Figure 2.6 a small hole in the counter array allows for the uninteracted tracks to pass through the forward hodoscope without hitting the counters. For small values of p_t^2 it is possible for a beam track to pass through the counter hole and be rejected by the forward hodoscope trigger. The other source of inefficiency is the strict requirements for reconstruction in the beam spectrometer. Since we use a 2.5% interaction target the vast majority of beam tracks travel through the same path in the beam spectrometer drift chambers. The ionization from the uninteracted beam tracks creates over time chemical deposits on the wires residing on the "beam spot". The deposits are localized at the "beam spot" and do not reduce detection efficiency for the entire length of the wire. As was the case for the trigger inefficiencies, beam tracks with low p_t^2 and momentum transfer travel close to the beam trajectory and have a higher probability to be affected by chamber inefficiencies. Since the requirement for the reconstruction of a beam track is that no more than one wire hit is missing in the outgoing beam chambers, small changes in the chamber efficiency can translate into significant changes in the number of events accepted by the spectrometer.

Given the comments on inefficiency for beam track reconstruction near $p_t^2 = 0$ and the effect of background on the slow proton p_t^2 distribution for high values of p_t^2, we do not consider the observed distributions for p_t^2 as the production distributions. We expect the observed and produced distributions to have similar slopes if we fit away from the

"problem regions", and use samples for which strict selection cuts have been applied. The fitting function we use is

$$I = normalization \times \exp\{-slope \times p_t^2\}$$

The range we fit is limited to bins 3 to 18. Since the bin size for all p_t^2 plots is 0.01 (GeV/c)2), the corresponding p_t^2 values are 0.025 to 0.195 (GeV/c)^2. We limit the range of p_t^2 used for fitting, because the problems mentioned above do not allow for a meaningful comparison of the slopes of the two final state protons, especially for different sets of selection criteria.

Figure 3.24 shows the slow proton p_t^2 distribution for soft Cherenkov identification and six different sets of selection criteria. For Figures 3.24.a and 3.24.b it is clear that the distribution cannot be fit by a single slope. This is due to significant background in the high p_t^2 region. The nonlinear shape of the slope is not as pronounced in Figure 3.24.c, where we apply the rapidity and x_F selection (cut numbers (4) and (5) in the selection outline list). This is probably due to rejection of target dissociation events with missing particles. In the next Figure (3.24.d) we enforce two different cuts for the fast proton, so that we can check if there are correlations between the final state proton distributions. The solid line (and fit shown) is the result of the cut $p_{t,fast}^2$<0.1 (GeV/c)^2 and the dotted line is the result of the stricter cut $p_{t,fast}^2$<0.05 (GeV/c)^2. The application of the $p_{t,fast}^2$ cuts changes the slope of the distribution from 9.5 to 10.2 and 10.6 respectively. Therefore, although some correlation exists, it is not very significant. The last two plots in Figure 3.24 show the effect of the missing mass squared (MM2) cut. In 3.24.e we relax the $p_{t,fast}^2$<0.1 (GeV/c)^2 requirement and apply two missing mass squared cuts: for the solid line -σ<MM2<σ and for the dotted line -σ<MM2<σ/2. In 3.24.f the same cuts are applied, but in addition to the MM2 cut we require that $p_{t,fast}^2$<0.1 (GeV/c)^2 as in 3.24.d. Except for small changes in the observed slope, the effects of the missing mass squared cut on the $p_{t,slow}^2$ distributions are minimal. Comparing the slope in 3.24.c to the last two plots

the change is from 9.5 to 9.9 and 10.6 respectively. Looking at all six plots in Figure 3.24 we find that the fitted slope of the p_t^2 distribution changes very little as a function of selection cuts, except for the application of the missing longitudinal momentum (MPl) cut. This cut (3.24.b) changes the slope from 6.6 to 9.4 and removes all events with large longitudinal momentum imbalance. After this selection step the slope varies only between 9.4 and 10.6.

The slopes are more consistent for the fast proton distribution where the identity of the proton is not in doubt. In Figure 3.27 the same selection criteria are applied for the fast proton with the exception that the selection $p_{t,fast}^2$<0.1 (GeV/c)^2 is replaced by $p_{t,slow}^2$<0.1 (GeV/c)^2. Here the slopes vary between 8.8 and 11.9. For all six plots we do not see the obvious change of slope as a function of p_t^2, that is apparent in the slow proton distributions. The difference is that there are no doubts about the identity of the fast proton, while for the slow proton it is possible to assign as slow proton transverse momentum due to missing particles.

Figures 3.25, 3.26 and 3.28, 3.29 show the slow and fast proton distributions for the same cuts but for alternative Cherenkov identification criteria. There is a consistent change in the slopes of both protons at all selection stages. The distributions are consistently "broader" with slopes smaller in absolute value when compared with the corresponding slopes for "soft" Cherenkov identification. The systematic favoring of events with large p_t^2 for the final state protons is due to our inability to use the four central cells of the Cherenkov counter for positive particle identification. Since the alternative Cherenkov cuts demand one or both pions be positively identified, the requirement is equivalent to demanding one or both pions have enough transverse momentum to move outside the four central cells of the Cherenkov counter. This happens either because they have enough transverse recoil momentum (high mass for the "parent" central meson), or because the "parent" central meson is produced with high transverse momentum.

Therefore strict Cherenkov identification favors events with higher transverse momentum for the central meson which translates (due to momentum conservation) to high transverse momentum for the final state protons. We expect this systematic effect to be more significant for events near threshold, where recoil momentum is limited. We also expect positive identification in the Cherenkov counter to generate a correlation in the relative orientation of the final state protons.

For completeness the (t) distributions are shown in Figures 3.30 to 3.35. The above discussion about the p_t^2 distributions applies. The only thing to mention here is that the poor resolution for the target proton longitudinal momentum makes it necessary to apply energy-momentum conservation in order to calculate the four momentum transfer of the target (slow) proton.

Table 3.1. Ratio of integrals: $\frac{\text{Signal}}{\text{Background}}$, estimated from the fits in Figures 3.1 to 3.3. The integration range is [-σ,σ], centered at the peak of the Gaussian.

Figure #	Signal+Background	Background	$\frac{\text{Signal}}{\text{Background}}$
3.1a	107261.90	21377.79	4.0
b	35948.14	7018.40	4.1
c	25788.21	4576.63	4.6
d	16608.80	2512.53	5.6
e	15396.56	1891.35	7.1
f	10452.20	1127.28	8.3
3.2a	28310.11	4963.84	4.7
b	18485.29	2913.46	5.3
c	14353.11	2108.61	5.8
d	8701.91	1091.35	7.0
e	7848.86	736.16	9.7
f	4912.42	365.72	12.4
3.3a	3819.43	539.50	6.1
b	3732.81	502.97	6.4
c	3324.43	451.38	6.4
d	1936.11	202.83	8.5
e	1660.36	131.04	11.7
f	1057.95	50.69	19.9

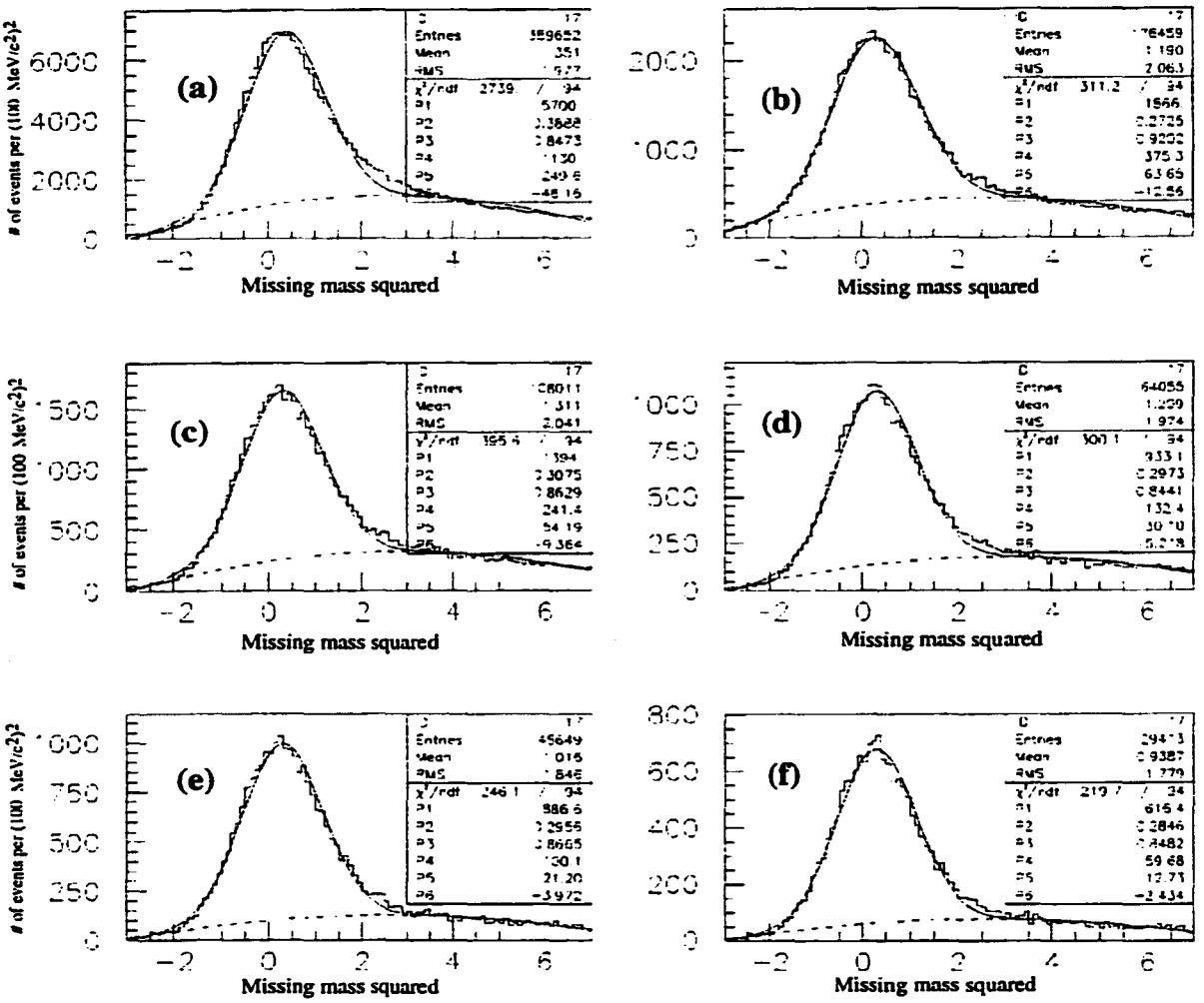

Figure 3.1 Missing mass squared as a function of selection criteria. The fitting function is a Gaussian plus a second order polynomial: $f(x) = p_1 \exp\left[(x - p_2)/\sqrt{2}p_3\right]^2 + p_4 + p_5 x + p_6 x^2$. The dotted line represents the polynomial only. The selection cuts are:

(a) Vertex requirements and two (Cherenkov) pion compatible tracks in multiparticle spectrometer.

(b) Same as (a) and rapidity gap between the slow proton and any one of the two pions greater than 1.8.

(c) Same as (b) and x_F for the central meson (X) in the interval [-0.1,0.0].

(d) Same as (c) and p_t^2<0.1 (GeV/c)^2 for the fast (beam) proton.

(e) Same as (c) and p_t^2<0.1 (GeV/c)^2 for the slow (target) proton.

(f) Same as (c) and p_t^2<0.1 (GeV/c)^2 for both protons.

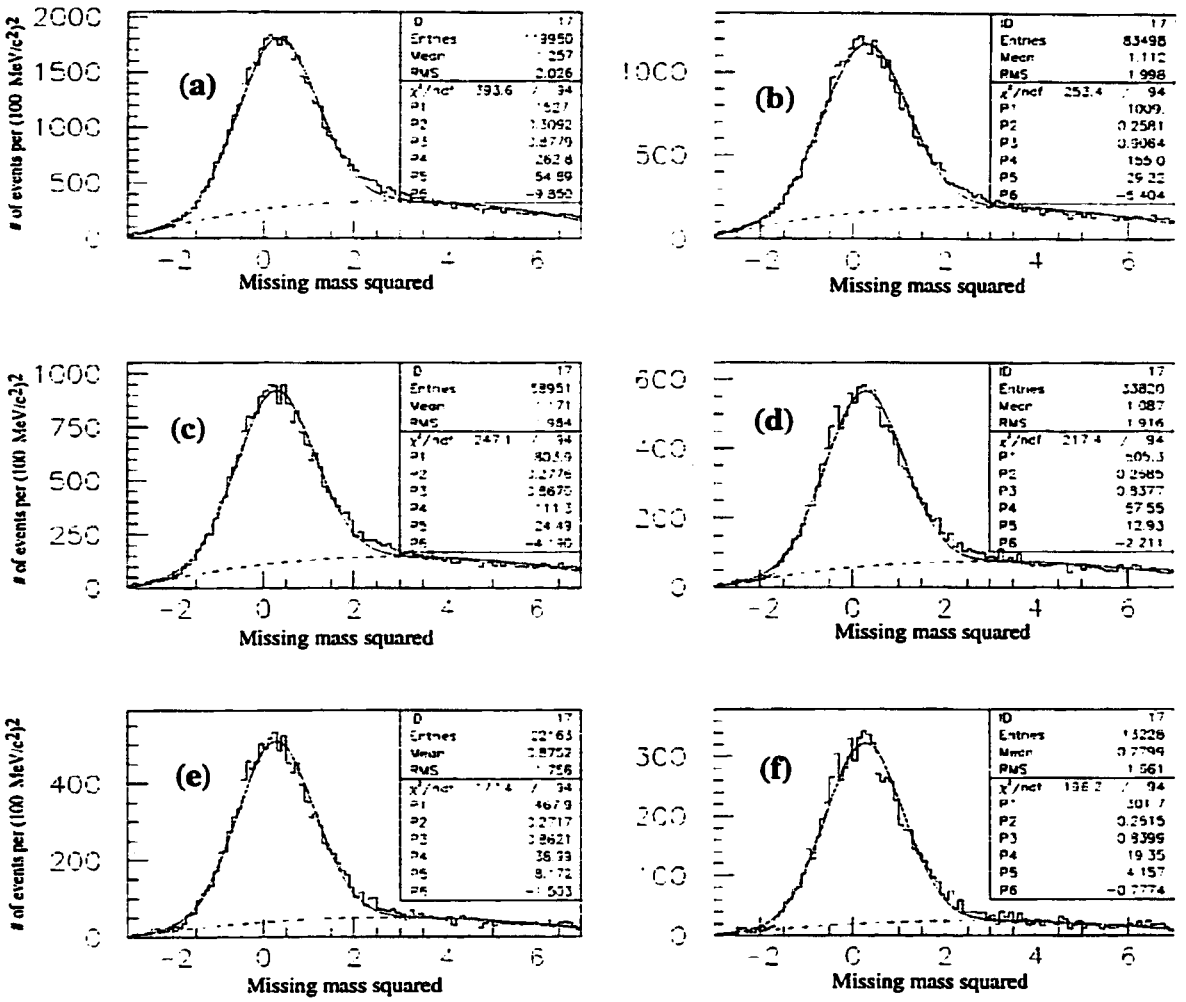

Figure 3.2 Missing mass squared as a function of selection criteria. The Cherenkov requirement is at least one particle in multiparticle spectrometer "exactly pion". Fitting function: $f(x) = p_1 \exp\left[(x-p_2)/\sqrt{2}p_3\right]^2 + p_4 + p_5 x + p_6 x^2$. The selection cuts are:

(a) Vertex requirements, two (Cherenkov) pion compatible tracks in multiparticle spectrometer and at least one of them "exactly pion".

(b) Same as (a) and rapidity gap between the slow proton and any one of the two pions greater than 1.8.

(c) Same as (b) and x_F for the central meson (X) in the interval [-0.1,0.0].

(d) Same as (c) and p_t^2<0.1 (GeV/c)^2 for the fast (beam) proton.

(e) Same as (c) and p_t^2<0.1 (GeV/c)^2 for the slow (target) proton.

(f) Same as (c) and p_t^2<0.1 (GeV/c)^2 for both protons.

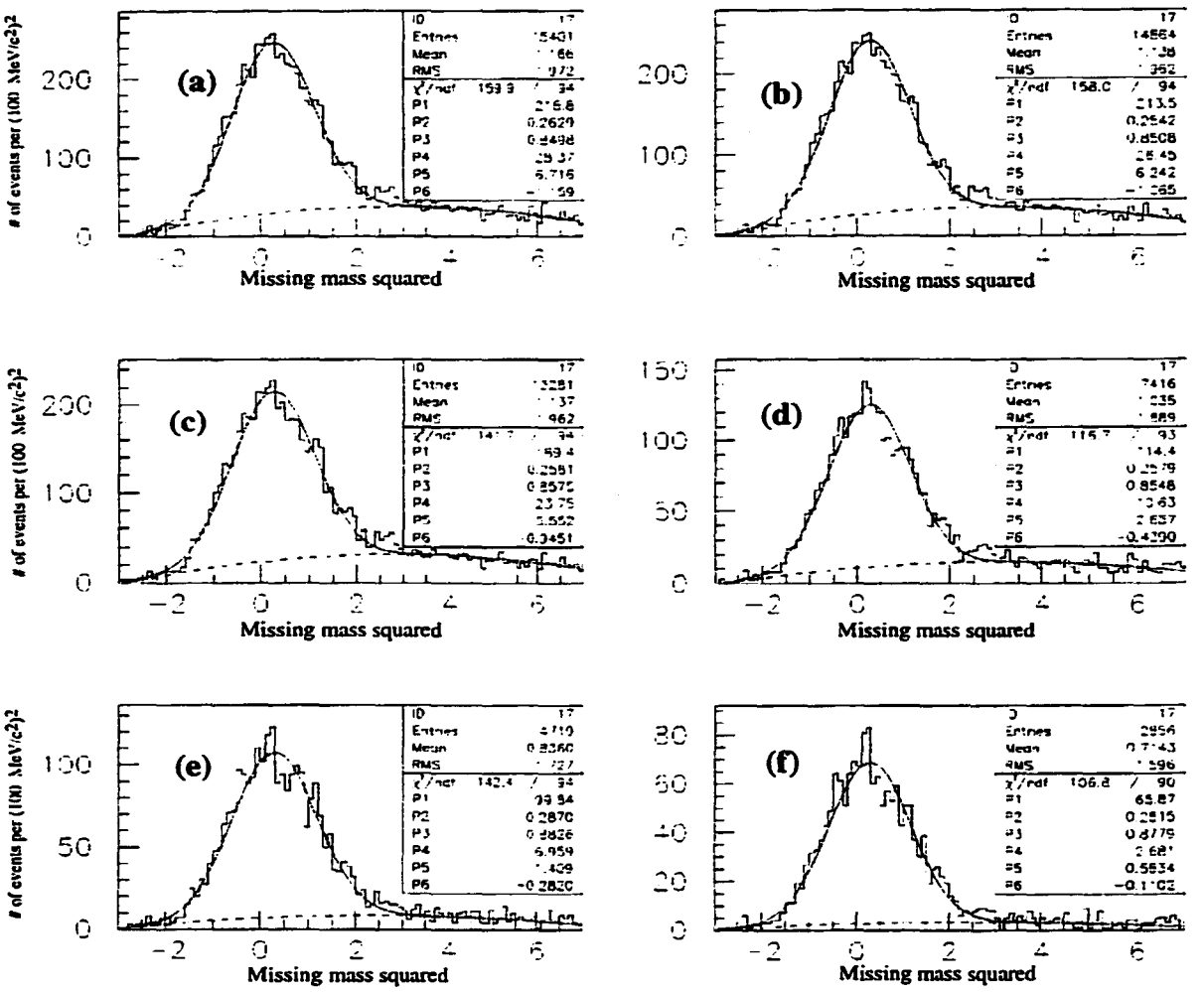

Figure 3.3 Missing mass squared as a function of selection criteria. The Cherenkov requirement is both particles in multiparticle spectrometer are "exactly pion". Fitting function: $f(x) = p_1 \exp\left[(x-p_2)/\sqrt{2}p_3\right]^2 + p_4 + p_5 x + p_6 x^2$. The selection cuts are:

(a) Vertex requirements and two "exactly pion" tracks in multiparticle spectrometer.

(b) Same as (a) and rapidity gap between the slow proton and any one of the two pions greater than 1.8.

(c) Same as (b) and x_F for the central meson (X) in the interval [-0.1,0.0].

(d) Same as (c) and p_t^2<0.1 (GeV/c)^2 for the fast (beam) proton.

(e) Same as (c) and p_t^2<0.1 (GeV/c)^2 for the slow (target) proton.

(f) Same as (c) and p_t^2<0.1 (GeV/c)^2 for both protons.

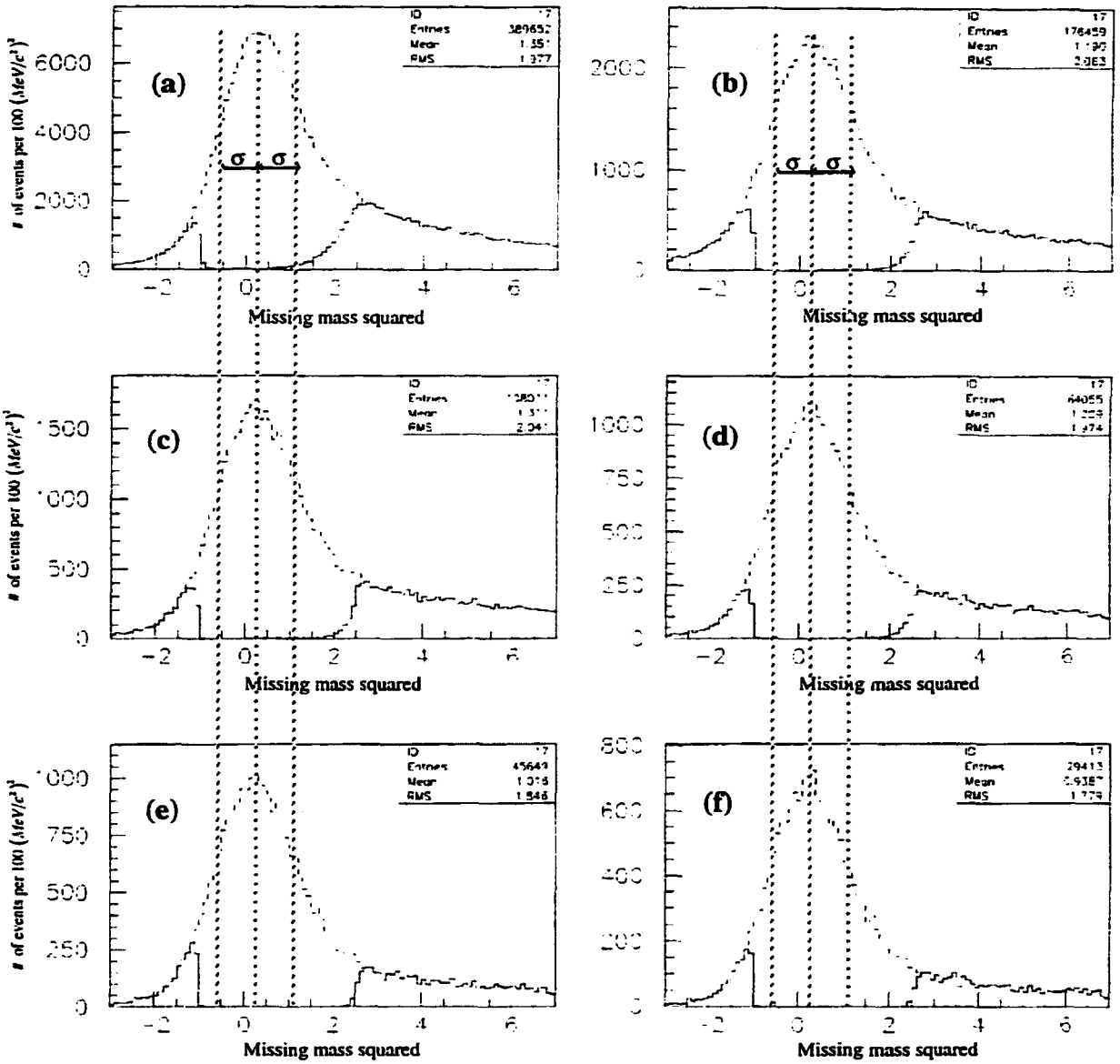

Figure 3.4 Missing mass squared (MM2) before (dash) and after (solid line) the application of missing longitudinal momentum selection cut, for "soft" Cherenkov identification. The vertical lines are drawn to within $\pm\sigma$ from the peak of the Gaussian representing the missing proton signal. The selection cuts are:

(a) Vertex requirements and two (Cherenkov) pion compatible tracks in multiparticle spectrometer.

(b) Same as (a) and rapidity gap between the slow proton and any one of the two pions greater than 1.8.

(c) Same as (b) and x_F for the central meson (X) in the interval [-0.1,0.0].

(d) Same as (c) and p_t^2<0.1 (GeV/c)^2 for the fast (beam) proton.

(e) Same as (c) and p_t^2<0.1 (GeV/c)^2 for the slow (target) proton.

(f) Same as (c) and p_t^2<0.1 (GeV/c)^2 for both protons.

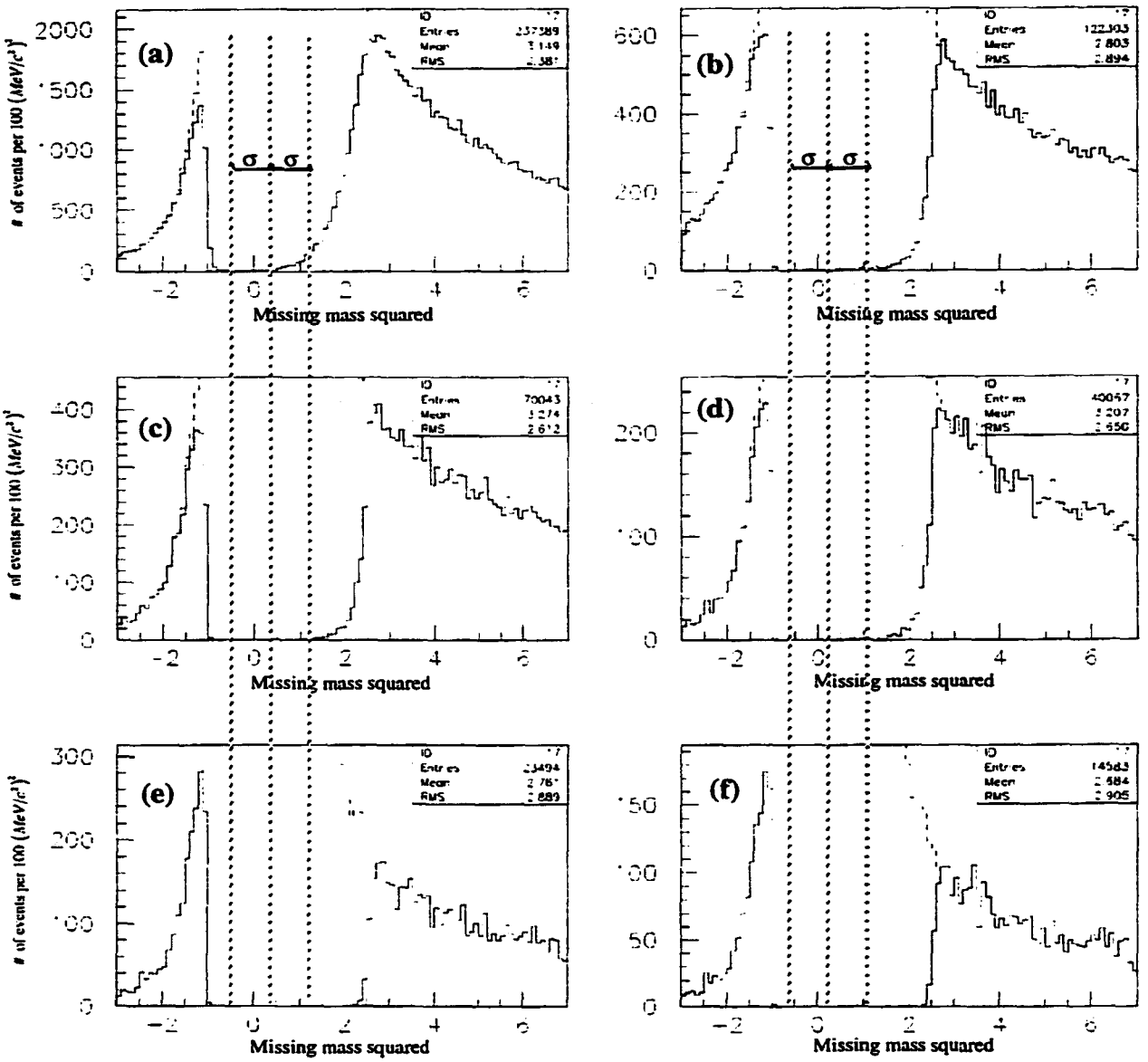

Figure 3.5 Same as previous, with scale set by cut events. Missing mass squared (MM2) before (dash) and after (solid line) the application of missing longitudinal momentum selection cut, for "soft" Cherenkov identification. The vertical lines are drawn to within $\pm\sigma$ from the peak of the Gaussian representing the missing proton signal. The selection cuts are:

(a) Vertex requirements and two (Cherenkov) pion compatible tracks in multiparticle spectrometer.

(b) Same as (a) and rapidity gap between the slow proton and any one of the two pions greater than 1.8.

(c) Same as (b) and x_F for the central meson (X) in the interval [-0.1,0.0].

(d) Same as (c) and p_t^2<0.1 (GeV/c)^2 for the fast (beam) proton.

(e) Same as (c) and p_t^2<0.1 (GeV/c)^2 for the slow (target) proton.

(f) Same as (c) and p_t^2<0.1 (GeV/c)^2 for both protons.

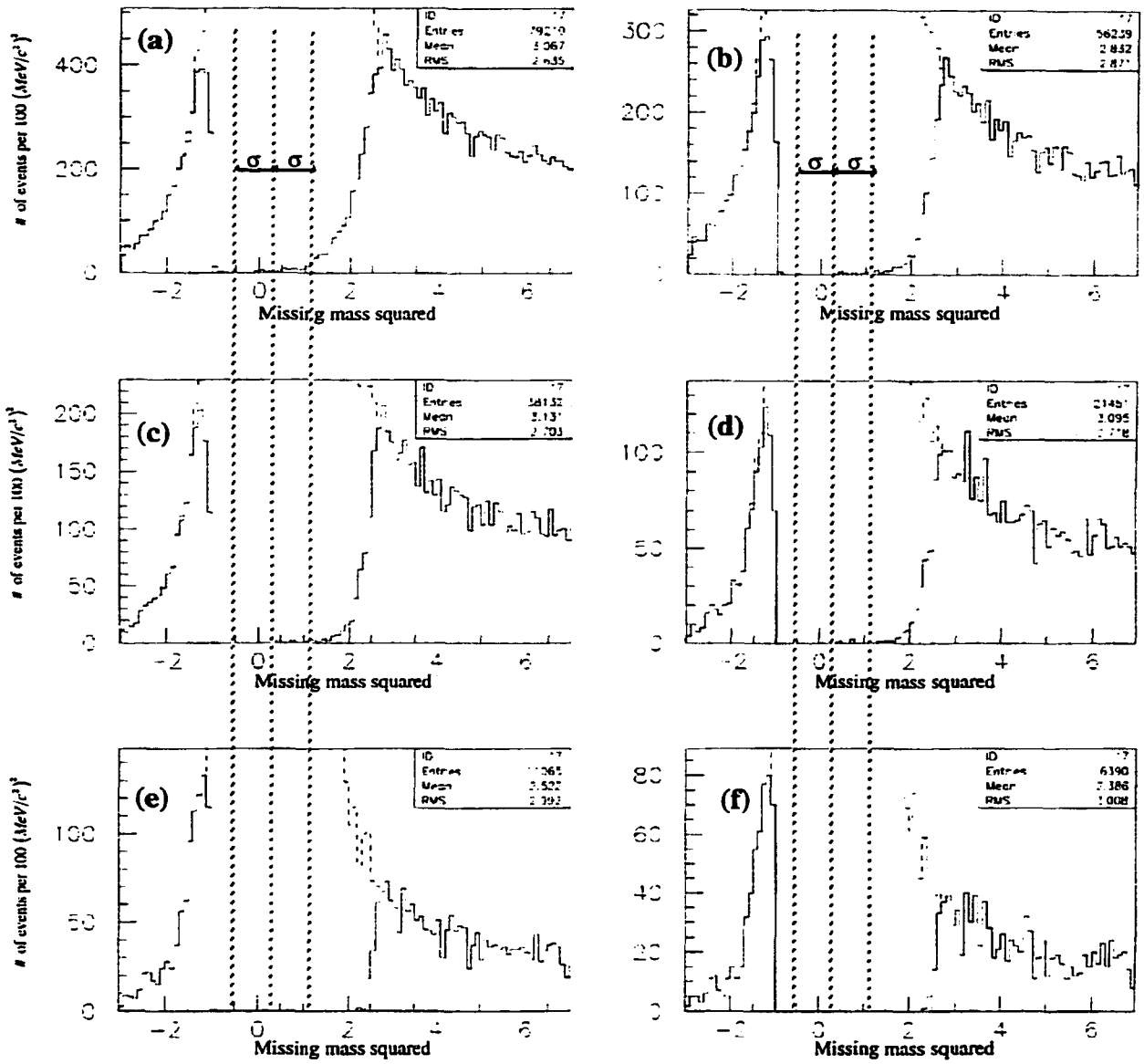

Figure 3.6 Missing mass squared (MM2) before (dash) and after (solid line) the application of missing longitudinal momentum selection cut, for "at least one exactly pion" Cherenkov identification. The vertical lines are drawn to within $\pm\sigma$ from the peak of the Gaussian representing the missing proton signal. The selection cuts are:

(a) Vertex requirements, two (Cherenkov) pion compatible tracks in multiparticle spectrometer and at least one of them "exactly pion".

(b) Same as (a) and rapidity gap between the slow proton and any one of the two pions greater than 1.8.

(c) Same as (b) and x_F for the central meson (X) in the interval [-0.1,0.0].

(d) Same as (c) and p_t^2<0.1 (GeV/c)^2 for the fast (beam) proton.

(e) Same as (c) and p_t^2<0.1 (GeV/c)^2 for the slow (target) proton.

(f) Same as (c) and p_t^2<0.1 (GeV/c)^2 for both protons.

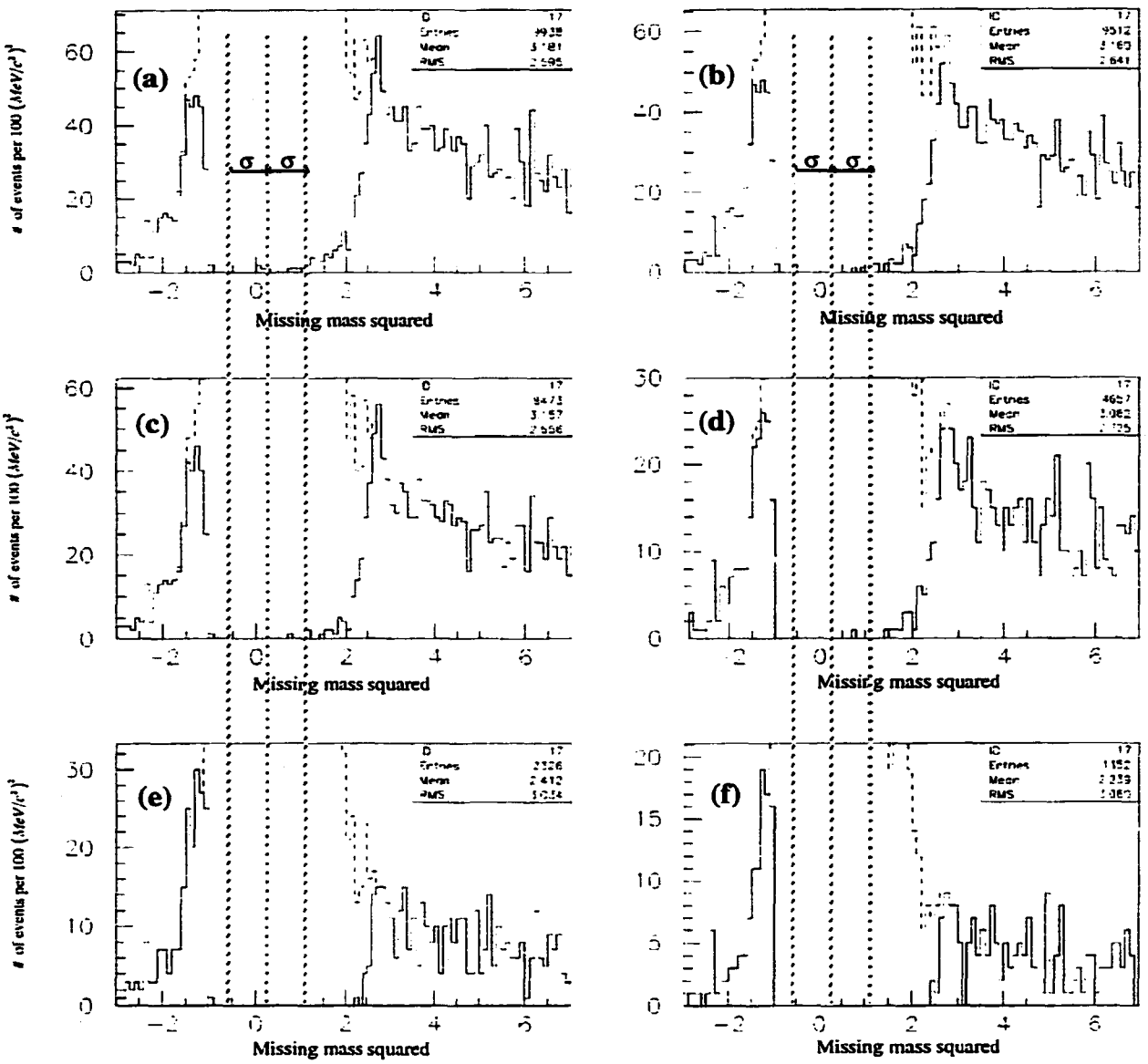

Figure 3.7 Missing mass squared (MM2) before (dash) and after (solid line) the application of missing longitudinal momentum selection cut, for "both exactly pion" Cherenkov identification. The vertical lines are drawn to within $\pm\sigma$ from the peak of the Gaussian representing the missing proton signal. The selection cuts are:

(a) Vertex requirements and two "exactly pion" tracks in multiparticle spectrometer.

(b) Same as (a) and rapidity gap between the slow proton and any one of the two pions greater than 1.8.

(c) Same as (b) and x_F for the central meson (X) in the interval [-0.1,0.0].

(d) Same as (c) and p_t^2<0.1 (GeV/c)^2 for the fast (beam) proton.

(e) Same as (c) and p_t^2<0.1 (GeV/c)^2 for the slow (target) proton.

(f) Same as (c) and p_t^2<0.1 (GeV/c)^2 for both protons.

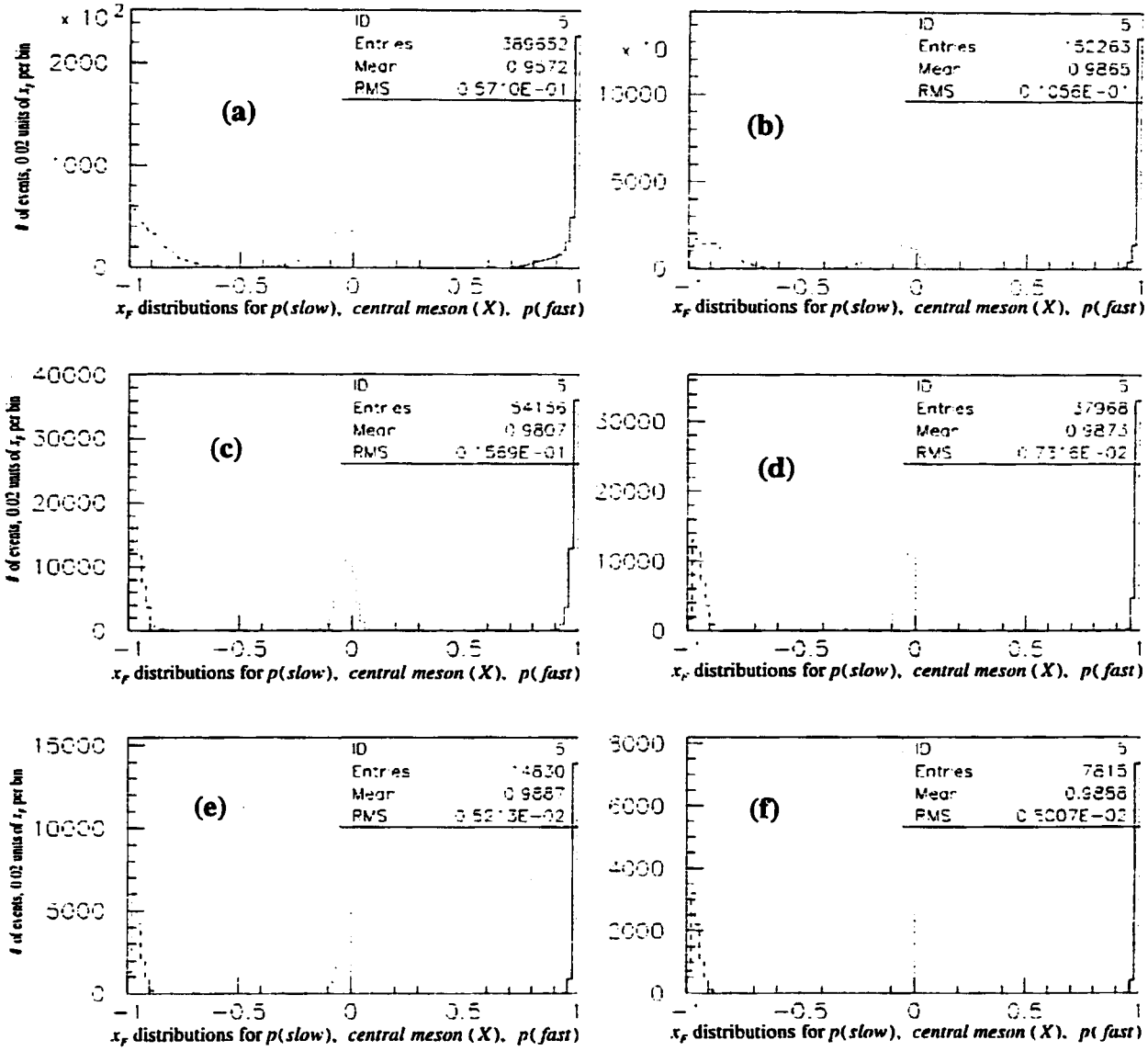

Figure 3.8 x_F distributions for final state protons and intermediate meson (X) with "soft" Cherenkov identification selection. The selection cuts are:

(a) Vertex requirements and two (Cherenkov) pion compatible tracks in multiparticle spectrometer.

(b) And missing longitudinal momentum within 1 GeV/c (-1<MPl<1 GeV/c)

(c) And rapidity gap between the slow proton and any one of the two pions greater than 1.8.

(d) And x_F for the central meson (X) in the interval [-0.1,0.0].

(e) And p_t^2<0.1 (GeV/c)^2 for both final state protons.

(f) And missing mass squared within [$-\sigma,\sigma/2$] (-0.56<MM2<0.70).

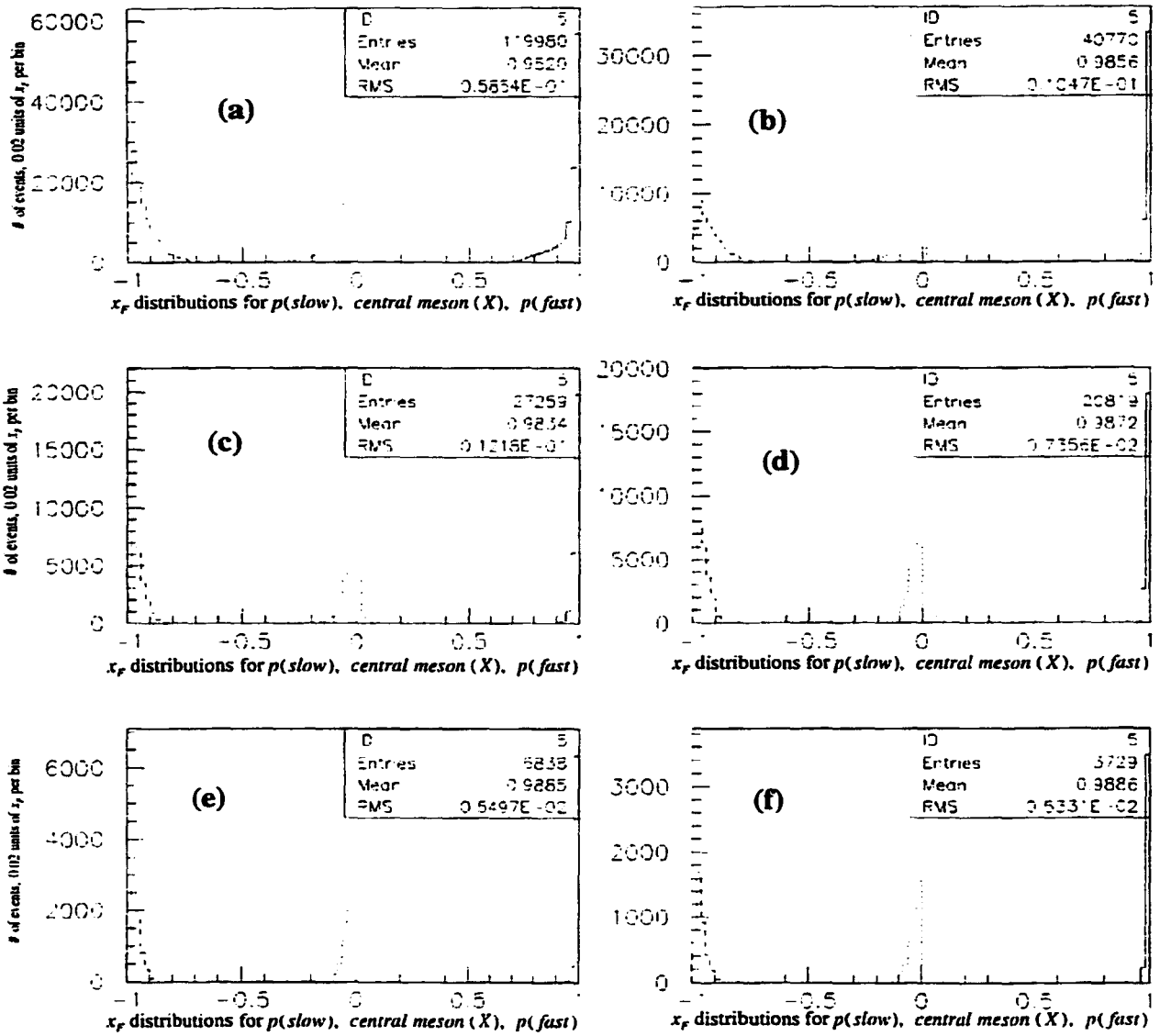

Figure 3.9 x_F distributions for final state protons and intermediate meson (X) with at least one "exactly pion" Cherenkov identification selection. The selection cuts are:

(a) Vertex requirements, two (Cherenkov) pion compatible tracks in multiparticle spectrometer and at least one of them "exactly pion".

(b) And missing longitudinal momentum within 1 GeV/c (-1<MPl<1 GeV/c)

(c) And rapidity gap between the slow proton and any one of the two pions greater than 1.8.

(d) And x_F for the central meson (X) in the interval [-0.1,0.0].

(e) And p_t^2<0.1 (GeV/c)^2 for both final state protons.

(f) And missing mass squared within [-σ,σ/2] (-0.56<MM2<0.70).

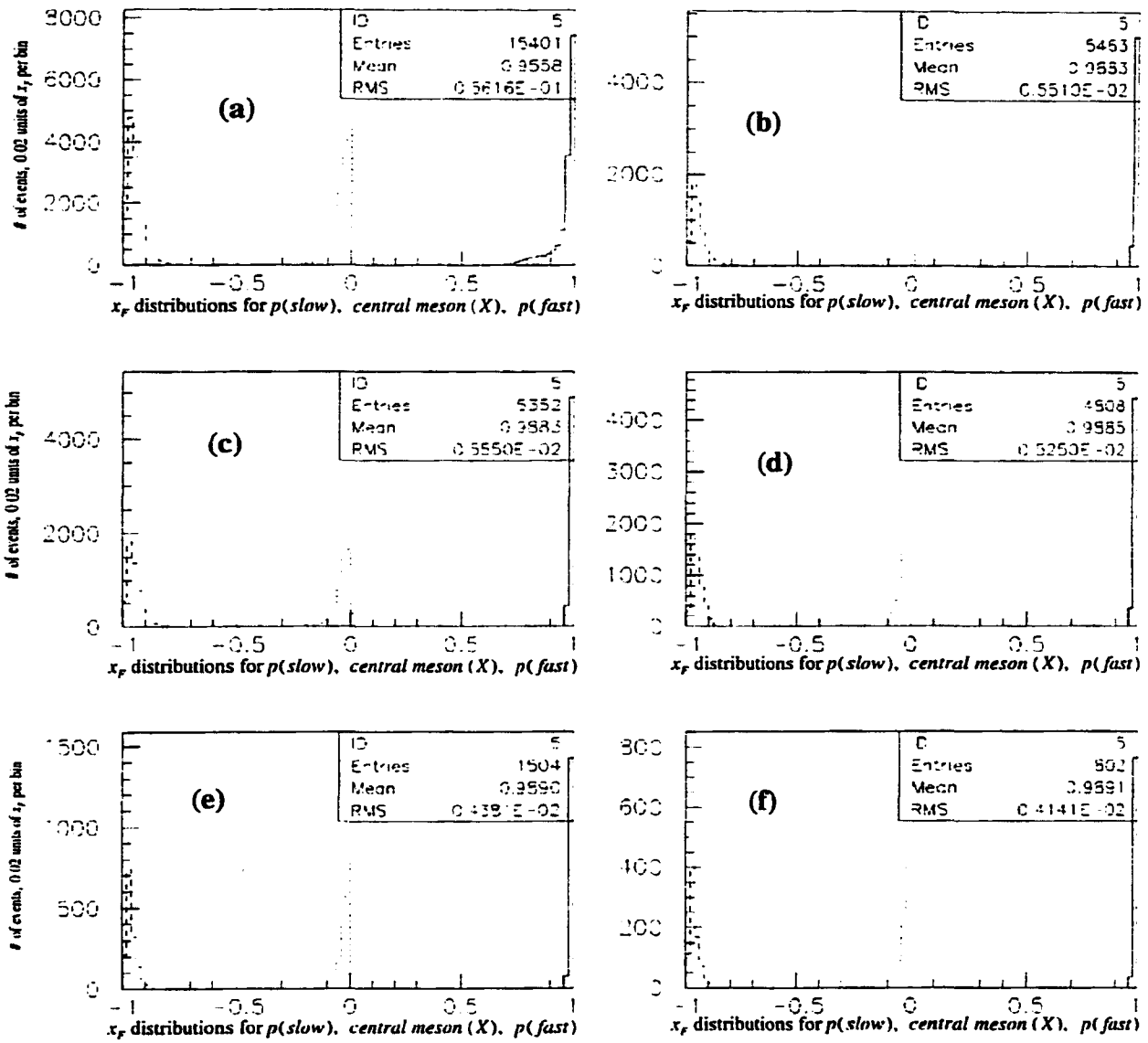

Figure 3.10 x_F distributions for final state protons and intermediate meson (X) with two "exactly pion" tracks in multiparticle spectrometer (Cherenkov identification). The selection cuts are:

(a) Vertex requirements and two "exactly pion" tracks in multiparticle spectrometer.
(b) And missing longitudinal momentum within 1 GeV/c (-1<MPl<1 GeV/c)
(c) And rapidity gap between the slow proton and any one of the two pions greater than 1.8.
(d) And x_F for the central meson (X) in the interval [-0.1,0.0].
(e) And p_t^2<0.1 $(GeV/c)^2$ for both final state protons.
(f) And missing mass squared within [$-\sigma,\sigma/2$] (-0.56<MM2<0.70).

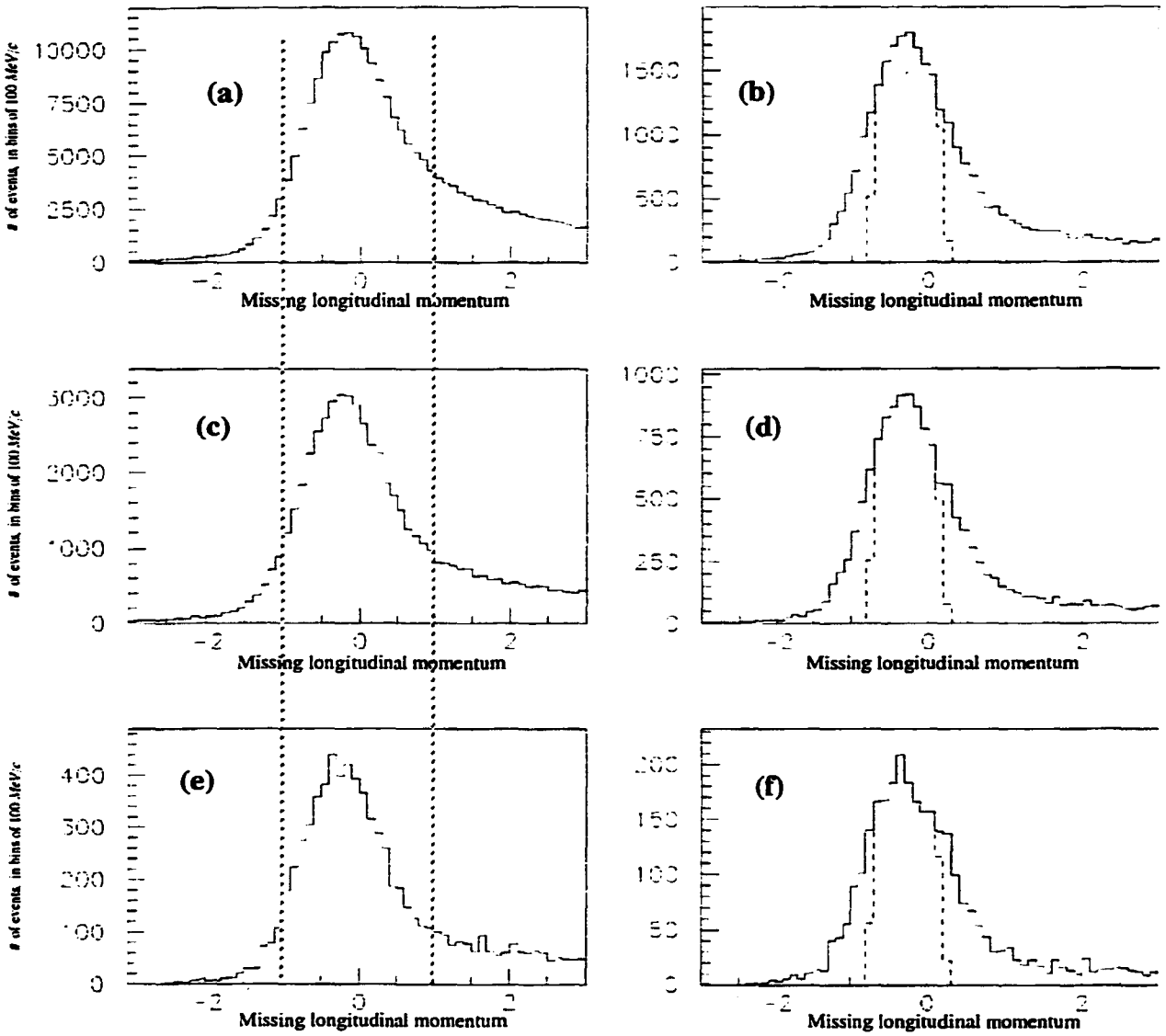

Figure 3.11 Missing longitudinal momentum (MPI) as a function of selection criteria:
(a) Vertex requirements and two (Cherenkov) pion compatible tracks in multiparticle spectrometer. This is the series of selection criteria used to define the data sample. The cut at [-1,1] GeV/c is marked by the vertical lines.
(b) Solid line: MPI after the following cuts: Rapidity gap between the slow proton and any one of the two pions greater than 1.8. x_F for the central meson (X) in the interval [-0.1,0.0]. p_t^2<0.1 (GeV/c)^2 for slow(target) proton.
Dashed line: in addition to previous cuts require the mmissing mass squared selection -σ<MM2<σ which corresponds to -0.56<MM2<1.12 (GeV/c^2)^2.
(c), (d) Same as (a), (b) except that for Cherenkov identification we require at least one of the multiparticle spectrometer particles be identified as "exactly pion".
(e), (f) Same as (a), (b) except for strict Cherenkov identification. We require both particles in multiparticle pectrometer be identified as "exactly pion".

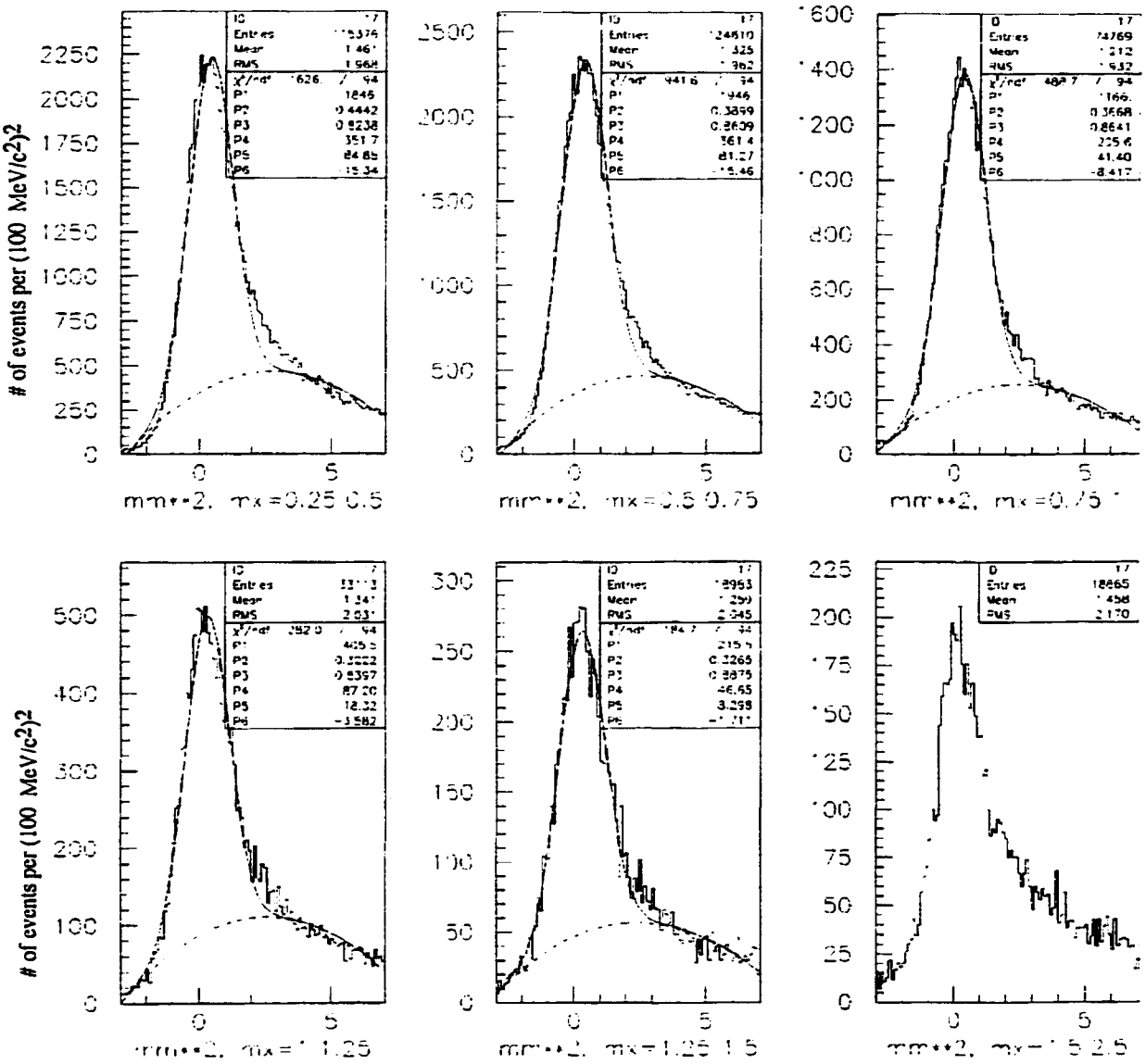

Figure 3.12 Missing mass squared for intervals of invariant mass of the X system. The X system invariant mass intervals are stated below each plot. The selection cuts are:
Vertex requirements and two (Cherenkov) pion compatible tracks in multiparticle spectrometer.

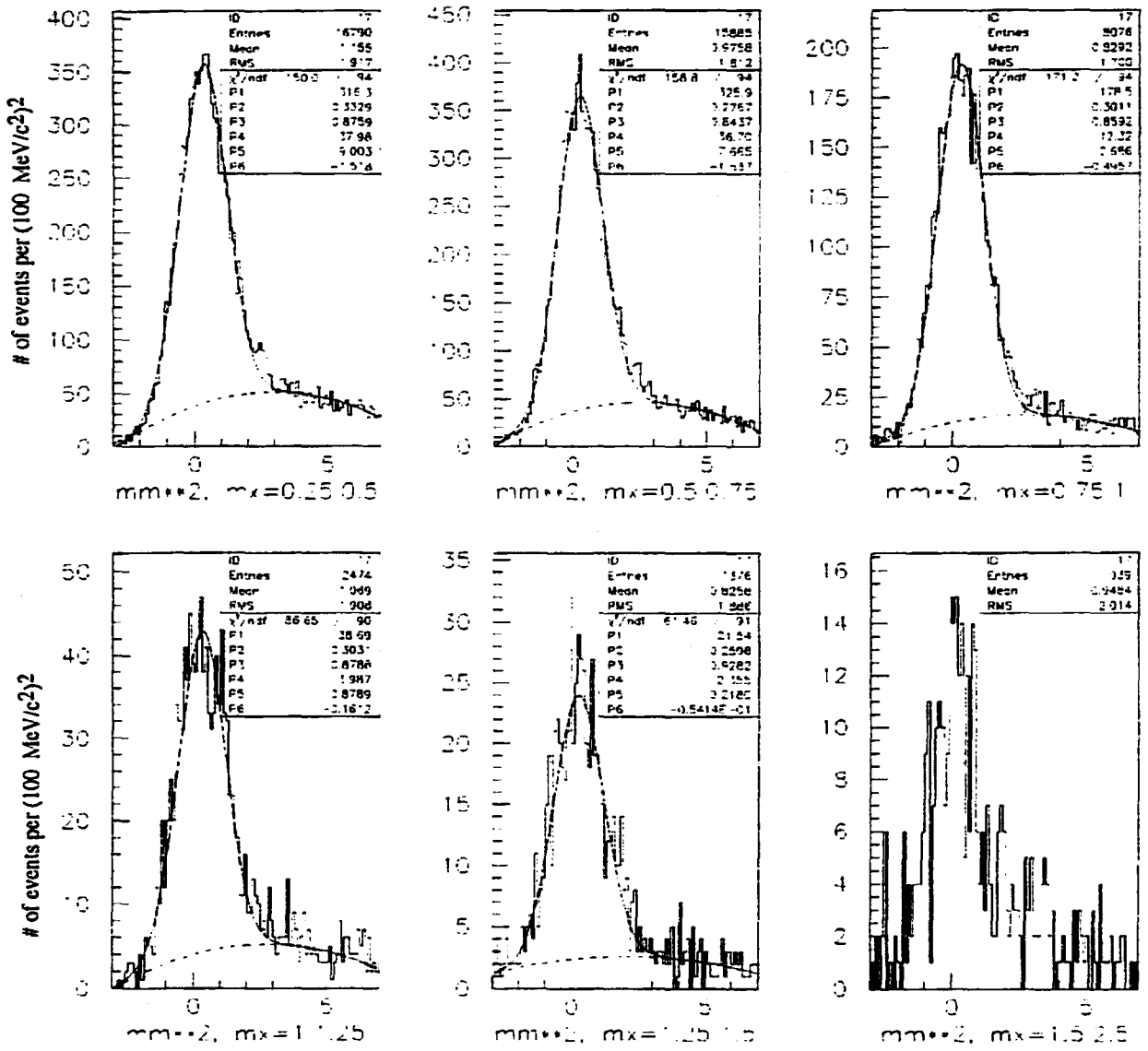

Figure 3.13 Missing mass squared for intervals of invariant mass of the X system. The X system invariant mass intervals are stated below each plot. The selection cuts are:

Vertex requirements and two (Cherenkov) pion compatible tracks in multiparticle spectrometer.

Missing longitudinal momentum (MPl) within 1 GeV/c (-1<MPl<1 GeV/c)

Rapidity gap between the slow proton and any one of the two pions greater than 1.8.

x_F for the central meson (X) in the interval [-0.1,0.0].

p_t^2<0.1 (GeV/c)^2 for both final state protons.

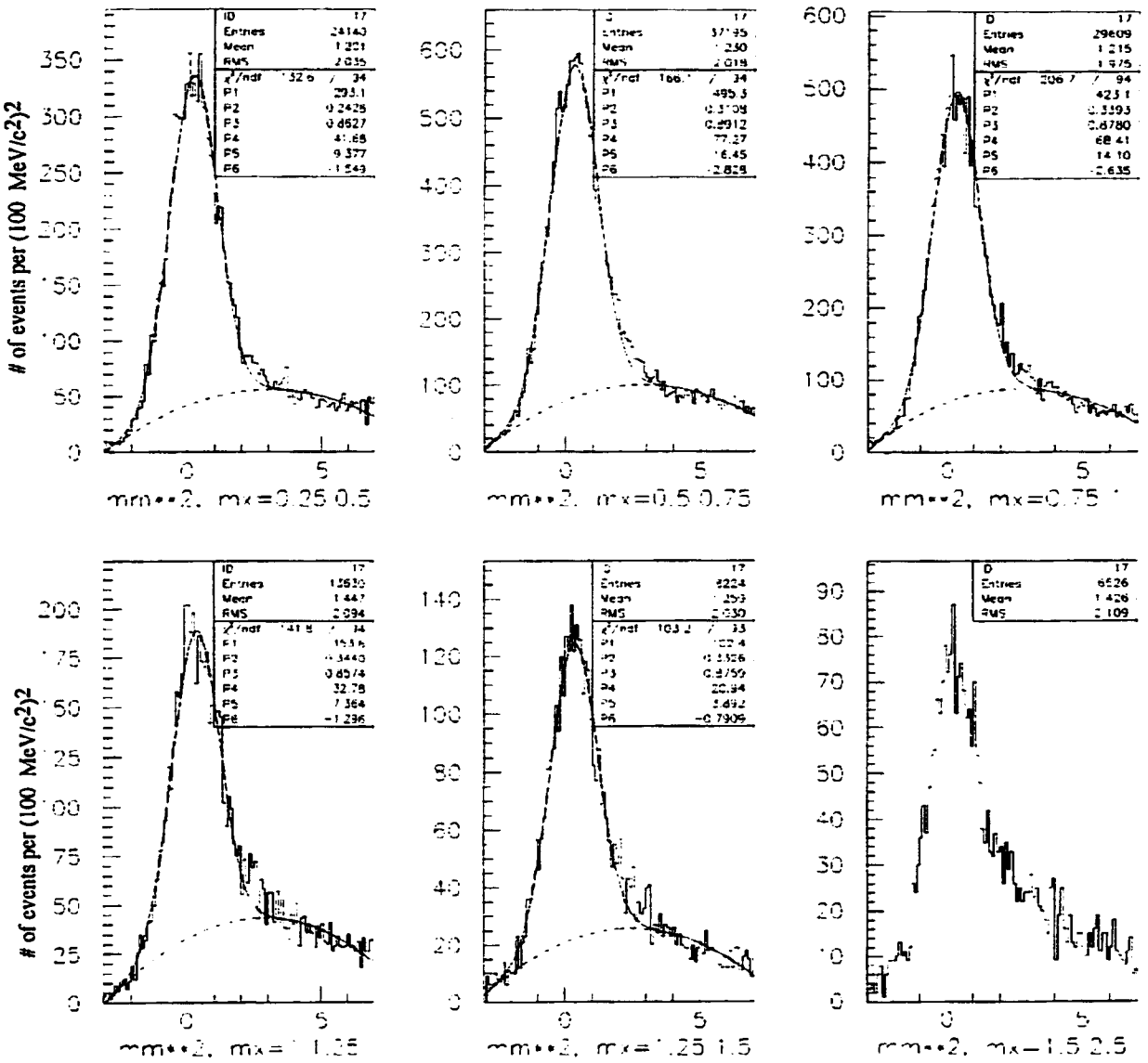

Figure 3.14 Missing mass squared for intervals of invariant mass of the X system. The X system invariant mass intervals are stated below each plot. The selection cuts are: Vertex requirements, two (Cherenkov) pion compatible tracks in multiparticle spectrometer and at least one of them "exactly pion".

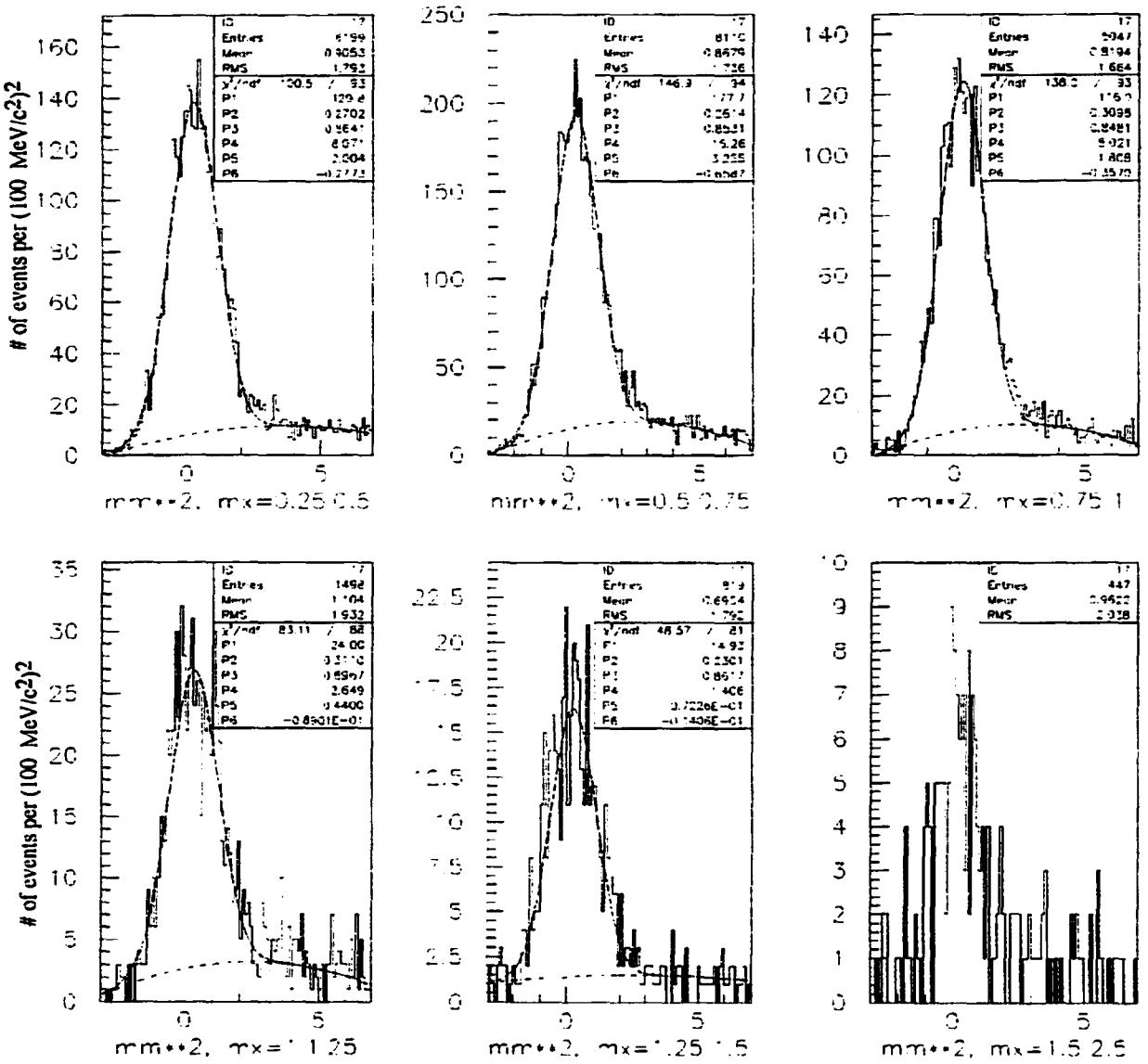

Figure 3.15 Missing mass squared for intervals of invariant mass of the X system. The X system invariant mass intervals are stated below each plot. The selection cuts are:

Vertex requirements, two (Cherenkov) pion compatible tracks in multiparticle spectrometer and at least one of them "exactly pion".

Missing longitudinal momentum (MPl) within 1 GeV/c (-1<MPl<1 GeV/c)

Rapidity gap between the slow proton and any one of the two pions greater than 1.8.

x_F for the central meson (X) in the interval [-0.1,0.0].

p_t^2<0.1 (GeV/c)^2 for both final state protons.

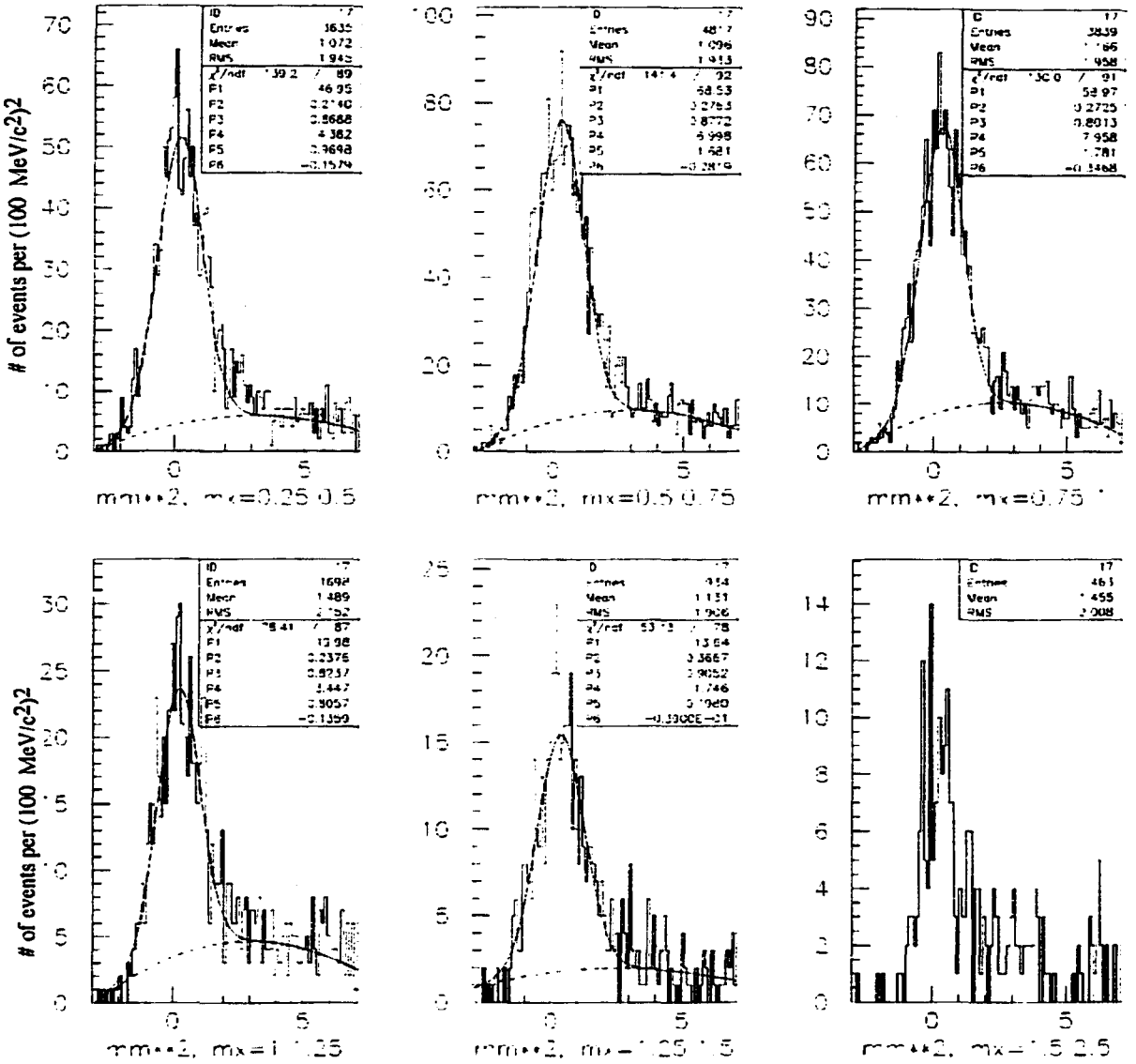

Figure 3.16 Missing mass squared for intervals of invariant mass of the X system. Invariant mass intervals are stated below each plot. The selection cuts are:
Vertex requirements and two "exactly pion" tracks in multiparticle spectrometer.

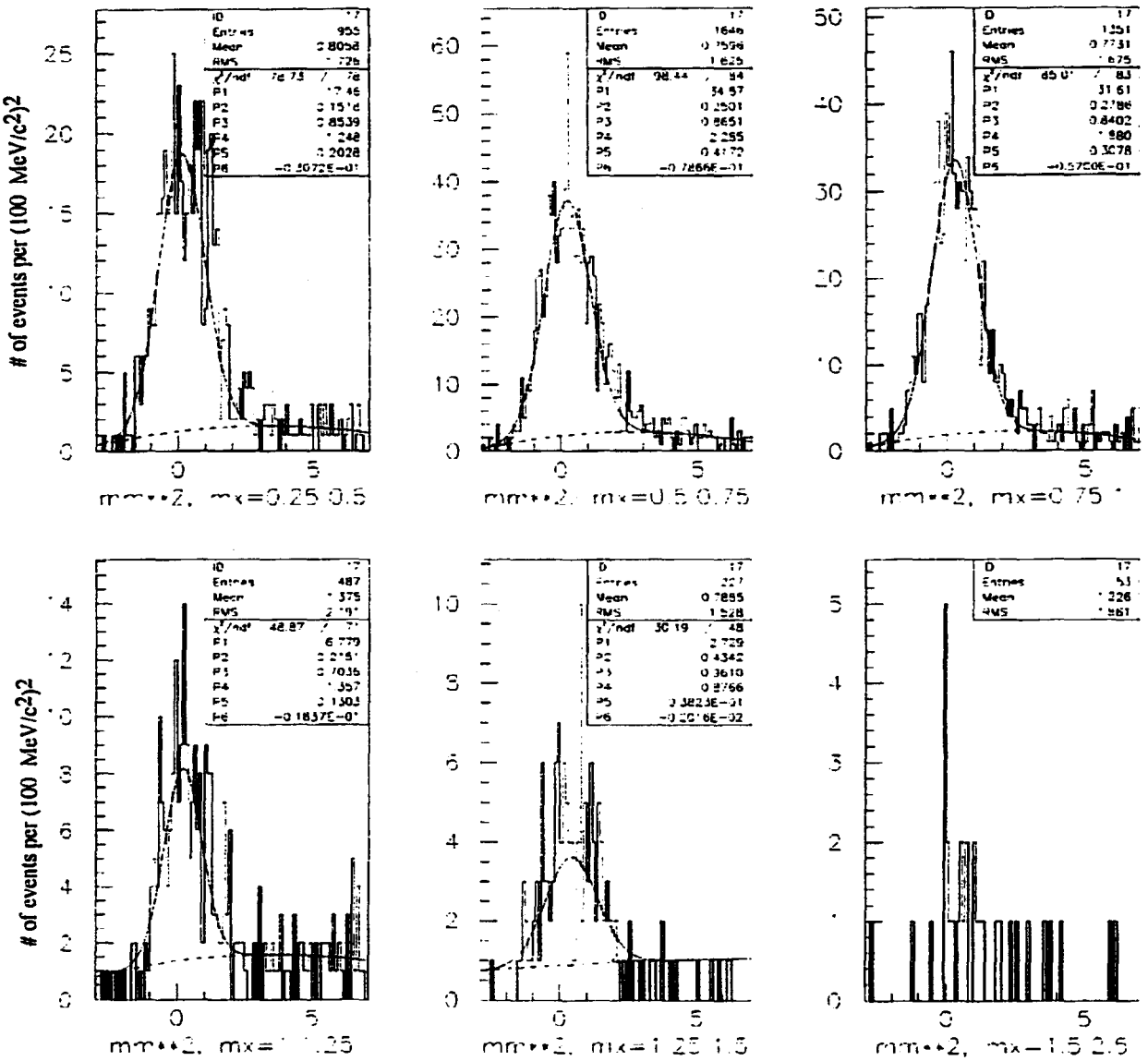

Figure 3.17 Missing mass squared for intervals of invariant mass of the X system. The X system invariant mass intervals are stated below each plot. The selection cuts are:

Vertex requirements and two "exactly pion" tracks in multiparticle spectrometer.
Missing longitudinal momentum (MPl) within 1 GeV/c (-1<MPl<1 GeV/c)
Rapidity gap between the slow proton and any one of the two pions greater than 1.8.
x_F for the central meson (X) in the interval [-0.1,0.0].
p_t^2<0.1 (GeV/c)^2 for both final state protons.

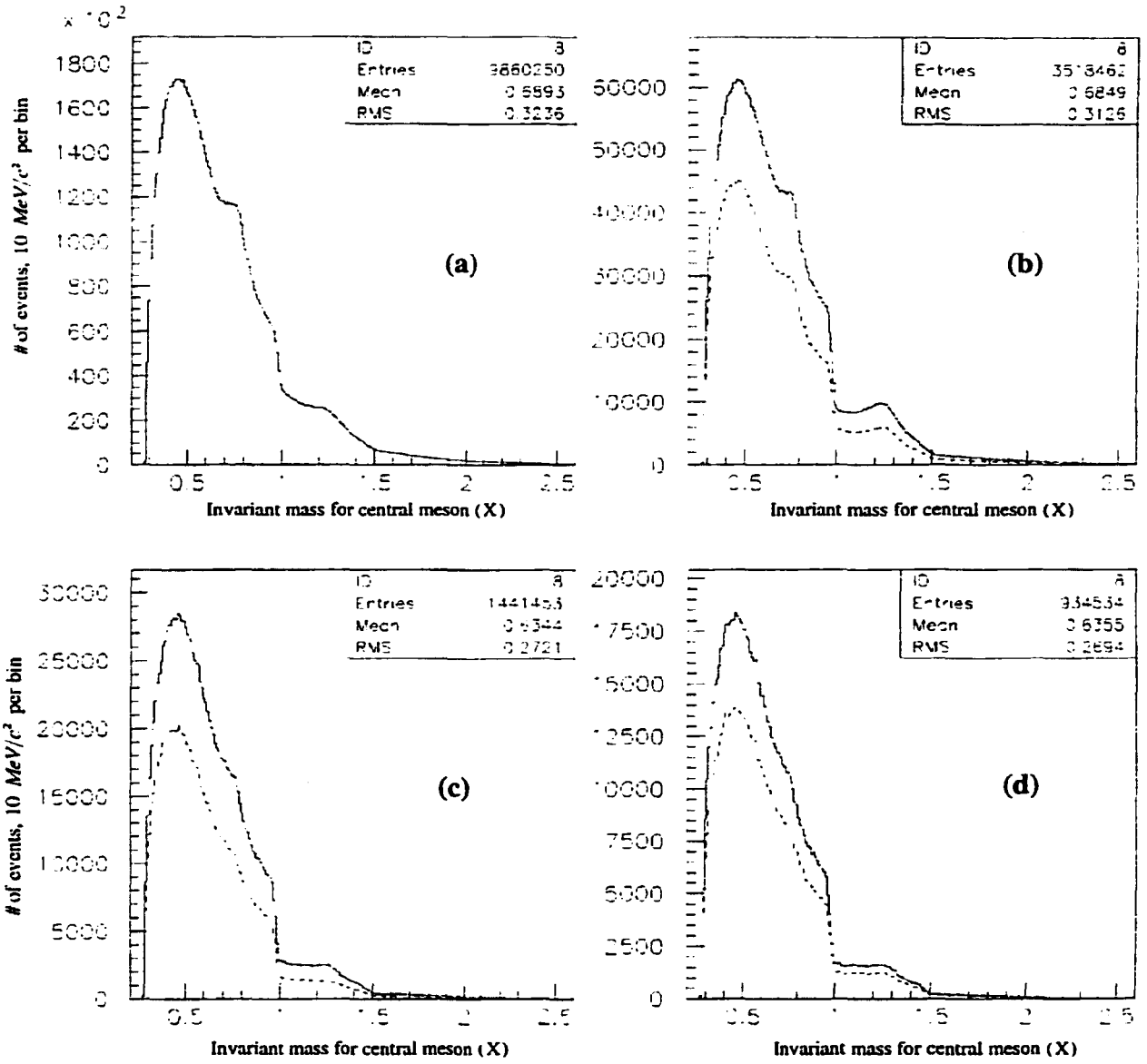

Figure 3.18 Invariant mass as a function of selection criteria, "soft" Cherenkov identification. The selection cuts are:

(a) Vertex requirements and two (Cherenkov) pion compatible tracks in multiparticle spectrometer.
And missing longitudinal momentum within 1 GeV/c (-1<MPl<1 GeV/c)

(b) Solid: Same as (a) and rapidity gap between the slow proton and any one of the two pions greater than 1.8.
Dash: and x_F for the central meson (X) in the interval [-0.1,0.0].

(c) Solid: Same as (b) and p_t^2<0.1 (GeV/c)^2 for the slow (target) proton.
Dash: and p_t^2<0.1 (GeV/c)^2 for the fast (beam) proton.

(d) All previous cuts except for p_t^2<0.1 (GeV/c)^2 for the fast (beam) proton and
Solid: missing mass squared within [−σ,σ] (-0.56<MM2<1.12).
Dash: missing mass squared within [−σ,σ/2] (-0.56<MM2<0.70).

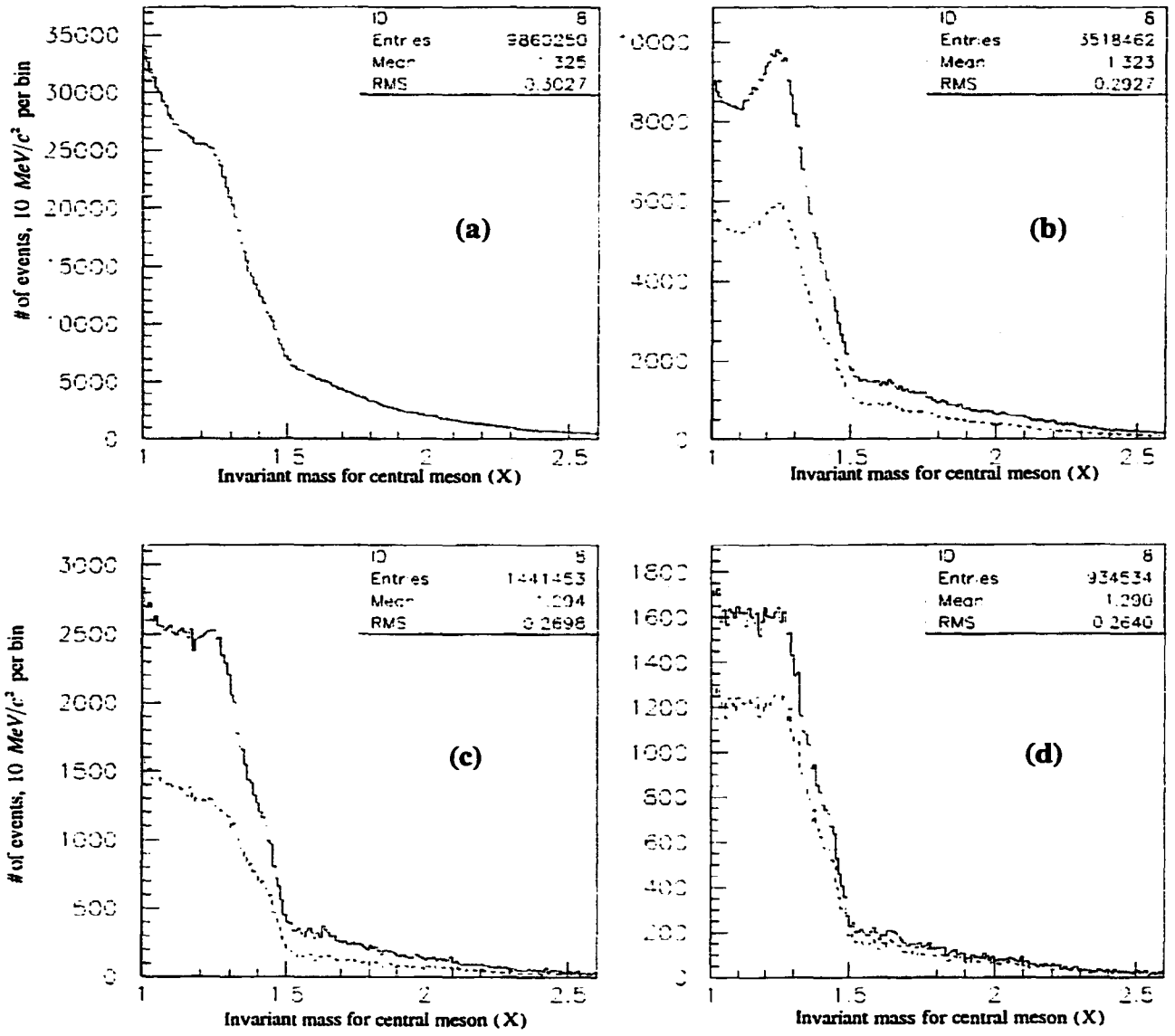

Figure 3.19 Detail of invariant mass as a function of selection criteria, "soft" Cherenkov identification. The selection cuts are:

(a) Vertex requirements and two (Cherenkov) pion compatible tracks in multiparticle spectrometer.
And missing longitudinal momentum within 1 GeV/c (-1<MPl<1 GeV/c)

(b) Solid: Same as (a) and rapidity gap between the slow proton and any one of the two pions greater than 1.8.
Dash: and x_F for the central meson (X) in the interval [-0.1,0.0].

(c) Solid: Same as (b) and p_t^2<0.1 (GeV/c)^2 for the slow (target) proton.
Dash: and p_t^2<0.1 (GeV/c)^2 for the fast (beam) proton.

(d) All previous cuts except for p_t^2<0.1 (GeV/c)^2 for the fast (beam) proton and
Solid: missing mass squared within [−σ,σ] (-0.56<MM2<1.12).
Dash: missing mass squared within [−σ,σ/2] (-0.56<MM2<0.70).

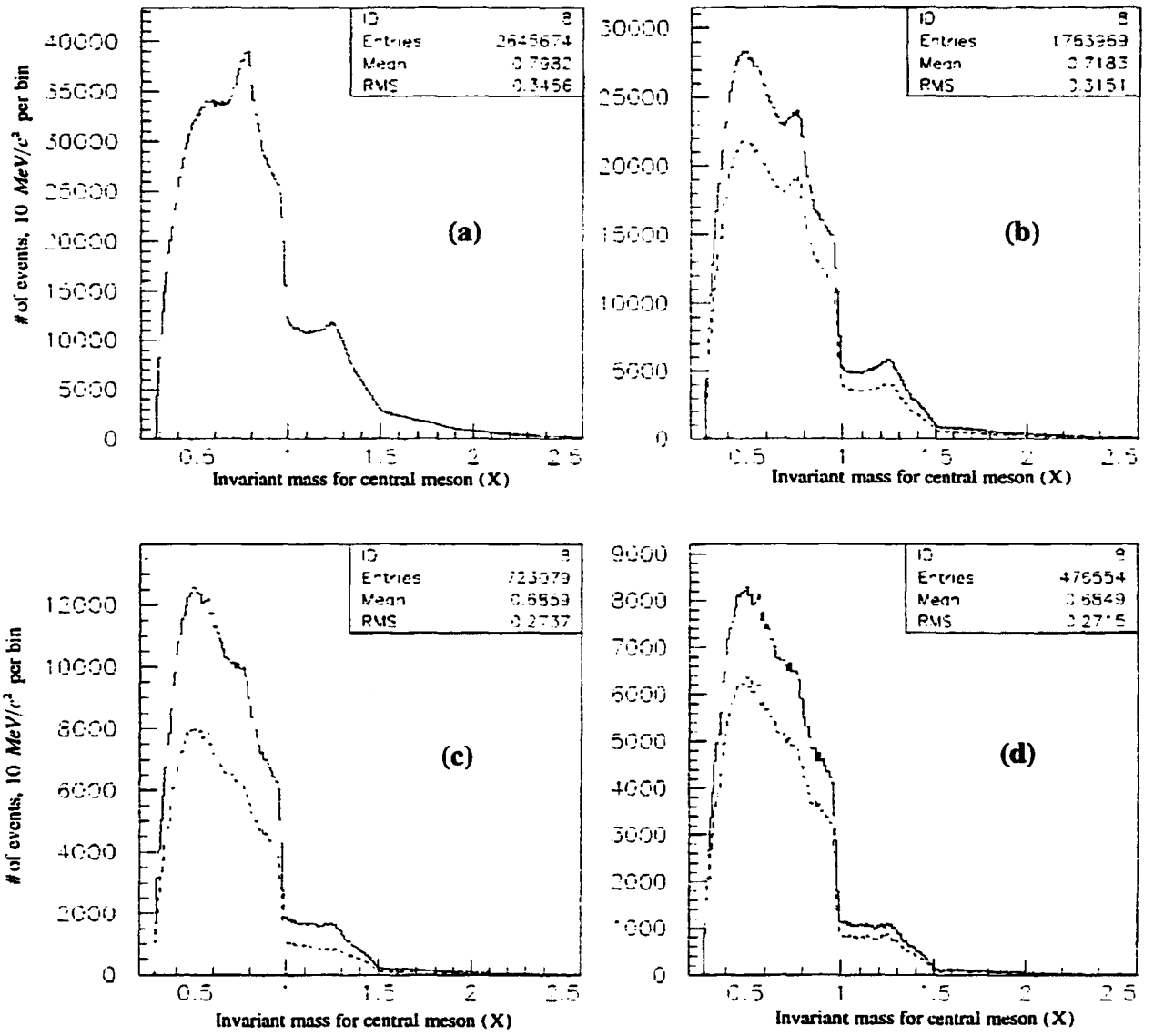

Figure 3.20 Invariant mass as a function of selection criteria, one "exactly pion" Cherenkov identification. The selection cuts are:

(a) Vertex requirements, two (Cherenkov) pion compatible tracks in multiparticle spectrometer and at least one of them "exactly pion".
And missing longitudinal momentum within 1 GeV/c (-1<MPl<1 GeV/c)

(b) Solid: Same as (a) and rapidity gap between the slow proton and any one of the two pions greater than 1.8.
Dash: and x_F for the central meson (X) in the interval [-0.1,0.0].

(c) Solid: Same as (b) and p_t^2<0.1 (GeV/c)^2 for the slow (target) proton.
Dash: and p_t^2<0.1 (GeV/c)^2 for the fast (beam) proton.

(d) All previous cuts except for p_t^2<0.1 (GeV/c)^2 for the fast (beam) proton and
Solid: missing mass squared within [−σ,σ] (-0.56<MM2<1.12).
Dash: missing mass squared within [−σ,σ/2] (-0.56<MM2<0.70).

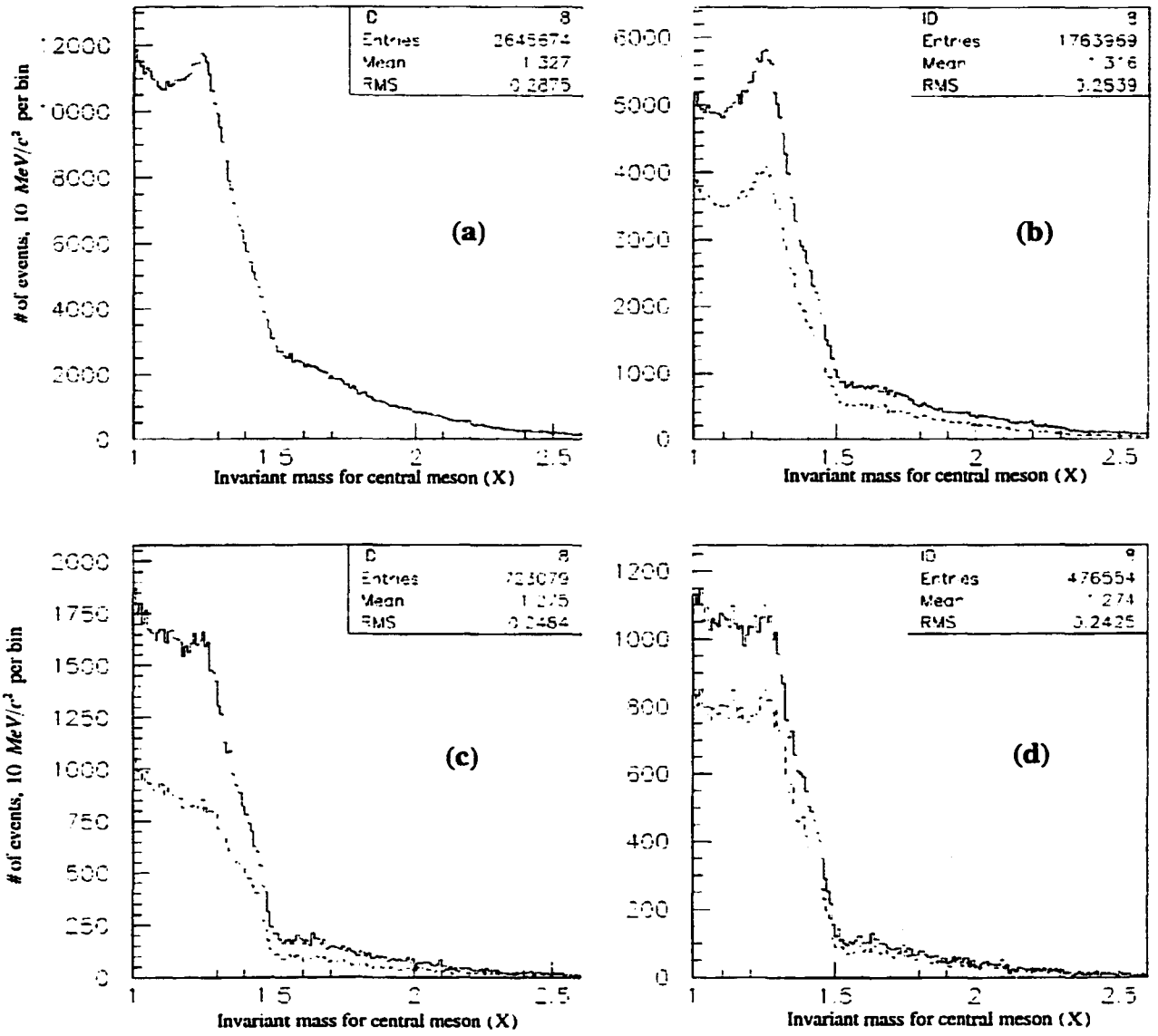

Figure 3.21 Detail of invariant mass as a function of selection criteria, one "exactly pion" Cherenkov identification. The selection cuts are:

(a) Vertex requirements, two (Cherenkov) pion compatible tracks in multiparticle spectrometer and at least one of them "exactly pion".
And missing longitudinal momentum within 1 GeV/c (-1<MPl<1 GeV/c)

(b) Solid: Same as (a) and rapidity gap between the slow proton and any one of the two pions greater than 1.8.
Dash: and x_F for the central meson (X) in the interval [-0.1,0.0].

(c) Solid: Same as (b) and p_t^2<0.1 (GeV/c)^2 for the slow (target) proton.
Dash: and p_t^2<0.1 (GeV/c)^2 for the fast (beam) proton.

(d) All previous cuts except for p_t^2<0.1 (GeV/c)^2 for the fast (beam) proton and
Solid: missing mass squared within [−σ,σ] (-0.56<MM2<1.12).
Dash: missing mass squared within [−σ,σ/2] (-0.56<MM2<0.70).

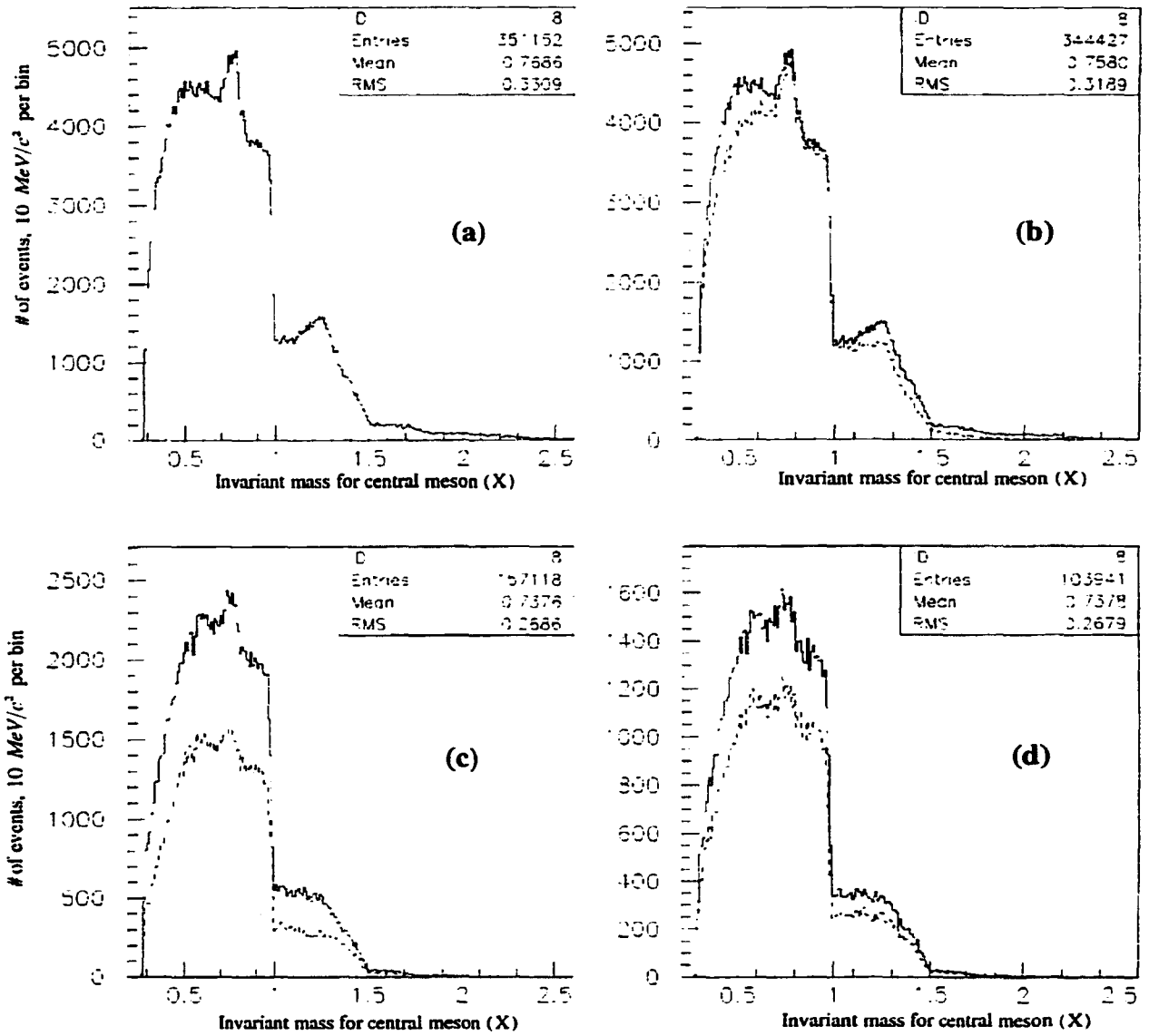

Figure 3.22 Invariant mass as a function of selection criteria, two "exactly pion" Cherenkov identification. The selection cuts are:

(a) Vertex requirements and two "exactly pion" tracks in multiparticle spectrometer. And missing longitudinal momentum within 1 GeV/c (-1<MPl<1 GeV/c)

(b) Solid: Same as (a) and rapidity gap between the slow proton and any one of the two pions greater than 1.8.

Dash: and x_F for the central meson (X) in the interval [-0.1,0.0].

(c) Solid: Same as (b) and p_t^2<0.1 (GeV/c)^2 for the slow (target) proton.

Dash: and p_t^2<0.1 (GeV/c)^2 for the fast (beam) proton.

(d) All previous cuts except for p_t^2<0.1 (GeV/c)^2 for the fast (beam) proton and

Solid: missing mass squared within [−σ,σ] (-0.56<MM2<1.12).

Dash: missing mass squared within [−σ,σ/2] (-0.56<MM2<0.70).

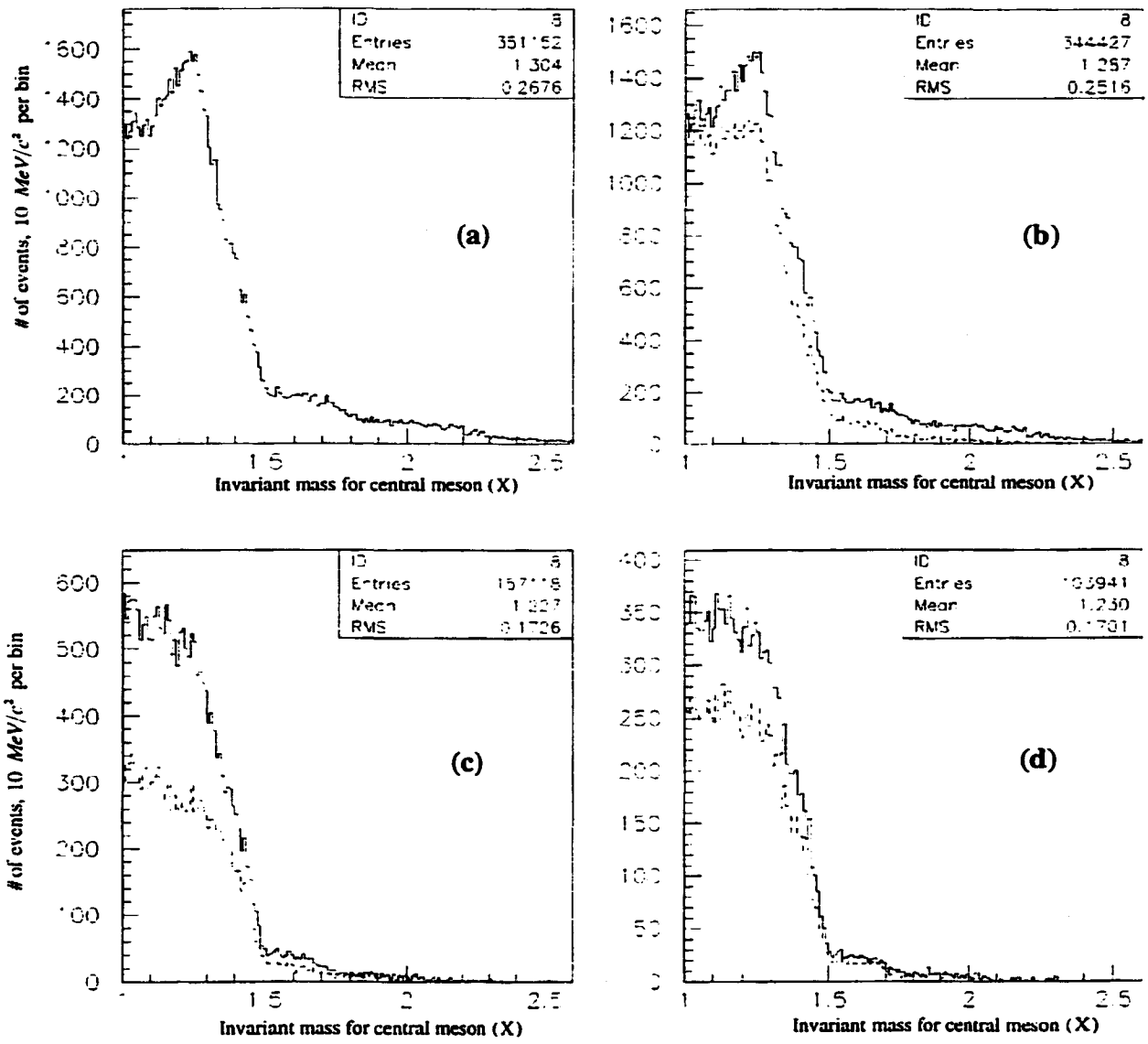

Figure 3.23 Detail of invariant mass as a function of selection criteria, two "exactly pion" Cherenkov identification. The selection cuts are:

(a) Vertex requirements and two "exactly pion" tracks in multiparticle spectrometer. And missing longitudinal momentum within 1 GeV/c (-1<MPl<1 GeV/c)

(b) Solid: Same as (a) and rapidity gap between the slow proton and any one of the two pions greater than 1.8.

Dash: and x_F for the central meson (X) in the interval [-0.1,0.0].

(c) Solid: Same as (b) and p_t^2<0.1 $(GeV/c)^2$ for the slow (target) proton.

Dash: and p_t^2<0.1 $(GeV/c)^2$ for the fast (beam) proton.

(d) All previous cuts except for p_t^2<0.1 $(GeV/c)^2$ for the fast (beam) proton and

Solid: missing mass squared within [−σ,σ] (-0.56<MM2<1.12).

Dash: missing mass squared within [−σ,σ/2] (-0.56<MM2<0.70).

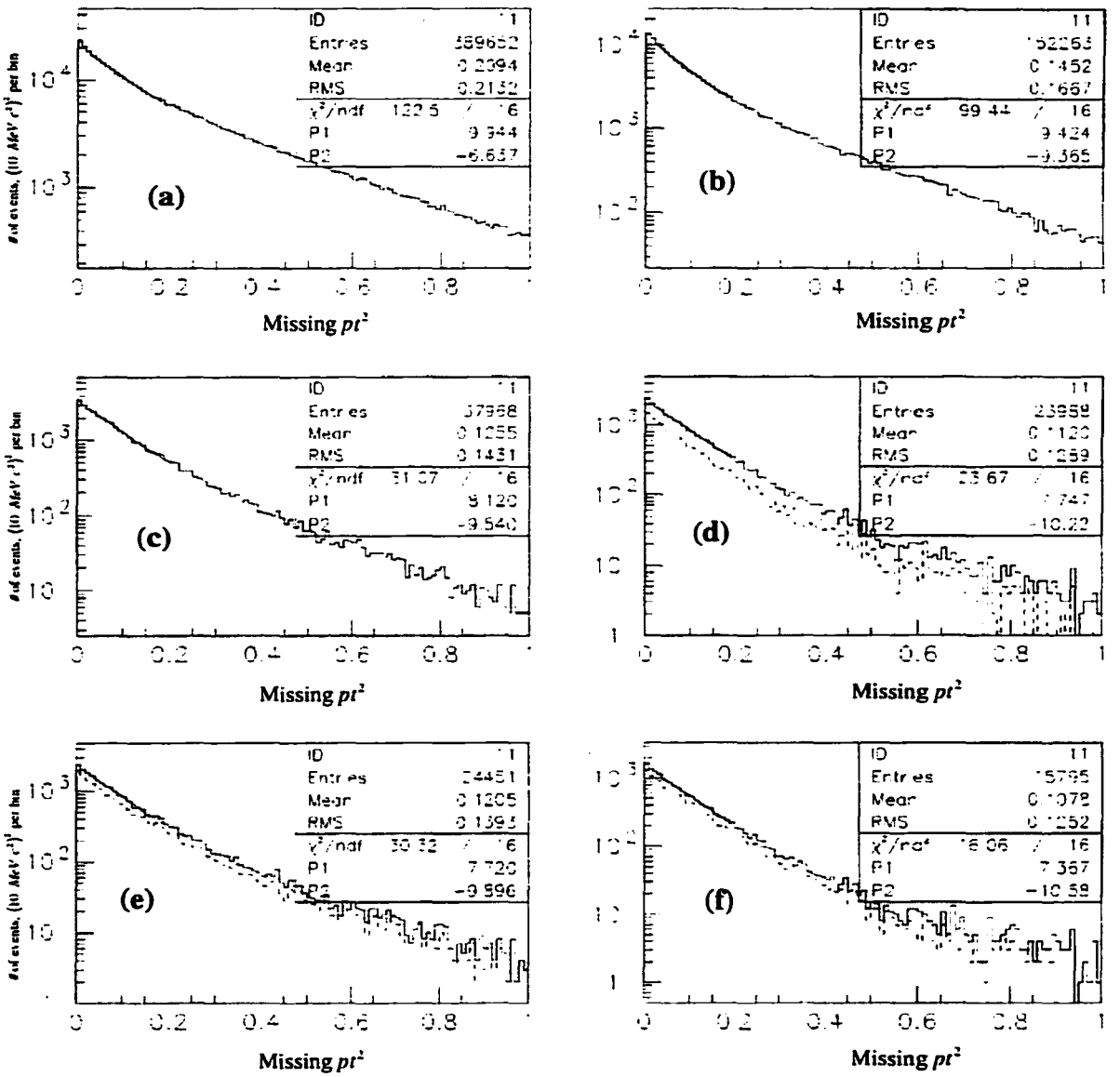

Figure 3.24 Missing p_t^2, assigned to slow (target) proton, "soft" Cherenkov identification. The selection cuts are:

(a) Vertex requirements and two (Cherenkov) pion compatible tracks in multiparticle spectrometer.

(b) Same as (a) and missing longitudinal momentum (MPl) within -1<MPl<1 GeV/c^2

(c) Same as (b) and rapidity gap between the slow proton and any one of the two pions greater than 1.8 and x_F for the central meson (X) in the interval [-0.1,0.0].

(d) Solid: And p_t^2<0.1 (GeV/c)^2 for the fast (beam) proton. Dash: p_t^2<0.05 (GeV/c)^2

(e) Solid: same as (c) and missing mass squared within [−σ,σ] (-0.56<MM2<1.12). Dash: same as (c) and missing mass squared within [−σ,σ/2] (-0.56<MM2<0.70).

(f) Solid, Dash: same as (e) and p_t^2<0.1 (GeV/c)^2 for the fast (beam) proton

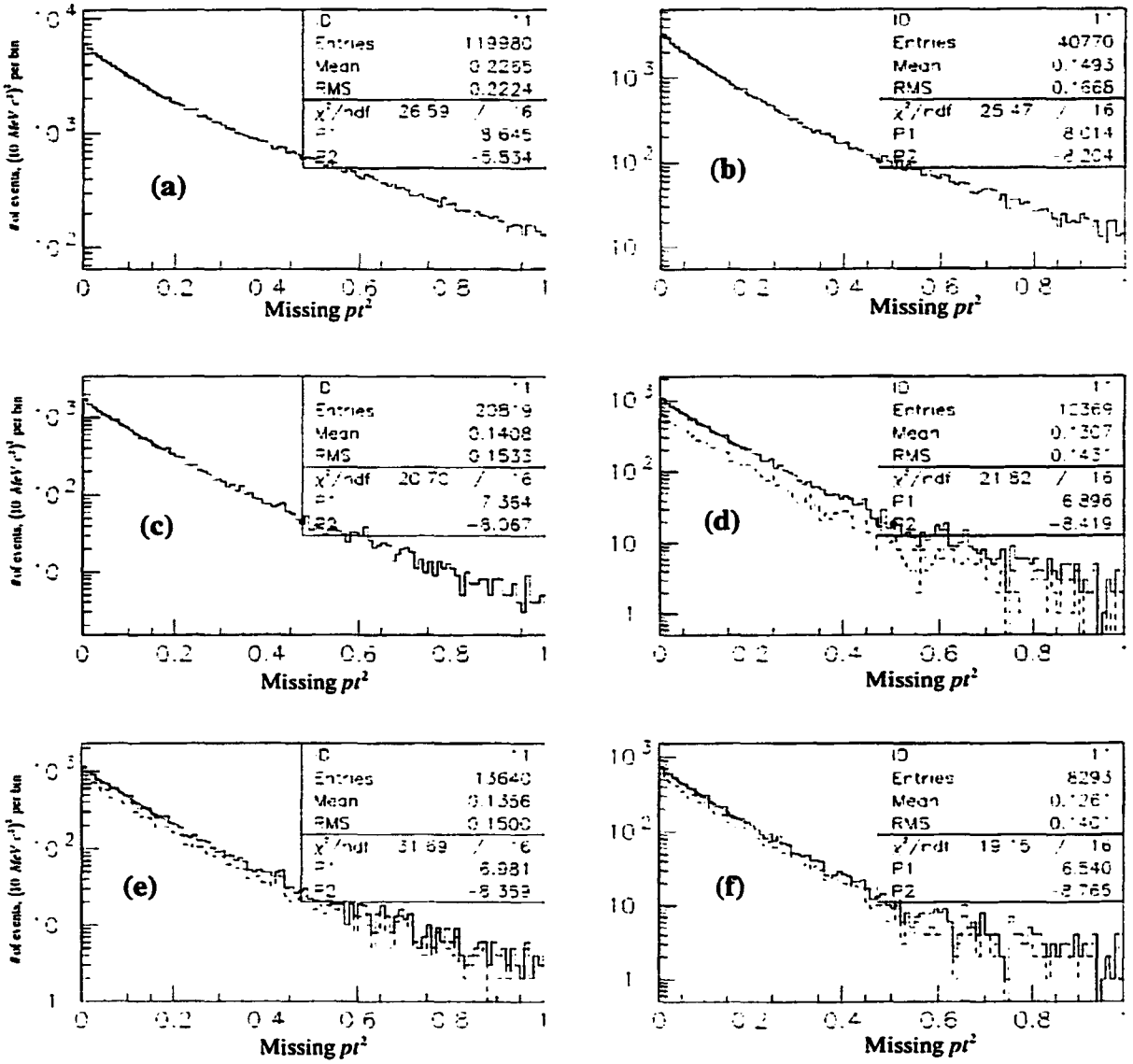

Figure 3.25 Missing p_t^2, assigned to slow (target) proton, one exactly pion Cherenkov identification. The selection cuts are:

(a) Vertex requirements and two (Cherenkov) pion compatible tracks in multiparticle spectrometer and at least one of them "exactly pion".

(b) Same as (a) and missing longitudinal momentum (MPl) within -1<MPl<1 GeV/c^2

(c) Same as (b) and rapidity gap between the slow proton and any one of the two pions greater than 1.8 and x_F for the central meson (X) in the interval [-0.1,0.0].

(d) Solid: And p_t^2<0.1 (GeV/c)^2 for the fast (beam) proton. Dash: p_t^2<0.05 (GeV/c)^2.

(e) Solid: same as (c) and missing mass squared within [$-\sigma,\sigma$] (-0.56<MM2<1.12). Dash: same as (c) and missing mass squared within [$-\sigma,\sigma/2$] (-0.56<MM2<0.70).

(f) Solid, Dash: same as (e) and p_t^2<0.1 (GeV/c)^2 for the fast (beam) proton

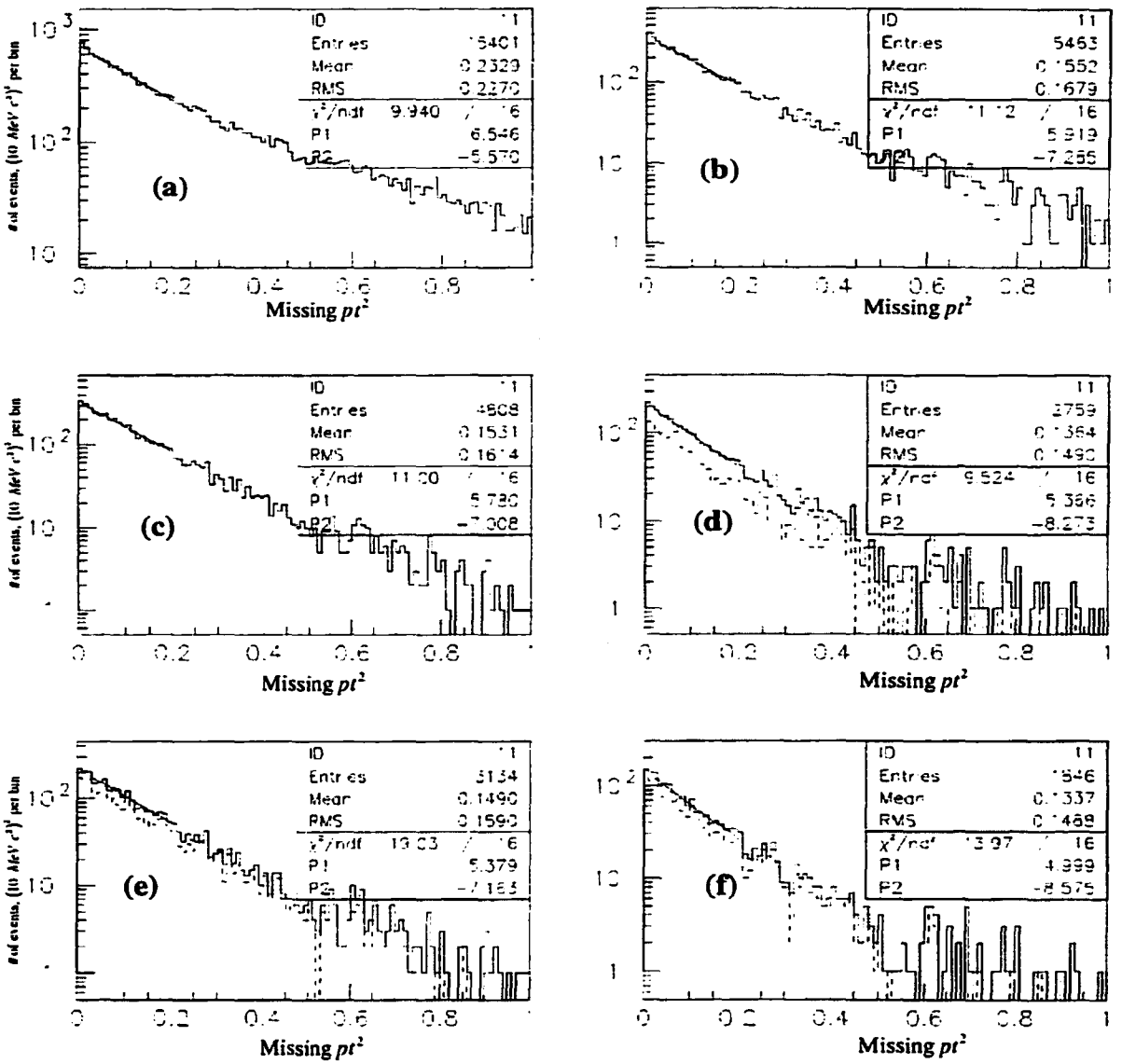

Figure 3.26 Missing p_t^2, assigned to slow (target) proton, two exactly pion Cherenkov identification. The selection cuts are:

(a) Vertex requirements and two "exactly pion" tracks in multiparticle spectrometer.

(b) Same as (a) and missing longitudinal momentum (MPl) within -1<MPl<1 GeV/c^2

(c) Same as (b) and rapidity gap between the slow proton and any one of the two pions greater than 1.8 and x_F for the central meson (X) in the interval [-0.1,0.0].

(d) Solid: And p_t^2<0.1 (GeV/c)^2 for the fast (beam) proton. Dash: p_t^2<0.05 (GeV/c)^2.

(e) Solid: same as (c) and missing mass squared within [−σ,σ] (-0.56<MM2<1.12). Dash: same as (c) and missing mass squared within [−σ,σ/2] (-0.56<MM2<0.70).

(f) Solid, Dash: same as (e) and p_t^2<0.1 (GeV/c)^2 for the fast (beam) proton

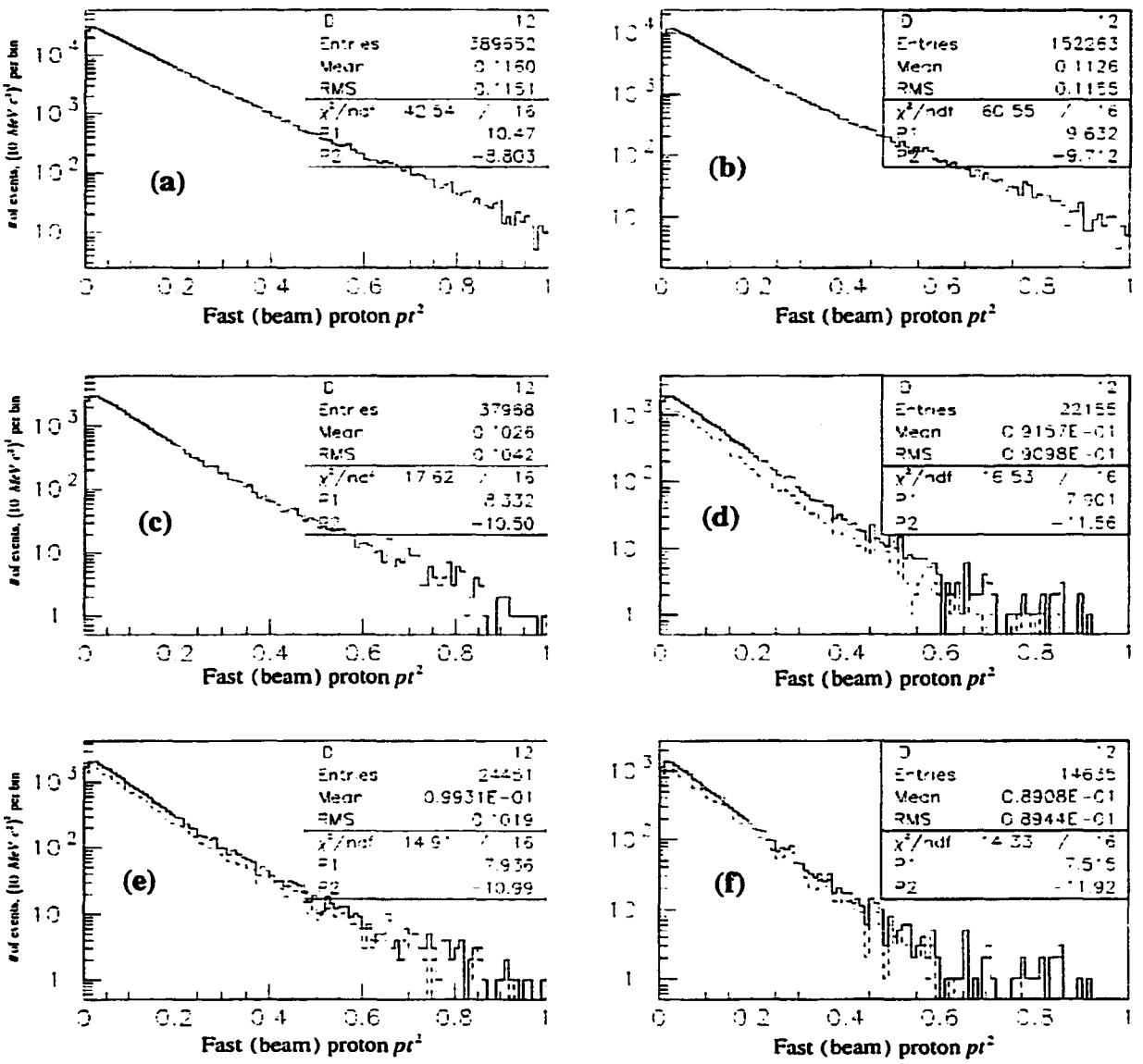

Figure 3.27 p_t^2 for fast (beam) proton, "soft" Cherenkov identification. The selection cuts are:

(a) Vertex requirements and two (Cherenkov) pion compatible tracks in multiparticle spectrometer.

(b) Same as (a) and missing longitudinal momentum (MPl) within -1<MPl<1 GeV/c^2

(c) Same as (b) and rapidity gap between the slow proton and any one of the two pions greater than 1.8 and x_F for the central meson (X) in the interval [-0.1,0.0].

(d) Solid: And p_t^2<0.1 (GeV/c)^2 for the fast (beam) proton. Dash: p_t^2<0.05 (GeV/c)^2.

(e) Solid: same as (c) and missing mass squared within [−σ,σ] (-0.56<MM2<1.12). Dash: same as (c) and missing mass squared within [−σ,σ/2] (-0.56<MM2<0.70).

(f) Solid, Dash: same as (e) and p_t^2<0.1 (GeV/c)^2 for the fast (beam) proton

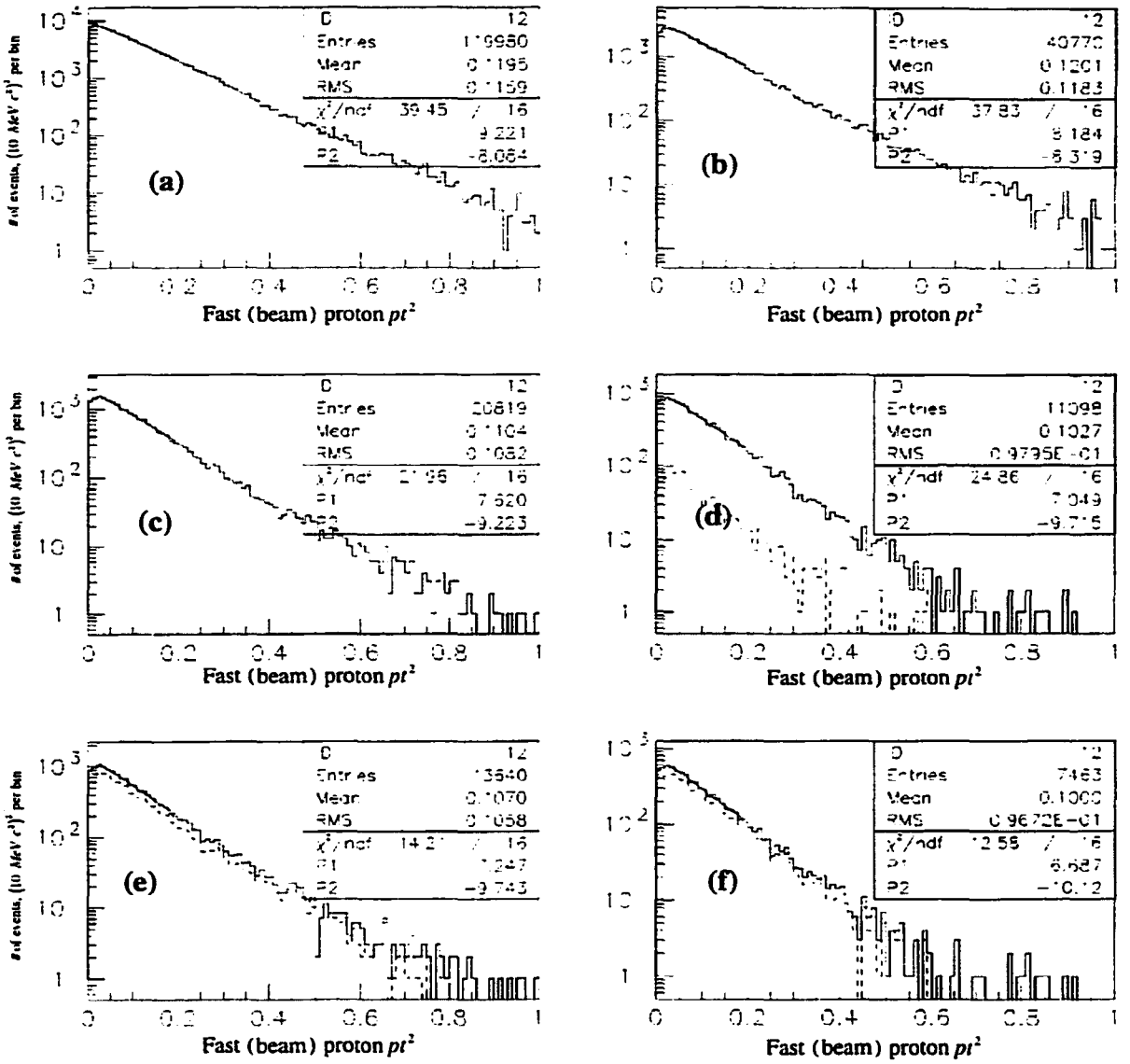

Figure 3.28 p_t^2 for fast (beam) proton, one exactly pion Cherenkov identification. The selection cuts are:

(a) Vertex requirements and two (Cherenkov) pion compatible tracks in multiparticle spectrometer and at least one of them "exactly pion".

(b) Same as (a) and missing longitudinal momentum (MPl) within -1<MPl<1 GeV/c^2

(c) Same as (b) and rapidity gap between the slow proton and any one of the two pions greater than 1.8 and x_F for the central meson (X) in the interval [-0.1,0.0].

(d) Solid: And p_t^2<0.1 (GeV/c)^2 for the fast (beam) proton. Dash: p_t^2<0.05 (GeV/c)^2.

(e) Solid: same as (c) and missing mass squared within [$-\sigma,\sigma$] (-0.56<MM2<1.12). Dash: same as (c) and missing mass squared within [$-\sigma,\sigma/2$] (-0.56<MM2<0.70).

(f) Solid, Dash: same as (e) and p_t^2<0.1 (GeV/c)^2 for the fast (beam) proton

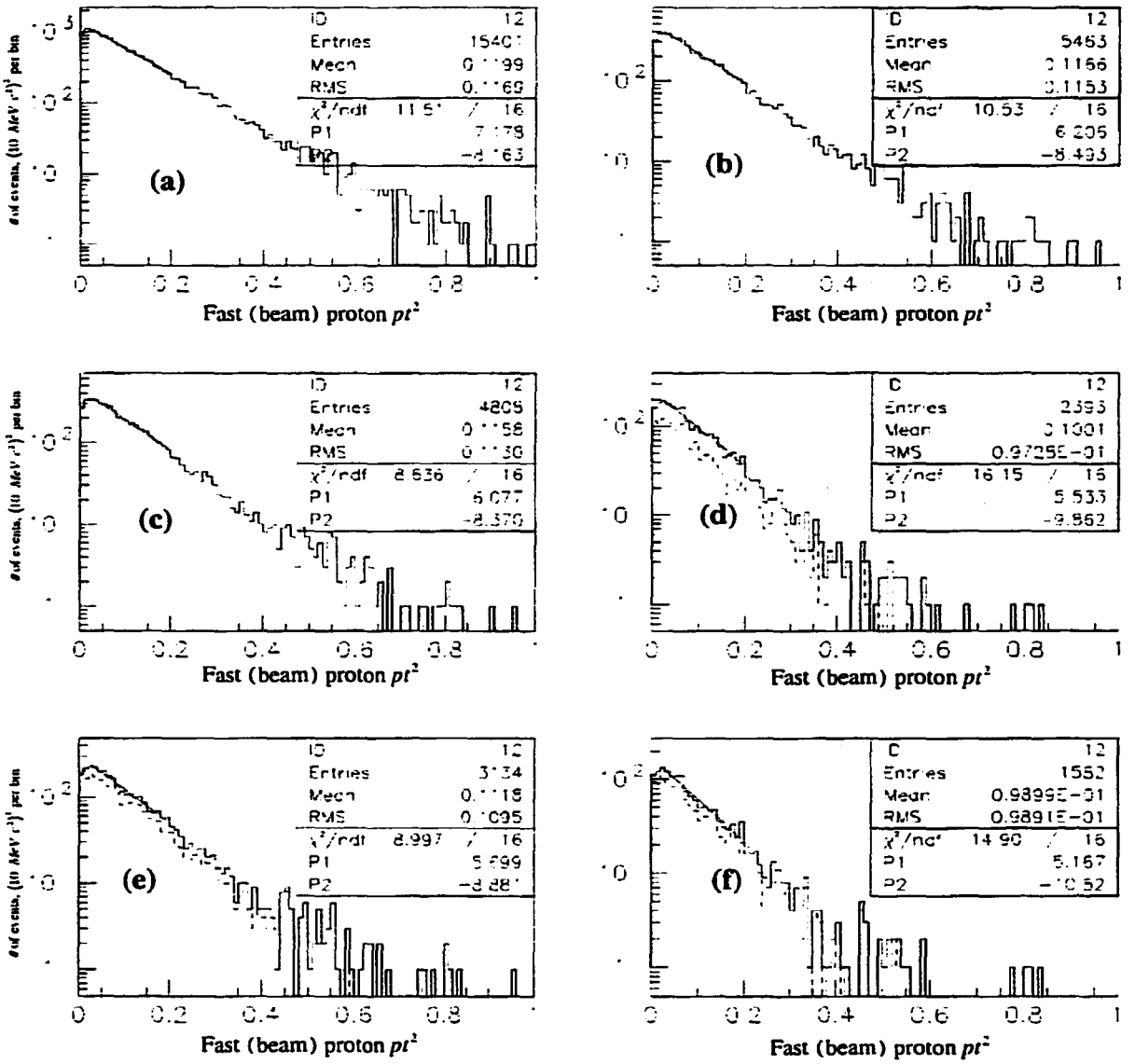

Figure 3.29 p_t^2 for fast (beam) proton, two exactly pion Cherenkov identification. The selection cuts are:

(a) Vertex requirements and two "exactly pion" tracks in multiparticle spectrometer.

(b) Same as (a) and missing longitudinal momentum (MPl) within -1<MPl<1 GeV/c^2

(c) Same as (b) and rapidity gap between the slow proton and any one of the two pions greater than 1.8 and x_F for the central meson (X) in the interval [-0.1,0.0].

(d) Solid: And p_t^2<0.1 (GeV/c)^2 for the fast (beam) proton. Dash: p_t^2<0.05 (GeV/c)^2.

(e) Solid: same as (c) and missing mass squared within [$-\sigma,\sigma$] (-0.56<MM2<1.12). Dash: same as (c) and missing mass squared within [$-\sigma,\sigma/2$] (-0.56<MM2<0.70).

(f) Solid, Dash: same as (e) and p_t^2<0.1 (GeV/c)^2 for the fast (beam) proton

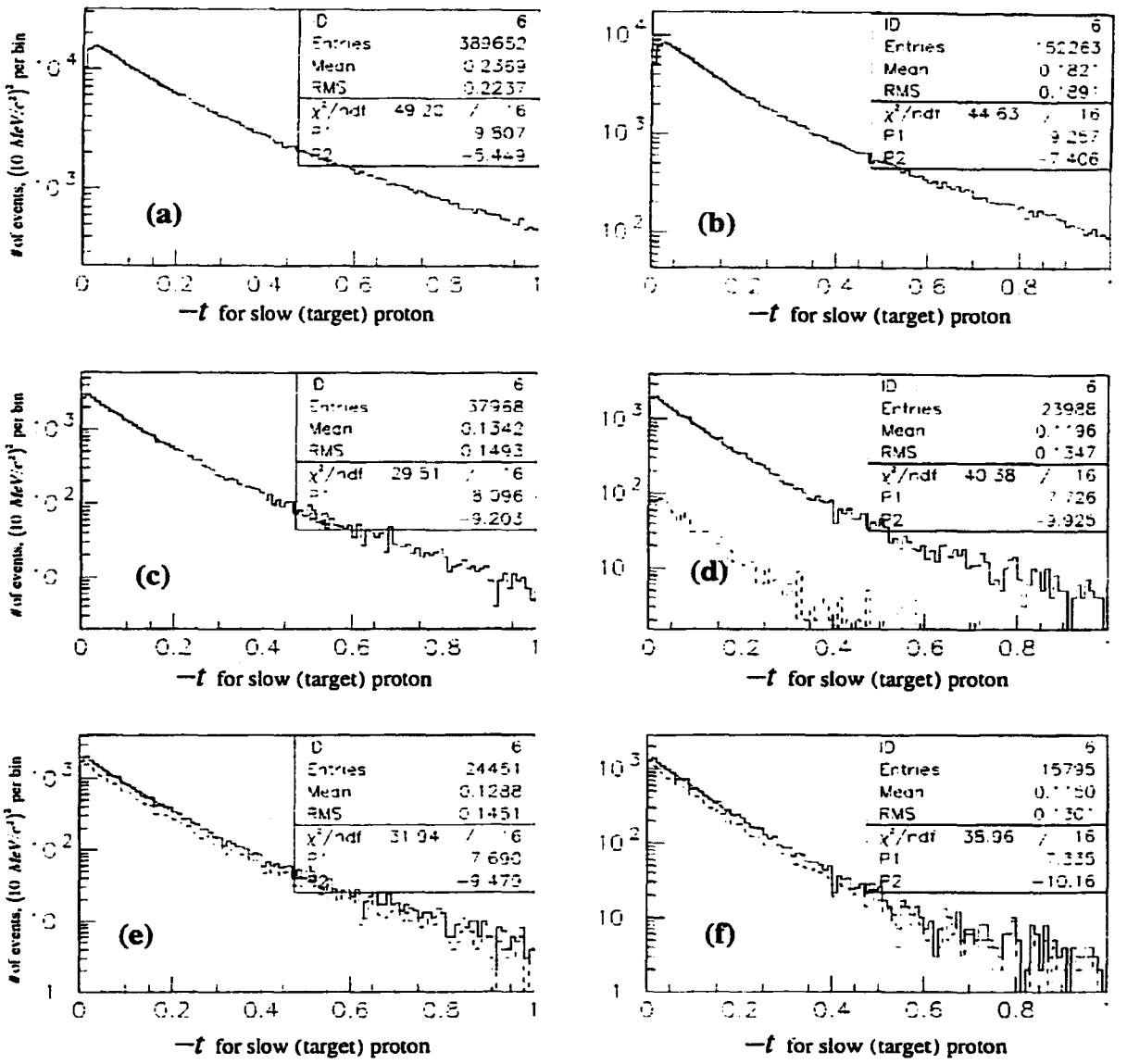

Figure 3.30 $-t$ (4-momentum transfer) for slow (target) proton, "soft" Cherenkov identification. The selection cuts are:

(a) Vertex requirements and two (Cherenkov) pion compatible tracks in multiparticle spectrometer.

(b) Same as (a) and missing longitudinal momentum (MPl) within -1<MPl<1 GeV/c

(c) Same as (b) and rapidity gap between the slow proton and any one of the two pions greater than 1.8 and x_F for the central meson (X) in the interval [-0.1,0.0].

(d) Solid: And p_t^2<0.1 (GeV/c)^2 for the fast (beam) proton. Dash: p_t^2<0.05 (GeV/c)^2

(e) Solid: same as (c) and missing mass squared within [−σ,σ] (-0.56<MM2<1.12). Dash: same as (c) and missing mass squared within [−σ,σ/2] (-0.56<MM2<0.70).

(f) Solid, Dash: same as (e) and p_t^2<0.1 (GeV/c)^2 for the fast (beam) proton

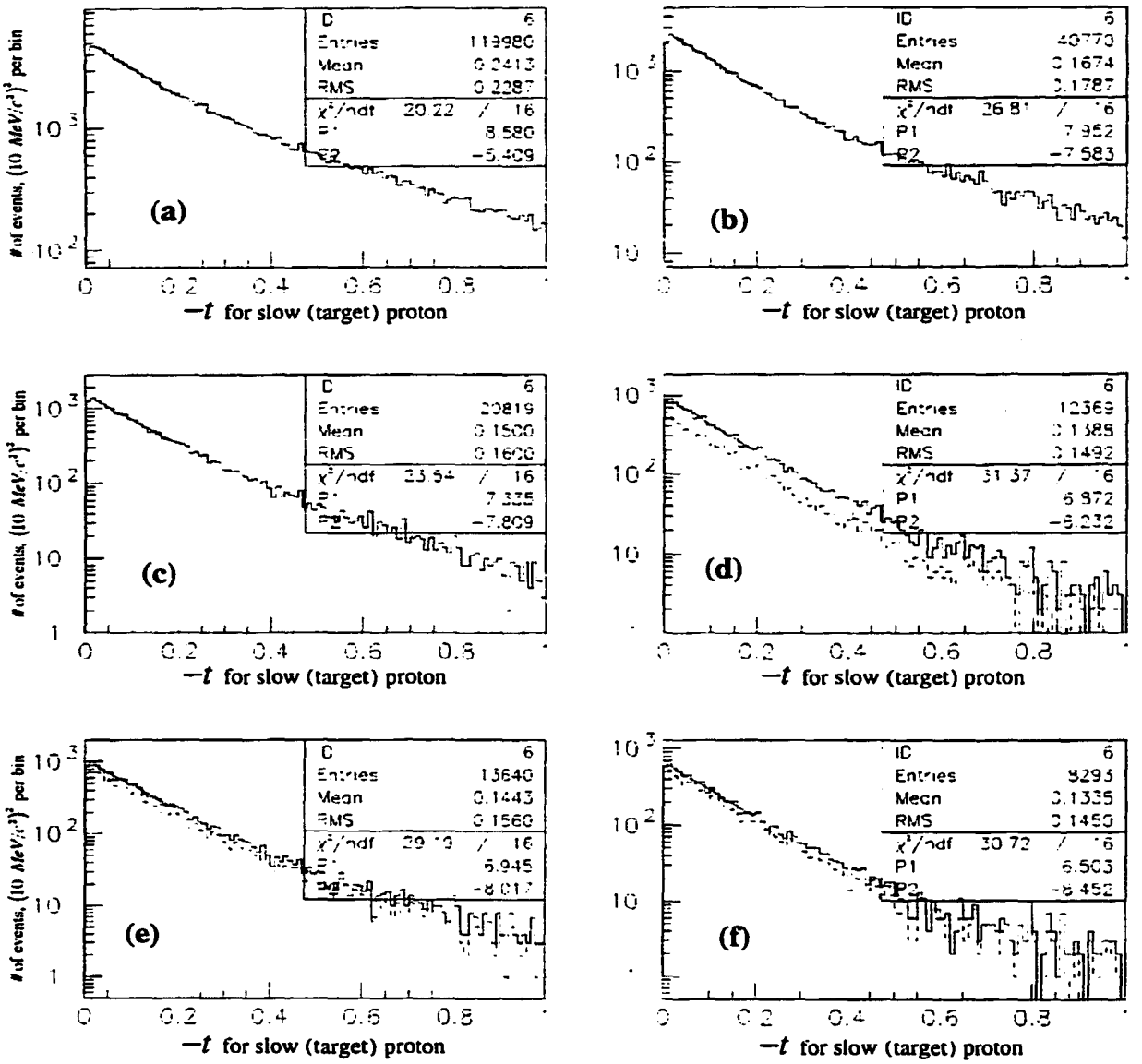

Figure 3.31 $-t$ (4-momentum transfer) for slow (target) proton, one exactly pion Cherenkov identification. The selection cuts are:

(a) Vertex requirements and two (Cherenkov) pion compatible tracks in multiparticle spectrometer and at least one of them "exactly pion".

(b) Same as (a) and missing longitudinal momentum (MPl) within -1<MPl<1 GeV/c

(c) Same as (b) and rapidity gap between the slow proton and any one of the two pions greater than 1.8 and x_F for the central meson (X) in the interval [-0.1,0.0].

(d) Solid: And p_t^2<0.1 (GeV/c)^2 for the fast (beam) proton. Dash: p_t^2<0.05 (GeV/c)^2.

(e) Solid: same as (c) and missing mass squared within [−σ,σ] (-0.56<MM2<1.12). Dash: same as (c) and missing mass squared within [−σ,σ/2] (-0.56<MM2<0.70).

(f) Solid, Dash: same as (e) and p_t^2<0.1 (GeV/c)^2 for the fast (beam) proton

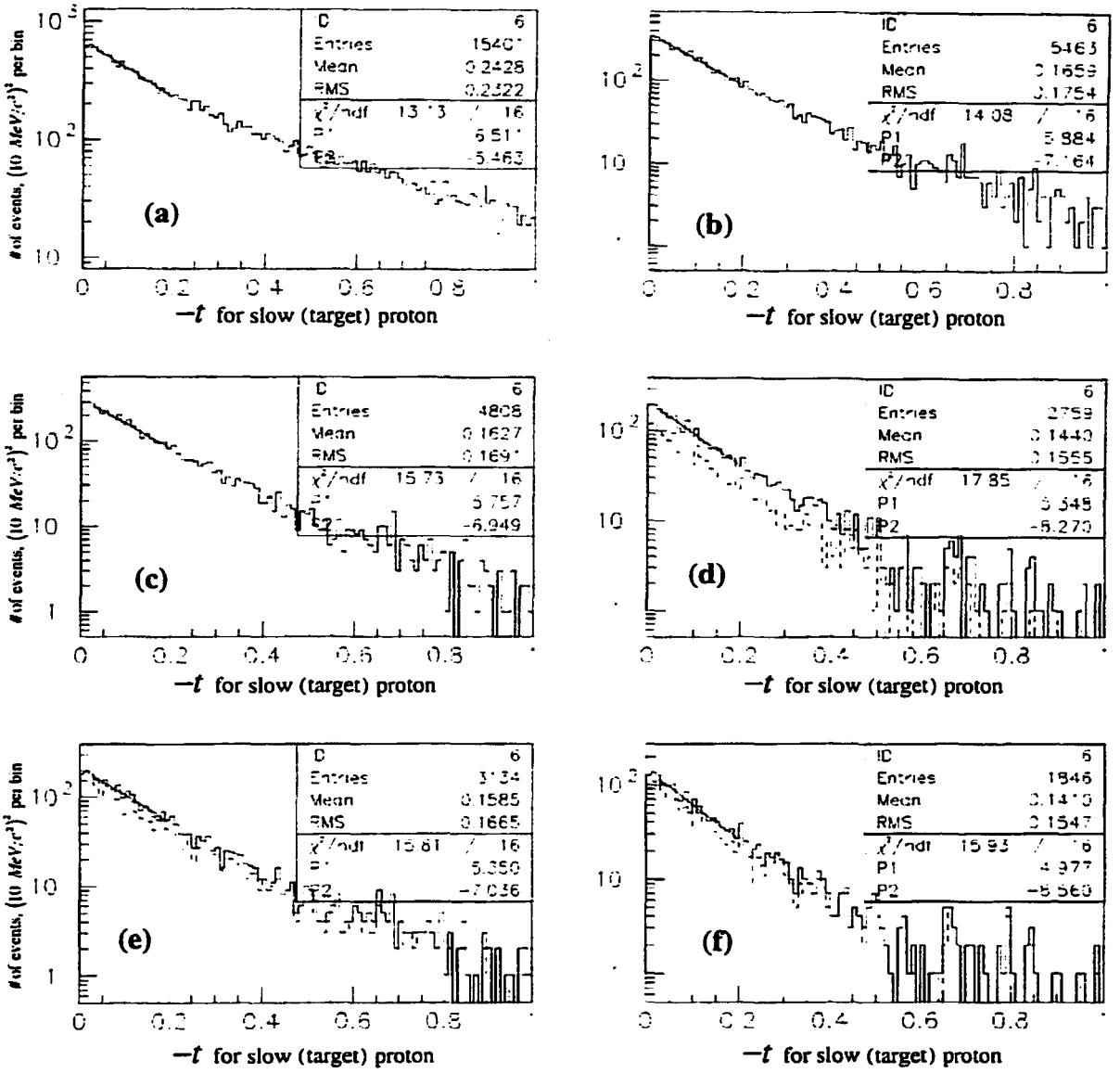

Figure 3.32 $-t$ (4-momentum transfer) for slow (target) proton, two exactly pion Cherenkov identification. The selection cuts are:

(a) Vertex requirements and two "exactly pion" tracks in multiparticle spectrometer.

(b) Same as (a) and missing longitudinal momentum (MPl) within -1<MPl<1 GeV/c

(c) Same as (b) and rapidity gap between the slow proton and any one of the two pions greater than 1.8 and x_F for the central meson (X) in the interval [-0.1,0.0].

(d) Solid: And p_t^2<0.1 (GeV/c)^2 for the fast (beam) proton. Dash: p_t^2<0.05 (GeV/c)^2.

(e) Solid: same as (c) and missing mass squared within [−σ,σ] (-0.56<MM2<1.12). Dash: same as (c) and missing mass squared within [−σ,σ/2] (-0.56<MM2<0.70).

(f) Solid, Dash: same as (e) and p_t^2<0.1 (GeV/c)^2 for the fast (beam) proton

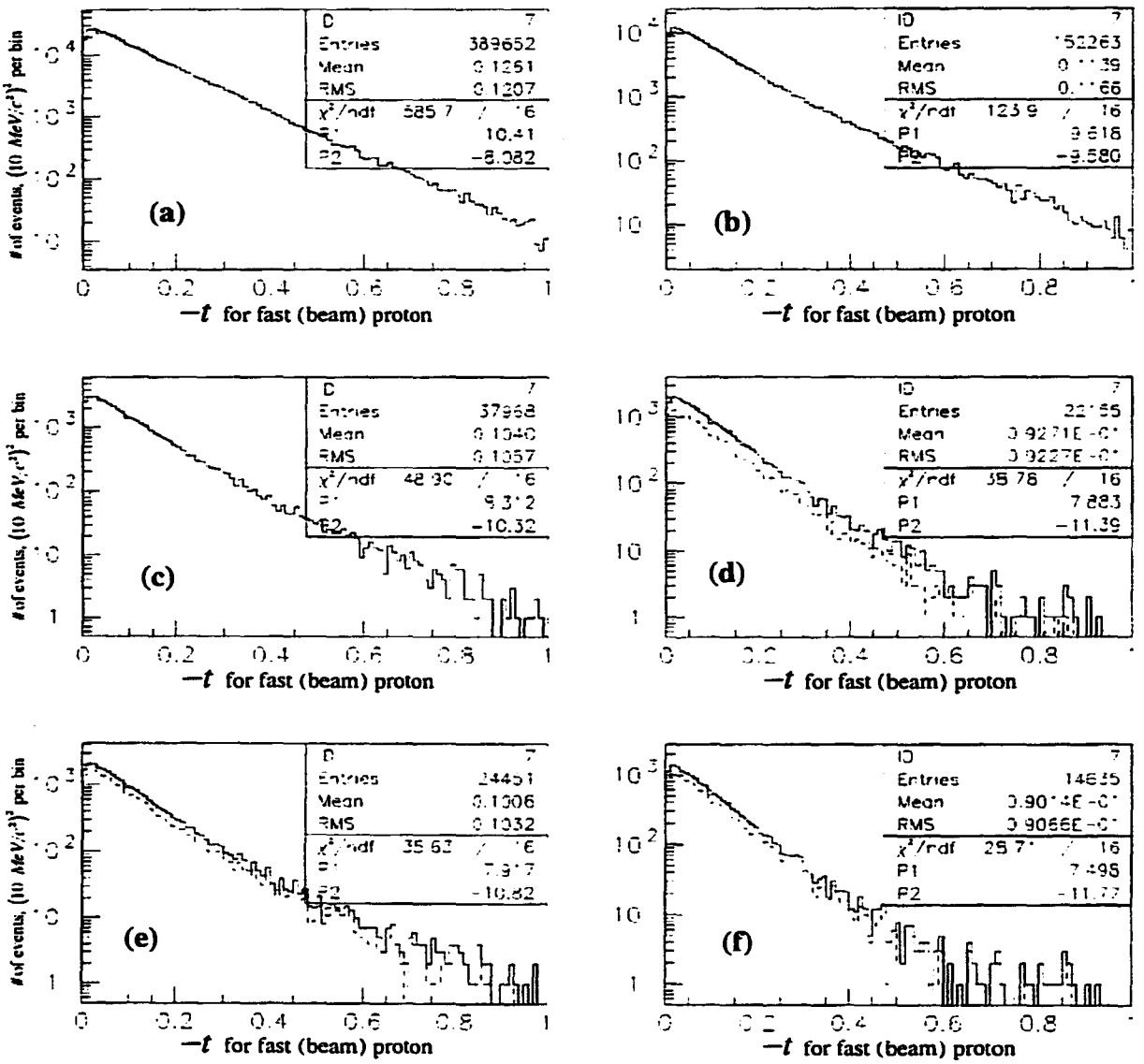

Figure 3.33 $-t$ (4-momentum transfer) for fast (beam) proton, "soft" Cherenkov identification. The selection cuts are:

(a) Vertex requirements and two (Cherenkov) pion compatible tracks in multiparticle spectrometer.

(b) Same as (a) and missing longitudinal momentum (MPl) within -1<MPl<1 GeV/c

(c) Same as (b) and rapidity gap between the slow proton and any one of the two pions greater than 1.8 and x_F for the central meson (X) in the interval [-0.1,0.0].

(d) Solid: And p_t^2<0.1 (GeV/c)^2 for the fast (beam) proton. Dash: p_t^2<0.05 (GeV/c)^2.

(e) Solid: same as (c) and missing mass squared within [−σ,σ] (-0.56<MM2<1.12). Dash: same as (c) and missing mass squared within [−σ,σ/2] (-0.56<MM2<0.70).

(f) Solid, Dash: same as (e) and p_t^2<0.1 (GeV/c)^2 for the fast (beam) proton

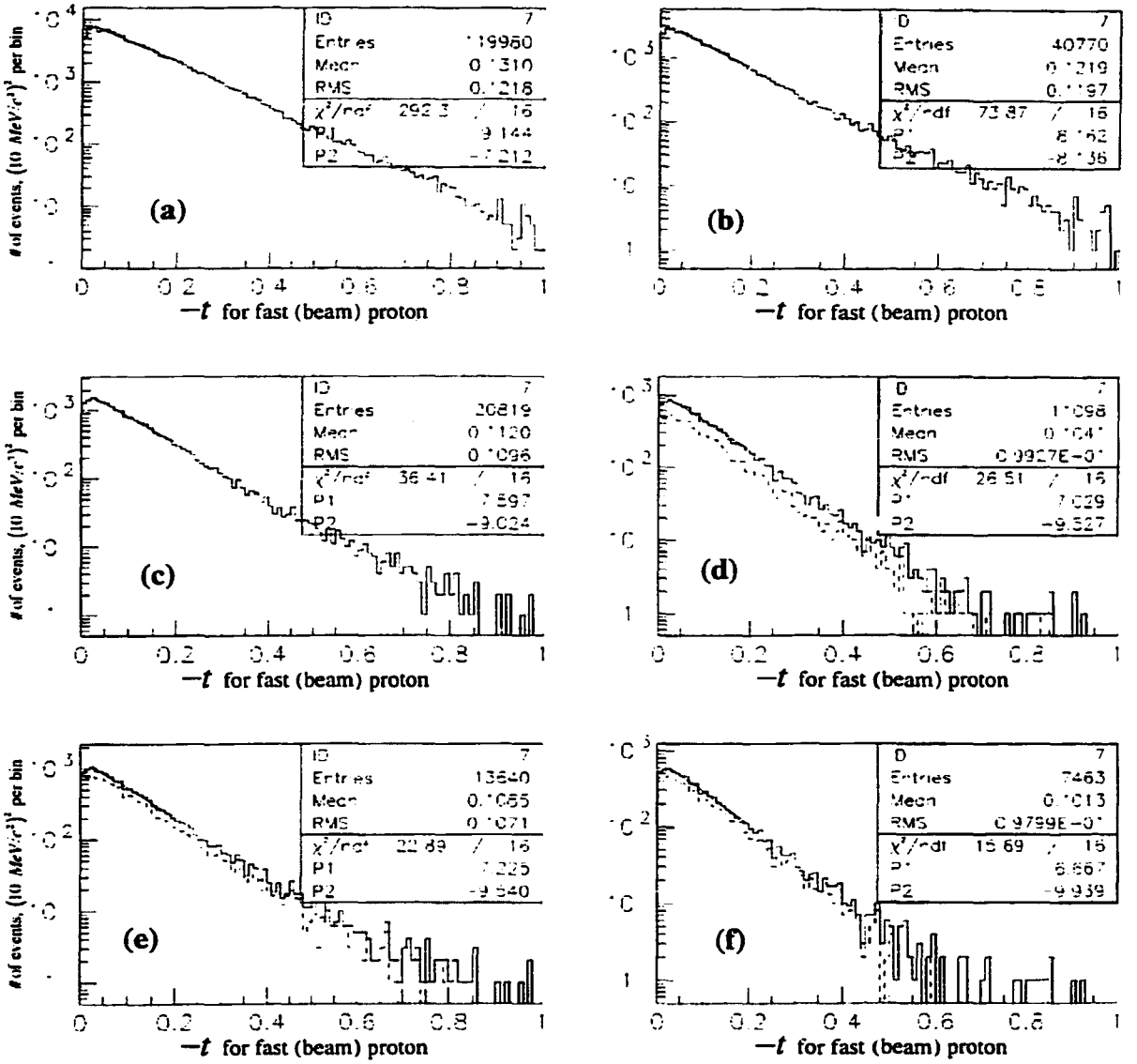

Figure 3.34 $-t$ (4-momentum transfer) for fast (beam) proton, one exactly pion Cherenkov identification. The selection cuts are:

(a) Vertex requirements and two (Cherenkov) pion compatible tracks in multiparticle spectrometer and at least one of them "exactly pion".

(b) Same as (a) and missing longitudinal momentum (MPl) within -1<MPl<1 GeV/c

(c) Same as (b) and rapidity gap between the slow proton and any one of the two pions greater than 1.8 and x_F for the central meson (X) in the interval [-0.1,0.0].

(d) Solid: And p_t^2<0.1 (GeV/c)^2 for the fast (beam) proton. Dash: p_t^2<0.05 (GeV/c)^2.

(e) Solid: same as (c) and missing mass squared within [$-\sigma,\sigma$] (-0.56<MM2<1.12). Dash: same as (c) and missing mass squared within [$-\sigma,\sigma/2$] (-0.56<MM2<0.70).

(f) Solid, Dash: same as (e) and p_t^2<0.1 (GeV/c)^2 for the fast (beam) proton

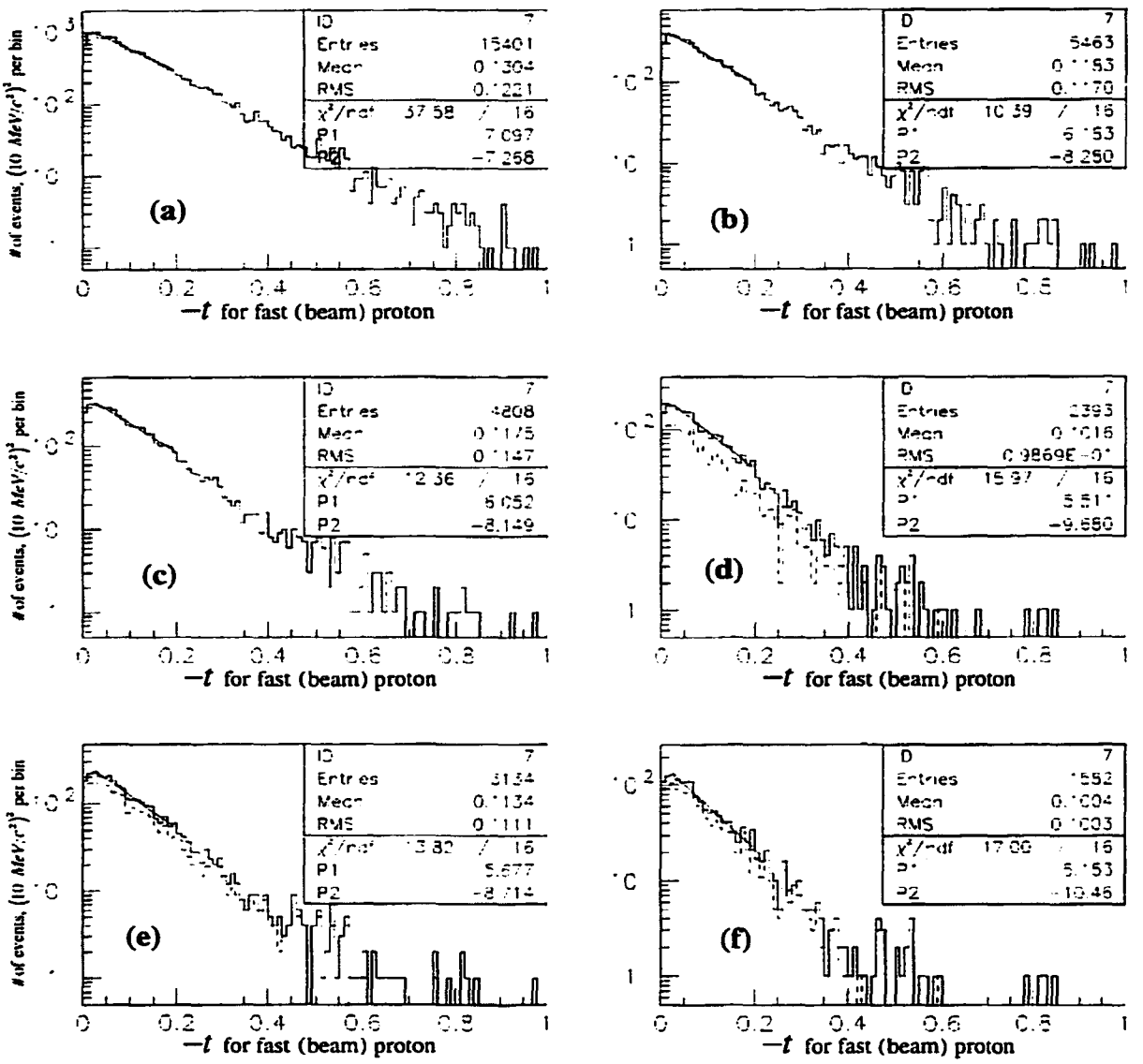

Figure 3.35 $-t$ (4-momentum transfer) for fast (beam) proton, two exactly pion Cherenkov identification. The selection cuts are:

(a) Vertex requirements and two "exactly pion" tracks in multiparticle spectrometer.

(b) Same as (a) and missing longitudinal momentum (MPl) within -1<MPl<1 GeV/c

(c) Same as (b) and rapidity gap between the slow proton and any one of the two pions greater than 1.8 and x_F for the central meson (X) in the interval [-0.1,0.0].

(d) Solid: And p_t^2<0.1 (GeV/c)^2 for the fast (beam) proton. Dash: p_t^2<0.05 (GeV/c)^2.

(e) Solid: same as (c) and missing mass squared within [−σ,σ] (-0.56<MM2<1.12). Dash: same as (c) and missing mass squared within [−σ,σ/2] (-0.56<MM2<0.70).

(f) Solid, Dash: same as (e) and p_t^2<0.1 (GeV/c)^2 for the fast (beam) proton

CHAPTER 4

ANALYSIS

4.1 Outline

We want to identify the spin parity of the intermediate meson state (X) as a function of mass and other production variables such as transverse momentum and relative scattering angle for the final state protons. For spin parity determination it is necessary to use the angular distribution of the final state pions. We proceed in two distinct steps. First we express the observed distribution as an expansion of moments multiplied by the corresponding spherical harmonics. We use the moments expansion and the detector Monte Carlo simulation to find a new set of acceptance corrected moments, describing the produced distribution. For the second step, the acceptance corrected moments are used to find production amplitudes with definite spin parity, consistent with the acceptance corrected distribution.

The presentation is organized in four sections. The first section describes the Monte Carlo sample used for "acceptance correction" of the observed distributions. Here a discussion of the possible sets of variables we can use for event description is included, along with the choice of variables used for this analysis. The second section describes the statistical analysis method used to find the acceptance corrected expansion coefficients (acceptance corrected moments). In the third section we describe the procedure used to extract amplitudes from the acceptance corrected moments. The ambiguities in the determination of the production amplitudes lead to eight valid solutions for each analysis bin. We discuss the method we use to select one of the eight as the most probable to correspond to the production amplitudes and the procedure used for continuation of the solutions across analysis bins. In the fourth and final section we investigate the

dependence of the results on the final state variables. In particular we address recent interest in the correlation between production amplitudes and the relative angle of the scattering planes for the final state protons.

4.2 Monte Carlo Detector Simulation

As stated in the introduction, the kinematics of the reaction justify treating production of the two pion system as a two step process (see Figure 1.1).

$$pp \rightarrow p_{fast}(X)p_{slow}$$
$$(X) \rightarrow \pi^+\pi^-$$

Therefore we express the production and decay in terms of variables reflecting this assumption. In our analysis decoupling between the production of the intermediate meson and its final decay through the strong interaction is crucial. We do not consider any correlations between the final state protons and the decay products of the intermediate meson (X).

First we specify the variables necessary to define production. There are three particles in the final state (two final state protons and the central meson). Therefore three four-momentum vectors are necessary. The 3x4=12 variables can be reduced using four energy momentum conservation constraints, and two constraints due to the known mass of the final state protons. Therefore, 12-4-2=6 independent variables are necessary to define production. We choose:

M_X	mass of the (X) system
x_F	Feynman x of (X)
pt_s^2	transverse momentum squared for p_{slow}
φ_s	the angle of the scattering plane in the overall center of mass system for p_{slow}
pt_f^2	transverse momentum squared for p_{fast}
φ_f	the angle of the scattering plane in the overall center of mass system for p_{fast}

Of the six variables we use for the description of the first step of the reaction, one is a trivial rotation of the event around the beam axis. This becomes obvious if we substitute the two angles that specify the proton scattering planes (φ_s & φ_f) with two new variables: one specifying the relative angle between the scattering planes (φ_{fs}) and one specifying the overall orientation of the event in the detector. This second angle can be any one of the two angles mentioned earlier (φ_s or φ_f). Although the physics is independent of overall rotations and the production properties can be expressed using just five variables, detector acceptance is not independent of overall rotations and all six variables must be used for detector corrections.

For the decay of the intermediate particle we have 2x4=8 independent variables and application of energy momentum conservation along with the known mass of the final state pions leaves 8-4-2=2 independent variables. The mass of the intermediate meson is an independent variable for production and is considered known here. The variables we choose are the angles that specify the orientation of the π^+:

$\cos(\theta)$	polar angle
φ	azimuthal angle

We define the two angles in the Gottfried-Jackson frame because it is a convenient coordinate system for the application of the helicity formalism [51,52]. The coordinate system is defined at the center of mass of the intermediate meson and the axis orientation is determined by:

Z axis	The direction of the momentum transfer of the beam or target proton.
Y axis	The normal to the plane defined by the momentum transfers at the overall center of mass frame.
X axis	the cross product $\hat{x} = \hat{y} \times \hat{z}$

The set of variables chosen to specify the production and decay processes is not unique. One of the alternative choices would be to substitute the transverse momentum of the final state protons with their four momentum transfer (t). The choice of variables is somewhat arbitrary. In this particular case we prefer the transverse momentum since it is directly measured.

We can express the differential cross section (therefore the observed intensity) in terms of the variables just specified. We start with the Lorentz invariant cross section for four particles in the final state (two protons and two pions). The Lorentz invariant cross section is:

$$d\sigma = \frac{(2\pi)^4}{4p_{cm}\sqrt{s}}\left(\sum_{\lambda}|M_{\lambda}|^2\right)d\Phi_4\left(P;p_f,p_+,p_-,p_s\right)$$

where the summation is performed over the four possible helicity final states for the final state protons. We express the Lorentz invariant phase space as a product of production and decay phase space:

$$\begin{aligned}
d\Phi_4\left(P;p_f,p_+,p_-,p_s\right) &= \delta^4\left(P-\sum_{i=1}^{4}p_i\right)\prod_{i=1}^{4}\frac{d^4p_i}{(2\pi)^3}\delta\left(p_i^2-m_i^2\right) = \\
&= \delta^4\left(P-\left(p_f+q+p_s\right)\right)\prod_{i=f,s}\frac{d^4p_i}{(2\pi)^3}\delta\left(p_i^2-m_i^2\right) \\
&\quad \times \delta^4(q-p_+-p_-)(2\pi)^3\frac{d^4p_X}{(2\pi)^3}\delta\left(q^2-M_X^2\right)dM_X^2 \\
&\quad \times \prod_{i=+,-}\frac{d^4p_i}{(2\pi)^3}\delta\left(p_i^2-m_i^2\right) = \\
&= \delta^4\left(P-\left(p_f+q+p_s\right)\right)\prod_{i=f,s,X}\frac{d^4p_i}{(2\pi)^3}\delta\left(p_i^2-m_i^2\right) \\
&\quad \times \delta^4(q-p_+-p_-)\prod_{i=+,-}\frac{d^4p_i}{(2\pi)^3}\delta\left(p_i^2-m_i^2\right)\ (2\pi)^3dM_X^2 = \\
&= d\Phi_3\left(P;p_f,q,p_s\right)d\Phi_2\left(q;p_+,p_-\right)\ (2\pi)^3 2M_X dM_X
\end{aligned}$$

We introduce the four momentum vector of the intermediate meson (X) that obeys the equalities:

$$q = p_+ + p_- \qquad\qquad q^2 = M_X^2$$

We integrate the phase space factors to eliminate the delta functions. It is convenient to integrate the production phase space in the overall center of mass frame and the decay phase space in the center of mass of the intermediate meson. After elimination of the delta functions:

$$d\Phi_3\left(P; p_f, q, p_s\right) = \frac{\sqrt{s}}{2^4(2\pi)^9} \frac{dp_{t,f}^2 d\varphi_f dp_{t,s}^2 d\varphi_s dx_F}{E_s \left| E_s p_{z,f} - E_f p_{z,s} \right|}$$

$$d\Phi_2\left(q; p_+, p_-\right) = \frac{1}{2^2(2\pi)^6} \frac{\sqrt{\left(\frac{M_X}{2}\right)^2 - m_\pi^2}}{M_X} d(\cos\theta) d\varphi .$$

If we omit constants absorbed in the normalization the overall cross section becomes:

$$d^8\sigma = \left(\sum_\lambda |M_\lambda|^2 \right) \frac{1}{E_s \left| E_s p_{z,f} - E_f p_{z,s} \right|} \sqrt{\left(\frac{M_X}{2}\right)^2 - m_\pi^2} \; dp_{t,f}^2 d\varphi_f dp_{t,s}^2 d\varphi_s dx_F dM_X \; d(\cos\theta) d\varphi$$

After defining the invariant cross section formally, we can proceed to specify the Monte Carlo sample generated for detector acceptance corrections. We see from the discussion above that a total number of 8 variables is needed for the specification of an event. For detector acceptance corrections we would like to bin the data and Monte Carlo sample into bins of all eight variables. This way, provided that acceptance does not change rapidly from one analysis bin to the next and that there are no bins with zero acceptance, we would be able to correct the sample for acceptance inefficiencies without assumptions about the distribution of the produced event sample. In practice, the large number of variables necessary for event definition makes such an approach unfeasible. Binning in all eight variables rapidly reduces the number of events per bin and diminishes the statistical significance of the measurement. Therefore we have to integrate the event distribution in some of the variables. The variables we choose to integrate over are the ones for which the detector acceptance is good and we have confidence in the measurement of the distribution

directly from the data. For the Monte Carlo we generate 10^7 events with production distributions:

M_X	mass of the (X) system	Flat between [0.28, 2.30] GeV/c^2
x_F	Feynman x of (X)	Flat between [-0.2,0.1]
pt_s^2	transverse momentum squared for p_{slow}	According to $\exp\{-7p_{t,s}^2\}$
φ_s	the angle of the scattering plane in the overall center of mass system for p_{slow}	Flat for whole range
pt_f^2	transverse momentum squared for p_{fast}	According to $\exp\{-7p_{t,f}^2\}$
φ_f	the angle of the scattering plane in the overall center of mass system for p_{fast}	Flat for whole range

$\cos(\theta)$	Azimuthal and polar angles for	Flat
φ	(+) pion in Gottfried Jackson frame.	Flat

The remaining variables are calculated from energy and momentum conservation. We match the data for the transverse momentum distributions of the final state protons. The invariant mass of the intermediate meson (M_X) and its decay angles ($\cos(\theta)$, φ) are generated flat because we use narrow bins for acceptance corrections of all three variables. For the final state proton angles we observe a flat distribution in the data, and the Monte Carlo sample shows weak acceptance dependencies as a function of these angles. The situation for the last of the generated variables (x_F) is more complicated. The acceptance of the detector and the production distribution vary rapidly as a function of x_F. Because it is difficult to generate reliably a Monte Carlo sample that matches the produced data in the whole x_F range, we choose to perform the analysis in a small range of x_F where we expect an almost flat distribution for the produced data sample. This is the x_F range [-0.1,0.0]. This reduces the Monte Carlo sample used to 3.3×10^6 events.

We generate the production variables of each event in the overall center of momentum reference frame, and the decay variables in the Gottfried-Jackson frame. We use these variables to calculate the momentum vectors of the four final state particles (two protons and two pions) in the laboratory reference frame. The momentum vectors are written to output tapes in a standard format used for all E766/E690 Monte Carlo studies. The generator output is used as input to the detector simulation code. This is code specifically written for the simulation of this detector. Details about detector simulation can be found elsewhere [46,50]. Generated particles are propagated through the simulated detector, and the resulting "measurements" are written to output tape in a format identical to the output format of the detector acquisition system. From this point on the analysis of the data and Monte Carlo samples is identical. We process the Monte Carlo events with the same track reconstruction (processor simulation) and vertex reconstruction (PASS2) code. The analysis code used to process and select the data is also used for the Monte Carlo sample. There is only one significant difference between the PASS2 output of the Monte Carlo and detector data samples: each Monte Carlo event is accompanied by a data block containing the momentum vectors produced by the generator. We use this information to compare the generated and reconstructed momentum vectors for detector resolution studies and to check for errors in the reconstruction routines. The generator data block is also used for acceptance studies and for verification of the generated event distribution.

We now proceed to present some of the acceptance properties of the detector and compare the Monte Carlo and observed data samples. The comparison can be used as justification for the choices we made generating the Monte Carlo events. The data sample contains topologies other than the topology of interest, while the Monte Carlo sample contains just one topology. Thus, comparisons between the two samples make sense only after the application of topology selection requirements.

We show in Figure 4.1 the detector acceptance as a function of mass for a series of selection criteria. There are six plots in this figure, two plots for each set of Cherenkov identification requirements. In Figures 4.1.a and 4.2.b we apply only "soft" Cherenkov selection criteria. We require that the multiparticle spectrometer particles are compatible with pion identification but not necessarily incompatible with other assignments. The first distribution in Figure 4.1.a (solid line) is the invariant mass of the generated events in the x_F interval [-0.1,0.0]. The next line (hardly distinguishable from the previous one) corresponds to the reconstructed mass distribution for Monte Carlo events that satisfy the vertex and "soft" Cherenkov identification requirements. Subsequent lines in Figures 4.1.a and 4.1.b show the reconstructed invariant mass distribution with the application of additional selection criteria. The additional selection cut that distinguishes each line from the previous is shown in the figure. For all selection criteria, although a significant part of the signal is rejected, we do not observe sharp changes in the mass distribution. Acceptance as a function of mass changes much slower than the "features" observed in the data. For more restrictive Cherenkov identification criteria, the acceptance changes significantly as a function of mass. But the acceptance varies only slowly when compared with the observed data sample invariant mass distribution. In Figures 4.1.c and 4.1.d we show the effect of the selection criteria used in Figures 4.1.a and 4.1.b when we require that at least one of the multiparticle spectrometer particles is compatible only with pion identity in the Cherenkov counter. The strict Cherenkov requirement applied to both multiparticle spectrometer tracks produces Figures 4.1.e and 4.1.f. Even more important than the smooth variation of the acceptance as a function of mass is the fact that there are no regions with zero acceptance. This means that given enough Monte Carlo statistics, we can correct any region of the data for any combination of the selection criteria presented above. Nevertheless we have a higher confidence in our results when the size of the correction we need to apply is small. A case where large corrections are necessary can be seen in Figure 4.1.f, for invariant masses above 1.8 GeV/c^2.

In the following presentation we will be showing the data distributions of a variable after integration over all other variables that describe the data set. Therefore it is important to keep in mind the comparable distributions. For example, we cannot integrate over invariant mass, since in this case the distributions for data and Monte Carlo are different. In this case we have to integrate for different regions of invariant mass. This is the case for Figure 4.2, where we compare the x_F distributions for Monte Carlo and data samples. There are three columns and three rows of figures. The three columns correspond to three different regions of mass with boundaries: threshold, 0.6, 1.0, 1.5 GeV/c^2. The three columns correspond to the three different Cherenkov requirements mentioned earlier. For Figure 4.2 all distributions are normalized to have an integral equal to unity. Although the generated distribution is flat while the data distribution is expected to peak around x_F=0, we see a very good matching between Monte Carlo and Data distributions. This testifies to the rapidly changing acceptance as a function of x_F. More careful examination shows that the Monte Carlo distribution exceeds the data distribution for values of x_F away from x_F=0 while the reverse is true at x_F=0. This is expected because the data distribution as a function of x_F indeed is not flat. It falls away from x_F=0. Nevertheless it is varying slow enough in the region where we perform the analysis ($x_F \in$ [-0.1,0.0]) to make a flat distribution a good approximation. Also notice that in the x_F region where we perform the analysis there are no bins with zero acceptance.

Acceptance as a function of the remaining production variables is shown in Figures 4.3 to 4.6. The first three figures present the acceptance of the Monte Carlo sample as a function of the transverse momentum for the final state protons, while Figure 4.6 shows the acceptance as a function of the relative angle (φ_{fs}) of the final state protons. For all four figures there is no significant dependence of detector acceptance as a function of the production variables. A more detailed look reveals some small dependencies not significant in the present analysis.

Figure 4.3 shows the slope of the generated and reconstructed Monte Carlo p_t^2 distributions for the two final state protons. For all reconstructed data distributions in this page, we use "soft" Cherenkov identification criteria. Figures 4.4 and 4.5 contain the same distributions for alternative Cherenkov identification cuts. The reasons for weak acceptance dependence in terms of the final state proton p_t^2 were presented in the description of the p_t^2 distributions for the detector data sample. As was the case for the detector data, we see a small loss of events for high values of beam track $p_{t,f}^2$ (Figure 4.3.d), but it appears only for high values of $p_{t,f}^2$ and involves a small number of events. A significant difference between the data and Monte Carlo samples can be seen in the $p_{t,f}^2$=0 region of the fast (beam) proton distribution. In the data sample we observe a "dip" in the $p_{t,f}^2$=0 region. The "dip" is due to the minimum momentum transfer requirements imposed by the third level of the on-line trigger (TG3). At the time of completion of this study we did not have a reliable model of the effect of the TG3 on the data sample, therefore the effect of the TG3 was omitted in the Monte Carlo detector simulation. This is a problem, since we do not correct for a class of events lost due to trigger inefficiency, but again it involves a small number of events. For this analysis we use bins of p_t^2 much wider than the small region affected by trigger inefficiency which further dilutes the effect. Since acceptance dependencies as a function of p_t^2 are very small, the use of the Monte Carlo for acceptance corrections has the net effect of simply multiplying the sample by a normalization constant, independent of the generated p_t^2 distribution. Figure 4.6 shows the distribution of the relative angle between the transverse momentum vectors of the two final state protons (φ_{fs}). After application of all data selection cuts we do not observe any dependence of detector acceptance on this variable.

4.3 Moments Analysis

Here I describe the method used to apply detector acceptance corrections to the observed data sample and express the produced distribution as a moments expansion. The base

functions used are the spherical harmonics ($Y_{lm}(\Omega)$). Before describing the "moments method" I express the observed distribution as an expansion of production and decay amplitudes for the intermediate meson X. The form of the amplitude expansion is used to illustrate the advantages of the moments method. Starting from the definition of the invariant cross section:

$$d^8\sigma = (phase\ space)\left(\sum_{\lambda}|M_{\lambda}|^2\right)dp^2_{t,f}d\varphi_f dp^2_{t,s}d\varphi_s dx_F dM_X \;\; d(\cos\theta)d\varphi$$

we can write the produced intensity as:

$$I = (phase\ space)\left(\sum_{\lambda}|U_{\lambda}|^2\right)$$

For the decay of a state with definite spin, we can write the amplitude for the angular dependence of the decay particles using the appropriate $D^l_{m,m'}$ function. Here l,m is the spin and helicity projection of the initial state (the intermediate meson X) and m' is the sum of helicities of the final state particles. For the whole process (production and subsequent decay of the intermediate meson X), the amplitude is the product of the production amplitude for a state with definite spin parity times the appropriate $D^l_{m,m'}$ function. In this study the final state particles (pions) have spin zero, therefore $m' = 0$ and the $D^l_{m,0}$ reduce to the spherical harmonics $Y_{l,m}(\Omega)$. Thus we can write the produced intensity as:

$$I(x,\Omega) = (phase\ \ space)|U|^2 =$$
$$= (phase\ \ space)\sum_{\substack{l,l'\\ m,m'}} Y^*_{lm}(\Omega)\alpha^*_{lm}(x)\alpha_{l'm'}(x)Y_{l'm'}(\Omega)$$

where the production amplitudes $\alpha_{lm}(x)$ depend on all production variables ($x \rightarrow M_X, p^2_{t,f}, p^2_{t,s}, x_F, \varphi_{fs}$) and the dependence on the decay variables ($\Omega \rightarrow \cos\theta, \varphi$) is known. Summation over helicity states has been omitted in the last formula.

The goal of the study is the determination of the production amplitudes. Therefore the first step is to recover the produced intensity distribution from the observed data distribution. The relation between the two intensities can be written as:

$$I_{obs}(x,\Omega) = A(x,\Omega) I_{prod}(x,\Omega)$$

where $A(x,\Omega)$ is the detector acceptance. We divide the sample in bins of the production variables and integrate the production variables within this bin. For a particular analysis bin:

$$I_{obs}(\Omega) = A(\Omega) I_{prod}(\Omega)$$

We perform the integration in bins where acceptance changes very slowly and can be considered a constant. To this end we either integrate using small bins of a production variable (e.g. M_X) or large bins of a production variable for which the acceptance does not change rapidly (e.g. p_t^2).

We express the produced distribution as an expansion in spherical harmonics:

$$I_{prod}(\Omega) = \sum_{\substack{l \\ m}} T_{lm} \mathrm{Y}_{lm}(\Omega) = \sum_{\substack{l \\ m \geq 0}} t_{lm} \, \mathrm{Re}\{\mathrm{Y}_{lm}(\Omega)\}$$

The advantages are twofold: First, the spherical harmonics form a complete basis for the description of any angular distribution. Second, and most important, limited spin assignments lead to limited terms in the series that expresses the angular dependence. This is why we started this section expressing the produced intensity as a function of production and decay amplitudes. If the maximum spin value in the sample is $l_{\max}$ the maximum non-zero expansion coefficient (moment) is $t_{2l_{\max}\,2l_{\max}}$. Notice that we write the expansion twice, once using the full $\mathrm{Y}_{lm}(\Omega)$ and once using only the real part of $\mathrm{Y}_{lm}(\Omega)$ with terms limited to $m \geq 0$. The reasons for the simplification are:

$T_{l-m} = (-1)^m T_{lm}^*$ because $I_{prod}(\Omega)$ is real.

$T_{l-m} = (-1)^m T_{lm}$ because parity is conserved in the strong interaction.

Therefore the T_{lm} are real and the imaginary part of the $Y_{lm}(\Omega)$ cancels out. It is easy to prove the relationship:

$t_{lm} = T_{lm}$ for $m = 0$ and $t_{lm} = 2T_{lm}$ for $m \neq 0$

In the following we simply write $Y_{lm}(\Omega)$ as a shorthand for $\mathrm{Re}\{Y_{lm}(\Omega)\}$ and we represent the pair of indices l,m with a single Greek index (e.g. $\lambda \leftrightarrow l,m$). We can rewrite the relationship between produced and observed distributions as:

$$I_{obs}(\Omega) = A(\Omega) I_{prod}(\Omega) = A(\Omega) \sum_{\lambda} t_{\lambda} Y_{\lambda}(\Omega)$$

and operating on both sides with $\int d\Omega Y_{\mu}(\Omega)$

$$\int \underbrace{d\Omega Y_{\mu}(\Omega) I_{acc}(\Omega)} = \sum_{\lambda} \underbrace{\left\{ \int d\Omega Y_{\mu}(\Omega) A(\Omega) Y_{\lambda}(\Omega) \right\}} t_{\lambda} \Rightarrow$$

$$b_{\mu} \qquad = \sum_{\lambda} \qquad A_{\mu\lambda} \qquad t_{\lambda}$$

We refer to the integrals of the accepted distribution as ***experimental moments***, b_{μ}. The expansion coefficients for the produced distribution we call ***acceptance corrected moments*** , t_{λ}. In practice the quantity b_{μ} is a function of the observed events and can be obtained from (see Appendix C):

$$b_{\mu} = \sum_{i=1}^{N_{obs}} Y_{\mu}(\Omega_i)$$

The ***acceptance correlations*** $A_{\mu\lambda}$ depend on the detector acceptance only. They can be calculated using the Monte Carlo sample:

$$A_{\mu\lambda} = \frac{1}{N_{mc\,gen}} \sum_{i=1}^{N_{mc\,obs}} Y_{\mu}(\Omega_i) Y_{\lambda}(\Omega_i)$$

Given the experimental moments $\{b_\mu\}$ and the computed $A_{\mu\lambda}$ we want to find the best set of coefficients $\{t_\lambda\}$ that minimize the difference :

$$\boxed{d_\mu \equiv b_\mu - \sum_\lambda \mathrm{A}_{\mu\lambda} t_\lambda}$$

We can limit the number of acceptance corrected moments $\{t_\lambda\}$ to λ_{max} and the number of differences $\{d_\mu\}$ to μ_{max}. If $\lambda_{max} < \mu_{max}$ we have an over constrained problem. We find the best set of coefficients $\{t_\lambda\}$ by minimizing the χ^2:

$$\boxed{\chi^2 \equiv \sum_{\mu\mu'} d_\mu \left[E(b)^{-1}\right]_{\mu\mu'} d_{\mu'}}$$

where $E(b)$ is the error matrix of the experimental moments. Requiring that $\frac{\partial \chi^2}{\partial t_\lambda} = 0$ for all allowed expansion coefficients in $\{t_\lambda\}$, we get a system of λ_{max} equations with λ_{max} unknowns that can be solved using standard matrix inversion.

Details about the statistical method we use to solve the problem are described in appendices A to C. In A we describe the statistical method and the system of equations used for the determination of the $\{t_\lambda\}$. In B we justify the form of the error matrices for the experimental moments $E(b)$, and acceptance corrected moments $E(t)$:

$$E(b)_{\mu\mu'} = \sum_{i=1}^{N_{obs}} \mathrm{Y}_\mu(\Omega_i)\mathrm{Y}_{\mu'}(\Omega_i) \qquad\qquad E(t) = \mathrm{A}^{-1} E(b) \mathrm{A}^{T-1}$$

Here A stands for the acceptance correlations matrix $A_{\mu\lambda}$. The last of the three appendices (C) comments on the computation of the integrals mentioned earlier using the discrete data and Monte Carlo samples.

I close the presentation of the statistical method with a note about the normalization used for the moments expansion. The expansion of the intensities for observed and produced distributions are (see Appendix A):

$$I_{prod}(x_i,\Omega) = \sum_{\substack{l \\ m\geq 0}} t_{lm}(x_i)\,\mathrm{Re}\{Y_{lm}(\Omega)\}$$

$$I_{obs}(x_i,\Omega) = \sum_{\substack{l \\ m\geq 0}} b_{lm}(x_i)\frac{1}{\varepsilon(m)}\,\mathrm{Re}\{Y_{lm}(\Omega)\} \qquad \text{where } \varepsilon(m) = \begin{cases} 1 & m = 0 \\ 1/2 & m \neq 0 \end{cases}$$

Here x_i notes the production variable bin i. For the definition of the spherical harmonics I omit a factor $\sqrt{1/4\pi}$. With this normalization $Y_{00}(\Omega) = 1$. Thus the values of the experimental (b_{00}) and accepted corrected (t_{00}) moments with $lm = 00$ are: $b_{00} = N_{obs.}$ and $t_{00} = N_{prod.}$ respectively. This follows from:

$$N_{prod} \equiv \int I_{prod}(\Omega)d\Omega = \sum_{\substack{l \\ m\geq 0}} t_{lm} \int \mathrm{Re}\{Y_{lm}(\Omega)\}d\Omega = t_{00}$$

$$N_{obs} \equiv \int I_{obs}(\Omega)d\Omega = \sum_{\substack{l \\ m\geq 0}} b_{lm} \int \mathrm{Re}\{Y_{lm}(\Omega)\}d\Omega = b_{00}$$

Therefore plotting the value of t_{00} as a function of mass corresponds to plotting the acceptance corrected mass spectrum.

4.4 Application of Method of Moments

Before I present the acceptance corrected moments for the selected data, I use the Monte Carlo events to verify the validity of the method. I divide the 10×10^6 Monte Carlo events into two samples. The first 2×10^6 events are used as the "data" sample, and the remaining 8×10^6 as the usual Monte Carlo sample. Here, the produced distribution corresponds to the generated Monte Carlo distribution. This is the distribution we expect to recover after acceptance corrections to the "data". We present the results of this exercise using the experimental (b_{lm}) and acceptance corrected moments (t_{lm}). For this sample, it is very easy to interpret the b_{lm} and t_{lm} plots because the distributions are very simple. For

the Monte Carlo sample we generated events "flat" in $\cos(\theta)$ and φ. The produced and observed intensities as a function of the moments are:

$$I_{prod}(x_i,\Omega) = \sum_{\substack{l \\ n.\geq 0}} t_{lm}(x_i)\,\mathrm{Re}\{Y_{lm}(\Omega)\}$$

$$I_{obs}(x_i,\Omega) = \sum_{\substack{l \\ m\geq 0}} b_{lm}(x_i)\frac{1}{\varepsilon(m)}\mathrm{Re}\{Y_{lm}(\Omega)\} \qquad \text{where } \varepsilon(m) = \begin{cases} 1 & m = 0 \\ 1/2 & m \neq 0 \end{cases}$$

Therefore, after applying acceptance corrections to the "data" sample, we should find for the acceptance corrected coefficients:

$$t_{lm} = \begin{cases} N_{prod} \text{ for } & lm = 00 \\ 0 \quad \text{for } & lm \neq 00 \end{cases}$$

The equation above ignores statistical fluctuations. The values stated are the expected values in the limit of infinite statistics. For this sample, if the detector has perfect acceptance, and the selection criteria do not reject any of the "recorded" events, we expect the experimental moments $\{b_{lm}\}$ to be equal to the acceptance corrected moments $\{t_{lm}\}$. In the case that acceptance is not perfect, or the selection cuts reject part of the signal, but both detector acceptance and selection cuts leave the final state angular distribution unaltered, we still expect $b_{lm} = 0$ for $lm \neq 00$.

Therefore, for this test sample, it is easy to recognize if the detector alters the $\cos(\theta)$, φ distributions. We just look for deviations of experimental moments with $lm \neq 00$ from the nominal value $b_{lm\neq 00} = 0$. Figure 4.7 (spans two pages) presents the values of the experimental moments as a function of invariant mass for the intermediate meson (X). We use all allowed values of l,m up to $l_{\max}m_{\max} = 88$. Since $0 \leq m \leq l$ there are $(l_{\max}+1)(l_{\max}+2)/2 = 45$ experimental moments for this figure. We use a "standard" set of selection criteria, described in the figure legend. For b_{00} we see the accepted mass spectrum, which is the same as Figure 4.1.b. With the exception of $b_{lm=20}$ and $b_{lm=40}$ all $b_{lm\neq 00}$ are very close to the nominal value for the entire mass spectrum.

Since the detector acceptance and the selection criteria we use cause some of the moments to deviate from their nominal value, we can check if the method of moments allows us to recover the expected values for the acceptance corrected moments (t_{lm}). The results of the method are shown in Figures 4.8 and 4.9. In the first case (Figure 4.8) we allow the maximum possible number of coefficients ($l_{max}m_{max} = 88$). We use the same number of experimental and acceptance corrected moments. Therefore we find an exact solution and we do not have an over-constrained problem. In the second case (Figure 4.9), we limit the number of allowed acceptance corrected moments to $l_{max} = 4$, $m_{max} = 2$. The reason for the particular choices of upper limits will become apparent in the presentation of the amplitude analysis for the real data sample. We can see from Figures 4.8 and 4.9 that (within statistical errors) we restore the number of events produced, and the original angular distributions. In both cases t_{00} as a function of mass is consistent with a constant while all $t_{lm\neq 00}$ are consistent with zero.

We can quantify the "consistent with zero" statement using a formal χ^2 calculation. We use the plots of the acceptance corrected moments (t_{lm}) as a function of mass to perform a fit to a straight line. The slope is fixed to be equal to zero. Therefore we perform a fit to a constant and calculate the average value $\langle t_{lm} \rangle$ and the χ^2 associated with the fit. The χ^2 is defined as:

$$\chi^2_{lm} \equiv \frac{1}{N_{bins} - 1} \sum_{i=1}^{N_{bins}} \frac{\left(t_{lm}(i) - \langle t_{lm} \rangle\right)^2}{\sigma^2_{lm}(i)}$$

Where (i) notes the mass bin used. The average and χ^2 values are presented in Table 4.1. Although we are interested in the χ^2 of the acceptance corrected moments (t_{lm}) the table includes the same calculation for the experimental moments (b_{lm}). This allows us to compare how acceptance modifies the experimental moments from their nominal value. Note that the acceptance corrected t_{00} is close to twice the value of b_{00} which corresponds to detector acceptance close to 50%.

After demonstrating the validity of the method with the Monte Carlo sample, we can proceed to present the experimental and acceptance corrected moments for the detector data sample. We apply the same method and same selection cuts as in the case of the Monte Carlo example. We fit two sets of acceptance corrected moments (t_{lm}). The first set includes all possible t_{lm} up to $lm = 88$ (45 total). The second set is restricted to moments with $l \leq 4$, $m \leq 2$ (12 total). In both cases we limit the experimental moments to $l_{max} m_{max} = 88$. The results of the two fits are presented in Figures 4.12 and 4.13. The experimental moments (b_{lm}), common for the two fits, are shown in Figure 4.11.

We use a limited set of coefficients for the experimental (b_{lm}), and acceptance corrected (t_{lm}), moments expansions. The number of coefficients has to be limited, because it is not practical to work with very large sets of moments. To set the appropriate limits, we use the method with different sets of coefficients. We look at the resulting experimental and acceptance corrected moments, for cases where the moments are consistently equal to zero, throughout the mass spectrum. If both experimental and acceptance corrected moments are consistently equal to zero above a certain l or m value, we can set this value as the limit for both expansions. We can set separate limits for experimental and acceptance corrected moments. For the latter, it is sufficient to find that above certain values of l, or m, the acceptance corrected moments are consistently equal to zero. This is the case for the acceptance corrected moments plotted in Figure 4.12. We see that all moment with $l > 4$ or $m > 2$ are consistently zero. Therefore we are justified to use a limited set of acceptance corrected moments for the fit presented in Figure 4.13.

Unlike the Monte Carlo sample, the data sample is not uniformly distributed as a function of invariant mass. Because the number of events changes rapidly as a function of mass, it is difficult to see the relative values of the acceptance corrected moments. We remedy this problem in Figures 4.14 and 4.15, where we normalize the moments presented in Figures 4.12 and 4.13 with respect to t_{00}. For every mass bin we divide every t_{lm} with

the value of t_{00}. The errors are scaled the same way. Instead of plotting the error bar σ_{lm} we plot σ_{lm}/t_{00}. For the analysis of the angular distributions we are mostly interested in the relative values of the acceptance corrected moments. The relative values of the moments allow us to measure the relative intensities of states with different spin parity assignments. Our ability to measure relative values of acceptance corrected moments is limited by the statistical significance of the sample in the high invariant mass region. As can be seen from the values of b_{00} and t_{00}, the number of observed and produced events with mass above 1.5 GeV/c^2 is very small. From the "normalized to t_{00}" plots, we see that the errors in this region are very large. Therefore we do not have confidence in the values of t_{lm} for M_X>1.5 GeV/c^2. Furthermore, the small statistics do not allow one to apply the amplitude analysis successfully above 1.5 GeV/c^2.

A note on the relative statistics of the Monte Carlo "data" used for the example and the actual data used for the analysis. Although we use 2×10^6 generated events for this example, the statistics are much smaller than the statistics for the data sample. For the example, we generate events "flat" in the x_F region [-0.2,0.1]. The selection requirements restrict the x_F to [-0.1,0.0]. This requirement alone rejects 2/3 of the events. After the "standard" selection cuts 99×10^3 events survive and are used for the computation of experimental and acceptance corrected moments shown in the figures. The statistics is much better for the real data sample. For this calculation 635×10^3 events are used in the particular production bin. The small number of Monte Carlo events is not due to poor detector acceptance. Most events are rejected because they were not generated within the production bin we study. The ratio of the number of events used to the number of events produced for the particular production bin is 0.502, therefore the acceptance is about 50%.

4.5 Amplitudes Analysis for a Single Production Bin

The acceptance corrected moments provide a description of the produced event distribution. We use this distribution to determine the production amplitudes. As stated earlier, the produced distribution can be expresses as:

$$I_{prod}(x,\Omega) = (phase\ \ space)\sum_{h}|U_h|^2$$

The summation over the four helicity states of the final state protons is an external variable and final states of different helicity do not interfere. The incoherency of the different helicity terms makes the general problem unsolvable, because of the large number of degrees of freedom generated by four, in principle, independent sets of production amplitudes. We make a crucial assumption when we analyze the amplitudes:

> Either the production amplitude is independent of the final state proton helicities, or just one of the helicity states dominates in the production region where the interaction is studied.

In either case we have a single coherent term and we can write:

$$I_{prod}(x,\Omega) = |U|^2 = \sum_{\substack{l,l' \\ m,m'}} \mathrm{Y}^*_{lm}(\Omega)\alpha^*_{lm}(x)\alpha_{l'm'}(x)\mathrm{Y}_{l'm'}(\Omega)$$

where in the last step we let the phase space factors be absorbed in the amplitude expression. If we compare the last expression with the intensity distribution as a function of the acceptance corrected moments:

$$I_{prod}(\Omega) = \sum_{\substack{l \\ m\geq 0}} t_{lm}\,\mathrm{Re}\{\mathrm{Y}_{lm}(\Omega)\}$$

we see that we need to build a system of equations relating amplitudes to moments.

The first step in this procedure is to take advantage of parity conservation in the strong interaction and simplify the expression that defines the intensity distribution as a function of production amplitudes. For this analysis I follow an article by Chung and Trueman [52, 53, 54]. We define the production amplitudes using base states that are eigenstates of the reflectivity operator, instead of the usual spin operator $|lm\rangle$ base. The choice of the reflectivity basis is appropriate for this analysis, because it uses the parity conservation constraint to simplify the form of the density matrix. I should emphasize again that the base kets are defined in the Gottfried Jackson frame. The Jacob and Wick [51] helicity formalism used by Chung and Trueman is valid only in a coordinate system with the Y-axis perpendicular to the production plane. The operator is defined as the product of the parity operator and a rotation along the Y-axis:

$$\Pi_y \equiv Pe^{-i\pi J_y}$$

For a coordinate system where particle momenta lie in the X-Z plane (i.e. production plane), Π_y commutes with Lorentz transformations in the X-Z plane and rotations about the Y-axis. In such a coordinate system a particle with momentum $\vec{p}$, spin J, parity η, and spin projection along the momentum axis (helicity) λ is transformed by the reflectivity operator as:

$$\Pi_y|\vec{p}, J(\eta), \lambda\rangle = \eta(-1)^{J-\lambda}|\vec{p}, J(\eta), -\lambda\rangle$$

The procedure that relates states with definite helicity and states that are described by the usual spin operators and are at rest in the coordinate system ($\vec{p} = 0$) is given by Jacob and Wick. In our case, the state at rest is the intermediate meson (X). For the intermediate meson the reflectivity operator results in the transformation:

$$\Pi_y|0, J(\eta), m\rangle = \eta(-1)^{J-m}|0, J(\eta), -m\rangle$$

From now on we drop the $\vec{p} = 0$ momentum quantum number in the ket notation. We can define eigenstates of the reflectivity operator as:

$$|\varepsilon, J(\eta), m\rangle = \vartheta(m)\left[|\varepsilon, J(\eta), m\rangle - \varepsilon\eta(-1)^{J-m}|\varepsilon, J(\eta), -m\rangle\right] \quad \text{where} \quad \vartheta(m) = \begin{cases} 1/\sqrt{2}, & 0 < m \\ 1/2 & m = 0 \\ 0 & m < 0 \end{cases}$$

In our case, since we study decay into two pseudoscalar states, the parity quantum number is restricted to $\eta = (-1)^J$. Therefore we can simplify the definition:

$$|\varepsilon lm\rangle = \vartheta(m)\left[|lm\rangle - \varepsilon(-1)^m|l-m\rangle\right] \quad \text{where} \quad \vartheta(m) = \begin{cases} 1/\sqrt{2}, & 0 < m \\ 1/2 & m = 0 \\ 0 & m < 0 \end{cases}$$

For bosons, the eigenvalues of the reflectivity operator are $\varepsilon = \pm 1$. So instead of base functions (ordinary base, quantization along Z-axis):

$$|lm\rangle, \quad \text{where} \quad -l \le m \le l$$

we use base functions (reflectivity base):

$$|\varepsilon lm\rangle, \quad \text{where} \quad \varepsilon = +,- \text{ and } 0 \le m \le l$$

The new base functions introduce a new quantum number, the reflectivity $\varepsilon = +,-$, and restrict $0 \le m \le l$ to positive values only. As expected, the number of base states is the same for the ordinary and reflectivity bases. Instead of letting the spin projection quantum number span negative and positive values we have always $m \ge 0$, and the additional reflectivity quantum number gives the expected number of states. The $m = 0$ states are identical in both bases, and have reflectivity $\varepsilon = -$ in the reflectivity base.

The result is the separation of the production intensity into two incoherent terms, one for each reflectivity quantum number.

$$I_{prod}(x, \Omega) = |U|^2 = |A_+|^2 + |A_-|^2$$

Where the reflectivity amplitudes are:

$$A_\varepsilon = \sum_{\substack{l \\ 0 \le m \le l}}{}^{\varepsilon} a_{lm}(x)^{\varepsilon} Y_{lm}(\Omega)$$

The definition of the ${}^{\varepsilon}Y_{lm}(\Omega)$ is analogous to the definition of the reflectivity states:

$$ {}^{\varepsilon}Y_{lm}(\Omega) \equiv \vartheta(m)\left[\, Y_{lm}(\Omega) \;-\; \varepsilon(-1)^{m}\, Y_{l-m}(\Omega)\right] \quad \text{where} \quad \vartheta(m) = \begin{cases} 1/\sqrt{2}, & 0 < m \\ 1/2 & m = 0 \\ 0 & m < 0 \end{cases} $$

Here I repeat that use of the spherical harmonics instead of the general spin functions is due to the fact that the intermediate meson decays into two spinless particles.

The reason for the simplification can be best expressed in terms of the density matrix formalism. The parity conservation constraint restricts the density matrix:

$$ \rho^{ll'}_{mm'} = \langle l,m|\rho|l',m'\rangle = (-1)^{m-m'}\, \rho^{ll'}_{-m-m'} \quad \text{for ordinary base} \quad |lm\rangle,\ -l \le m \le l $$

$$ {}^{\varepsilon\varepsilon'}\rho^{ll'}_{mm'} = \langle \varepsilon,l,m|\rho|\varepsilon',l',m'\rangle = \delta_{\varepsilon\varepsilon'}\, {}^{\varepsilon\varepsilon'}\rho^{ll'}_{mm'} \text{ for reflectivity base } |\varepsilon lm\rangle, \quad \varepsilon = +,- \;\&\; 0 \le m \le l $$

Therefore, in the reflectivity base, parity conservation diagonalizes the density matrix with respect to the reflectivity quantum number:

$$ {}^{\varepsilon}\rho = \begin{pmatrix} {}^{(-)}\rho & 0 \\ 0 & {}^{(+)}\rho \end{pmatrix} $$

Thus there are no interference terms between states of different reflectivity. Proof of the relations outlined above can be found in Chung and Trueman [52].

Before outlining the method used for the determination of amplitudes, we state the number of parameters that need to be determined. It is obvious that we cannot solve the problem for an unlimited number of amplitudes. We use the observed acceptance corrected moments to limit the maximum number of amplitudes, therefore the number of acceptance corrected moments, that are allowed to enter the calculation. I will first present a simple counting of the number of parameters that must be determined, given a maximum spin value for the resonances observed in our sample. Then I will present the number of acceptance corrected moments necessary for the determination. To avoid confusion, in the

following I use different symbols for the indices of amplitudes and acceptance corrected moments. For amplitudes I use the lower case indices l,m (i.e. ${}^{\varepsilon}a_{lm}$), and for acceptance corrected moments upper case indices L,M (i.e. t_{LM}).

The number of amplitudes allowed, given a maximum spin quantum number $l_{\max}$, is $(l_{\max}+1)^2$. Because the amplitude is a complex number, the number of real parameters is $2(l_{\max}+1)^2$. From the form of the intensity formula, there are two arbitrary parameters that we cannot measure: the overall phases for the (−) and (+) reflectivity amplitudes. Therefore the number of measurable amplitude parameters is $2(l_{\max}+1)^2-2$. There is an exception to the last formula, the trivial case $l_{\max}=0$ for which only one arbitrary phase exists.

If we allow a maximum spin value $l_{\max}$, the maximum index for the acceptance corrected moments is $L_{\max}=2l_{\max}$. The last relation follows from the expansions of the intensity distribution $I(\Omega)$, as a function of amplitudes and acceptance corrected moments. The amplitude expansion involves products of Y_{lm}, while the moments expansion is linear in Y_{LM}. We have seen already that parity conservation restricts $0 \le M \le L$. Thus the number of moments necessary to describe the sample is
$(L_{\max}+1)(L_{\max}+2)/2=(2l_{\max}+1)(l_{\max}+1)$.

Given a maximum spin value ($l_{\max}$), the table below presents the number of real parameters needed to determine all amplitudes and the number of independent acceptance corrected moments measured:

maximum spin value ($l_{\max}$)	0	1	2	3	4
# of real amplitude parameters ($2(l_{\max}+1)^2-2$)	1	6	16	30	48
# of moments $(2l_{\max}+1)(l_{\max}+1)$	1	6	15	28	45

Thus using an upper limit for the number of spin states allows us to restrict the values of the amplitudes, but does not allow us to determine all amplitude parameters.

It is possible to restrict the number of amplitudes we consider by restricting m to values smaller than the $m \leq l$ constraint. Again, the relation between the amplitude and moments indices is $M_{max} = 2m_{max}$. Looking at the acceptance corrected moments in Figure 4.12 we see that we can set $M_{max} = 2$, which corresponds to $m_{max} = 1$. Now the number of amplitudes is reduced to $1 + 3l_{max}$, and the number of real parameters we can determine to $2(1 + 3l_{max}) - 2 = 6l_{max}$. The number of moments is equal to $1 + 2 + 3(L_{max} - 1) =$ $= 3L_{max} = 6l_{max}$. The exception mentioned earlier for the trivial case $l_{max} = 0$ is valid for the formulas presented here also. Now the table of parameters becomes:

maximum spin value (l_{max})	0	1	2	3	4
# of real amplitude parameters ($6l_{max}$)	1	6	12	18	24
# of moments ($6l_{max}$)	1	6	12	18	24

For the determination of the appropriate limits of L and M we look at the acceptance corrected moments distributions. In Figure 4.12 we allow all possible L and M up to $LM = 88$. We see that all t_{LM} with $L > 4$ are consistent with zero. There are deviations near threshold, but they are very small when compared to the value of t_{00}. In addition, for all values of L, all t_{LM} with $M > 1$ are consistent with zero. So we proceed with the second significant assumption in our study :

We restrict the amplitudes to $l \leq 2$ and $m \leq 1$.

All amplitudes that do not satisfy the limits above are assumed to be exactly zero. The statement above is just an approximation. We do not measure with infinite precision, therefore we cannot rule out the presence of amplitudes outside the limits we just defined. The plots of the acceptance corrected moments assure us that if such amplitudes exist, they

are sufficiently small that they do not alter the determination the dominant amplitudes. The above limits are driven by the data set and apply for particular region of the production variables for which the acceptance corrected moments were computed. Thus if the kinematic region of the analysis changes, a new determination of the L, M range is required.

With this restriction in mind we can proceed to define the method we use to determine the amplitudes from the acceptance corrected moments. The amplitudes we are going to determine (including the spectroscopic notation) are:

${}^{-}a_{00}$	${}^{-}a_{10}$	${}^{-}a_{20}$	${}^{-}a_{11}$	${}^{-}a_{21}$	${}^{+}a_{11}$	${}^{+}a_{21}$
S_0	P_0	D_0	P_-	D_-	P_+	D_+

For this analysis I use a method developed by S.U. Chung [53,54]. We first write the dependence of amplitudes and acceptance corrected moments in terms of the angle φ. In terms of the experimental moments the intensity can be written as:

$$I_{prod}(\Omega) = \sum_{\substack{l\le 2 \\ 0\le m\le l}} t_{lm}\,\mathrm{Re}\{Y_{lm}(\Omega)\} = f_0(\theta) + 2f_1(\theta)\cos\varphi + 2f_2(\theta)\cos 2\varphi$$

in terms of the amplitudes:

$$I_{prod}(x,\Omega) = |A_-|^2 + |A_+|^2 = \left|h_0(\theta) + \sqrt{2}h_-(\theta)\cos\varphi\right|^2 + \left|\sqrt{2}h_+(\theta)\sin\varphi\right|^2$$

Comparing the two expressions:

$$f_0(\theta) = |h_0(\theta)|^2 + |h_-(\theta)|^2 + |h_+(\theta)|^2$$
$$f_1(\theta) = \sqrt{2}\,\mathrm{Re}\{h_0(\theta)h_-^*(\theta)\}$$
$$f_2(\theta) = \frac{1}{2}\left\{|h_-(\theta)|^2 - |h_+(\theta)|^2\right\}$$

The functions $f_0(\theta), f_1(\theta), f_2(\theta)$ are the sum of well defined products of the acceptance corrected moments and Legendre polynomials. The functions $h_0(\theta), h_-(\theta), h_+(\theta)$ are the sum of products of Legendre polynomials and the amplitudes we seek to determine. We can eliminate dependence on the $h_+(\theta)$ amplitude sum:

$$f_a(\theta) \equiv f_0(\theta) + 2f_2(\theta) = |h_0(\theta)|^2 + |\sqrt{2}h_-(\theta)|^2$$
$$f_b(\theta) \equiv \quad 2f_1(\theta) \quad = 2\,\mathrm{Re}\{h_0(\theta)\sqrt{2}h_-^*(\theta)\}$$

The next step is to define the complex function:

$$g(\theta) \;= \frac{1}{\sqrt{2}}\{h_0(\theta) + \sqrt{2}h_-(\theta)\}$$
$$g(-\theta) = \frac{1}{\sqrt{2}}\{h_0(\theta) - \sqrt{2}h_-(\theta)\}$$

The relation between $g(\theta)$ and $g(-\theta)$ owes to the symmetry properties of the Legendre polynomials that result in: $h_0(-\theta) = h_0(\theta)$, $h_\pm(-\theta) = -h_\pm(\theta)$. It is easy to show that the function $g(\theta)$ has the property:

$$\left.\begin{aligned} f_a(\theta) &= |g(\theta)|^2 + |g(-\theta)|^2 \\ f_b(\theta) &= |g(\theta)|^2 - |g(-\theta)|^2 \end{aligned}\right\} \quad \Rightarrow \quad 2|g(\theta)|^2 = f_a(\theta) + f_b(\theta)$$

With the last relation it becomes clear why $g(\theta)$ was defined. We use expressions of the acceptance corrected moments functions ($f-$ *functions*), and the amplitude functions ($h-$ *functions*), in terms of $g(\theta)$. Notice that the complex polynomial $g(\theta)$ relates to acceptance corrected moments ($f-$ *functions*) as a modulo squared, while it has a linear relationship to the amplitudes ($h-$ *functions*). We proceed to determine $g(\theta)$ through the acceptance corrected moments, and use it to build a system of linear equations for the amplitudes we seek to determine. In addition, we use $g(\theta)$ to identify the ambiguities (number of different, consistent solutions) in the problem. After $g(\theta)$ and $h_0(\theta)$, $h_-(\theta)$ are determined we can find $h_+(\theta)$ from:

$$f_2(\theta) = \frac{1}{2}\{|h_-(\theta)|^2 - |h_+(\theta)|^2\} \quad \Rightarrow \quad |h_+(\theta)|^2 = |h_-(\theta)|^2 - 2f_2(\theta)$$

First I am going to present the explicit formalism used for the determination of the negative reflectivity amplitudes. After the explicit relations give us a feeling for the method, I present the ambiguities of the problem and the number of consistent solutions we can find. In order to examine the ambiguities in the problem, it is necessary to express all

functions as polynomials in a single variable. We accomplish this with a change of variable:

$$u = \tan\frac{\theta}{2} \quad \Rightarrow \quad \cos\theta = \frac{1-u^2}{1-u^2} \quad \text{and} \quad \sin\theta = \frac{2u}{1-u^2}$$

With the change in variable ($\theta \rightarrow u$) it is convenient to replace the $Y_{LM}(\Omega)$ dependence on the functions $d^L_{M'0}(\theta)$ with a new set of functions $e^L_{M'0}(\theta)$:

$$d^L_{M',M}(\theta) = \left(\cos\frac{\theta}{2}\right)^{2L} e^L_{M',M}\left(\tan\frac{\theta}{2}\right) = \frac{1}{\left(1+u^2\right)^L} e^L_{M',M}(u)$$

Then we can express the $f-$ *functions* in terms of acceptance corrected moments using:

$$\left(1+u^2\right)^4 \frac{1}{\varepsilon(M)} f_M(u) = \sum_{l=0,4} \sqrt{2L+1}\, t_{LM} \left(1+u^2\right)^{4-L} e^L_{M'0}(u) \quad \text{where } \varepsilon(m) = \begin{cases} 1 & m=0 \\ 1/2 & m \neq 0 \end{cases}$$

The functions $e^L_{M'0}(u)$ can be found in the S.U. Chung preprint [54]. Here I note that the $e^L_{M',M}(u)$ are polynomials of order $L-M'$. Therefore the product $\left(1+u^2\right)^4 \frac{1}{\varepsilon(M)} f_M(u)$ is a polynomial in u of order $2L_{\max} = 8$. We can construct the polynomial $G(u)$:

$$G(u) \equiv \left(1+u^2\right)^2 \sqrt{2} g(u) = a_4 u^4 - a_3 u^3 + a_2 u^2 - a_1 u + a_0$$

from the complex roots of the polynomial:

$$|G(u)|^2 = \left(1+u^2\right)^4 2|g(u)|^2 = \left(1+u^2\right)^4 \{f_a(u) + f_b(u)\} =$$
$$= \left(1+u^2\right)^4 f_0(u) + \left(1+u^2\right)^4 2 f_1(u) + \left(1+u^2\right)^4 2 f_2(u)$$

The explicit dependence on the acceptance corrected moments is:

$$\begin{aligned}
\left(1+u^2\right)^4 f_0(u) = \{ & \; t_{00} & -\sqrt{3}t_{10} & +\sqrt{5}t_{20} & -\sqrt{7}t_{30} & +3t_{40} \}u^8 \\
+ \{ & 4t_{00} & -2\sqrt{3}t_{10} & -2\sqrt{5}t_{20} & +8\sqrt{7}t_{30} & -48t_{40} \}u^6 \\
+ \{ & 6t_{00} & & -6\sqrt{5}t_{20} & & +108t_{40} \}u^4 \\
+ \{ & 4t_{00} & +2\sqrt{3}t_{10} & -2\sqrt{5}t_{20} & -8\sqrt{7}t_{30} & -48t_{40} \}u^2 \\
+ \{ & \; t_{00} & +\sqrt{3}t_{10} & +\sqrt{5}t_{20} & +\sqrt{7}t_{30} & +3t_{40} \}
\end{aligned}$$

$$
\begin{aligned}
(1+u^2)^4 2f_1(u) = \{ & -\sqrt{6}t_{11} \quad +\sqrt{30}t_{21} \quad -2\sqrt{21}t_{31} \quad +6\sqrt{5}t_{41}\}u^7 \\
+\{ & -3\sqrt{6}t_{11} \quad +\sqrt{30}t_{21} \quad +4\sqrt{21}t_{31} \quad -36\sqrt{5}t_{41}\}u^5 \\
+\{ & -3\sqrt{6}t_{11} \quad -\sqrt{30}t_{21} \quad +4\sqrt{21}t_{31} \quad +36\sqrt{5}t_{41}\}u^3 \\
+\{ & -\sqrt{6}t_{11} \quad -\sqrt{30}t_{21} \quad -2\sqrt{21}t_{31} \quad -6\sqrt{5}t_{41}\}u
\end{aligned}
$$

$$
\begin{aligned}
(1+u^2)^4 2f_2(u) = \{ & \sqrt{30}t_{22} \quad -\sqrt{21}\sqrt{10}t_{32} \quad +9\sqrt{10}t_{42}\}u^6 \\
+\{ & 2\sqrt{30}t_{22} \qquad\qquad\qquad -24\sqrt{10}t_{42}\}u^4 \\
+\{ & \sqrt{30}t_{22} \quad +\sqrt{21}\sqrt{10}t_{32} \quad +9\sqrt{10}t_{42}\}u^2
\end{aligned}
$$

Assuming that we can construct the polynomial $G(u)$ from the values of the acceptance corrected moments, we can use:

$$G(u) = (1+u^2)^2 \sqrt{2} g(u) = (1+u^2)^2 \{h_0(\theta) + \sqrt{2} h_-(\theta)\}$$

to find a set of linear equations relating the coefficients of $G(u)$ and the production amplitudes. As was the case for the $f-$*functions*, we can express the $h-$*functions* in terms of $e^L_{M0}(\theta)$:

$$h_0(u) = \frac{\sum_{l=0,2} \sqrt{2l+1}\ {}^{-}a_{l0} (1+u^2)^{2-l} e^l_{00}(u)}{(1+u^2)^2}$$

$$h_-(u) = \frac{\sum_{l=1,2} \sqrt{2l+1}\ {}^{-}a_{l1} (1+u^2)^{2-l} e^l_{10}(u)}{(1+u^2)^2}$$

$$h_+(u) = \frac{\sum_{l=1,2} \sqrt{2l+1}\ {}^{+}a_{l1} (1+u^2)^{2-l} e^l_{10}(u)}{(1+u^2)^2}$$

The result (in spectroscopic notation) is:

$$(1+u^2)^2 h_0(u) = S_0(1+u^2)^2 + \sqrt{3}P_0(1-u^4) + \sqrt{5}D_0(1-4u^2+u^4)$$

$$\sqrt{2}(1+u^2)^2 h_-(u) = -2\sqrt{3}P_-(u+u^3) - 2\sqrt{15}D_-(u-u^3)$$

$$\sqrt{2}(1+u^2)^2 h_+(u) = -2\sqrt{3}P_+(u+u^3) - 2\sqrt{15}D_+(u-u^3)$$

Expressing $G(u)$ as a function of the amplitudes we find:

$$\left.\begin{aligned} a_4 &= S_0 - \sqrt{3}P_0 + \sqrt{5}D_0 \\ a_3 &= 2\sqrt{3}P_- - 2\sqrt{15}D_- \\ a_2 &= 2S_0 - 4\sqrt{5}D_0 \\ a_1 &= 2\sqrt{3}P_- + 2\sqrt{15}D_- \\ a_0 &= S_0 + \sqrt{3}P_0 + \sqrt{5}D_0 \end{aligned}\right\} \quad \Rightarrow \quad \begin{aligned} 6S_0 &= 2a_0 + a_2 + 2a_4 \\ 2\sqrt{3}P_0 &= a_0 - a_4 \\ 6\sqrt{5}D_0 &= a_0 - a_2 + a_4 \\ 4\sqrt{3}P_- &= a_1 + a_3 \\ 4\sqrt{15}D_- &= a_1 - a_3 \end{aligned}$$

After the negative reflectivity amplitudes are determined we can follow the same procedure for the determination of the two positive reflectivity amplitudes P_+, D_+.

Although in the solution outlined above it looks as if we find definite phases for the five negativity amplitudes, this is not true. There is an arbitrary phase in the determination of the polynomial $G(u)$. This will become clear as we proceed to present the multiple amplitude solutions we can find, given a set of acceptance corrected moments.

In order to count the number of consistent solutions we start with the order of the polynomial:

$$|G(u)|^2 = (1+u^2)^4\{f_0(u) + 2f_1(u) + 2f_2(u)\} = \sum_{k=0,2L_{max}} (-1)^k a'_k u^k$$

The fact that: $|G(u)|^2$ is a polynomial in u of order $2L_{max}$=8 is guaranteed by the form of the $f-functions$. There is no guarantee that for an arbitrary set of acceptance corrected moments the polynomial can be written as a modulo squared of a complex polynomial of order L_{max}. For now we assume this to be the case, and write the polynomial:

$$G(u) = (1+u^2)^{L_{max}}\sqrt{2}g(u) = c_0\prod_{k=1}^{L_{max}}(u-u_k) = \sum_{k=1}^{L_{max}}(-1)^k a'_k u^k$$

where c_0 is a complex constant and u_k are the complex roots of the polynomial. These are the so called "Barrelet zeros". From $|G(u)|^2 = \sum_{k=0,2L_{max}} (-1)^k a'_k u^k$ we find eight roots. If our hypothesis is correct, we find pairs of roots, where if u_i is a root u_i^* is a root also. We use

L_{max} unique roots to construct the polynomial $G(u) = \sum_{k=1}^{L_{max}} (-1)^k a_k u^k$. For our case ($L_{max}$=4), the explicit construction is:

$$a_4 = \sqrt{a_8'}$$
$$a_3 = a_4(u_1 + u_2 + u_3 + u_4)$$
$$a_2 = a_4(u_1u_2 + u_1u_3 + u_1u_4 + u_2u_3 + u_2u_4 + u_3u_4)$$
$$a_1 = a_4(u_1u_2u_3 + u_2u_3u_4 + u_3u_4u_1 + u_4u_1u_2)$$
$$a_0 = a_4u_1u_2u_3u_4$$

We can immediately see the arbitrary choices that can give multiple solutions. First, there is an arbitrary phase in the definition of a_4. This will result in an arbitrary overall phase for the amplitudes we determine. Second, we can arbitrarily pick from the four pairs of solutions for $|G(u)|^2$ either root u_i or root u_i^*. There are $2^{L_{max}}$ ways to define the set of roots we use for the definition of $G(u)$. Since a set of solutions $\{u_1, u_2, \ldots u_{L_{max}}\}$ and the complex conjugate set $\{u_1^*, u_2^*, \ldots u_{L_{max}}^*\}$ gives the same solution ($G(u)$ versus $G^*(u)$), there are $2^{L_{max}-1}$ unique negative reflectivity solutions to the problem. Therefore in our case (L_{max}=4) we expect 8 unique solutions.

As mentioned earlier, if we use the negative reflectivity solution to determine the reflectivity (+) amplitudes. Since $|h_+(\theta)|^2 = |h_-(\theta)|^2 - 2f_2(\theta)$, we first check if for the negative reflectivity amplitudes give $|h_-(\theta)|^2 - 2f_2(\theta) \geq 0$. If not, the particular solution is eliminated from the list of acceptable solutions. Otherwise we define a new $G(u)$ polynomial that obeys:

$$|G(u)|^2 = |h_-(\theta)|^2 - 2f_2(\theta)$$

$$G(u) = (1+u^2)^{L_{max}} h_+(u) = c_0 \prod_{k=1}^{L_{max}} (u - u_k)$$

Here there is a significant difference that reduces the number of distinct solutions. From the definition of the functions $e^{l}_{m0}(u)$

$$e^{l}_{m0}(u) = \frac{(-1)^m}{l!\sqrt{(l+m)!(l-m)!}} u^m \sum_{k=0}^{l-m} \frac{(-1)^k u^{2k}}{(l-m-k)!(l-k)!(m+k)!k!}$$

and the expression of $h_+(u)$ in terms of the functions $e^{l}_{m0}(u)$, we find that there is always a trivial solution u=0. The reason for this is that for all terms of the sum that defines $h_+(u)$, m=1. If we write the positive reflectivity polynomial as $\left(1+u^2\right)^{l_{max}} h_+(u) = u\sum_{k=0}^{l_{max}-1} a_k u^k$, the form of $e^{l}_{m0}(u)$ allows only terms with k even (recall that $L_{max} = 2l_{max}$). Therefore we can rewrite the positive reflectivity polynomial as:

$$G(u) = \left(1+u^2\right)^{l_{max}} h_+(u) = c_0 u \prod_{k=1}^{l_{max}-1}\left(u^2 - r_k\right)$$

So for each root we have the additional symmetry that if u is a valid solution $-u$ is also a valid solution. There are $l_{max}-1$ unique r_k roots. Considering that the complex conjugate is also a root, there are $2^{l_{max}-2}$ ways to define the set of roots that we use for the definition of $G(u)$ (assuming $l_{max} \geq 2$). For the case considered here $l_{max} = 2$. Thus there is at most one reflectivity (+) set of amplitudes for each reflectivity (-) set.

In conclusion the maximum number of valid solutions per production bin is eight. The problem of identifying any one of the eight solutions as the most probable solution is going to be addressed at the same time we present a procedure to relate solutions across production variable bins.

It was mentioned earlier that there is no guarantee that we can find a complex polynomial $G(u)$, such that its modulo squared ($|G(u)|^2$) is equal to the polynomial defined by the acceptance corrected moments (t_{LM}). Such a constraint does not exist in the fitting procedure that determines the acceptance corrected moments. Statistical fluctuations can "move" the ideal set of t_{LM} we could obtain using unlimited statistics to a set for which no

amplitude solution exists. We estimate the effect of statistical fluctuations by repeatedly regenerating sets of t_{LM}, distributed according to the error matrix $E(t)$. For each new set of acceptance corrected moments we repeat the amplitude analysis and if a solution is found we keep it in a data file. This procedure has the additional benefit of allowing us to determine how the statistical errors of the t_{LM} propagate to the amplitude solutions. The statistical method we use to determine the acceptance corrected moments, t_{LM}, also provides their statistical correlations through the error matrix $E(t)$. In order to generate randomly a new set of t_{LM} that exhibits the same statistical behavior (correlations) we have to define a unitary transformation that diagonalizes the error matrix $E(t)$. The diagonal matrix is the error matrix of a multivariable Gaussian with 12 independent variables. We generate a new set of parameters according to this multivariable Gaussian distribution. In other words we throw 12 random numbers, each one distributed according to a Gaussian with sigma equal to the square root of the corresponding element of the diagonal matrix. We use the unitary transformation to "rotate" each set of 12 independent variables, to a set of t_{LM} that exhibit the proper statistical behavior. In matrix notation the relation between the diagonal matrix $G(\sigma^2)$ and the error matrix $E(t)$ is:

$$E(t) = U\, G(\sigma^2)\, U^T$$

We use standard matrix diagonalization techniques to determine U. The relation between each set of Gaussian distributed, independent parameters (g_{LM}), to a new set of properly correlated acceptance corrected moments (t_{LM}), is given by:

$$t_{LM} = U\, g_{LM}$$

4.6 Amplitudes Analysis Across Production Bins

In the previous section we presented procedures that use the angular distribution of the final state pions to determine the amplitudes of the intermediate meson (X). We do not

make any attempt to correlate the multiple solutions along production bins. In order to present the amplitude as a function of the production variables (e.g. invariant mass) we need a method to relate the solutions across production variable bins. We demonstrated that the number of distinct solutions per bin is between zero and eight. Since we "throw" the acceptance corrected moments multiple times for each production bin, we find multiple sets of solutions per bin. Each one of the solution sets contains anywhere between zero and eight distinct solutions.

We proceed to present a method that allows us to label each one of the eight solutions. We can use this label to relate distinct solutions across production bins (e.g. across bins of invariant mass). In order to identify such a label we have to look at the roots of the polynomial $|G(u)|^2$ (the polynomial we use for amplitude determination, see section 4.5), and see how the complex roots evolve as a function of the production variables. It can be proven that the roots (the so called Barrelet zeros) trace a continuous trajectory as a function of production variables in the complex plane [55]. Thus we identify the solutions through their trajectory. It can also be proven that the trajectory is continuous and unique as long as it does not cross the real axis. If the root trajectory crosses the real axis, it bifurcates and there is more than one way to continue the solution on the complex plane. We will show that for the particular sample we study, in the production region where we perform the study, there is no crossing of the real axis. Because we "rethrow" the acceptance corrected moments for each analysis bin, we can find multiple sets of roots and have the additional benefit of a statistical interpretation of the study.

Figure 4.16 shows all roots found as a function of invariant mass for the selection cuts specified in the figure. As mentioned earlier, the eight roots of the polynomial $|G(u)|^2$ come in pairs. If u_k is a root, then u_k^* is also a root. In Figure 4.16 we plot only the roots that have positive imaginary part (four out of eight). We plot the roots only if at least one

out of a maximum of eight amplitude solutions was found. The number of entries per figure is the product of:

-- # of roots, equal to 4

-- # of mass bins within the mass range we plot, in this case 5

-- # of times we "throw" the t_{lm}, and find at least one amplitude solution. For this figure we "throw" the t_{lm} 100 times, therefore we expect this number to be anywhere between 0 and 100.

The resulting number of entry points per plot is between 0 and 2000. Except for the mass region $0.3 < M_X < 0.5\ GeV/c^2$ there are four very clear clusters where the entries concentrate. Because the root trajectories are restricted to small regions on the complex plane, we can use the regions to label the roots. Labeling the roots is equivalent to labeling the amplitude solutions. The procedure we use to identify the roots is:

-- Read the phases of all four roots. Of the eight roots I pick four with positive imaginary part.

-- If two roots in $[\,0\,,\pi/2\,]$ and two roots in $[\,\pi/2,\ \pi\,]$ save the indices. Otherwise tag the solution as unacceptable and reject the solution. Except near threshold all solutions have two roots per quadrant.

-- I tag the root pairs as

$[\ 0\ ,\pi/2\,] \rightarrow$ roots u_1 & u_4

$[\,\pi/2,\ \pi\ ] \rightarrow$ roots u_2 & u_3

I use the modulo of the roots to tag roots within the pair. The conditions are:

$[\ 0\ ,\pi/2\,]\quad u_1 < u_4$

$[\ 0\ ,\pi/2\,]\quad u_2 > u_3$

The root labels are also shown in Figure 4.16. We now use the labeled roots to assign labels for the multiple amplitude solutions:

Solution #	Roots combination
1	u_1, u_2, u_3, u_4
2	u_1^*, u_2, u_3, u_4
3	u_1, u_2^*, u_3, u_4
4	u_1, u_2, u_3^*, u_4
5	u_1, u_2, u_3, u_4^*
6	u_1^*, u_2^*, u_3, u_4
7	u_1^*, u_2, u_3^*, u_4
8	u_1^*, u_2, u_3, u_4^*

It is easy to see from Figure 4.16 that the number of times we find valid amplitude solutions is related to the statistical significance of the sample. The number of entries for mass regions above 1 GeV/c^2 is much smaller than in the mass regions below 1 GeV/c^2, and only a few entries can be seen above 1.5 GeV/c^2.

In Figure 4.17 we plot the modulo of all valid amplitude solutions as a function of mass. In Figure 4.18 we present the same plots for only one of the eight amplitude solutions (solution #6). This is a clear demonstration that we can identify and label the solutions following the trajectory of the polynomial roots on the complex plane. We see a continuous distribution as a function of mass and no "jumping" between solutions.

Of the eight solutions shown in Figure 4.17 we select #6 as the most probable to correspond to the produced amplitudes. We expect the dominant amplitude near threshold to be the lowest energy configuration, namely S-wave. We select the solution that has the highest S-wave module in the first 10 mass bins (first 400 MeV/c^2). As can be seen in Figure 4.17 and 4.18 there is a clearly separable solution satisfying this criterion (solution #6). Since we are able to identify and follow the solution as a function of mass through the complex roots of the polynomial, we can select one of the eight solutions for the whole mass spectrum.

Figure 4.18 presents the modulo of the amplitudes found for solution # 6 as a superposition of all solutions found and labeled #6, after throwing the acceptance corrected moments (t_{lm}) multiple times. Instead of plotting multiple entries, we can plot the average and the associated variance. This is done in Figure 4.19. For this figure instead of amplitude ($|^{\varepsilon}a_{lm}|$) we plot amplitude squared ($|^{\varepsilon}a_{lm}|^2$). The reason for plotting the amplitude squared is that it makes comparison with the t_{lm} plots easier. There is a simple relation between the number of events per bin (equal to t_{00}) and the amplitudes squared:

$$t_{00} = |S_0|^2 + |P_0|^2 + |D_0|^2 + |P_-|^2 + |D_-|^2 + |P_+|^2 + |D_+|^2$$

So a loose interpretation would be that the modulo squared is equal to the number of events per wave. We should not take that analogy too far because it ignores interference effects.

From Figure 4.19 it is obvious that S-wave production dominates for the particular region of the production variable where we carry the analysis. Because the number of events per bin decreases rapidly after 1 GeV/c^2, it is difficult to see the relative values of waves in the high mass region. Figure 4.20 presents the same waves normalized to $|S_0|^2$. We can see large modulie in the region above 1 GeV/c^2, for the D_0, P_+, D_+ waves where the well known $f_2(1270)$ resonance is expected, but they are small compared to $|S_0|^2$. For Figures 4.19 and 4.20 we use the restriction $p_{t,f}^2, p_{t,s}^2 < 0.1\,(GeV/c)^2$. Figures 4.21 and 4.22 use the same cuts, except that now we look at events with high transverse momentum for the fast proton ($p_{t,f}^2 > 0.1\ (GeV/c)^2$). As expected the S-wave is not as dominant in this figure. In particular in Figure 4.22 we observe a very clear $f_2(1270)$ signal in the D_0 wave.

A final consistency check is presented in Figures 4.23 to 4.26. We compare the acceptance corrected distributions estimated from detector events selected with different Cherenkov identification criteria. In the first case we require that both particles reconstructed in the multiparticle spectrometer are tagged by the Cherenkov counter as pion compatible. In the second case we impose the additional requirement that at least one of the

two particles is tagged by the Cherenkov counter as "exactly pion" (incompatible with any other assignment). The comparison tests both our ability to correct for angular acceptance and the significance of missidentified events. For example events that correspond to central production of K^+K^- are excluded from the second sample. We judge the acceptance corrected distributions looking at the acceptance corrected moments (t_{lm}). In Figure 4.23 we superimpose the results obtained from the two samples. In the first case (boxes) we require just "soft" Cherenkov identification. In the second case (crosses) we add the requirement that at least one of the two particles is "exactly pion". Figure 4.24 presents the t_{lm} values plotted in Figure 4.23, for the mass region [1.1,1.9] GeV/c^2 only. For both Figures (4.23, 4.24) we require low p_t^2 for the fast (beam) proton (p_t^2<0.1 (GeV/c)^2). Figures 4.25 and 4.26 are identical to 4.23 and 4.24 except for the fast proton p_t^2 requirement (here p_t^2>0.1 (GeV/c)^2). In all four plots we observe very good agreement between samples isolated with different selection criteria. We see that there is a scale difference (estimation of overall number of events produced) that decreases as the invariant mass of the intermediate meson (X) increases. Despite the scale difference the acceptance corrected angular distributions (reflected in the relative values of the t_{lm}) are consistent for the two Cherenkov identification criteria. We attribute the scale difference to large acceptance corrections necessary near the x_F=-0.1 region. We can see from Figure 4.2 that detector acceptance improves as the mass of the intermediate meson (X) increases.

Table 4.1. Results from one parameter fits of the expansion coefficients as a function of mass. We perform the fits for three sets of coefficients: experimental moments (b_{lm}), and two sets of acceptance corrected moments (t_{lm}). The χ^2 is defined as: $\chi^2_{lm} \equiv \frac{1}{N_{bins}-1}\sum_{i=1}^{N_{bins}} \frac{\left(t_{lm}(i)-\langle t_{lm}\rangle\right)^2}{\sigma^2_{lm}(i)}$. Plots of the results are shown in figure 4.10.

	experimental moments (b_{lm})		acceptance corrected moments (t_{lm}) using all l,m allowed.		acceptance corrected moments (t_{lm}) using $l \le 4,\ m \le 2$	
l,m	average	χ^2	average	χ^2	average	χ^2
0,0	2000.837	24.208	4013.755	1.872	3869.000	1.302
1,0	79.286	2.885	18.184	0.807	3.306	0.579
1,1	-21.510	0.679	-7.796	1.286	-12.327	1.090
2,0	-649.367	28.547	5.245	1.601	-85.755	1.070
2,1	118.959	2.454	-2.245	1.078	31.367	0.914
2,2	-7.551	1.023	-6.755	1.243	-17.061	1.194
3,0	-53.816	2.656	55.531	1.249	16.388	0.908
3,1	14.347	0.942	-37.367	1.230	-47.490	0.877
3,2	4.143	0.834	4.408	1.103	15.367	1.018
3,3	9.204	0.865	21.878	0.844		
4,0	-74.408	5.355	32.020	1.542	-13.408	1.475
4,1	34.388	1.107	26.918	1.178	43.796	1.388
4,2	-1.020	1.083	49.245	1.217	22.224	0.870
4,3	-1.755	1.164	-12.551	1.676		
4,4	0.388	0.839	5.939	0.999		
5,0	13.633	1.110	60.694	1.295		
5,1	2.306	1.297	2.327	1.655		
5,2	-2.653	0.903	-24.837	1.263		
5,3	10.837	1.011	33.592	1.248		
5,4	0.469	0.967	28.918	1.234		
5,5	-2.000	1.281	-0.224	1.397		
6,0	5.388	1.485	4.143	1.564		
6,1	-4.122	1.176	22.224	1.318		
6,2	1.469	1.515	17.714	1.531		
6,3	-9.347	1.101	-55.367	1.611		
6,4	-4.673	1.089	-4.388	1.301		
6,5	6.265	1.510	-10.959	1.044		
6,6	-38.306	1.162	-9.837	1.081		
7,0	0.857	1.279	42.041	1.458		
7,1	2.265	1.144	4.653	1.895		
7,2	7.878	1.350	14.122	1.375		
7,3	-1.714	1.273	30.061	2.009		
7,4	-7.592	1.247	-0.224	1.317		
7,5	15.959	1.003	-10.061	1.268		
7,6	-23.490	1.292	15.796	0.987		
7,7	45.959	1.507	16.061	1.110		
8,0	14.347	1.299	-6.490	1.385		
8,1	-5.347	1.134	38.816	1.248		
8,2	3.327	0.910	10.224	1.178		
8,3	3.224	1.131	-6.939	1.887		
8,4	0.122	1.177	43.653	1.330		
8,5	0.224	0.779	-11.469	0.805		
8,6	2.735	1.004	-9.449	1.429		
8,7	-1.306	1.105	-21.898	1.390		
8,8	-20.224	1.087	-20.980	1.355		

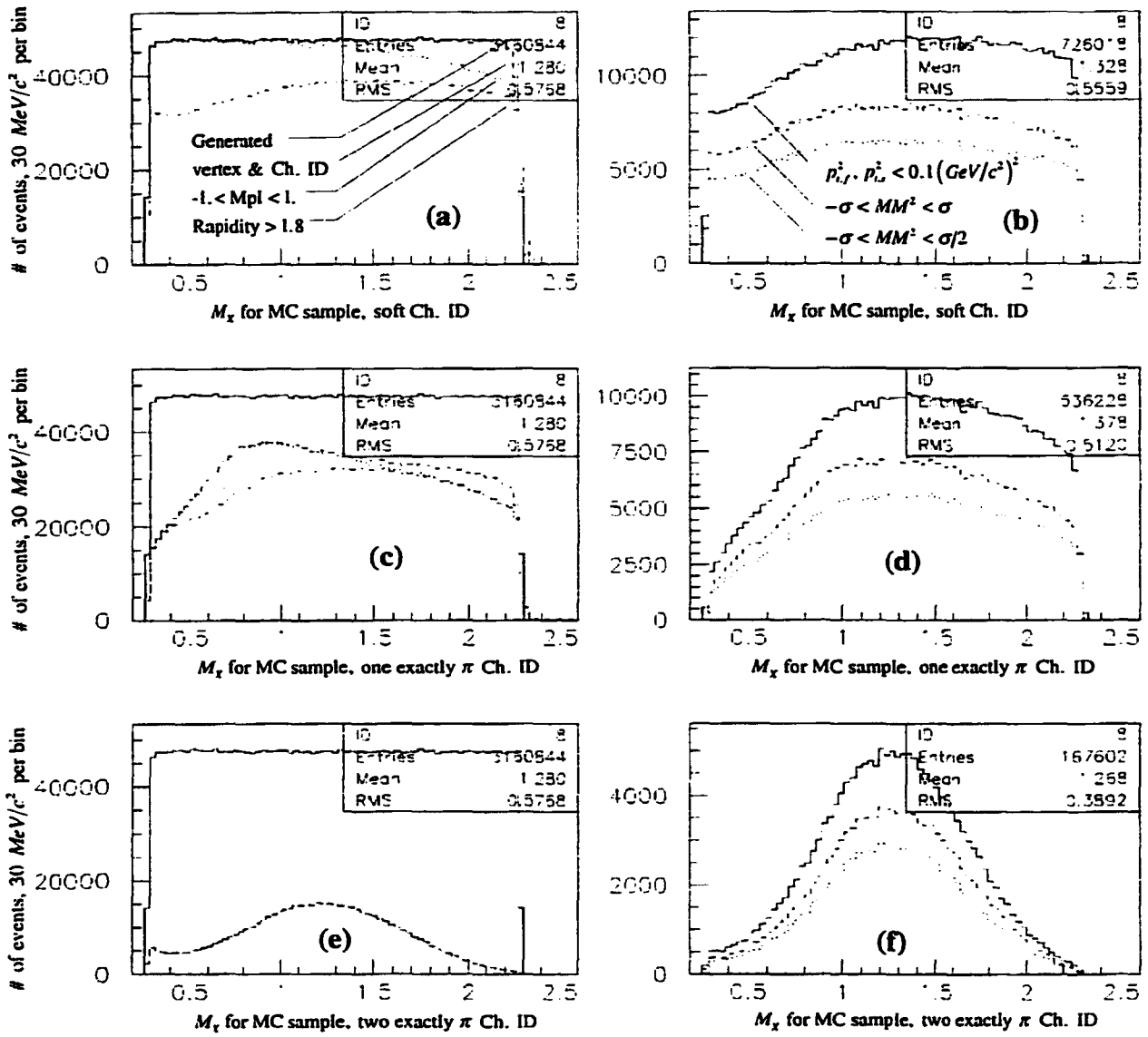

Figure 4.1 Acceptance as a function of mass for central meson (X), x_F in the interval [-0.1,0.0]. We plot the generated and reconstructed mass spectrum.

(a) -- Generated events.
-- Reconstructed events satisfying Vertex requirements and two (Cherenkov) pion compatible tracks in multiparticle spectrometer.
-- -1<MPl<1 GeV/c.
-- Rapidity gap>1.8 between the slow proton and any one of the two pions.

(b) -- $p_{t,f}^2, p_{t,s}^2 < 0.1\,(GeV/c)^2$. -- $-\sigma < MM^2 < \sigma$. -- $-\sigma < MM^2 < \sigma/2$

(c), (d) Same as (a), (b) except for Cherenkov identification. Here we require that at least one of the multiparticle spectrometer particles be identified as "exactly pion".

(d), (e) Same as (a), (b) except for Cherenkov identification. Here we require that both particles in multiparticle spectrometer be identified as "exactly pion".

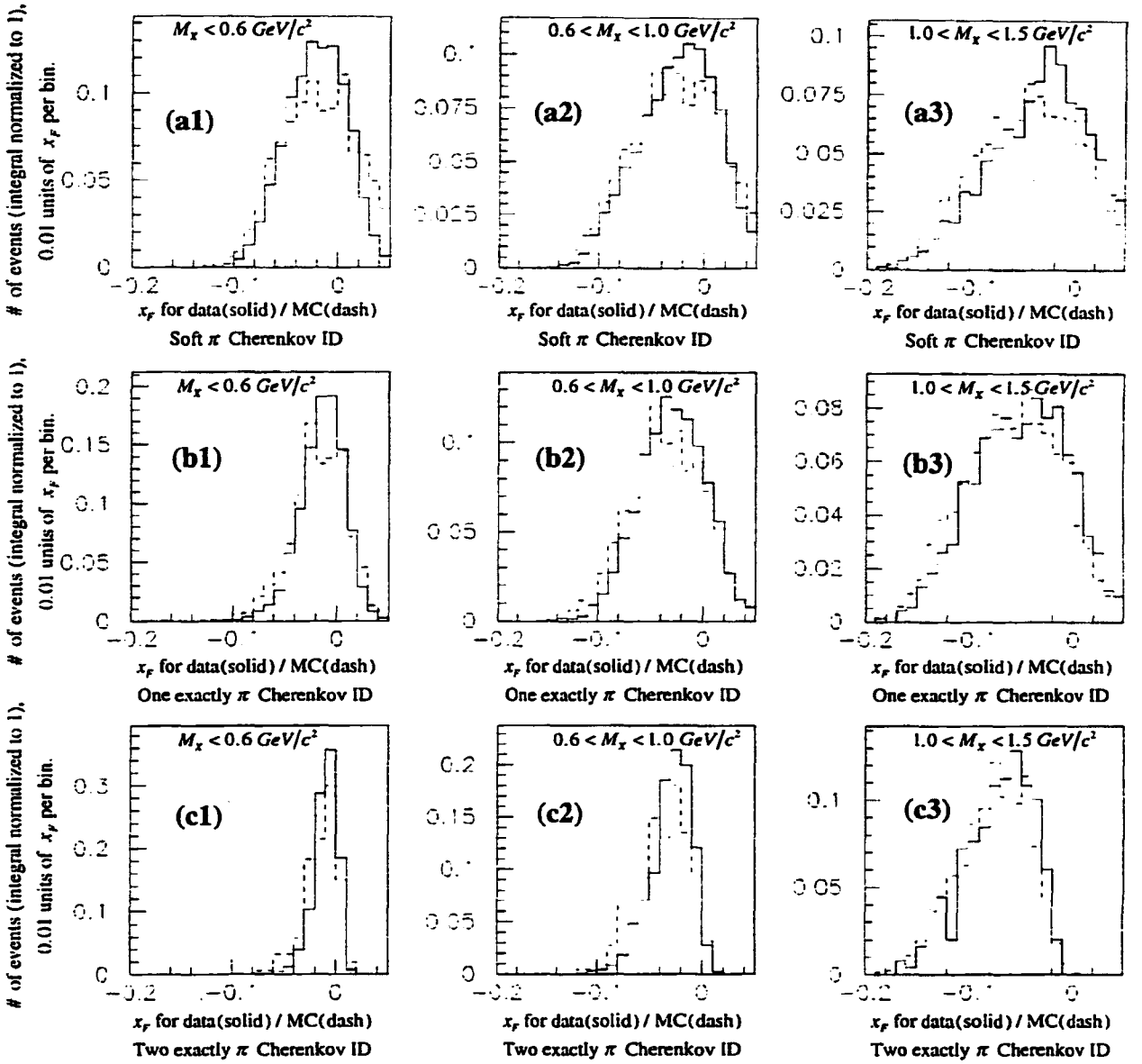

Figure 4.2 Comparison of x_F distributions for Data (solid), Monte Carlo (dash) after selection cuts. The three rows of plots show the distributions for three different Cherenkov identification requirements. The three columns show the distributions for three different mass regions. This is necessary since we integrate over mass and the Data/MC mass distributions are not the same. The Data and Monte Carlo distributions are normalized, so that the integral of each distribution is equal to unity. The selection requirements are: Vertex, Cherenkov ID, -1<MPI<1 GeV/c› Rapidity gap>1.8, $p_{t,s}^2 < 0.1\,(GeV/c)^2$, $-\sigma < MM^2 < \sigma$.

(a1,a2,a3) Soft Cherenkov ID
(b1,b2,b3) At least one "exactly pion" particle in Cherenkov counter.
(c1,c2,c3) Both multiparticle spectrometer particles "exactly pion" in Ch. counter.

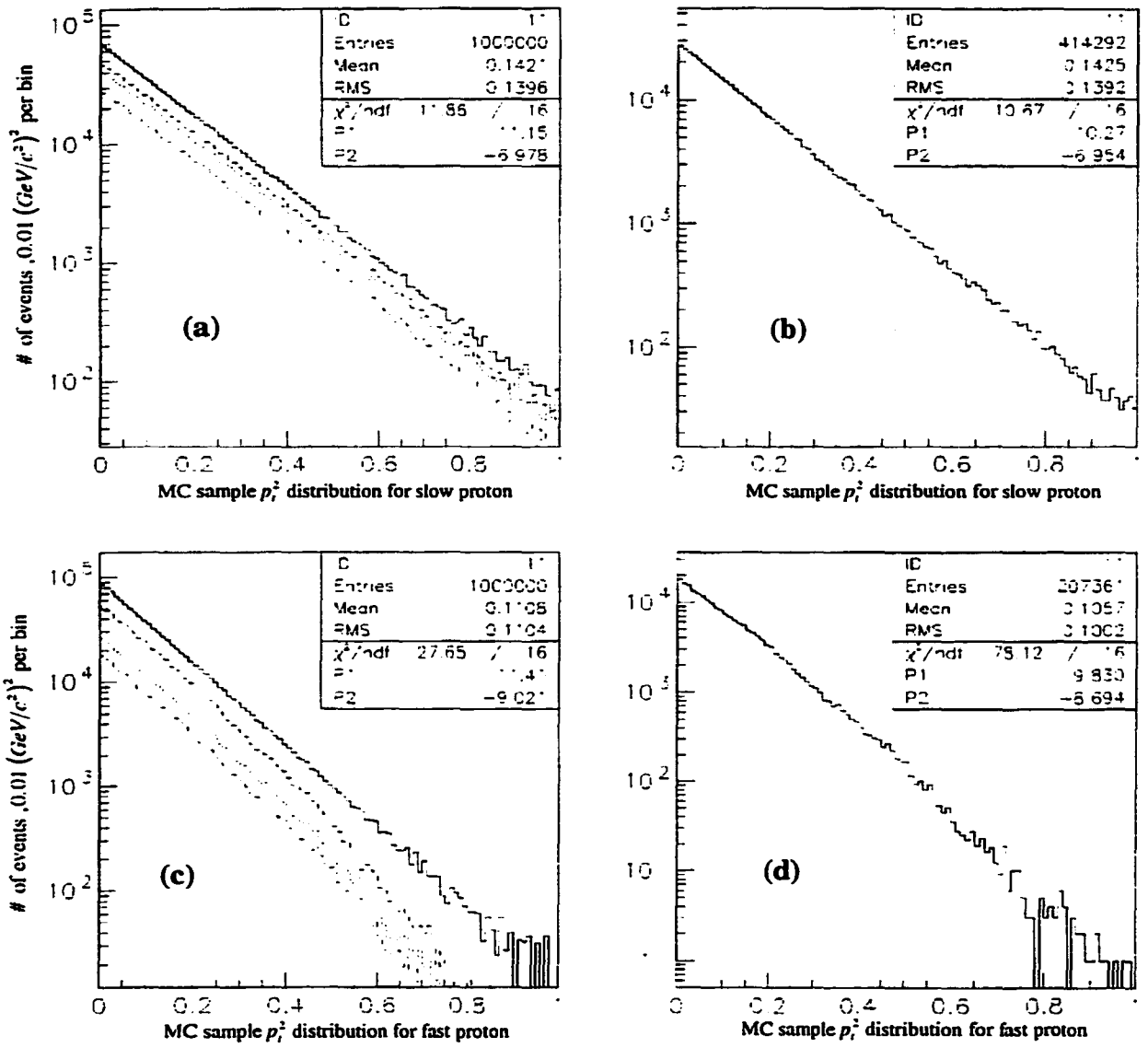

Figure 4.3 Monte Carlo sample p_t^2 distributions for slow and fast protons. We plot generated and reconstructed distributions for "soft" Cherenkov identification.

(a) -- Generated events, $p_{t,s}^2$ distribution.
-- Reconstructed events satisfying Vertex requirements, "soft" Cherenkov pion identification, & -1<MPI<1 GeV/c^2, & Rapidity gap>1.8.
-- & x_F in the interval [-0.1,0.0] -- & $-\sigma < MM^2 < \sigma$

(b) -- Fit for last distribution in (a).

(c) -- Generated events, $p_{t,f}^2$ distribution.
-- Reconstructed events satisfying Vertex requirements, "soft" Cherenkov pion ID, & -1<MPI<1 GeV/c^2, & Rapidity gap>1.8, & x_F in the interval [-0.1,0.0]
-- & $p_{t,s}^2 < 0.1\left(GeV/c^2\right)^2$ -- & $-\sigma < MM^2 < \sigma$

(d) -- Fit for last distribution in (c).

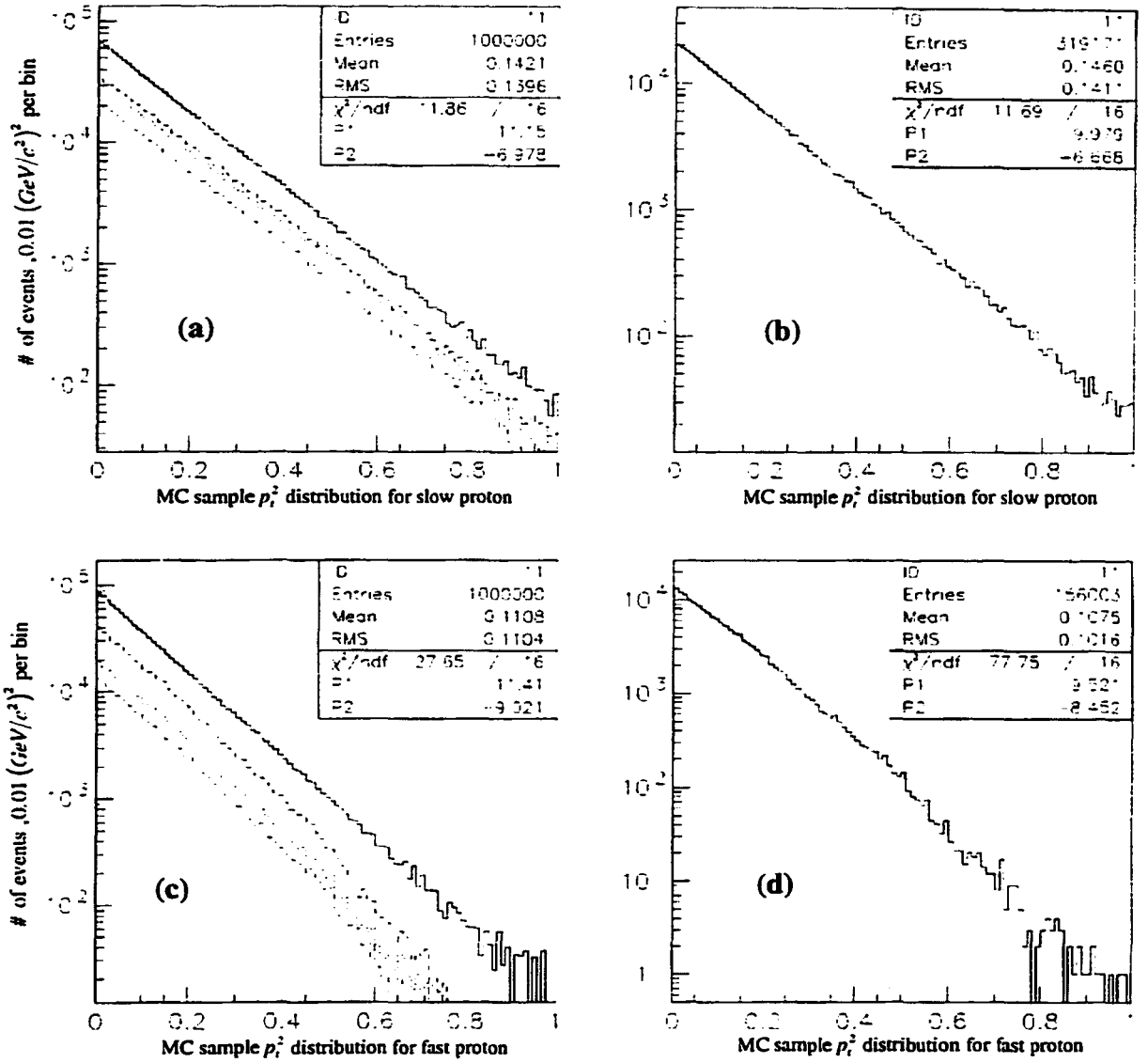

Figure 4.4 Monte Carlo sample p_t^2 distributions for slow and fast protons. We plot generated and reconstructed distributions for one "exactly pion" Cherenkov identification.

(a) -- Generated events, $p_{t,s}^2$ distribution.
-- Reconstructed events satisfying Vertex requirements, one "exactly pion" Cherenkov ID, & -1<MPI<1 GeV/c^2, & Rapidity gap>1.8.
-- & x_F in the interval [-0.1,0.0] -- & $-\sigma < MM^2 < \sigma$

(b) -- Fit for last distribution in (a).

(c) -- Generated events, $p_{t,f}^2$ distribution.
-- Reconstructed events satisfying Vertex requirements, one "exactly pion" Cherenkov ID, & -1<MPI<1 GeV/c^2, Rapidity gap>1.8, x_F in [-0.1,0.0]
-- & $p_{t,s}^2 < 0.1\left(GeV/c^2\right)^2$ -- & $-\sigma < MM^2 < \sigma$

(d) -- Fit for last distribution in (c).

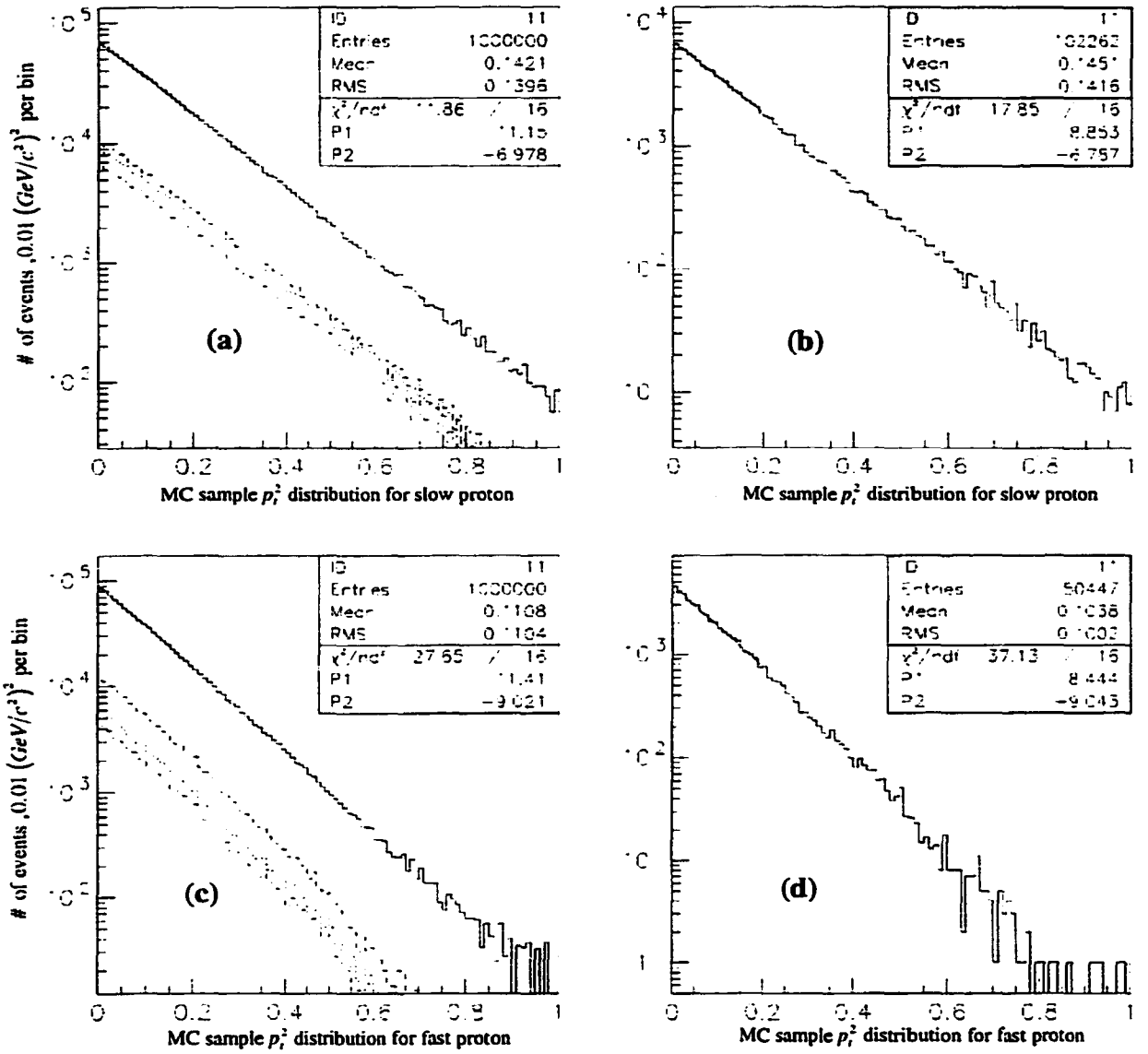

Figure 4.5 Monte Carlo sample p_t^2 distributions for slow and fast protons. We plot generated and reconstructed distributions for two "exactly pion" Cherenkov identification.

(a) -- Generated events, $p_{t,s}^2$ distribution.
-- Reconstructed events satisfying Vertex requirements, two "exactly pion" Cherenkov ID, & -1<MPl<1 GeV/c^2, & Rapidity gap>1.8.
-- & x_F in the interval [-0.1,0.0] -- & $-\sigma < MM^2 < \sigma$

(b) -- Fit for last distribution in (a).

(c) -- Generated events, $p_{t,f}^2$ distribution.
-- Reconstructed events satisfying Vertex requirements, two "exactly pion" Cherenkov ID, & -1<MPl<1 GeV/c^2, Rapidity gap>1.8, x_F in [-0.1,0.0]
-- & $p_{t,s}^2 < 0.1\left(GeV/c^2\right)^2$ -- & $-\sigma < MM^2 < \sigma$

(d) -- Fit for last distribution in (c).

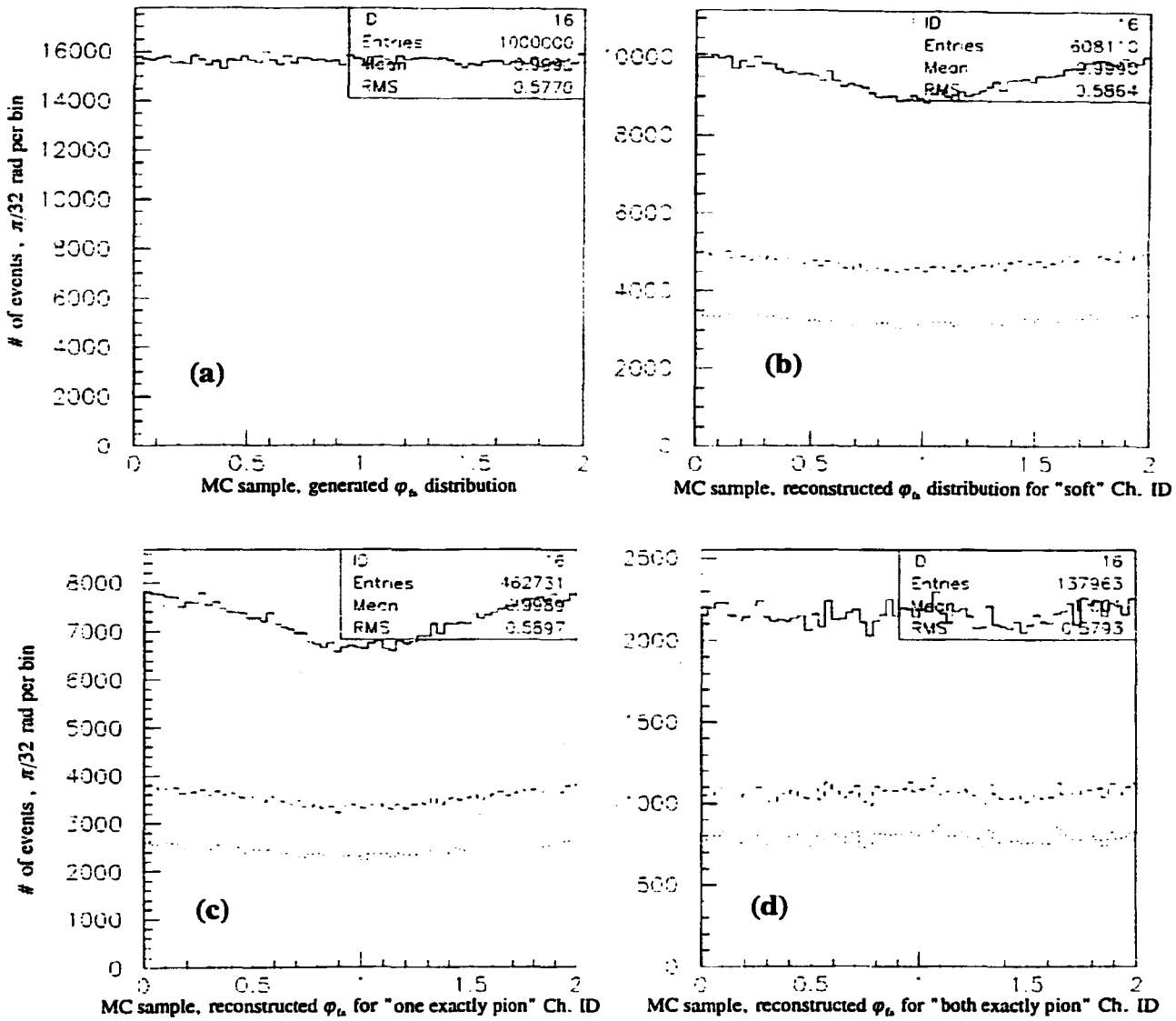

Figure 4.6 Monte Carlo sample φ_{fs} distributions (relative angle between final state fast and slow protons). We plot generated and reconstructed distributions for three Cherenkov identification criteria.

(a) – Generated events

(b) – Reconstructed events satisfying Vertex requirements, two "exactly pion" Cherenkov ID, & -1<MPI<1 GeV/c^2, & Rapidity gap>1.8, & x_F in the interval [-0.1,0.0]

– & $p_{t,s}^2 < 0.1\left(GeV/c^2\right)^2$

– & $-\sigma < MM^2 < \sigma$

(c) – Same as (b) except for Cherenkov requirement. At least one of the multiparticle spectrometer particles must be "exactly pion".

(d) – Same as (b) except for Cherenkov requirement. Both multiparticle spectrometer particles must be "exactly pion".

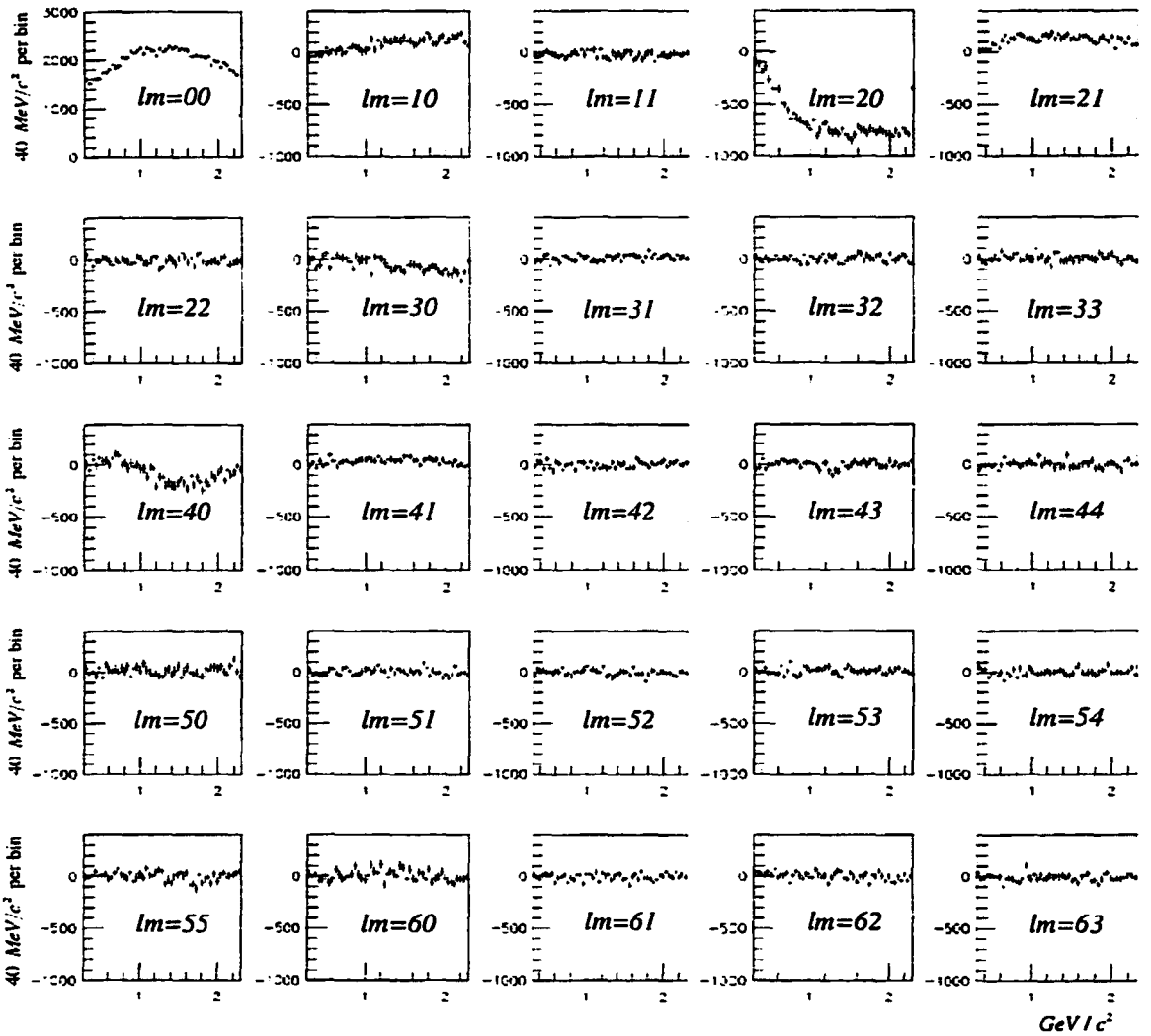

Figure 4.7 Experimental moments (b_{lm}) as a function of invariant mass for generated Monte Carlo sample. The events used satisfy the selection criteria:

-- Vertex requirements and two (Cherenkov) pion compatible tracks in multiparticle spectrometer and x_F in the interval [-0.1,0.0].

-- -1<MPl<1 GeV/c^2.

-- Rapidity gap>1.8 between the slow proton and any one of the two pions.

-- $p_{t,f}^2, p_{t,s}^2 < 0.1\,(GeV/c^2)^2$.

-- $-\sigma < MM^2 < \sigma$

Continued Next Page.

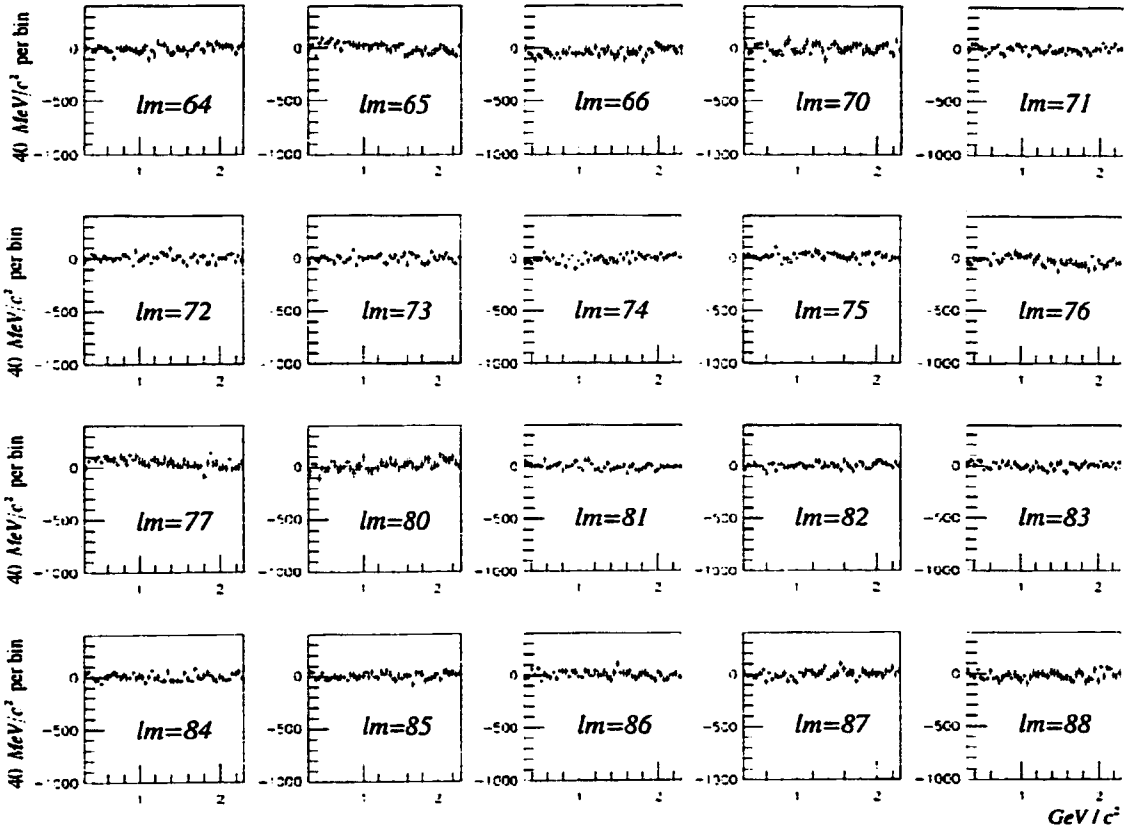

Figure 4.7 Continued.

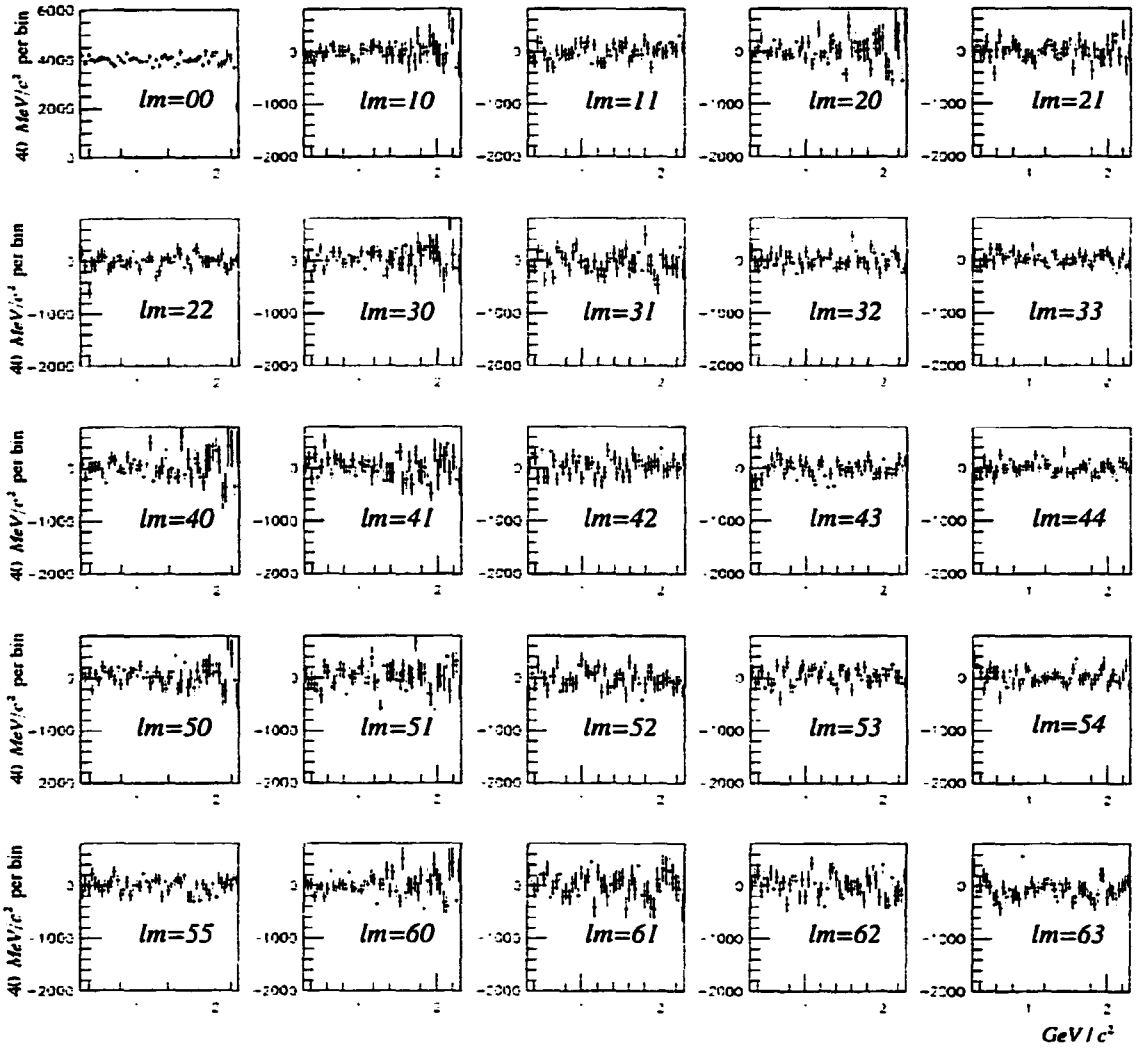

Figure 4.8 Acceptance corrected moments (t_{lm}) as a function of invariant mass for generated Monte Carlo sample. The events used satisfy the selection criteria:

-- Vertex requirements and two (Cherenkov) pion compatible tracks in multiparticle spectrometer and x_F in the interval [-0.1,0.0].

-- -1<MPI<1 GeV/c^2.

-- Rapidity gap>1.8 between the slow proton and any one of the two pions.

-- $p_{t,f}^2,\ p_{t,s}^2 < 0.1\,(GeV/c^2)^2$.

-- $-\sigma < MM^2 < \sigma$

Continued Next Page.

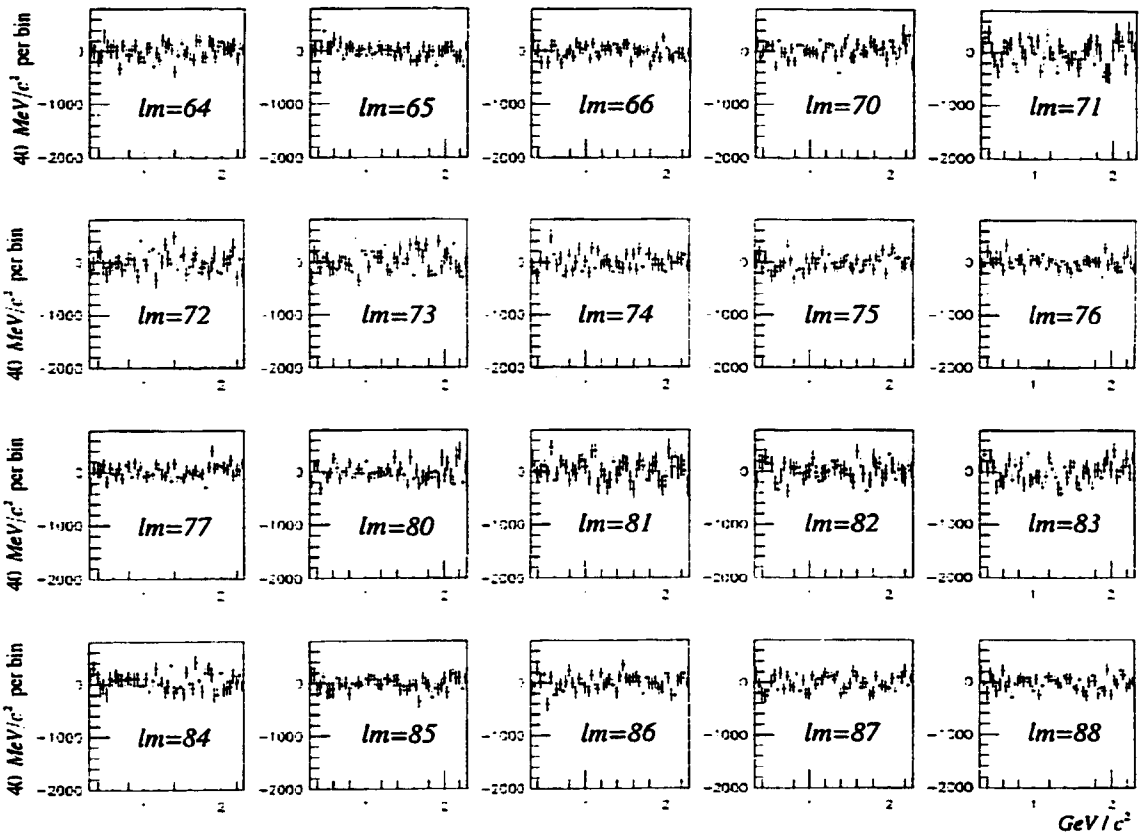

Figure 4.8 Continued.

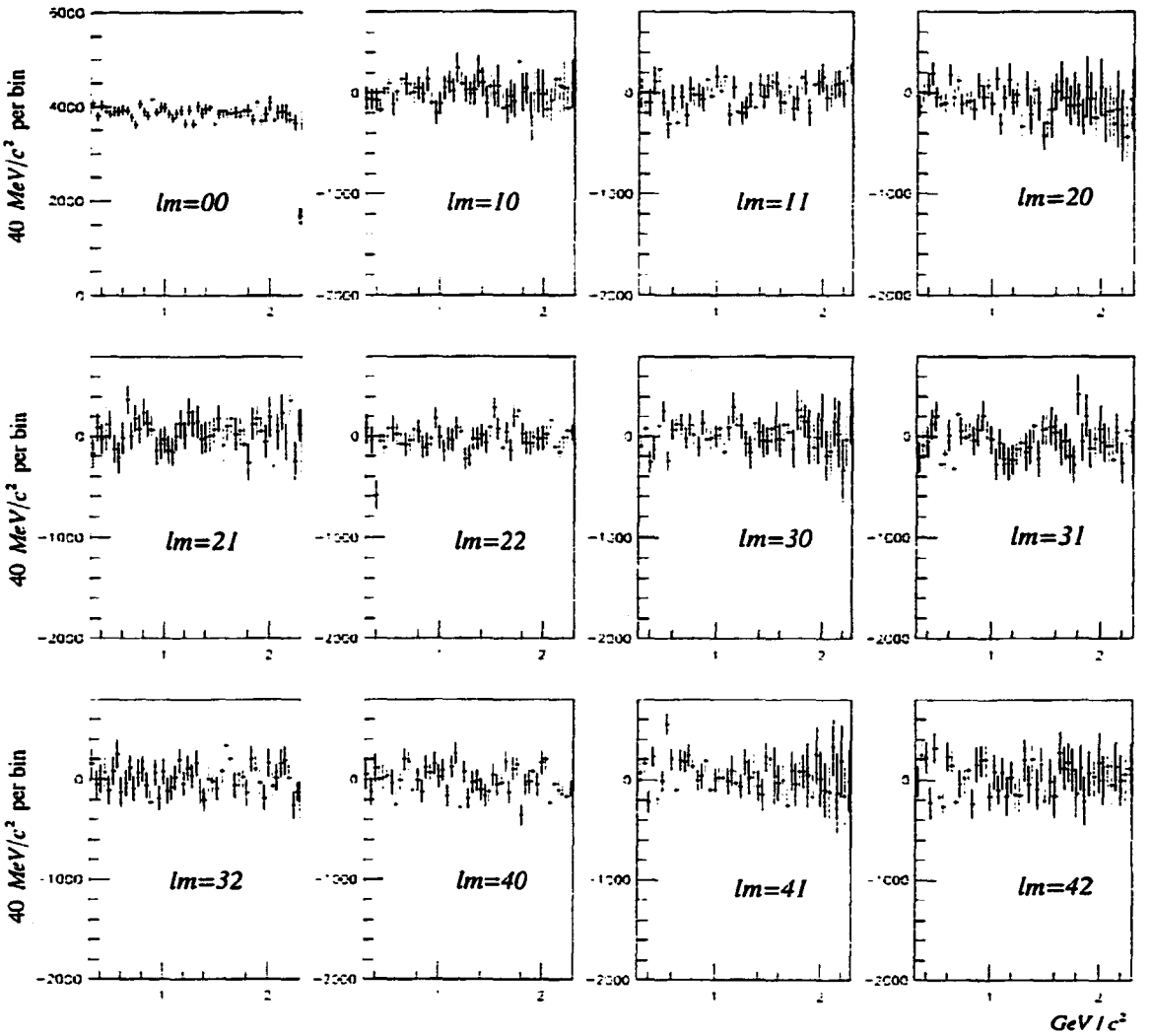

Figure 4.9 Acceptance corrected moments (t_{lm}) as a function of invariant mass for generated Monte Carlo sample. We allow moments with $l \leq 4$, $m \leq 2$. The events used satisfy the selection criteria:

– Vertex requirements and two (Cherenkov) pion compatible tracks in multiparticle spectrometer and x_F in the interval [-0.1,0.0].

– -1<MPI<1 GeV/c^2.

– Rapidity gap>1.8 between the slow proton and any one of the two pions.

– $p_{t,f}^2, p_{t,s}^2 < 0.1\,(GeV/c^2)^2$.

– $-\sigma < MM^2 < \sigma$

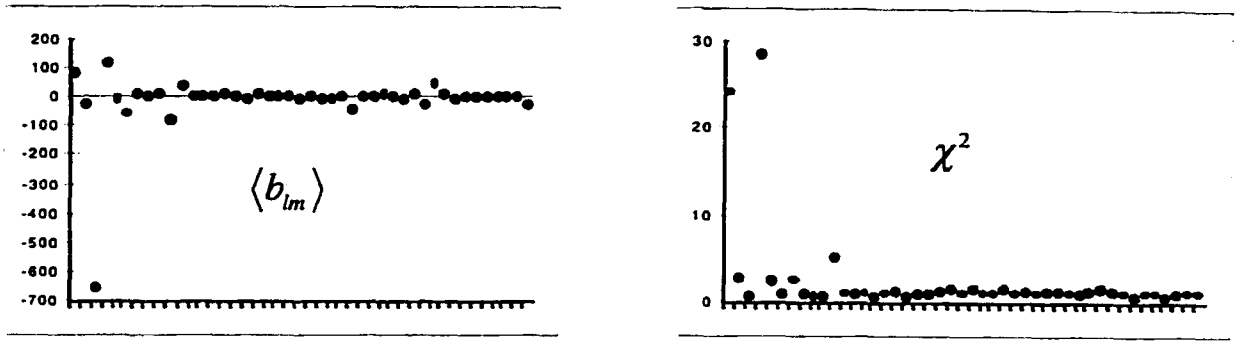

experimental moments (b_{lm})

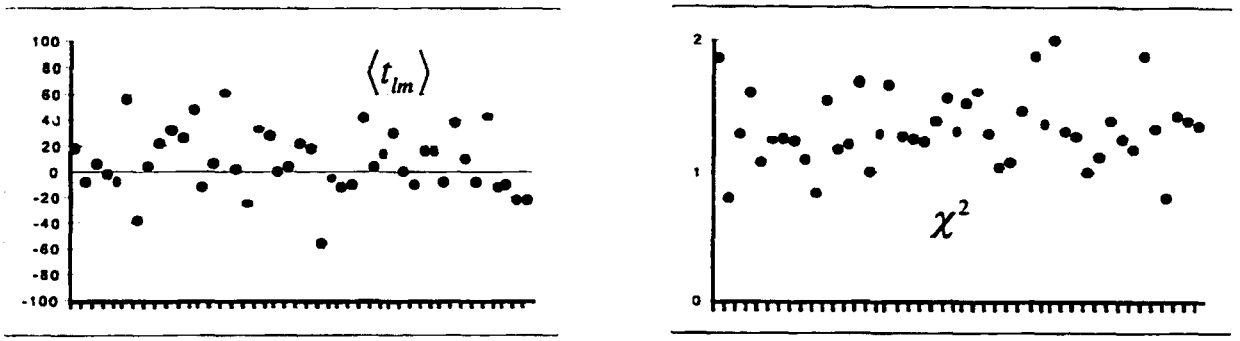

acceptance corrected moments (t_{lm}) using all l,m allowed.

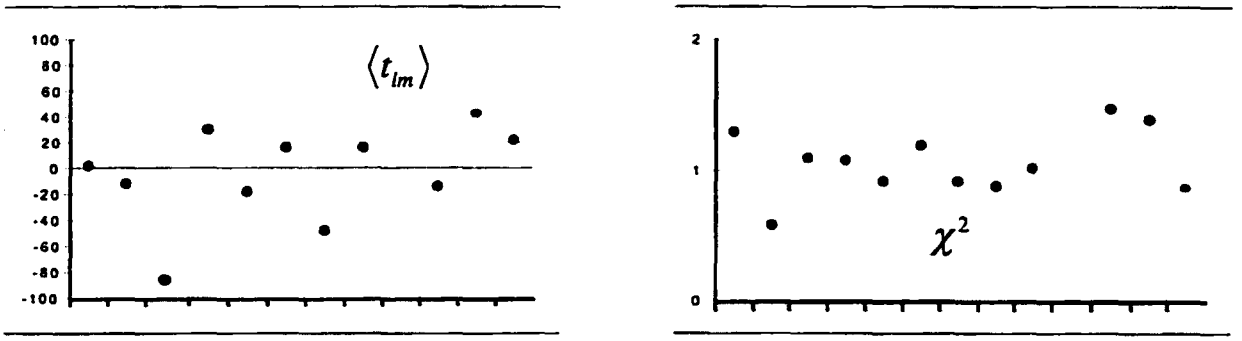

acceptance corrected moments (t_{lm}) using $l \leq 4,\ m \leq 2$

Figure 4.10 Results from one parameter fits of the expansion coefficients as a function of mass. We perform the fits for three sets of coefficients: experimental moments (b_{lm}), and two sets of acceptance corrected moments (t_{lm}). The χ^2 is defined as: $\chi^2_{lm} \equiv \frac{1}{N_{bins}-1} \sum_{i=1}^{N_{bins}} \frac{\left(t_{lm}(i) - \langle t_{lm} \rangle\right)^2}{\sigma^2_{lm}(i)}$. For the average value plots we omit the $lm = 00$ moment.

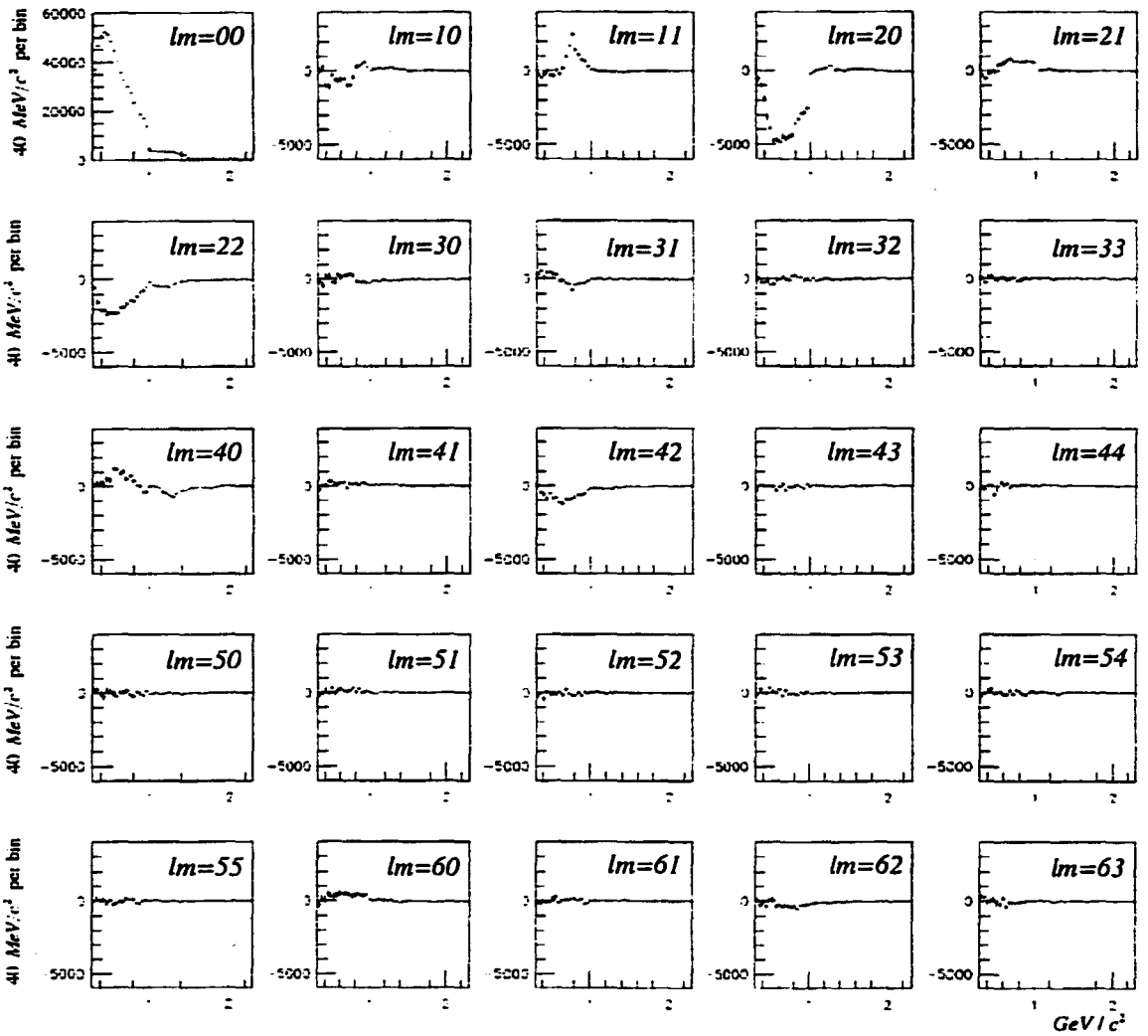

Figure 4.11. Experimental moments (b_{lm}) as a function of invariant mass for detector data sample. After selection cuts 635×10^3 events are selected for this set of plots. The events used satisfy the selection criteria:

-- Vertex requirements and two (Cherenkov) pion compatible tracks in multiparticle spectrometer and x_F in the interval [-0.1,0.0].

-- -1<MPl<1 GeV/c^2.

-- Rapidity gap>1.8 between the slow proton and any one of the two pions.

-- $p_{t,f}^2, p_{t,s}^2 < 0.1\left(GeV/c^2\right)^2$.

-- $-\sigma < MM^2 < \sigma$

Continued Next Page.

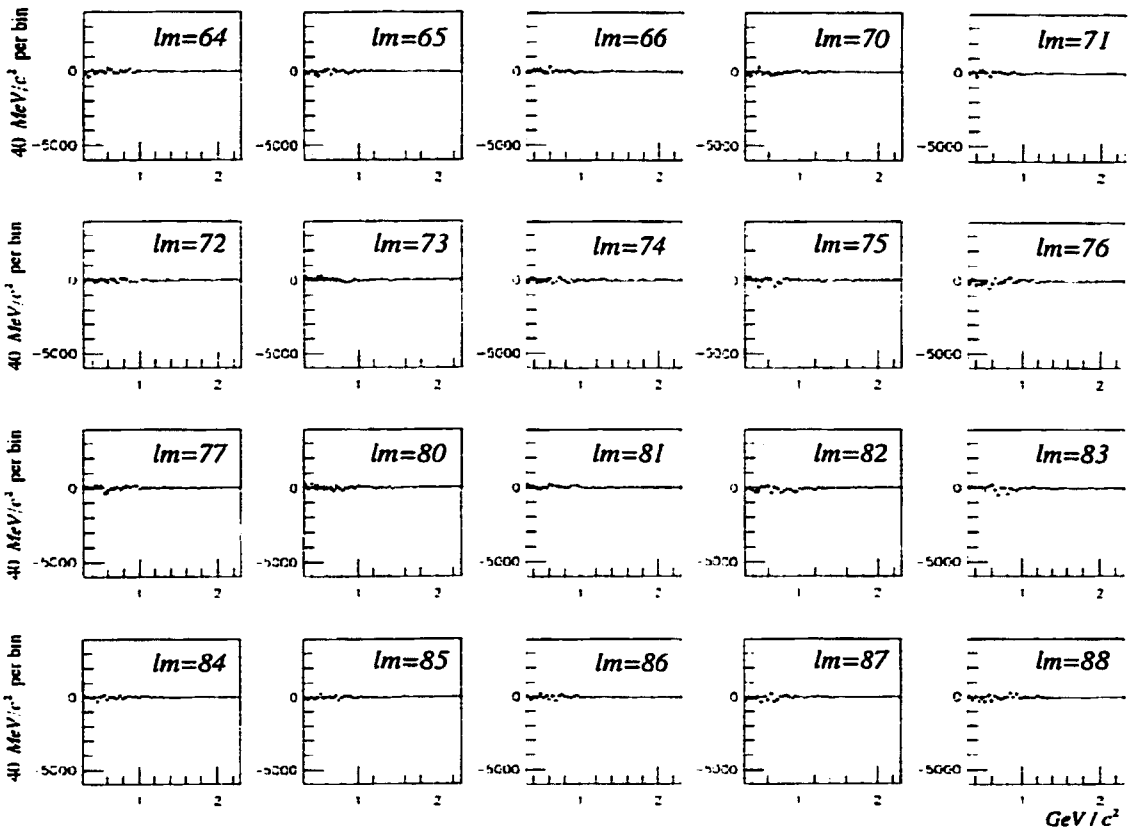

Figure 4.11. Continued.

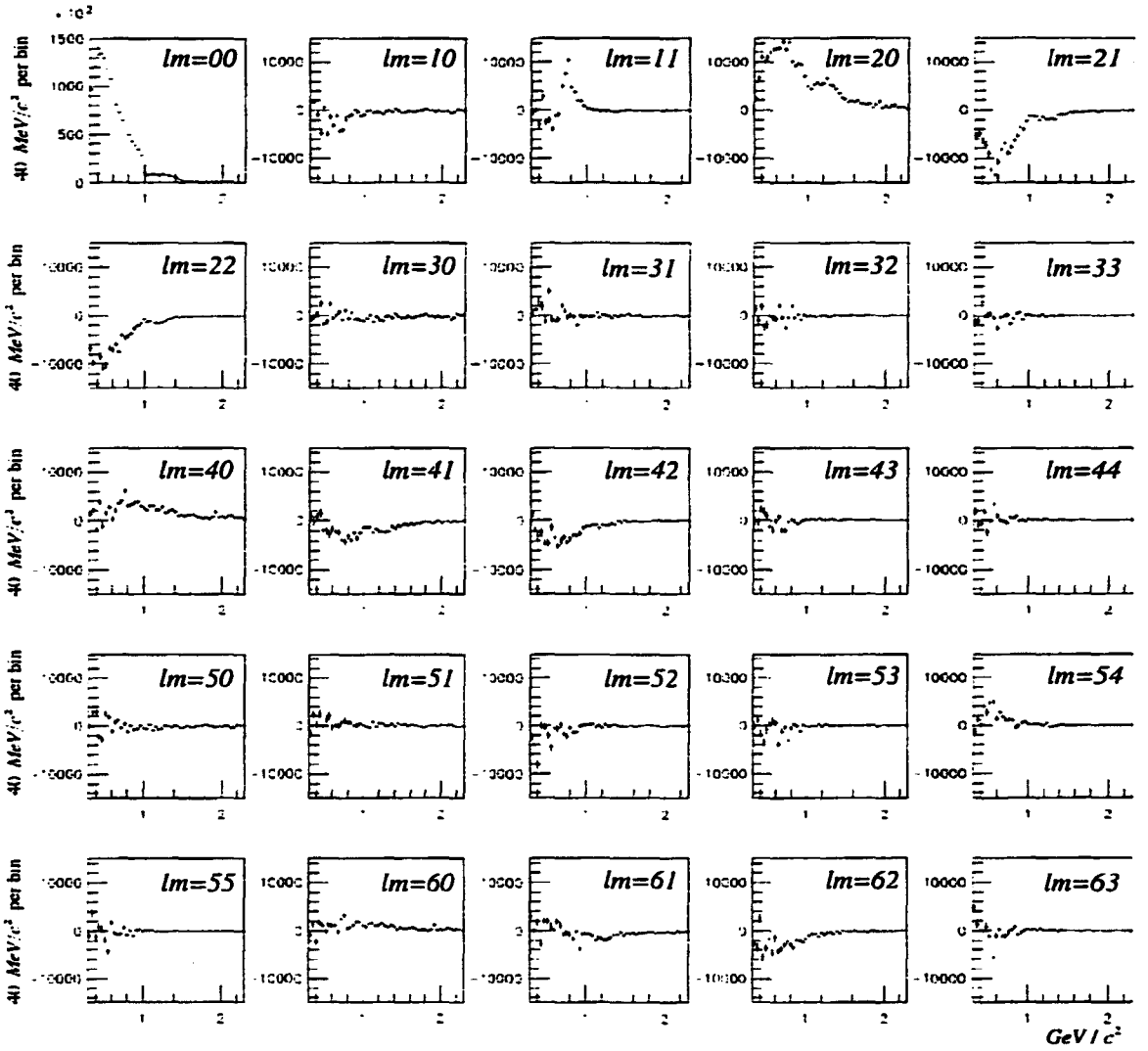

Figure 4.12. Acceptance corrected moments (t_{lm}) as a function of invariant mass for detector data sample. After selection cuts 635×10^3 events are selected for this set of plots. The events used satisfy the selection criteria:

-- Vertex requirements and two (Cherenkov) pion compatible tracks in multiparticle spectrometer and x_F in the interval [-0.1,0.0].

-- -1<MPl<1 GeV/c^2.

-- Rapidity gap>1.8 between the slow proton and any one of the two pions.

-- $p_{t,f}^2, p_{t,s}^2 < 0.1\,(GeV/c^2)^2$.

-- $-\sigma < MM^2 < \sigma$

Continued Next Page.

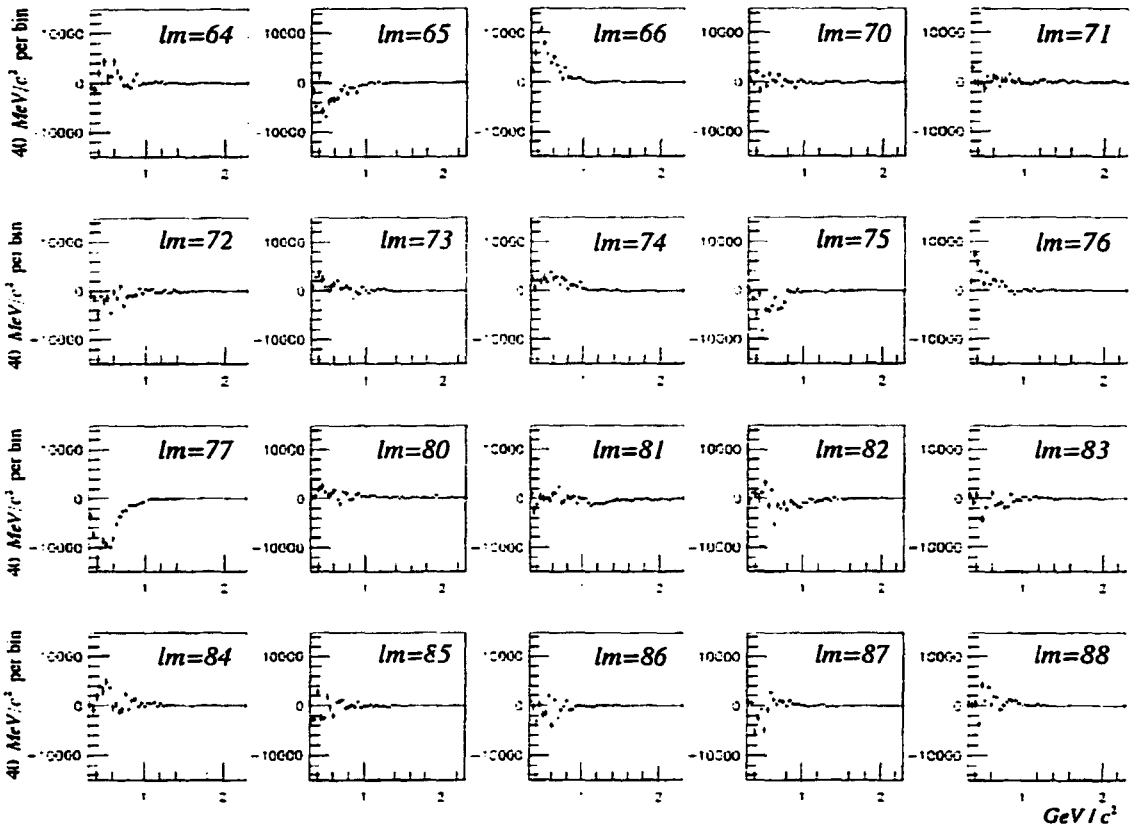

Figure 4.12. Continued.

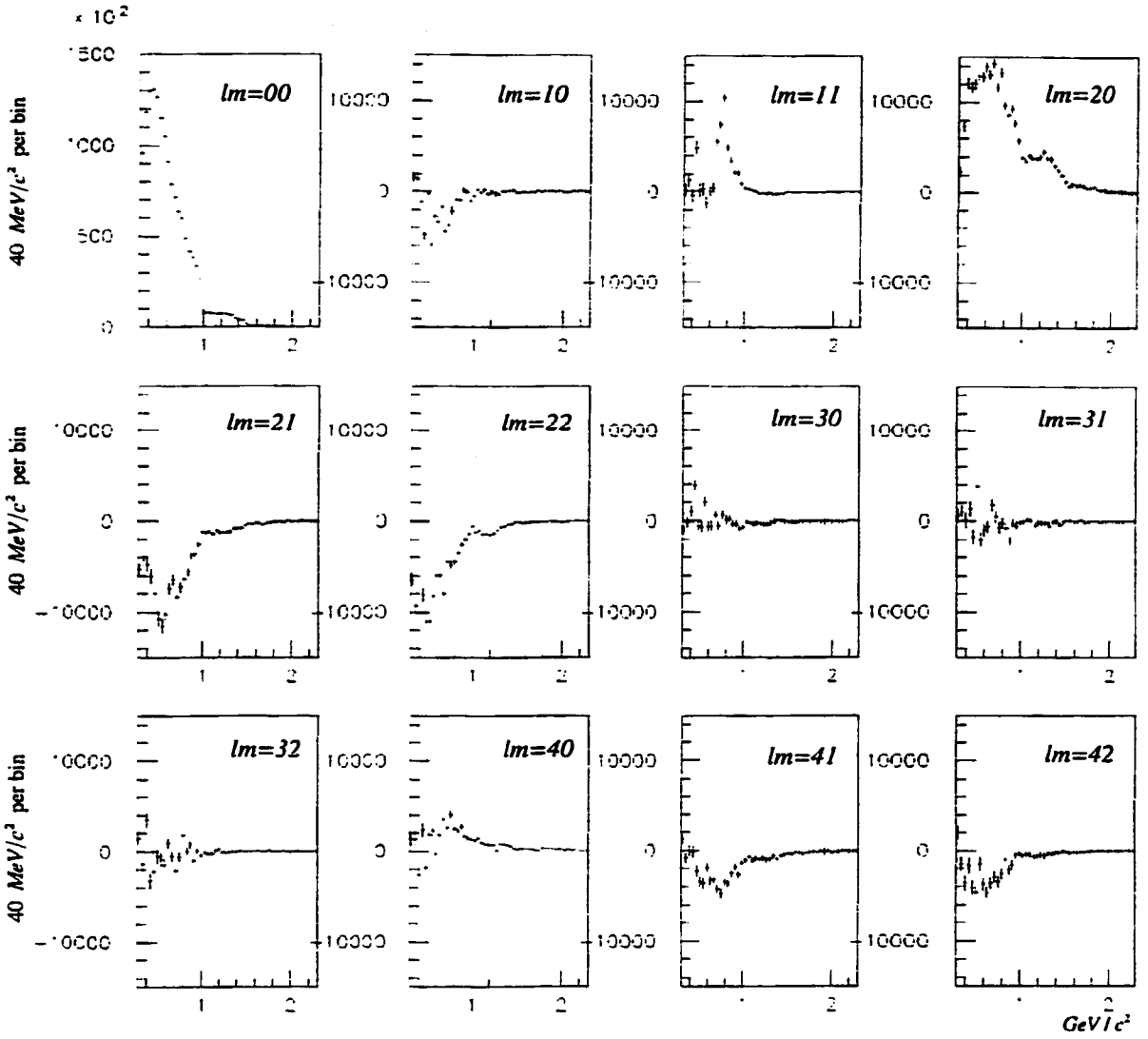

Figure 4.13. Acceptance corrected moments (t_{lm}) as a function of invariant mass for detector data sample. For this figure we restrict the t_{lm} to $l \leq 4$, $m \leq 2$. After selection cuts 635×10^3 events are selected for this set of plots. The events used satisfy the selection criteria:

-- Vertex requirements and two (Cherenkov) pion compatible tracks in multiparticle spectrometer and x_F in the interval [-0.1,0.0].

-- -1<MPI<1 GeV/c^2.

-- Rapidity gap>1.8 between the slow proton and any one of the two pions.

-- $p_{t,f}^2, p_{t,s}^2 < 0.1\,(GeV/c^2)^2$.

-- $-\sigma < MM^2 < \sigma$

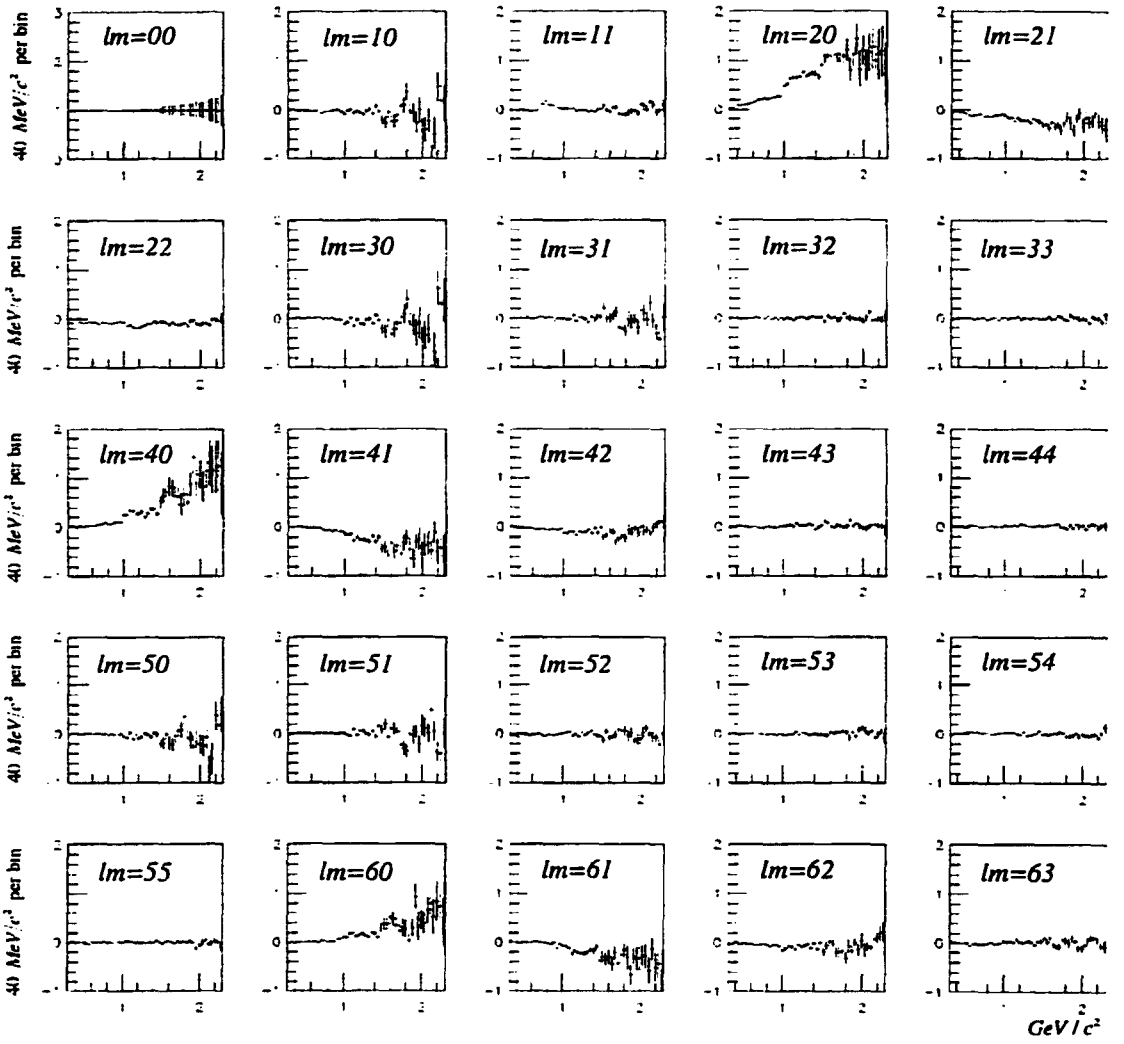

Figure 4.14 Acceptance corrected moments (t_{lm}) as a function of invariant mass for detector data sample. All moments (and associated error bars) are normalized to t_{00}. Although the normalized value of $t_{lm=00}$ is an exact ratio, we scale and present the associated error bars in order to indicate the uncertainty in the unormalized measurement. After selection cuts 635×10^3 events are selected for this set of plots. The events used satisfy the selection criteria:

-- Vertex requirements and two (Cherenkov) pion compatible tracks in multiparticle spectrometer and x_F in the interval [-0.1,0.0].

-- -1<MPI<1 GeV/c^2.

-- Rapidity gap>1.8 between the slow proton and any one of the two pions.

-- $p_{t,f}^2, p_{t,s}^2 < 0.1\left(GeV/c^2\right)^2$.

-- $-\sigma < MM^2 < \sigma$

Continued Next Page.

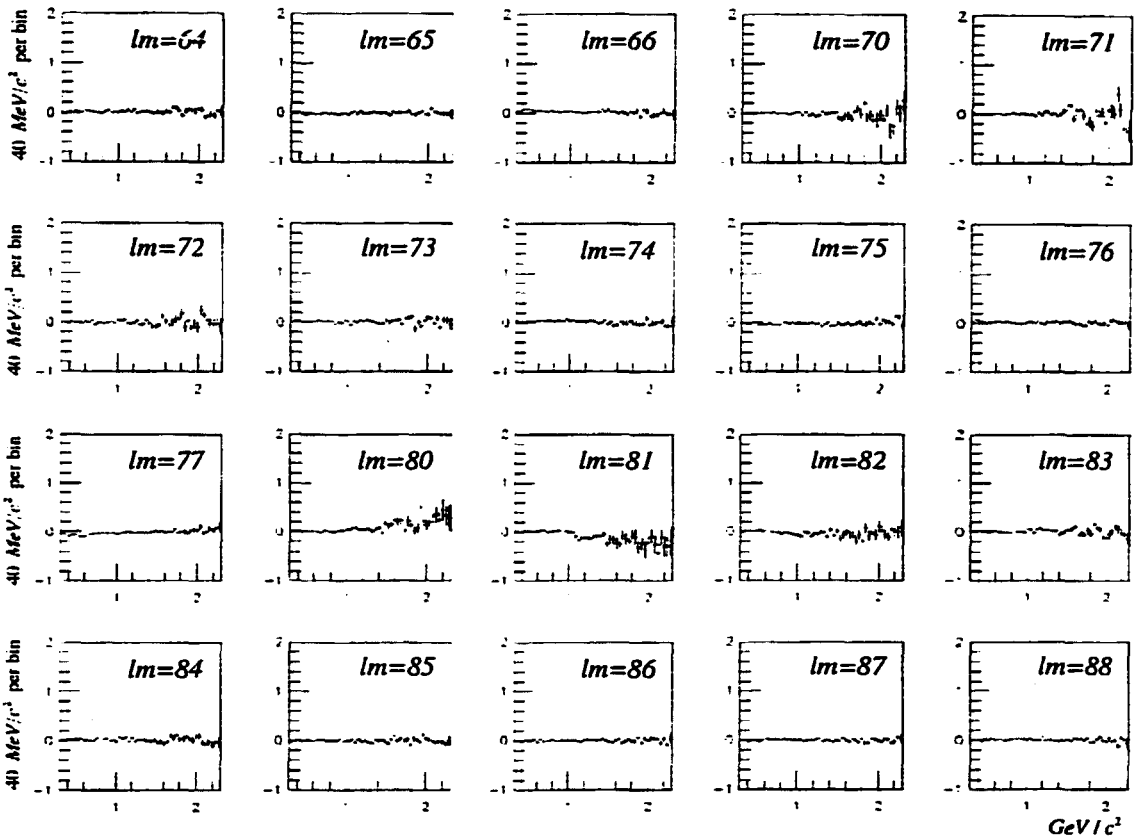

Figure 4.14. Continued.

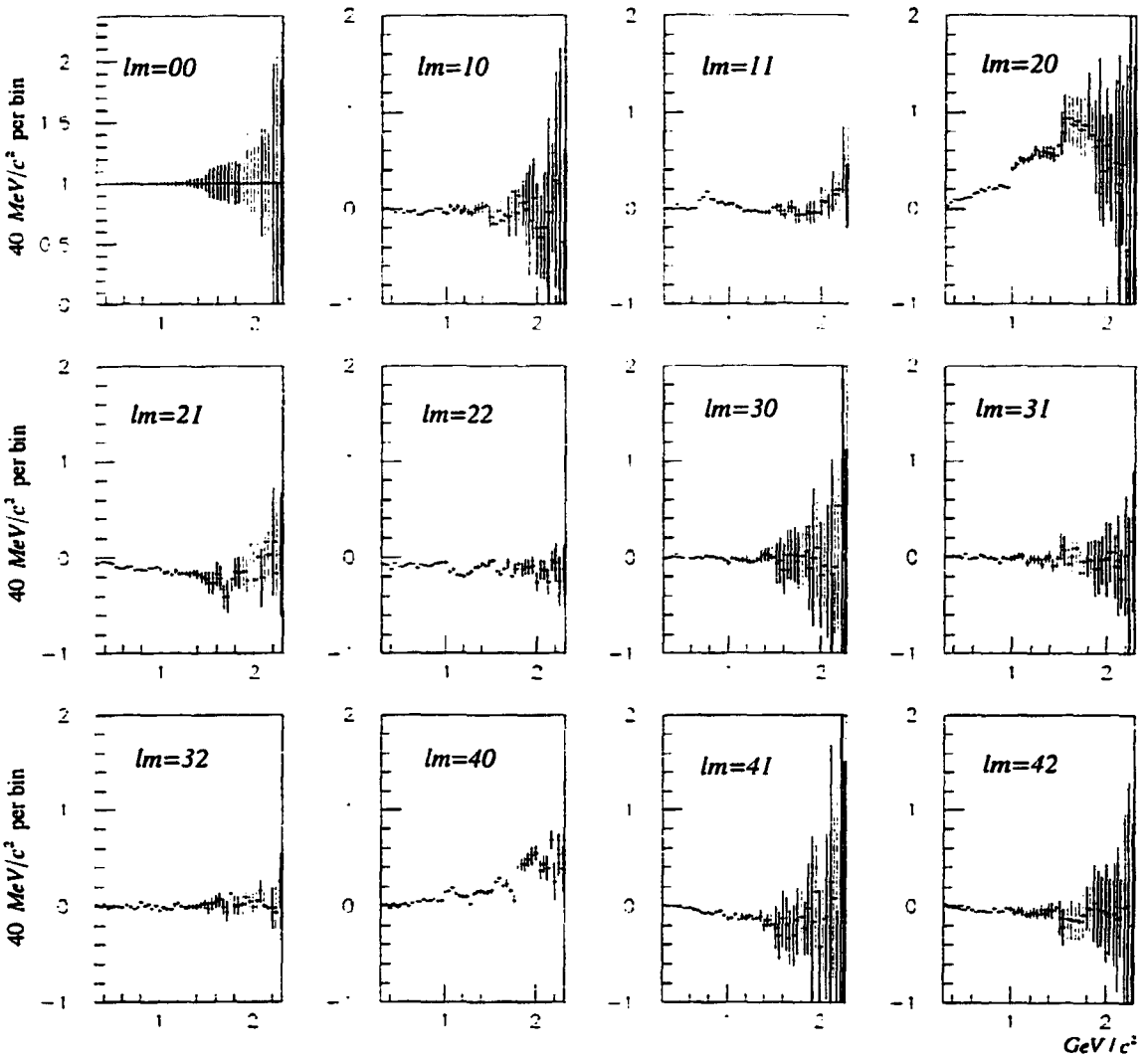

Figure 4.15. Acceptance corrected moments (t_{lm}) as a function of invariant mass for detector data sample. All moments are normalized to t_{00}. Although the normalized value of $t_{lm=00}$ is an exact ratio, we scale and present the associated error bars in order to indicate the uncertainty in the unormalized measurement. For this figure we restrict the t_{lm} to $l \leq 4$, $m \leq 2$. After selection cuts 635×10^3 events are selected for this set of plots. The events used satisfy the selection criteria:

-- Vertex requirements and two (Cherenkov) pion compatible tracks in multiparticle spectrometer and x_F in the interval [-0.1,0.0].

-- -1<MPI<1 GeV/c^2.

-- Rapidity gap>1.8 between the slow proton and any one of the two pions.

-- $p_{t,f}^2, p_{t,s}^2 < 0.1\,(GeV/c^2)^2$.

-- $-\sigma < MM^2 < \sigma$

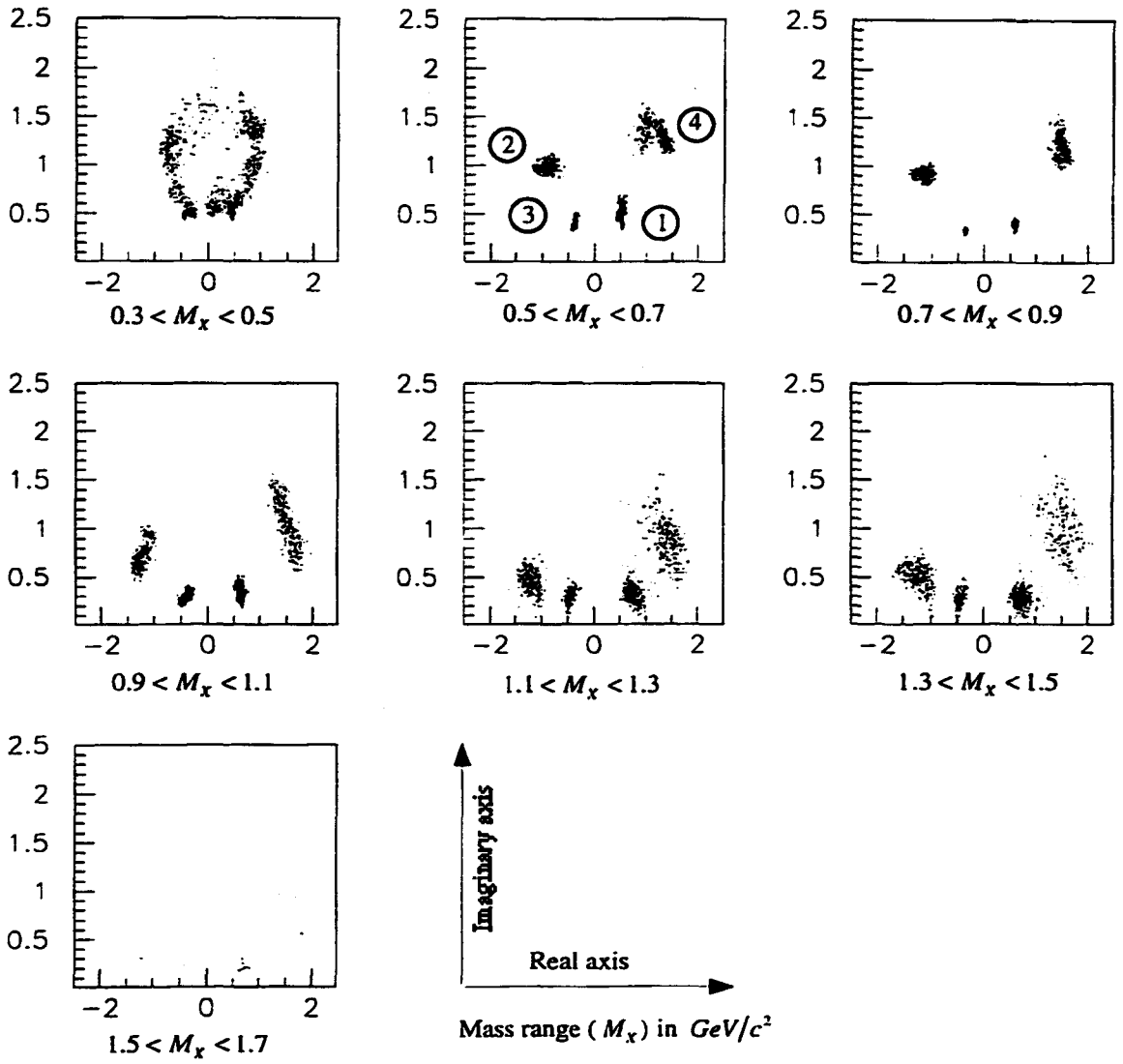

Figure 4.16 Roots $\{u_1, u_2, u_3, u_4\}$ of polynomial $|G(u)|^2$ for regions of invariant mass (M_X). There are 5 mass bins per 0.2 GeV/c^2 interval. We "throw" the acceptance corrected moments (t_{LM}) 100 times per mass bin, and plot only sets of roots that result in at least one valid amplitude solution. Thus we expect (4 roots)×(5 bins)×(0 to 100 root sets per 100 "throws")=0 to 2000 entries per plot.

The events used satisfy the selection criteria:

-- Vertex requirements and two (Cherenkov) pion compatible tracks in multiparticle spectrometer and x_F in the interval [-0.1,0.0].

-- -1<MPl<1 GeV/c^2.

-- Rapidity gap>1.8 between the slow proton and any one of the two pions.

-- $p_{t,f}^2, p_{t,s}^2 < 0.1\,(GeV/c^2)^2$.

-- $-\sigma < MM^2 < \sigma$

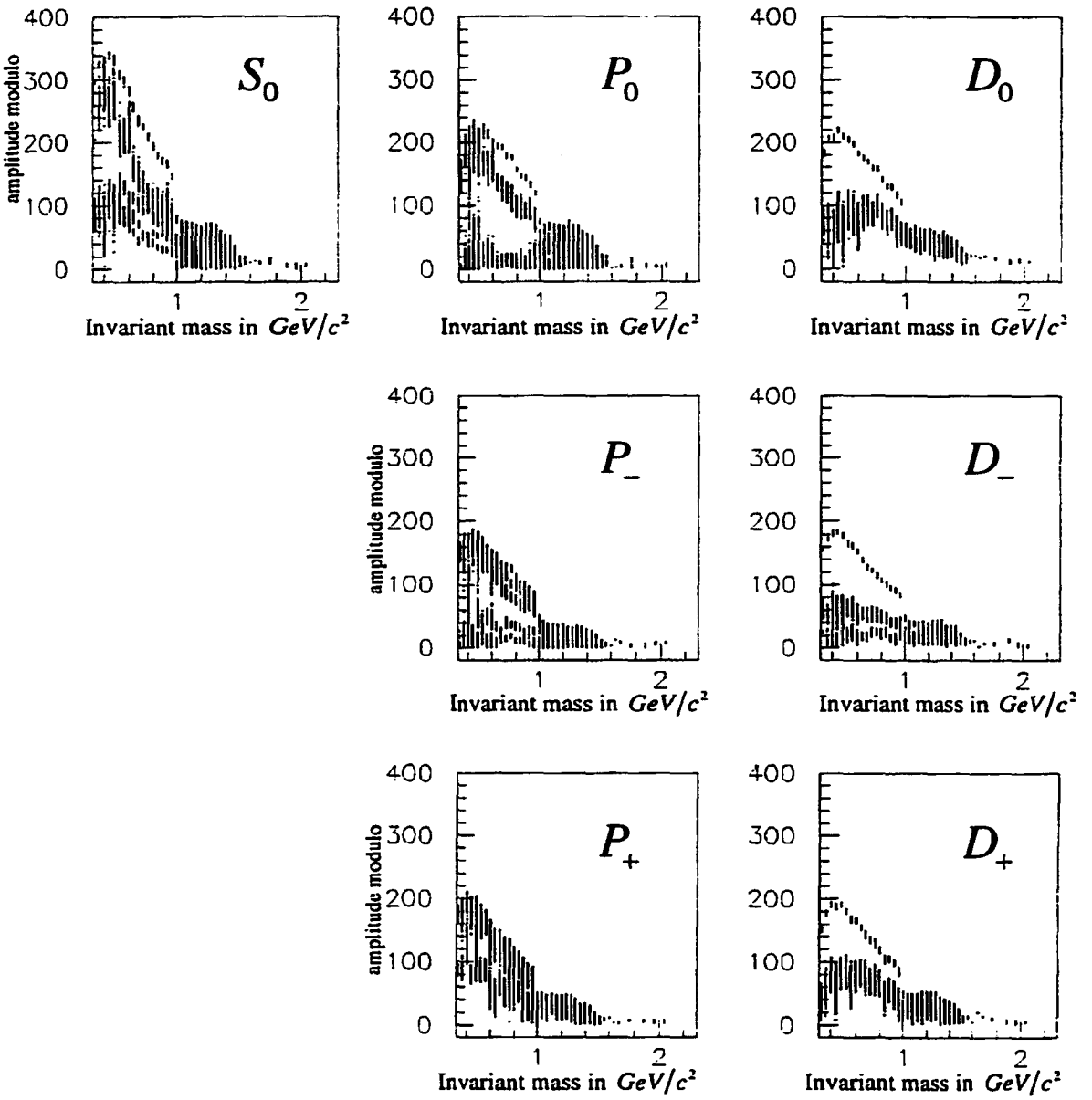

Figure 4.17 Modulo of all valid amplitude solutions as a function of mass. We superimpose all of the eight possible solutions.
The events used satisfy the selection criteria:

- Vertex requirements and two (Cherenkov) pion compatible tracks in multiparticle spectrometer and x_F in the interval [-0.1,0.0].
- -1<MPl<1 GeV/c^2.
- Rapidity gap>1.8 between the slow proton and any one of the two pions.
- $p_{t,f}^2, p_{t,s}^2 < 0.1\,(GeV/c)^2$.
- $-\sigma < MM^2 < \sigma$

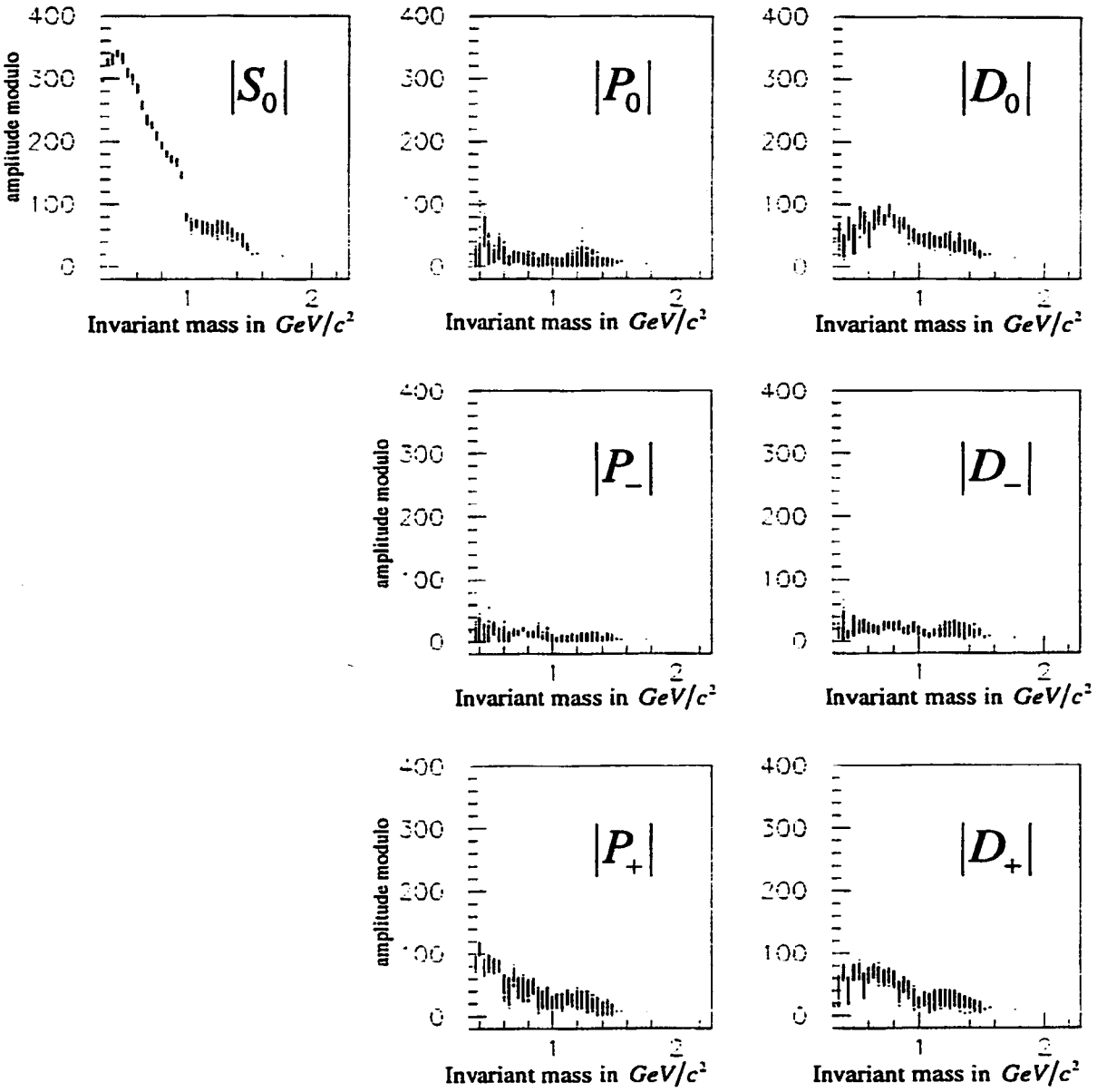

Figure 4.18 Modulo of all solutions labeled as solution #6, plotted as a function of invariant mass. We superimpose all labeled solutions. The events used satisfy the selection criteria:

-- Vertex requirements and two (Cherenkov) pion compatible tracks in multiparticle spectrometer and x_F in the interval [-0.1,0.0].

-- -1<MPl<1 GeV/c^2.

-- Rapidity gap>1.8 between the slow proton and any one of the two pions.

-- $p_{t,f}^2, p_{t,s}^2 < 0.1\,(GeV/c)^2$.

-- $-\sigma < MM^2 < \sigma$

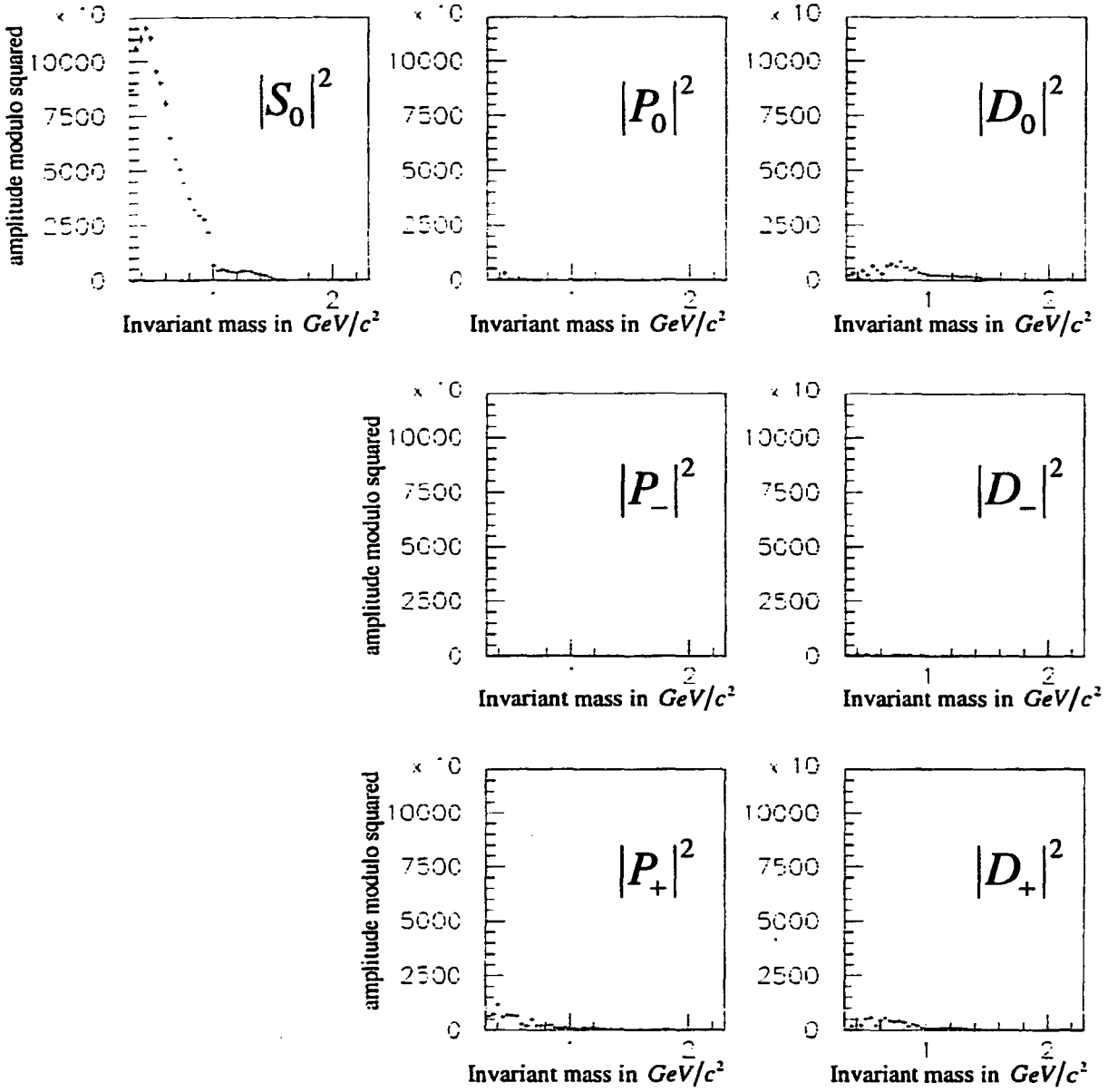

Figure 4.19 Modulo squared of all solutions labeled as solution #6, plotted as a function of invariant mass. We average all labeled solutions. The events used satisfy the selection criteria:

-- Vertex requirements and two (Cherenkov) pion compatible tracks in multiparticle spectrometer and x_F in the interval [-0.1,0.0].

-- -1<MPl<1 GeV/c^2.

-- Rapidity gap>1.8 between the slow proton and any one of the two pions.

-- $p_{t,f}^2, p_{t,s}^2 < 0.1\,(GeV/c)^2$.

-- $-\sigma < MM^2 < \sigma$

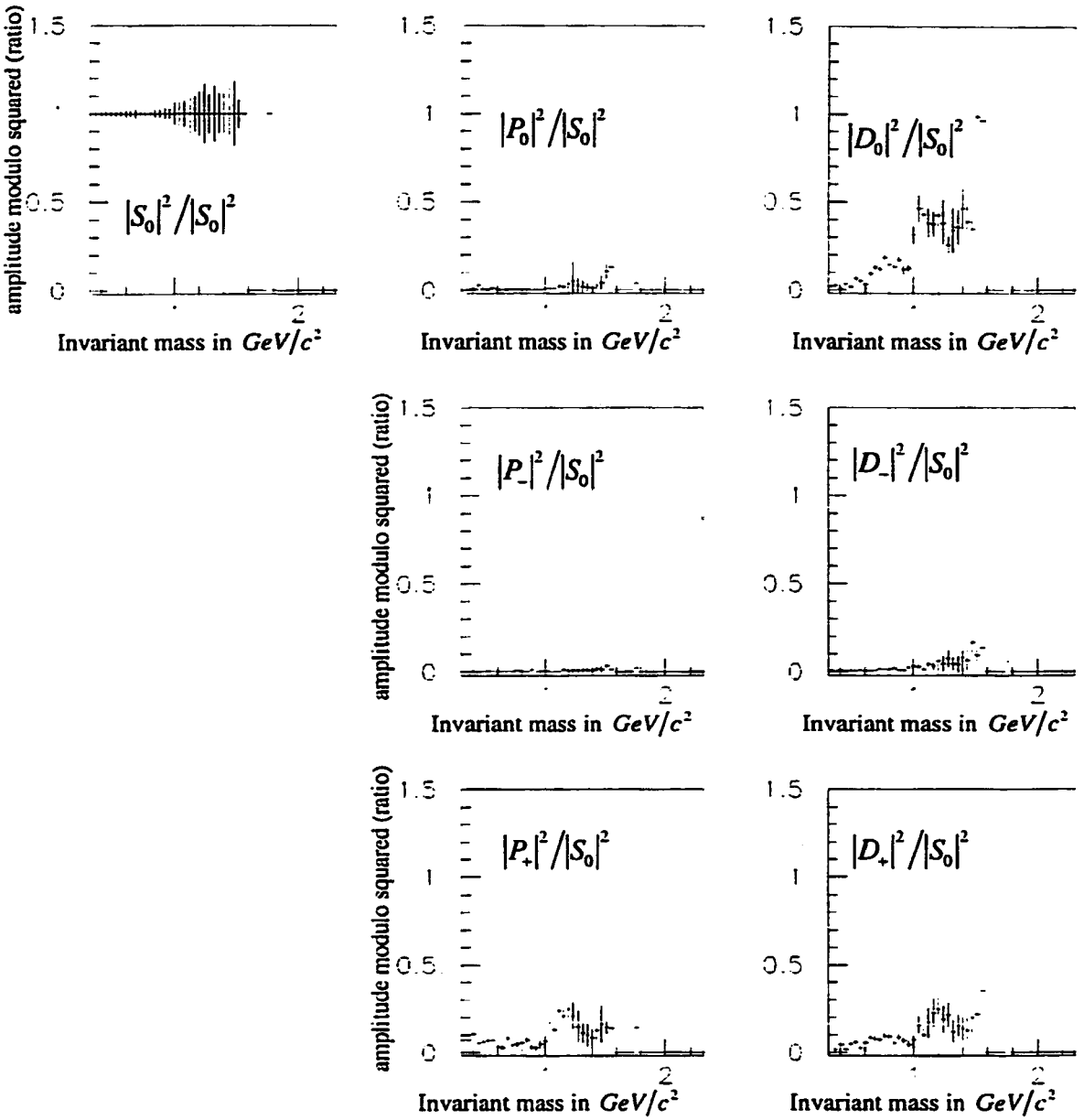

Figure 4.20 Normalized modulo squared of all solutions labeled as solution #6, plotted as a function of invariant mass. We average all labeled solutions and divide all modulo squared amplitudes by $|S_0|^2$. Although the normalized value of $|S_0|^2$ is an exact ratio, we scale and present the associated error bars in order to indicate the uncertainty in the unormalized measurement. The events used satisfy the selection criteria:

-- Vertex requirements and two (Cherenkov) pion compatible tracks in multiparticle spectrometer and x_F in the interval [-0.1,0.0].

-- -1<MPl<1 GeV/c^2.

-- Rapidity gap>1.8 between the slow proton and any one of the two pions.

-- $p_{t,f}^2, p_{t,s}^2 < 0.1\,(GeV/c)^2$. -- $-\sigma < MM^2 < \sigma$

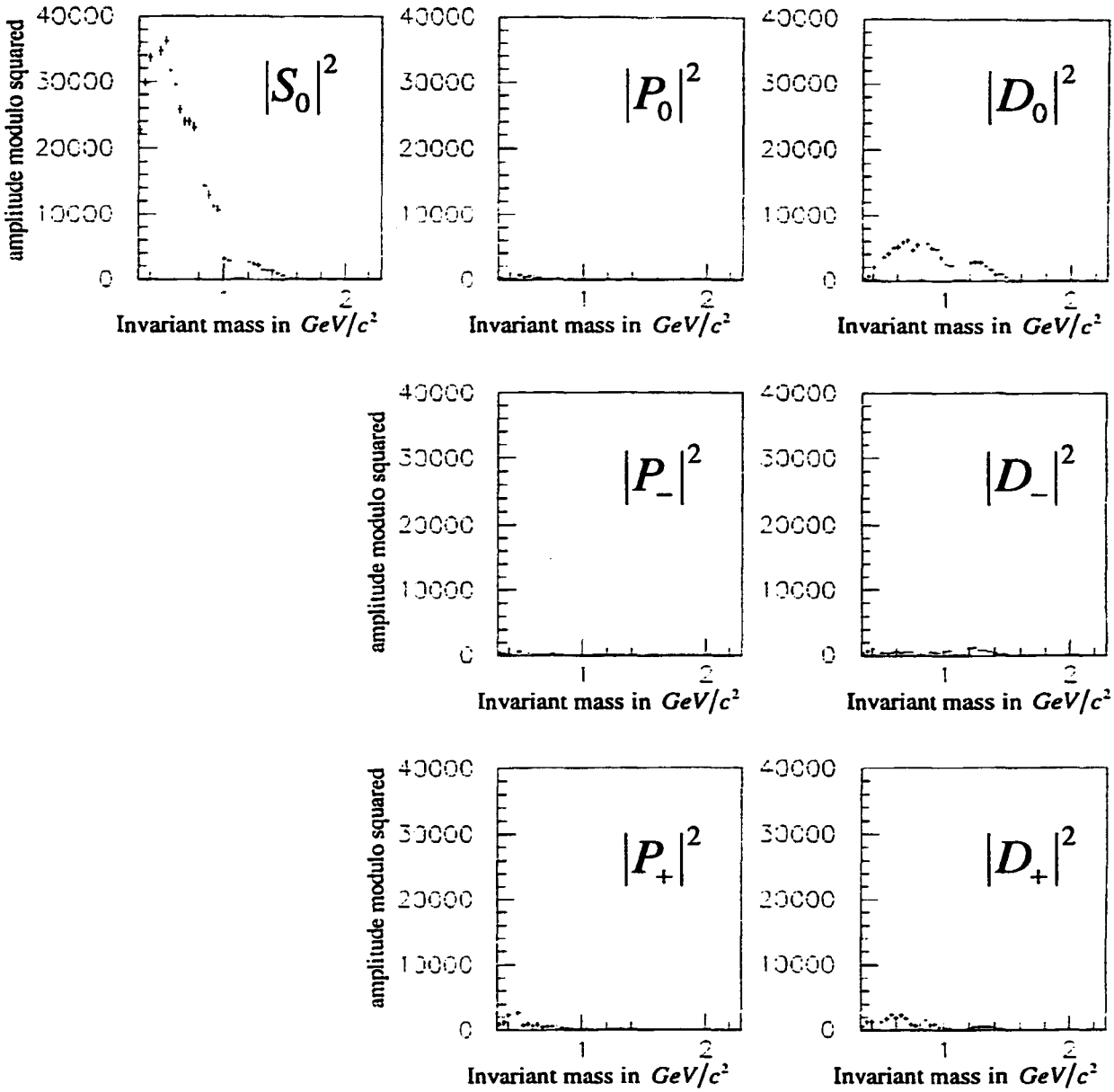

Figure 4.21 Use high p_t^2 fast protons and plot: Modulo squared of all solutions labeled as solution #6, plotted as a function of invariant mass. We average all labeled solutions. The events used satisfy the selection criteria:

-- Vertex requirements and two (Cherenkov) pion compatible tracks in multiparticle spectrometer and x_F in the interval [-0.1,0.0].

-- -1<MPl<1 GeV/c^2.

-- Rapidity gap>1.8 between the slow proton and any one of the two pions.

-- $p_{t,f}^2 > 0.1\left(GeV/c\right)^2$, $p_{t,s}^2 < 0.1\left(GeV/c\right)^2$.

-- $-\sigma < MM^2 < \sigma$

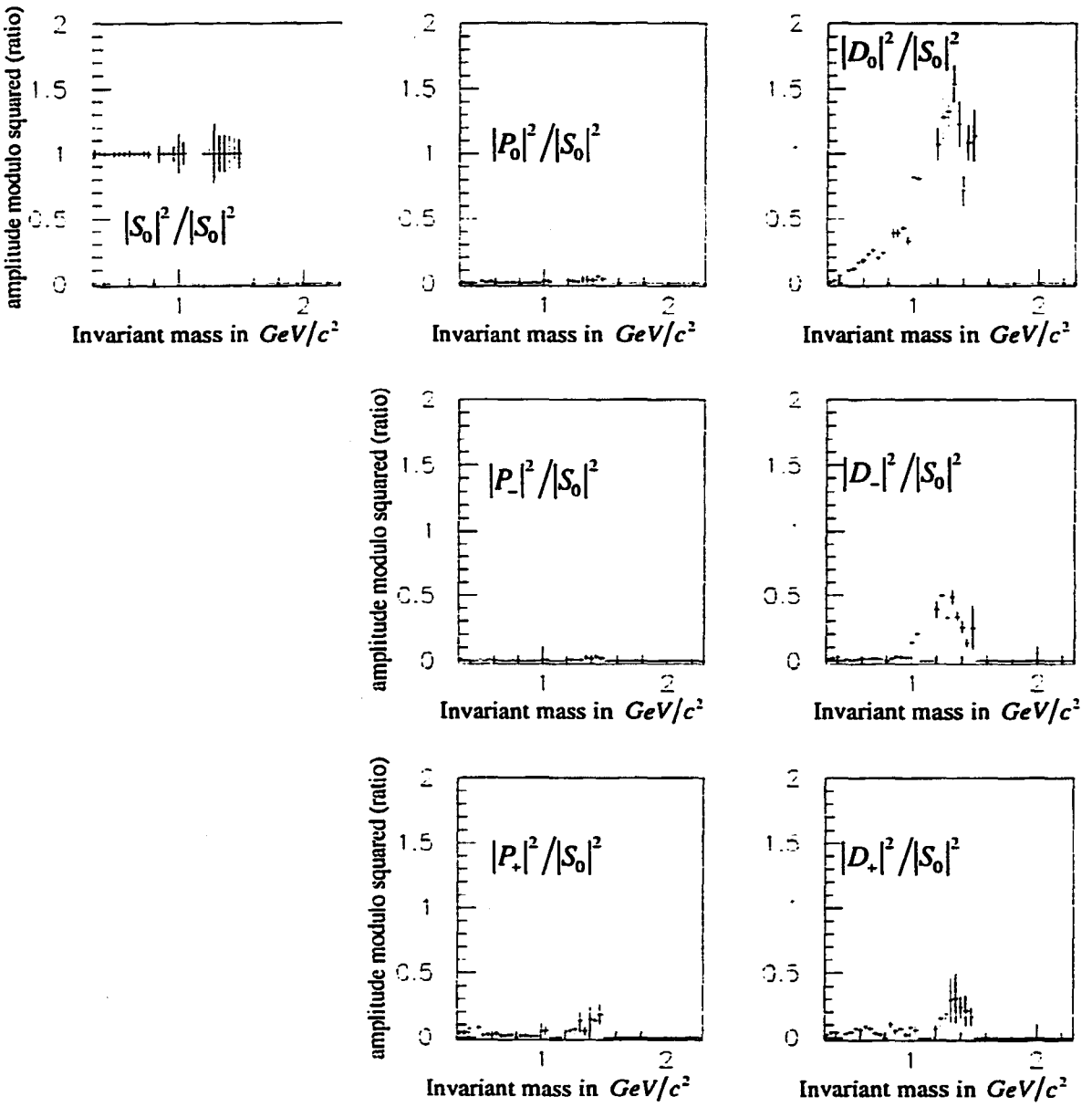

Figure 4.22 Use high p_t^2 fast protons and plot: Normalized modulo squared of all solutions labeled as solution #6, plotted as a function of invariant mass. We average all labeledsolutions and divide all modulo squared amplitudes by $|S_0|^2$ .The error bars for $|S_0|^2$ reflect the uncertainty in the determination of the unormalized value. The events used satisfy the selection criteria:

-- Vertex requirements and two (Cherenkov) pion compatible tracks in multiparticle spectrometer and x_F in the interval [-0.1,0.0].

-- -1<MPl<1 GeV/c^2.

-- Rapidity gap>1.8 between the slow proton and any one of the two pions.

-- $p_{t,f}^2 > 0.1\,(GeV/c)^2$, $p_{t,s}^2 < 0.1\,(GeV/c)^2$ -- $-\sigma < MM^2 < \sigma$

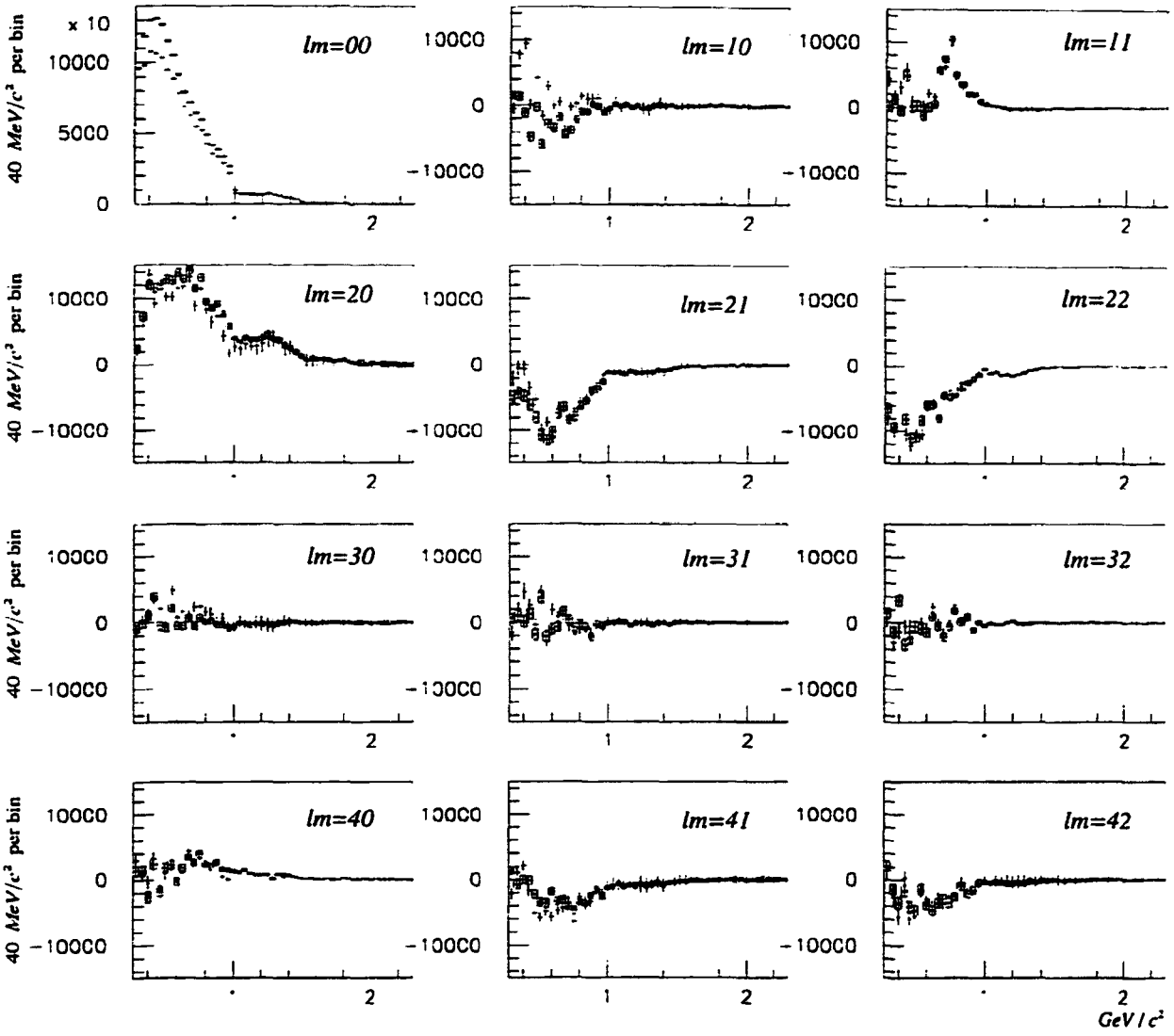

Figure 4.23 Acceptance corrected moments (t_{lm}) for two different Cherenkov ID requirements (low $p^2_{t,f}$, mass region for (X) [0.3,2.3] GeV/c^2). Boxes correspond to a sample satisfying "soft" Cherenkov ID criteria, crosses to a sample satisfying one "exactly pion" Cherenkov ID. The remaining selection criteria are:

-- Vertex requirements and x_F in the interval [-0.1,0.0].
-- -1<MPl<1 GeV/c.
-- Rapidity gap>1.8 between the slow proton and any one of the two pions.
-- $p^2_{t,f}, p^2_{t,s} < 0.1\,(GeV/c)^2$. -- $-\sigma < MM^2 < \sigma$

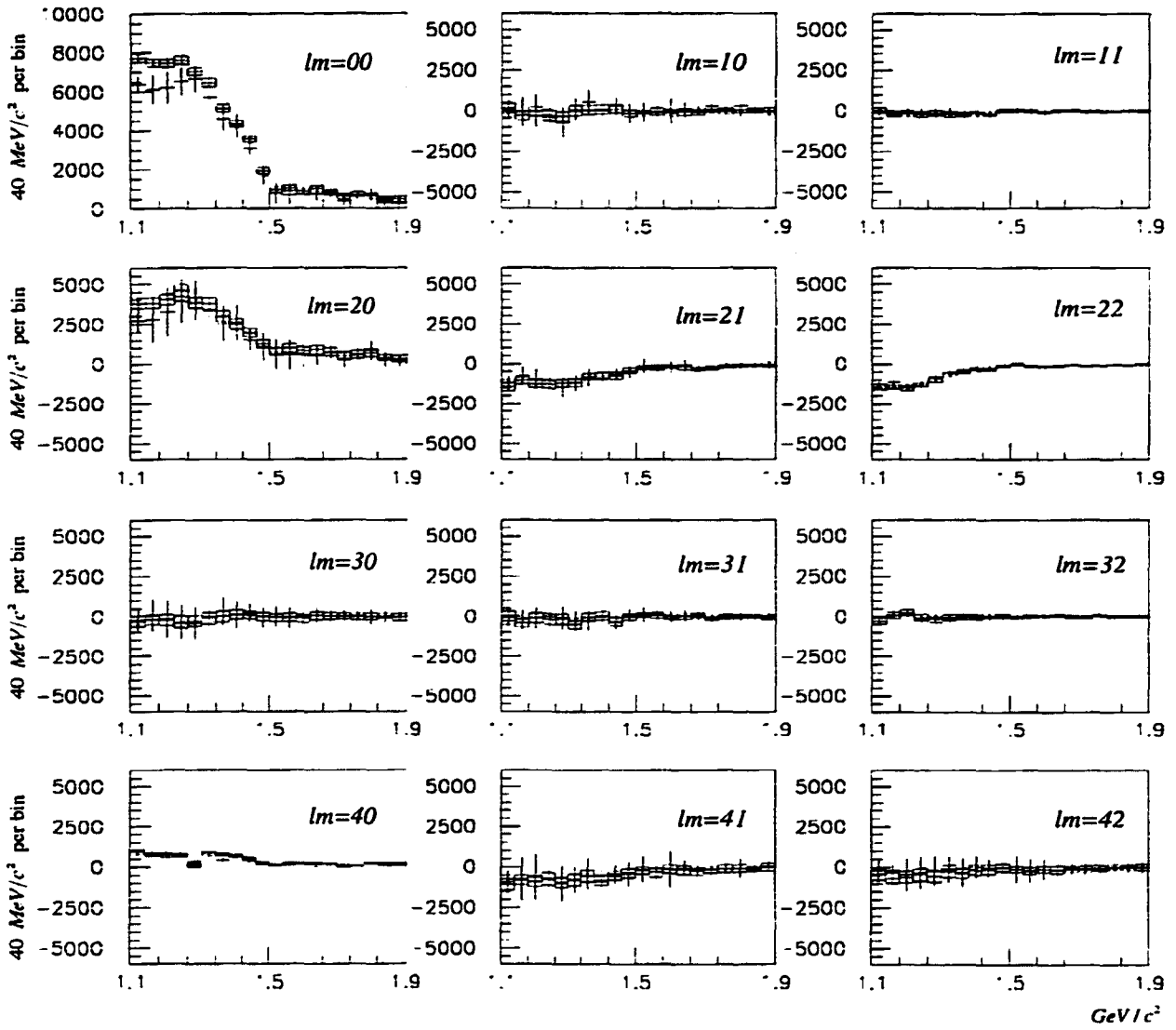

Figure 4.24 Acceptance corrected moments (t_{lm}) for two different Cherenkov ID requirements (low $p^2_{t,f}$, mass region for (X) [1.1,1.9] GeV/c^2). Boxes correspond to a sample satisfying "soft" Cherenkov ID criteria, crosses to a sample satisfying one "exactly pion" Cherenkov ID. The remaining selection criteria are:

-- Vertex requirements and x_F in the interval [-0.1,0.0].
-- -1<MPI<1 GeV/c.
-- Rapidity gap>1.8 between the slow proton and any one of the two pions.
-- $p^2_{t,f}, p^2_{t,s} < 0.1\left(GeV/c\right)^2$. -- $-\sigma < MM^2 < \sigma$

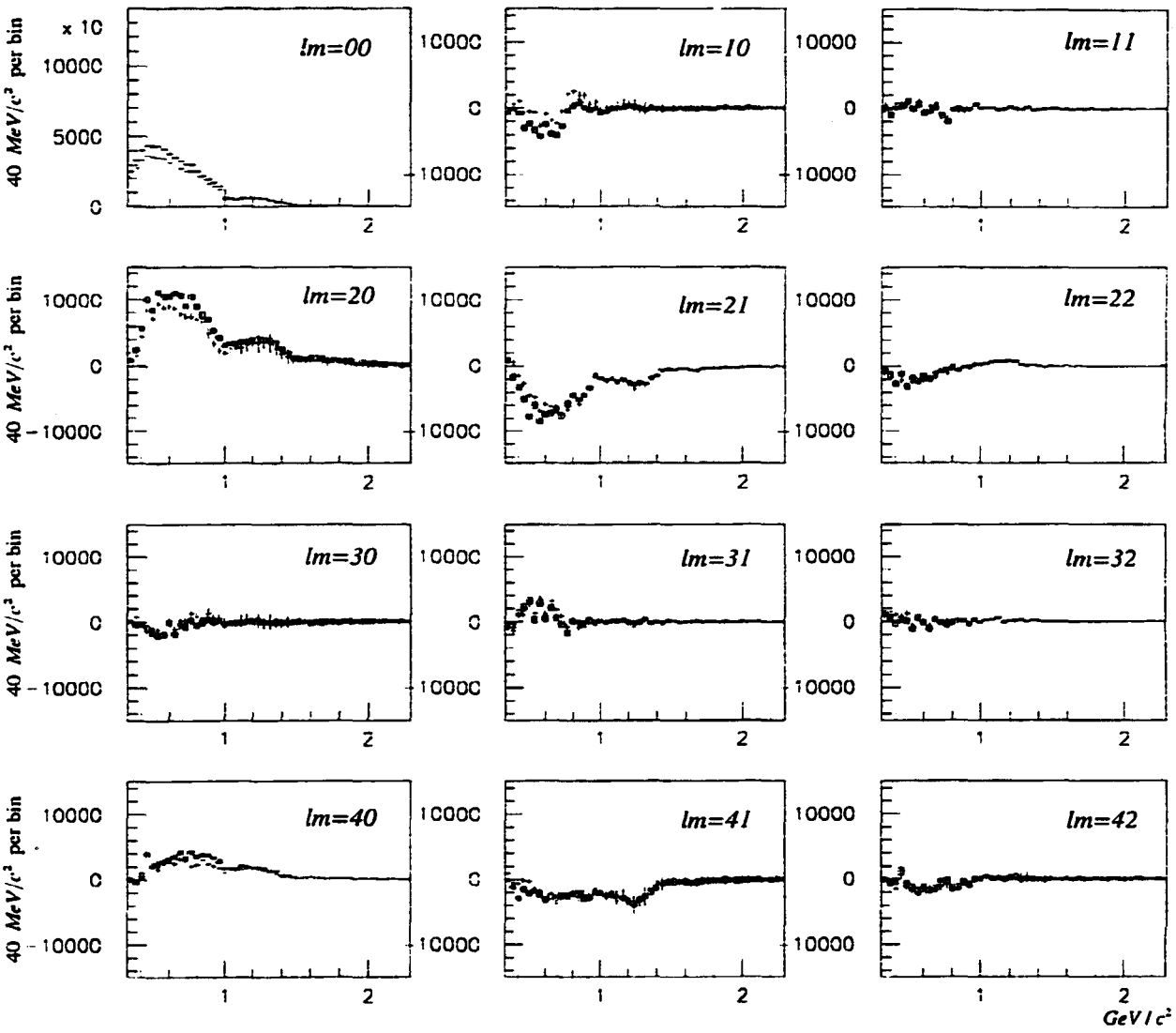

Figure 4.25 Acceptance corrected moments (t_{lm}) for two different Cherenkov ID requirements (high $p^2_{t,f}$, mass region for (X) [0.3,2.3] GeV/c^2). Boxes correspond to a sample satisfying "soft" Cherenkov ID criteria, crosses to a sample satisfying one "exactly pion" Cherenkov ID. The remaining selection criteria are:

– Vertex requirements and x_F in the interval [-0.1,0.0].

-- -1<MPl<1 GeV/c^2.

– Rapidity gap>1.8 between the slow proton and any one of the two pions.

-- $p^2_{t,f} > 0.1\,(GeV/c)^2$, $p^2_{t,s} < 0.1\,(GeV/c)^2$ -- $-\sigma < MM^2 < \sigma$

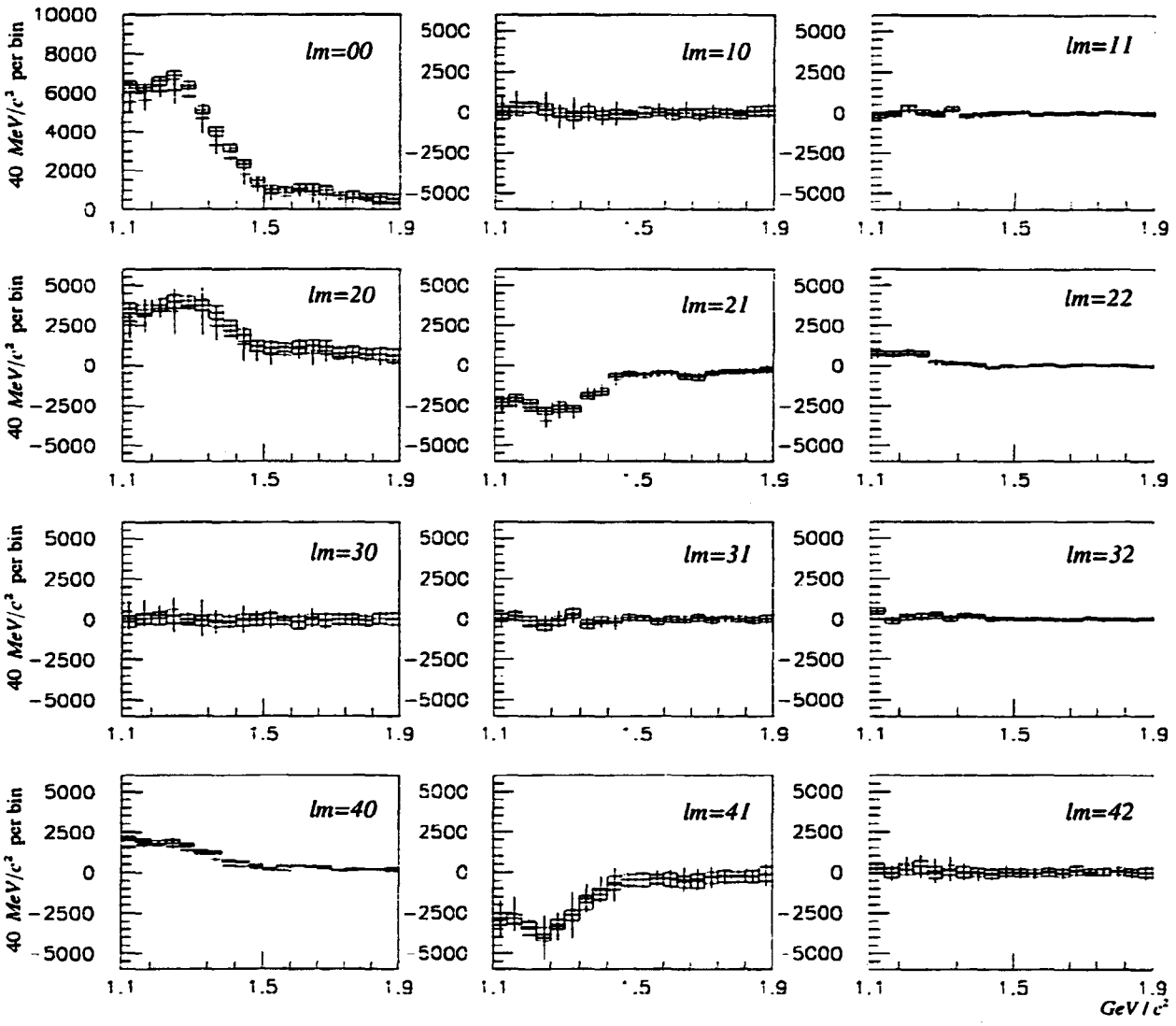

Figure 4.26 Acceptance corrected moments (t_{lm}) for two different Cherenkov ID requirements (high $p^2_{t,f}$, mass region for (X) [1.1,1.9] GeV/c^2). Boxes correspond to a sample satisfying "soft" Cherenkov ID criteria, crosses to a sample satisfying one "exactly pion" Cherenkov ID. The remaining selection criteria are:

-- Vertex requirements and x_F in the interval [-0.1,0.0].

-- -1<MPI<1 GeV/c^2.

-- Rapidity gap>1.8 between the slow proton and any one of the two pions.

-- $p^2_{t,f} > 0.1\,(GeV/c)^2$, $p^2_{t,s} < 0.1\,(GeV/c)^2$ -- $-\sigma < MM^2 < \sigma$

CHAPTER 5

CONCLUSIONS

In a study of the reaction:

$$pp \rightarrow p_{fast}(X)p_{slow}$$
$$\hookrightarrow \pi^+\pi^-$$

at $\sqrt{s} = 38.8$ GeV/c^2, where the dipion pairs are produced in the central x_F region (close to x_F=0), we find in a partial wave analysis that the S-wave is the dominant amplitude. In this analysis we find eight amplitude solutions consistent with the observed data set for dipion invariant mass up to 1.5 GeV/c^2. (For higher values of invariant mass the statistics are not adequate to perform a partial wave analysis). The assumption of S-wave dominance near threshold is sufficient to select a single, continuous solution throughout the considered mass spectrum. This result holds when we use events with small transverse momentum for both final state protons (p_t^2<0.1 (GeV/c)^2). When we allow high transverse momentum for the fast proton (p_t^2>0.1 (GeV/c)^2), we see significant D-wave contribution in the mass region above 1 GeV/c^2. The D-wave signal is due to the production of the well known $f_2(1270)$ and serves as confirmation of the amplitude analysis procedure. We avoid working with events that have high p_t^2 for the slow proton (high missing p_t^2) because we are concerned about background contamination of the sample.

Precision measurement of amplitudes produced in the reaction aid the mapping the low lying meson spectrum. The amplitudes we have measured can be used as input to phenomenological models of pion-pion scattering such as the ones by Morgan and Pennington [24,27,28] and Zou and Bugg [29]. Of even greater interest for these models is the relative cross section of pion and kaon production near $K\overline{K}$ threshold. This analysis will be combined with a similar analysis of the $K\overline{K}$ system in the same data [18] which

will provide a comprehensive analysis of the meson spectrum. The phenomenological models mentioned here do not provide a definite answer for the nature of observed resonances. They constrain the resonance identity across final state channels ($\pi\pi$ and $K\overline{K}$). Hopefully this constraint will lead to a clear assignment of observed states to the SU(3) multiplets. Having assigned the conventional states we can reliably identify extra states which would be interpreted as exotics. These measurements of central production amplitudes are interesting because of the expectation that the reaction is fertile ground for the production and observation of exotic mesons, in particular glueballs. When the four momentum transfer (t) is low for both protons, meson production is thought to be dominated by double Pomeron exchange. This exchange mechanism is the reason the reaction is considered a glue rich environment [1]. Our observation of S-wave dominance and absence of P-wave resonances (such as $\rho(770)$) are consistent with such a production mechanism.

The importance of final state channel coupling can be seen in the sharp drop of the S-wave amplitude at the M_X=1 GeV/c^2 mass region. The drop is related to the opening of the $K\overline{K}$ final state. We observe a second dramatic drop in the M_X=1.5 GeV/c^2 mass region. This is at the mass where the Crystal Barrel collaboration claims the existence of a 0^{++} glueball candidate. In an independent analysis [18] this experiment observes a 0^{++} state with the same mass and width in the $K\overline{K}$ final state. A future combined analysis will provide additional information regarding this case, although it is not as easy to develop phenomenological models in this mass region because the number of final state channels is not restricted to $\pi\pi$ and $K\overline{K}$.

Other possible studies using this data sample and analysis technique are: (1) the extension of the amplitude analysis above the 1.5 GeV/c^2 mass region and (2) the study of the produced amplitudes as a function of the relative angle between the two proton planes. As related to (1) this analysis uses only 10% of the total data sample. With a tenfold

increase in the data sample we would have sufficient statistics to study the mass region above 1.5 GeV/c^2. Study (2) is motivated by recent publications [35] which show a strong dependence of the observed states on the relative angle of the proton planes. This dependence is not explained by any production model. The excellent acceptance of our apparatus along with the high statistics data sample will allow us to make a comprehensive study of the dependencies.

APPENDIX A

METHOD OF MOMENTS
OR
LINEAR ALGEBRA METHOD

We want to determine the angular distribution of the produced events using an expansion:

$$I_{prod}(\Omega) = \sum_{\substack{l \\ m\geq 0}} t_{lm}\,\mathrm{Re}\{Y_{lm}(\Omega)\}$$

Since parity is conserved for the reaction we study, the expansion is restricted to $m \geq 0$ and the real part of the functions $Y_{lm}(\Omega)$. In the following we simply write $Y_{lm}(\Omega)$ as a shorthand for $\mathrm{Re}\{Y_{lm}(\Omega)\}$ and we compress the indices l,m to a single Greek index λ.

The detector has a limited acceptance. The observed event distribution can be written as:

$$I_{acc}(\Omega) = A(\Omega) I_{prod}(\Omega) = A(\Omega)\sum_{\lambda} t_\lambda Y_\lambda(\Omega)$$

Multiplying both sides with $Y_\mu(\Omega)$ and integrating over the solid angle:

$$\int d\Omega\, Y_\mu(\Omega) I_{acc}(\Omega) = \int d\Omega\, Y_\mu(\Omega) A(\Omega)\sum_{\lambda} t_\lambda Y_\lambda(\Omega) \Rightarrow$$

$$\int d\Omega\, Y_\mu(\Omega) I_{acc}(\Omega) = \sum_{\lambda}\left\{\int d\Omega\, Y_\mu(\Omega) A(\Omega) Y_\lambda(\Omega)\right\} t_\lambda \Rightarrow$$

$$b_\mu \qquad = \sum_{\lambda} \qquad A_{\mu\lambda} \qquad t_\lambda$$

We refer to the integrals of the accepted distribution as ***experimental moments*** , b_μ. The expansion coefficients for the produced distribution we call ***acceptance corrected moments*** , t_λ. In practice the quantity b_μ is a function of the observed events and can be obtained from (see Appendix C for the relationship between integrals and sums):

$$b_\mu = \sum_{i=1}^{N_{obs}} Y_\mu(\Omega_i)$$

The ***acceptance correlations*** $A_{\mu\lambda}$ depend on the detector acceptance only. They can be calculated using the Monte Carlo technique. First we generate $N_{mc\,gen}$ events random in the variables $\cos(\theta)$, φ. The events generated are run through the detector simulation. The result of the simulation is run through the analysis chain used for real events (track and vertex reconstruction, particle identification and analysis cuts). We use this sample to evaluate the ***acceptance correlations***:

$$A_{\mu\lambda} = \frac{1}{N_{mc\,gen}} \sum_{i=1}^{N_{mc\,obs}} Y_{\mu}(\Omega_i) Y_{\lambda}(\Omega_i)$$

Notice that we sum over the events that survive the analysis cuts $N_{mc\,obs}$ and normalize over the events generated $N_{mc\,gen}$.

Since we use randomly generated events to evaluate the ***acceptance correlations*** $A_{\mu\lambda}$, there is a statistical error associated with the computed values. For this study we generate a Monte Carlo sample ten times larger than the sample of observed events. Therefore the statistical error due to the finite size of the Monte Carlo sample is much smaller than the statistical error due to the number of observed events. In the following we do not propagate statistical errors due to the evaluation of $A_{\mu\lambda}$. We consider the calculation exact.

Given the experimental moments $\{b_{\mu}\}$ and the computed $A_{\mu\lambda}$ we want to find the best set of coefficients $\{t_{\lambda}\}$ that describe the data set. For the system of equations

$$b_{\mu} = \sum_{\lambda} A_{\mu\lambda} t_{\lambda}$$

we can limit the number of moments to λ_{max} and the number of equations to μ_{max}. If $\lambda_{max} < \mu_{max}$ we have an over constrained problem. The equality in the equation above holds only in the ideal case of infinite statistics. For sufficient statistics the $\{b_{\mu}\}$ are distributed as a multivariable Gaussian:

$$Distrib(\bar{b}) = cons \times e^{-\frac{1}{2}\chi^2} \quad , \quad \chi^2 = \mathbf{d}^T E(b)^{-1}\mathbf{d} \quad , \quad \mathbf{d} = \mathbf{b} - \bar{\mathbf{b}}$$

with error matrix

$$E(b)_{\mu\mu'} = \sum_{i=1}^{N_{obs}} Y_\mu(\Omega_i) Y_{\mu'}(\Omega_i)$$

The error matrix of the experimental moments $E(b)$ and the error matrix of the acceptance corrected moments $E(t)$

$$E(t) = A^{-1} E(b) A^{T-1}$$

are evaluated in Appendix B. Here A represents the acceptance correlations matrix. We can use the relationship between b_μ, t_λ and write

$$d_\mu \equiv b_\mu - \sum_\lambda A_{\mu\lambda} t_\lambda$$

The best fit to the data is given by the set of $\{t_\lambda\}$ that minimizes χ^2:

$$\boxed{\chi^2 \equiv \sum_{\mu\mu'} d_\mu \left[E(b)^{-1}\right]_{\mu\mu'} d_{\mu'}}$$

After some algebra:

$$\frac{\partial \chi^2}{\partial t_\kappa} = 0 \Rightarrow$$

$$\frac{\partial}{\partial t_\kappa} \sum_{\mu\mu'} \left(b_\mu - \sum_\lambda A_{\mu\lambda} t_\lambda \right) \left[E(b)^{-1}\right]_{\mu\mu'} \left(b_{\mu'} - \sum_{\lambda'} A_{\mu'\lambda'} t_{\lambda'} \right) = 0 \Rightarrow$$

$$-2 \sum_{\mu\mu'} A_{\mu\kappa} \left[E(b)^{-1}\right]_{\mu\mu'} \left(b_{\mu'} - \sum_{\lambda'} A_{\mu'\lambda'} t_{\lambda'} \right) = 0 \Rightarrow$$

$$\sum_{\mu\mu'} A_{\mu\kappa} \left[E(b)^{-1}\right]_{\mu\mu'} b_{\mu'} = \sum_{\lambda'} \left\{ \sum_{\mu\mu'} A_{\mu\kappa} \left[E(b)^{-1}\right]_{\mu\mu'} A_{\mu'\lambda'} \right\} t_{\lambda'} \Rightarrow$$

$$C_\kappa = \sum_\lambda D_{\kappa\lambda} t_\lambda$$

we get a system of λ_{max} equations with λ_{max} unknowns that can be solved using standard matrix inversion.

Examples

Although we use the same method as Grayer [26] for the acceptance corrections and the statistical analysis of the sample, there are some differences in the normalization conventions. Here I list the differences and present a few examples that make the formalism a bit more intuitive.

The definition of the expansion functions is:

$$Y_{lm}(\Omega) \equiv \mathrm{Re}\{Y_{lm}(\Omega)\} = (-1)^m \sqrt{\frac{2l+1}{4\pi}\frac{(l-m)!}{(l+m)!}} P_l^m(\cos\theta)\cos\phi$$

In the code I avoid the factor $\sqrt{\frac{1}{4\pi}}$ in the $Y_{lm}(\Omega)$ definition. As a result my conventions differ from Grayer's:

Grayer paper	my code
$Y_{lm}(\Omega)$	$\sqrt{4\pi}Y_{lm}(\Omega)$
t_{lm}	$\frac{1}{\sqrt{4\pi}} t_{lm}$
$A_{\lambda\mu} = \frac{4\pi}{N_{mc\,gen}} \sum_{i=1}^{N_{mc\,obs}} Y_\mu(\Omega_i) Y_\lambda(\Omega_i)$	$A_{\lambda\mu} = \frac{1}{N_{mc\,gen}} \sum_{i=1}^{N_{mc\,obs}} Y_\mu(\Omega_i) Y_\lambda(\Omega_i)$

The conventions above leave the intensity expansion unaltered:

$$I_{prod}(\Omega) = \sum_{\substack{l \\ m\geq 0}} t_{lm} Y_{lm}(\Omega)$$

but the integral of the produced distributions

$$\int I_{prod}(\Omega) d\Omega = t_{00} = N_{prod}$$

is different in my code than the Grayer convention $N_{prod} = \sqrt{4\pi} t_{00}$. The values of the acceptance correlations $A_{\mu\lambda}$ are identical for the two normalization conventions.

The use of the real part of the $Y_{lm}(\Omega)$ and the normalization convention leads to the orthogonality relation:

$$\int d\Omega \mathrm{Re}\{Y_{lm}(\Omega)\}\mathrm{Re}\{Y_{l'm'}(\Omega)\} = \delta_{lml'm'}\varepsilon(m), \quad \varepsilon(m)\begin{cases}1 & m=0\\ 1/2 & m\neq 0\end{cases}$$

From the orthogonality relation and the definition of t_λ, b_λ, we see that the expansions for $I_{prod}(\Omega)$, $I_{acc}(\Omega)$ are different

$$I_{prod}(\Omega) = \sum_{\substack{l\\ m\geq 0}} t_{lm}\,\mathrm{Re}\{Y_{lm}(\Omega)\}$$

$$I_{obs}(\Omega) = \sum_{\substack{l\\ m\geq 0}} b_{lm}\frac{1}{\varepsilon(m)}\mathrm{Re}\{Y_{lm}(\Omega)\}$$

The relation between t_λ and b_λ is illustrated by a trivial example. For acceptance independent of the solid angle we get:

$$A_{\lambda\mu} = A\delta_{\lambda\mu}\varepsilon(m), \qquad \varepsilon(m)=\begin{cases}1 & m=0\\ 1/2 & m\neq 0\end{cases}, \qquad \lambda \leftrightarrow l,m$$

where A is the acceptance for the particular analysis bin and it is a constant. In this case the equations that minimize χ^2 become:

$$\sum_{\mu\mu'} A_{\mu\kappa}\left[E(b)^{-1}\right]_{\mu\mu'} b_{\mu'} = \sum_{\lambda'}\left\{\sum_{\mu\mu'} A_{\mu\kappa}\left[E(b)^{-1}\right]_{\mu\mu'} A_{\mu'\lambda'}\right\} t_{\lambda'} \Rightarrow$$

$$\sum_{\mu\mu'} A\varepsilon(\kappa)\delta_{\mu\kappa}\left[E(b)^{-1}\right]_{\mu\mu'} b_{\mu'} = \sum_{\lambda'}\left\{\sum_{\mu\mu'} A\varepsilon(\mu)\delta_{\mu\kappa}\left[E(b)^{-1}\right]_{\mu\mu'} A\varepsilon(\mu')\delta_{\mu'\lambda'}\right\} t_{\lambda'} \Rightarrow$$

$$A\varepsilon^{\kappa}\sum_{\mu'}\left[E(b)^{-1}\right]_{\kappa\mu'} b_{\mu'} = A\varepsilon^{\kappa}\sum_{\mu'} A\varepsilon(\mu')\left[E(b)^{-1}\right]_{\kappa\mu'} t_{\mu'} \Rightarrow$$

$$\sum_{\mu'}\left[E(b)^{-1}\right]_{\kappa\mu'} b_{\mu'} = \sum_{\mu'} A\varepsilon(\mu')\left[E(b)^{-1}\right]_{\kappa\mu'} t_{\mu'}$$

so that for a non-singular $E(b)$:

$$t_\mu = \frac{1}{A\varepsilon(\mu)} b_\mu \quad \text{and} \quad t_{00} = \frac{1}{A} N_{obs}$$

If in addition we require that data are evenly distributed in solid angle:

$$E(b)_{\mu\mu'} = \sum_{i=1}^{N_{obs}} Y_{\mu}(\Omega_i) Y_{\mu'}(\Omega_i) = \delta_{\mu\mu'} \varepsilon(\mu) N_{obs} \Rightarrow$$

$$\sigma(b)_{\mu\mu'} \equiv \sqrt{E(b)_{\mu\mu'}} = \delta_{\mu\mu'} \sqrt{\varepsilon(\mu) N_{obs}} = \delta_{\mu\mu'} \begin{cases} \sqrt{N_{obs}} & m = 0 \\ \sqrt{N_{obs}/2} & m \neq 0 \end{cases}$$

and for the acceptance corrected moments we find:

$$E(t) = A^{-1} E(b) A^{T-1} \Rightarrow$$

$$E(t)_{\mu\mu'} = \sum_{\lambda\lambda'} A^{-1}_{\mu\lambda} E(b)_{\lambda\lambda'} A^{-1}_{\mu'\lambda'} \Rightarrow$$

$$E(t)_{\mu\mu'} = \sum_{\lambda\lambda'} \frac{1}{A\varepsilon^{\mu}} \delta_{\mu\lambda} \delta_{\lambda\lambda'} \varepsilon(\lambda) N_{obs} \frac{1}{A\varepsilon(\mu')} \delta_{\mu'\lambda'} \Rightarrow$$

$$E(t)_{\mu\mu'} = \delta_{\mu\mu'} \frac{1}{A} \frac{\varepsilon(\mu) N_{obs}}{\varepsilon(\mu)} \frac{1}{\varepsilon(\mu)} \frac{1}{A}$$

and

$$\sigma(t)_{\mu\mu'} \equiv \sqrt{E(t)_{\mu\mu'}} = \delta_{\mu\mu'} \frac{1}{A} \sqrt{\frac{N_{obs}}{\varepsilon^{\mu}}} = \delta_{\mu\mu'} \frac{1}{A} \begin{cases} \sqrt{N_{obs}} & m = 0 \\ \sqrt{2N_{obs}} & m \neq 0 \end{cases}$$

APPENDIX B

ERROR MATRIX

For a multivariable Gaussian distribution with independent parameters the event distribution is

$$G(\mathbf{u}) = \prod_{i=1}^{n} G(u_\lambda) = cons \times e^{-\frac{1}{2}S}, \quad cons = \frac{1}{\prod_{i=1}^{n} (2\pi\sigma_\lambda^2)^{1/2}}, \quad \text{and} \quad S = \sum_{\lambda=1}^{n} \frac{u_\lambda^2}{\sigma_\lambda^2} = \mathbf{u}^T (\sigma^2)^{-1} \mathbf{u}$$

We can transform to the case of correlated errors with a unitary transformation to another set of variables.

$$\mathbf{d} = \mathbf{U}\mathbf{u} \quad \Rightarrow \quad \mathbf{u} = \mathbf{U}^{-1}\mathbf{d} = \mathbf{U}^{\mathbf{T}}\mathbf{d}$$

where we have used the fact that since $\mathbf{u}$ and $\mathbf{d}$ are real, the transformation matrix $\mathbf{U}$ is also real. Then

$$S = \mathbf{u}^T (\sigma^2)^{-1} \mathbf{u} = \mathbf{d}^T [\mathbf{U} (\sigma^2)^{-1} \mathbf{U}^T] \mathbf{d} = \mathbf{d}^T E^{-1} \mathbf{d} \quad , \text{ with } \quad E^{-1} = \mathbf{U} (\sigma^2)^{-1} \mathbf{U}^T$$

and the matrix E is related to the standard deviations as follows

$$\begin{aligned} \langle d_\mu d_\nu \rangle &= \int_{-\infty}^{\infty} d_\mu d_\nu G(\vec{d}) \; d^n(\vec{d}) \\ &= \int_{-\infty}^{\infty} \Big(\sum_{\mu'\nu'} U_{\mu\mu'} u_{\mu'} U_{\nu\nu'} u_{\nu'} \Big) \; G(\vec{u}) \; d^n\vec{u} \\ &= \sum_{\mu'} U_{\mu\mu'} U_{\nu\mu'} \sigma_{\mu'}^2 = (\mathbf{U}\, \sigma^2\, \mathbf{U}^T)_{\mu\nu} = E_{\mu\nu} \end{aligned}$$

Therefore in the correlated case the Gaussian is given by

$$G(\vec{d}) = cons \times e^{-\frac{1}{2}S} \quad , \text{ with } \quad S = \mathbf{d}^T E^{-1} \mathbf{d} \quad , \text{ and } \quad E_{\mu\nu} = \langle d_\mu d_\nu \rangle$$

Here we have assumed that $\langle d_\mu \rangle = 0$. For a distribution not centered at zero we can use $d_\mu = b_\mu - \bar{b}_\mu$. Since displacement of the central values does not alter the distribution, the error matrix is the same for both sets of parameters.

In principle, to calculate the error matrix $E(b)$ we need to repeat the experiment an infinite number of times and calculate the standard deviations. Let's consider an infinite number of experiments with N_{obs} measurements for each experiment.

$$\begin{array}{llll}
\Omega_1^1 \quad \Omega_2^1 \quad . \; . \; . \quad \Omega_{N_{obs}}^1 & \rightarrow & b_\mu^1 = \sum_{k=1}^{N_{obs}} Y_\mu(\Omega_k^1) \\
\Omega_1^2 \quad \Omega_2^2 \quad . \; . \; . \quad \Omega_{N_{obs}}^2 & \rightarrow & b_\mu^2 = \sum_{k=1}^{N_{obs}} Y_\mu(\Omega_k^2) \\
\quad . \quad . \quad . & & . \\
\Omega_1^r \quad \Omega_2^r \quad . \; . \; . \quad \Omega_{N_{obs}}^r & \rightarrow & b_\mu^r = \sum_{k=1}^{N_{obs}} Y_\mu(\Omega_k^r) \\
\quad . \quad . \quad . & & . \\
\quad . \quad . \quad . & & .
\end{array}$$

From the definition of the error matrix

$$E(b)_{\mu\nu} = \frac{1}{N_r}\sum_{r=1}^{N_r}\left[(b_\mu^r - \bar{b}_\mu)(b_\nu^r - \bar{b}_\nu)\right] = \frac{1}{N_r}\left\{\sum_{r=1}^{N_r} b_\mu^r b_\nu^r\right\} - \bar{b}_\mu \bar{b}_\nu \quad , \text{ with } N_r \rightarrow \infty$$

For convenience in the proof that follows, we use two normalization conventions for the expected values of b_μ

$$\left.\begin{array}{l}
\bar{b}_\mu = \frac{1}{N_r}\sum_{r=1}^{N_r} b_\mu^r = \frac{1}{N_r}\sum_{r=1}^{N_r}\sum_{i=1}^{N_{obs}} Y_\mu(\Omega_i^r) \\
\langle b_\mu \rangle = \frac{1}{N_r N_{obs}}\sum_{r=1}^{N_r}\sum_{i=1}^{N_{obs}} Y_\mu(\Omega_i^r)
\end{array}\right\} \Rightarrow \quad \bar{b}_\mu = N_{obs}\langle b_\mu \rangle$$

We can rewrite the error matrix

$$\begin{aligned}
E(b)_{\mu\nu} &= \frac{1}{N_r}\left\{\sum_r\sum_{ij} Y_\mu(\Omega_i^r) Y_\nu(\Omega_j^r)\right\} - \bar{b}_\mu \bar{b}_\nu = \\
&= \frac{1}{N_r}\left\{\sum_r\sum_{i=j} Y_\mu(\Omega_i^r)\, Y_\nu(\Omega_j^r) + \sum_r\sum_{i\neq j} Y_\mu(\Omega_i^r)\, Y_\nu(\Omega_j^r)\right\} - \bar{b}_\mu \bar{b}_\nu = \\
&= \frac{1}{N_r}\left\{\sum_r\sum_{i} Y_\mu(\Omega_i^r)\, Y_\nu(\Omega_i^r) + N_{obs}N_r(N_{obs}-1)\langle b_\mu\rangle\langle b_\nu\rangle\right\} - \bar{b}_\mu \bar{b}_\nu
\end{aligned}$$

This is the result for a collection of experiments with a fixed number of observed events, N_{obs}. If we allow N_{obs} to be Poison distributed

$$E(b)_{\mu\nu} = \frac{1}{N_r}\left\{\sum_r\sum_{i=j} Y_\mu(\Omega_i^r)\, Y_\nu(\Omega_j^r)\right\} + \bar{b}_\mu \bar{b}_\nu - \bar{b}_\mu \bar{b}_\nu$$

The steps above require more explanation. We start the proof assuming a collection of experiments with exactly the same number of observed events, N_{obs}. We divide the calculation of

$$\frac{1}{N_r}\left\{\sum_r \sum_{ij} Y_\mu(\Omega_i^r) Y_\nu(\Omega_j^r)\right\}$$

to two cases: $i \neq j$ and $i = j$.

For the case $i \neq j$ we group the summation over r into m sums with n terms each.

$$\frac{1}{N_r}\sum_{\{m\}}\sum_{\{n\}}\sum_{i\neq j} Y_\mu(\Omega_i^{nm})\, Y_\nu(\Omega_j^{nm})$$

We group together n experiments that have **one** of the N_{obs} events with parameters Ω infinitely close. I give to this event from group m the index k. Then we can rearrange the sum.

$$\sum_{\{m\}}\sum_{\{n\}}\left\{Y_\mu(\Omega_k^{nm})\sum_{j\neq k} Y_\mu(\Omega_j^{nm}) + \sum_{\substack{i\neq k\\ i\neq j}} Y_\mu(\Omega_i^{nm}) Y_\nu(\Omega_j^{nm})\right\} =$$

$$\sum_{\{m\}}\left\{Y_\mu(\Omega_k^{nm})\sum_{\{n\}}\sum_{j\neq k} Y_\mu(\Omega_j^{nm}) + \sum_{\{n\}}\sum_{\substack{i\neq k\\ i\neq j}} Y_\mu(\Omega_i^{nm}) Y_\nu(\Omega_j^{nm})\right\}$$

Now we perform only the summation over n for the first of the terms in brackets. Since the rest of the events are not correlated and n can be arbitrarily large, the result of the summation is $n\langle b_\nu\rangle$.

$$\frac{1}{N_r}\sum_{\{m\}}\left\{Y_\mu(\Omega_k^{nm})\sum_{j\neq k} n\langle b_\nu\rangle + \sum_{\{n\}}\sum_{\substack{i\neq k\\ i\neq j}} Y_\mu(\Omega_i^{nm}) Y_\nu(\Omega_j^{nm})\right\} =$$

$$= \frac{1}{N_r}\sum_{\{m\}}\left\{Y_\mu(\Omega_k^{nm})(N_{obs}-1)n\langle b_\nu\rangle + \sum_{\{n\}}\sum_{\substack{i\neq k\\ i\neq j}} Y_\mu(\Omega_i^{nm}) Y_\nu(\Omega_j^{nm})\right\}$$

and summation over m

$$\frac{1}{N_r}(N_{obs}-1)n\langle b_\nu\rangle\sum_{\{m\}}\left\{Y_\mu(\Omega_k^{nm})\right\} + \frac{1}{N_r}\sum_{\{m\}}\left\{\sum_{\{n\}}\sum_{\substack{i\neq k\\ i\neq j}} Y_\mu(\Omega_i^{nm})Y_\nu(\Omega_j^{nm})\right\} =$$

$$=\frac{1}{N_r}nm(N_{obs}-1)\langle b_\mu\rangle\langle b_\nu\rangle + \frac{1}{N_r}\sum_{\{m\}}\left\{\sum_{\{n\}}\sum_{\substack{i\neq k\\ i\neq j}} Y_\mu(\Omega_i^{nm})Y_\nu(\Omega_j^{nm})\right\}$$

We started with $N_{obs}(N_{obs}-1)$ products of $Y_\mu(\Omega_i^r)Y_\nu(\Omega_j^r)$ and we separated the sum into two terms with $(N_{obs}-1)$ and $(N_{obs}-1)(N_{obs}-1)$ products each. We can repeat the same procedure for as many values the index k can take. That is N_{obs} times. We will get the same result in every iteration. So after we take into account that $N_r = nm$, we can rewrite the sum

$$\frac{1}{N_r}\sum_r\sum_{i\neq j} Y_\mu(\Omega_i^r)\,Y_\nu(\Omega_j^r) = N_{obs}(N_{obs}-1)\langle b_\mu\rangle\langle b_\nu\rangle$$

So far, we assumed that the number of observed events is fixed. We can consider the case above a subset of a collection of s groups of experiments with a fixed number of observed events (N_{obs}^s) in each group. The proof above applies for each one of the groups.

$$\frac{1}{N_r}\sum_r\sum_{i\neq j} Y_\mu(\Omega_i^t)\,Y_\nu(\Omega_j^t) = \frac{1}{N_s}\sum_s\left(\left(N_{obs}^t\right)^2 - N_{obs}^t\right)\langle b_\mu\rangle\langle b_\nu\rangle$$

$$=\langle b_\mu\rangle\langle b_\nu\rangle\frac{1}{N_s}\sum_s\left(\left(N_{obs}^t\right)^2 - N_{obs}^t\right)$$

In addition, we assume that the number of experiments in each group follows a Poisson distribution with average $\langle N_{obs}^s\rangle = N_{obs}$. For such a distribution

$$\left\langle {N_{obs}^s}^2\right\rangle = \left\langle N_{obs}^s\right\rangle^2 + \left\langle N_{obs}^s\right\rangle$$

With this substitution

$$\frac{1}{N_r}\sum_r\sum_{i\neq j} Y_\mu(\Omega_i^t)\,Y_\nu(\Omega_j^t) = \left\langle N_{obs}^s\right\rangle^2\langle b_\mu\rangle\langle b_\nu\rangle = \bar{b}_\mu\,\bar{b}_\nu$$

In conclusion

$$E(b)_{\mu\nu} = \frac{1}{N_r}\left\{\sum_r\sum_i Y_\mu(\Omega_i^r)\,Y_\nu(\Omega_i^r)\right\}$$

Since we perform the experiment only once, the best estimate of the error matrix is given by:

$$\boxed{E(b)_{\mu\nu} = \sum_i Y_\mu(\Omega_i) Y_\nu(\Omega_i)}$$

Error matrix $E(t)$

To find the error matrix for the ***acceptance corrected moments*** $E(t)$. we use the transformation $b_\mu = \sum_\lambda A_{\mu\lambda} t_\lambda$.

$$E(b)_{\mu\nu} = \frac{1}{N_r} \sum_{r=1}^{N_r} [b_\mu^r b_\nu^r - \bar{b}_\mu \bar{b}_\nu] =$$

$$= \frac{1}{N_r} \sum_{r=1}^{N_r} \left[\left(\sum_{\mu'} A_{\mu\mu'} t_{\mu'}^r \right) \left(\sum_{\nu'} A_{\nu\nu'} t_{\nu'}^r \right) \right] - \frac{1}{N_r} \sum_{r=1}^{N_r} \left[\left(\sum_{\mu'} A_{\mu\mu'} \bar{t}_{\mu'}^r \right) \left(\sum_{\nu'} A_{\nu\nu'} \bar{t}_{\nu'}^r \right) \right]$$

For both terms we can rearrange the summation

$$E(b)_{\mu\nu} = \sum_{\mu'\nu'} A_{\mu\mu'} A_{\nu\nu'} \left\{ \frac{1}{N_r} \sum_{r=1}^{N_r} \left[t_{\mu'}^r t_{\nu'}^r - \bar{t}_{\mu'}^r \bar{t}_{\nu'}^r \right] \right\}$$

The term in brackets is the definition of the error matrix for the acceptance corrected moments $E(t)_{\mu'\nu'}$. Therefore,

$$\boxed{E(b)_{\mu\nu} = \sum_{\mu'\nu'} A_{\mu\mu'} A_{\nu\nu'} E(t)_{\mu'\nu'}}$$

Finally, we can write in matrix notation

$$E(b)_{\mu\mu'} = \mathrm{A} E(t) \mathrm{A}^T \Rightarrow$$

$$E(t) = \mathrm{A}^{-1} E(b) \mathrm{A}^{T^{-1}} \Rightarrow$$

$$\boxed{E(t) = \left[\mathrm{A}^T E(b)^{-1} \mathrm{A} \right]^{-1}}$$

APPENDIX C

INTEGRATION WITH A DISCRETE SAMPLE

We described the linear algebra method using integrals over continuous variables $\cos\theta, \varphi$. In practice we observe a discrete sample of events with parameters $\cos\theta, \varphi$. The event distribution intensity can be written as:

$$I_{acc}(\Omega) = \sum_{i=1}^{N_{obs}} \delta(\Omega - \Omega_i)$$

This definition has the correct normalization:

$$\int d\Omega\, I_{acc}(\Omega) = \int d\Omega \sum_{i=1}^{N_{obs}} \delta(\Omega - \Omega_i) = N_{obs}$$

and all integrals involving angular distribution have to be replaced by sums over the observed events. For example, the definition of the experimental moments is:

$$b_\mu = \int d\Omega\, Y_\mu(\Omega) I_{acc}(\Omega) = \int d\Omega\, Y_\mu(\Omega) \sum_{i=1}^{N_{obs}} \delta(\Omega - \Omega_i) = \sum_{i=1}^{N_{obs}} Y_\mu(\Omega_i)$$

The acceptance moments were defined as

$$A_{\mu\lambda} = \int d\Omega\, Y_\mu(\Omega) A(\Omega) Y_\lambda(\Omega)$$

We perform the integration using the Monte Carlo method. We generate events uniformly distributed in solid angle and run them through a model of the detector. The Monte Carlo events are subject to the same reconstruction and analysis selection procedure as the real data. For a given bin in $\cos\theta, \varphi$ the acceptance function $A(\Omega)$ is given by the ratio of the number of events accepted by the analysis procedure to the number of events produced. The value of the acceptance moments can be obtained with numerical integration over bins of solid angle. Specifically:

$$A_{\mu\lambda} = \frac{1}{N_{bins}} \sum_{i=1}^{N_{bins}} n_i Y_\mu(\Omega_i) Y_\lambda(\Omega_i)$$

where n_i is the number of events that survive the analysis cuts in bin i. Alternatively we can sum over events observed.

$$A_{\mu\lambda} = \frac{1}{N_{prod}} \sum_{i=1}^{N_{obs}} Y_\mu(\Omega_i) Y_\lambda(\Omega_i)$$

BIBLIOGRAPHY

1. D. Robson, Nucl.Phys. **B130**, 328 (1977).
2. F.E Close, Rep. Prog. Phys. **51**, 833 (1988).
3. Particle Data Group, Phys. Rev. **D54**, 98 (1996).
4. C. Dionisi *et al.*, Nucl.Phys. **B169**, 1 (1980).
5. C. Edwards *et al.*, Phys.Rev.Lett. **49**, 259 (1982), Erratum-*ibid.* **50**, 219 (1983).
6. D. Aston *et al.*, Phys.Rev. **D32**, 2255 (1985).
7. T.A. Armstrong *et al.*, Z.Phys. **C34**, 23 (1987).
8. M.A. Sosa, Thesis, University of Guanajuato, Mexico (1995), article submitted to Phys. Rev. Lett.
9. G.B. West, Phys.Rev.Lett. **77**, 2622 (1996).
10. G.S. Bali *et al.*, Phys.Lett. **B309**, 378 (1993).
11. J. Sexton, A. Vaccarino, D. Weingarten, Phys.Rev.Lett. **75** 4563 (1995).
    H. Chen *et al.*, Nucl.Phys.Proc.Suppl. **34**, 357 (1994).
12. D. Alde *et al.*, Nucl.Phys. **B269**, 485 (1986).
13. C. Amsler *et al.*, Phys.Lett. **B291**, 347 (1992).
14. C. Amsler *et al.*, Phys.Lett. **B355**, 425 (1995).
15. R.M. Baltrusaitis *et al.*, Phys.Rev.Lett. **56**, 107 (1986).
16. L. Chen *et al.*, SLAC-PUB-5669 (1991).
17. T.A. Armstrong *et al.*, Phys.Lett. **B227**, 186 (1989).
18. M.A. Reyes *et al.*, FERMILAB-PUB-97-223-E (1997). Submitted to Phys. Rev. Lett.
19. D. Aston *et al.*, Nucl.Phys. **B301**, 525 (1988).
20. D.H. Weingarten, Sci.Am. **274,** 104 (1996).
21. D. Weingarten, Nucl.Phys.Proc.Suppl. **53**, 232 (1997), e-Print Archive: hep-lat/9608070.

22. N. A. Tornqvist, Z.Phys. **C68**, 647 (1995).

23. C. Amsler and F.E. Close, Phys.Lett. **B353**, 385 (1995).

24. K.L. Au , D. Morgan, M.R. Pennington, Phys.Rev. **D35**, 1633 (1987).

25. T. Akesson *et al.*, Nucl.Phys. **B264**, 154 (1986).

26. G. Grayer *et al.*, Nuclear Physics **B75**, 189 (1974).

27. D. Morgan, M.R. Pennington, Phys.Rev. **D48**, 1185 (1993).

28. D. Morgan, M.R. Pennington, Phys.Rev. **D48**, 5422 (1993).

29. B.S. Zou, D.V. Bugg, Phys. Rev. **D48**, 3948 (1993).

30. T.A. Armstrong, *et al.*, Z.Phys. **C51**, 351 (1991).

31. T.A. Armstrong, *et al.*, Phys.Lett. **B353**, 589 (1995).

32. A. Breakstone, *et al.*, Z.Phys. **C48**, 569 (1990).

33. D. Barberis, *et al.*, Phys.Lett. **B388**, 853 (1996).

34. D. Barberis, *et al.*, CERN-PPE-96-197, Submitted to Phys. Lett.

35. F. E. Close, A. Kirk , RAL-96-101, e-Print Archive: hep-ph/9701222.

36. J. A. Crittenden *et al.*, IEEE Trans. on Nucl. Sci. **NS-31**, 1028 (1984).

37. E. P. Hartouni *et al.*, IEEE Trans. on Nucl. Sci. **NS-36**, 1480 (1989).

38. E. P. Hartouni *et al.*, Nucl. Instr. Meth. **A317**, 161 (1992).

39. E. P. Hartouni *et al.*, Phys. Rev. Lett. **72**, 1322 (1994).

40 S. Y. Lee, Thesis, University of Massachusetts, UMAHEP-409 (1994) (unpublished).

41. J. Uribe *et al.*, Phys. Rev. **D49**, 4373 (1994).

42. M. Church , Ph.D. Thesis, Columbia University, Nevis-260 (1986) (unpublished).

43. B. Stern, Ph.D. Thesis, Columbia University, Nevis-266 (1988) (unpublished).

44. M. J. Forbush, Ph.D. Thesis, Texas A&M University, 1990 (unpublished).

45. J. Uribe, Ph.D. Thesis, University of Massachusetts, UMAHEP-385 (1993) (unpublished).

46. L. R. Wiencke , Ph.D. Thesis, Columbia University, Nevis-280 (1993) (unpublished).

47. D. C. Christian *et al.*, Nucl. Instr. Meth. **A345**, 62 (1994).

48. D. C. Christian, Internal Memo to BNL E766 and FNAL E690 (1987).

49. R. Dzhelyadin *et al.*, NIM **351**, 228 (1994).

50. E. E. Gottschalk , Ph.D. Thesis, Columbia University, Nevis-278 (1992) (unpublished).

51. M. Jacob ,G.C. Wick , Annals of Physics **7**, 404 (1959).

52. S.U. Chung ,T.L.Trueman , Phys.Rev. **D11**, 633 (1975).

53. S.U. Chung, BNL Preprint BNL-QGS94-23.

54. S.U. Chung , BNL Preprint BNL-QGS95-41.

55. E. Barrelet , Nuovo Cimento **V8A**, N.2, 331 (1972).